Enhancement of Millimeter-Band Transceivers with Gap Waveguide Technology

Carlos Sánchez Cabello

A dissertation submitted by in partial fulfillment of the requirements for the degree of Doctor of Philosophy in

Multimedia and Communications

Universidad Carlos III de Madrid

Advisor

Eva Rajo Iglesias

September 2022

To my mother

Acknowledgment

Well, what can I say but THANK YOU to all those who have contributed in one way or another to the success of this doctoral stage. Starting with my family, both the one I can still enjoy and the one that, unfortunately, is watching and caring for me from heaven.

Thanks also to my colleagues in the lab: Náfsika, who was at the same point as I am now last year; to Nelson, for his help with the processing of measurement data; and to Jose Manuel, for his help in the design and fabrication of the antenna measurement brackets. I must also mention Ashraf (Sweden), Francisco (Chile) and Luisfer (Oviedo), co-authors with whom I have collaborated in several publications and projects with theoretical and fabrication aspects. Also to Diego, for his dedication and exquisite attention to detail during the antenna measurement process at the University of Alcalá de Henares. I also owe a big thank you to Prof. Ahmed Kishk, for his warm welcome in his research group at Concordia University during my stay in Montreal, which made the -20^o Canadian winter not so hard.

And above all, thanks to the exceptional team that makes up the GEA Research Group, formed by José Luis, Luis and my tutor Eva at the head. Without her, nothing of this would have been possible. For transmitting me her enthusiasm, her work capacity and for being available at any time to solve the problems, not all of them technical, that have arisen during these 4 years.

From this period, I take with me an excellent learning experience, but also the good fortune to have had the opportunity to get to know you.

TO ALL OF YOU, THANK YOU.

Contents

Related Publications

A. Indexed JCR journals

- **C. Sanchez-Cabello**, L. F. Herran, and E. Rajo-Iglesias, "Ka-Band Diplexer for 5G mmWave Applications in Inverted Microstrip Gap Waveguide Technology," Electronics, vol. 9, no. 12, p. 2094, Dec. 2020.
  doi:10.3390/electronics9122094
  This publication is fully included in Chapter 2.
  Whenever material from this source is included in this thesis, it is singled out with typographic means and an explicit reference.

- **C. Sanchez-Cabello**, L. F. Herrán, A. U. Zaman, and E. Rajo-Iglesias, "Ka Band Microstrip Fed Slot Array Antenna with PMC Packaging," IET Microw. Antennas Propag., vol. 14, no. 14, pp. 1837–1845, Nov. 2020.
  doi:10.1049/iet-map.2020.0565
  This publication is fully included in Appendix.
  Whenever material from this source is included in this thesis, it is singled out with typographic means and an explicit reference.

- F. Pizarro, **C. Sanchez-Cabello**, J.-L. Vazquez-Roy, and E. Rajo-Iglesias, "Considerations of Impedance Sensitivity and Losses in Designing Inverted Microstrip Gap Waveguides," en, AEU - International Journal of Electronics and Communications, vol. 124, p. 153 353, Sep. 2020, issn: 1434-8411. doi:10.1016/j.aeue.2020.153353.

  This publication is fully included in Chapter 1.

  Whenever material from this source is included in this thesis, it is singled out with typographic means and an explicit reference.

- N. Memeletzoglou, **C. Sanchez-Cabello**, F. Pizarro-Torres, and E. Rajo-Iglesias, "Analysis of Periodic Structures Made of Pins Inside a Parallel Plate Waveguide," Symmetry, vol. 11, no. 4, p. 582, Apr. 2019. doi:10.3390/sym11040582

  This publication is not included in this thesis.

B. International Conferences

- **C. Sanchez-Cabello**, Z. Sipus, and E. Rajo-Iglesias, "Consideration in Designing Holey Glided-Symmetrical Structures in Gap Waveguide," in 2022 Mediterranean Microwave Symposium, Pizzo Calabro, Italy, May 2022. *(Pending publication URL).*

  This publication is partially included in Chapter 4.

  Some content from this source is included in this thesis, it is singled out with typographic means and an explicit reference.

- F. Pizarro, **C. Sanchez-Cabello**, E. Obreque, J. Rojas, E. Rajo-Iglesias, and M. Diaz, "3D-printed Patch Antenna for Satellite IoT Communications in CubeSat," in 2022 IEEE Global Communications Conference, Rio de Janeiro, Brasil, Dec. 2022. *(Submitted for acceptance).*

  This publication is not included in this thesis.

- L. Inclan-Sanchez, **C. Sanchez-Cabello**, J. L. Vazquez-Roy, and E. Rajo-Iglesias, "New EBG-Filter Design in Inverted Microstrip Gap Waveguide Technology," in 2017 IEEE International Symposium on Antennas and Propagation & USNC/URSI National Radio Science Meeting, San Diego, CA, USA, Jul. 2017, pp. 1663–1664.

  doi:10.1109/APUSNCURSINRSM.2017.8072874

  This publication is not included in this thesis.

- **C. Sanchez-Cabello**, L. Inclán-Sánchez, J. Vázquez-Roy, and E. Rajo-Iglesias, "Design of Antenna Feed with Amplified Power Distribution using Groove-Gap Waveguide Technology," in 2017 11th European Conference on Antennas and Propagation (EUCAP), Paris, France, Mar. 2017, pp. 1661–1664.

  doi:10.23919/EuCAP.2017.7928449

  This publication is fully included in Chapter 5.

  Whenever material from this source is included in this thesis, it is singled out with typographic means and an explicit reference.

- **C. Sanchez-Cabello** and E. Rajo-Iglesias, "Optimized Self-Diplexed Antenna in Gap Waveguide Technology," in 2015 IEEE International Symposium on Antennas and Propagation & USNC/URSI National Radio Science Meeting, Vancouver, BC, Canada, Jul. 2015, pp. 460–461.
  doi:10.1109/APS.2015.7304616
  This publication is partially included in Chapter 2.
  Whenever material from this source is included in this thesis, it is singled out with typographic means and an explicit reference.

- **C. Sanchez-Cabello** and E. Rajo-Iglesias, "Low Cost Self-Diplexed Antenna in Inverted Microstrip Gap Waveguide Technology," in 2014 International Symposium on Antennas and Propagation Conference Proceedings, Kaohsiung, Taiwan, Dec. 2014, pp. 169–170.
  doi:10.1109/ISANP.2014.7026584
  This publication is partially included in Chapter 2.
  Whenever material from this source is included in this thesis, it is singled out with typographic means and an explicit reference.

C. National Conferences

- **C. Sanchez-Cabello**, Luis Inclan-Sanchez, Jose Luis Vazquez-Roy, Eva Rajo-Iglesias, "Integración de Amplificador MMIC en Transición Microstrip Groove Gap Waveguide". 2016 Union Radio-Scientifique Internationale (URSI), Madrid, Spain; 09/2016. Webpage: URSI2016
  This publication is fully included in Chapter 5.
  Whenever material from this source is included in this thesis, it is singled out with typographic means and an explicit reference.

List of Figures

List of Figures

List of Tables

List of Tables

Introduction

It is known to all that year after year in modern society there is an urgent demand to consume wirelessly, and even stream ever larger multimedia content. High-frequency technologies have made it possible to go from transmitting analog voice and SMS text messages, to now transmitting live video in 4K quality from a mid-range smartphone. The way to measure these advances is by the bandwidth (Mb/s) reserved for each network user and the cost required to achieve it.

To achieve even higher bandwidths, it is essential to improve signal coding techniques or increase the frequency of the signal, for example: to the mmWave bands (25GHz - 100 GHz), where these high-frequency techniques come into play.

However, there is a frequency limit where current planar technology materials - such as the printed circuit boards used to build RF devices - are so lossy that they are not suitable at these mmWave frequencies. Current commercial solutions consist of guiding the electromagnetic energy with hollow metallic waveguides, but they suffer from the problem that as the frequency increases the diameter of these waveguides gets smaller and smaller, so manufacturing tolerances increase exorbitantly. Not to mention that they are usually manufactured in two parts, one upper and one lower, whose joints are not always perfect and produce energy losses.

With these issues in mind, in 2009 the theory and basic science of a new electromagnetic energy guidance technology called Gap Waveguide was proposed, which is based on the use of metasurfaces constructed with periodic elements similar to

a bed of nails. There are several implementations of this technology, but the three main ones are: Ridge, Groove and Inverted Microstrip Gap Waveguide. The latter is the most compatible with conventional planar manufacturing technologies and therefore the most cost-effective, although it also has drawbacks mainly in terms of losses when compared to the other versions.

This thesis aims to deepen the study of the Inverted Microstrip guidance technology, its limitations and to develop with it some of the needed components in RF systems such as filters, diplexers, amplifiers, antennas, etc.

Regarding the methodology for this thesis, a commercial simulation software for the analysis of antennas and components, CST Microwave Studio [1], has been used. AWR Microwave Office [2], a circuit simulator, has also been used to complement the simulations.

On the other hand, there is a laboratory for the manufacture of prototypes in printed technology (with some limitations in terms of resolution) and the corresponding measurement laboratory, which includes network analyzers up to 40 GHz, spectrum analyzers and an anechoic chamber.

In general, the work methodology has been:

-Study of the state of the art, i.e., bibliographic search of existing designs and identification of the characteristics of these that are intended to be improved.

-Design using simulation tools. Throughout the design phase of the different components and antennas, it is foreseeable that it will be necessary to carry out some kind of study or even the development of models to avoid trial-and-error designs.

-Manufacture and measurement of prototypes for experimental validation. In many cases this requires a previous phase of revision of tolerances and manufacturing limits, as well as a mechanical study.

-Publication of the results in JCR journals, as well as their presentation at in-

ternational congresses.

This thesis arose under the Spanish Ministry of Science and Innovation (MINECO) and European Regional Development Fund (ERDF) project, called "Antenna for Mobile Satellite Communications (SATCOM) in Ka-Band by means of metasurfaces (2016-2019)", with reference TEC2016-79700-C2-2-R. Under this contract, the author signed an FPI research contract.

Thesis Structure

This thesis is mainly divided into two parts. **Part I** is dedicated to the advances obtained with the Inverted Microstrip version of the Gap Waveguide technology whose scheme will be:

- Chapter 1: This chapter begins by describing in a general way, as an introduction to this first part of the thesis, the technology and basic science behind the discovery of the Gap Waveguide solutions. It then focuses on the design considerations when implementing Inverted Microstrip Gap components, as well as various loss and impedance studies.

- Chapter 2: Based on the findings presented in Chapter 2, this section proposes a novel Ka-band diplexer based on Inverted Microstrip Gap. It starts with the bandpass filter designs, and then, with the power divider that performs the diplexer function.

- Chapter 3: As a continuation of the previous chapter, this chapter proposes a hybrid diplexer-splitter for use with dual-band antennas in Inverted Microstrip Gap Waveguide (IMGW). Several dual-band radiating elements that may be compatible with integration into this antenna-diplexer module are also presented.

In **Part II** several advances in designs with the Groove Gap version are proposed. In detail:

- Chapter 4: Here we present the work developed with an antenna with a

sum and difference pattern. In this case, the implementation of Groove technology is made by using a periodic surface Glide Symmetric Holey EBG, whose main advantage lies in the significant reduction in manufacturing cost compared to its traditional version with periodic surfaces made together with pins.

- Chapter 5: This chapter describes the design process of a feed with distributed amplification in conventional pin-based Groove Gap waveguide technology. The integration of active circuits is a challenge for the Gap Waveguide technology that needs to be solved in order to achieve a complete transceiver in this technology.

In **Part III** the most important conclusions of this thesis, together with future lines of interest are presented.

- Appendix: This appendix presents the excellent results that the Gap Waveguide technology offers as a packaging solution for mm-Wave and higher band devices designed in conventional technologies such as microstrip. In particular, the development of a wideband antenna slot array ($> 10\%$) is described. The detailed design process of the corporate feed network and a subarray to study the radiation characteristics before modelling the complete system are presented including the final prototype.

Part I

Design of Inverted Microstrip Gap Waveguide Components

Chapter 1

Inverted Microstrip Gap Waveguide Design Considerations

1.1 Gap Waveguide Technology Background

The market economy and its globalization of the last two decades has had a strong impact on trade, especially in consumer electronics, shifting the pole of mass and low-cost manufacturing of this equipment to countries in the East and, mainly, to China. This has turned it into the giant we all know and on which supply chains throughout the West depend to a large extent.

In addition to the falling cost of Internet-enabled mobile devices such as smartphones and tablets, there have been advances in the miniaturisation of the transistors used in chipsets. This has led in recent years to increasingly demanding requirements for wireless consumption of digital content. As a result, there has been exponential growth and massive adoption around the world, changing the paradigm of multimedia consumption and personal communications. Displacing traditional desktop computers with personal mobile computing that makes intensive use of wireless communications; making the future slogan heard in the 2000's about the 3G mobile communication standard: "Every one, every time and every where" a reality. [3]

This is also facilitating the creation of new market niches such as the IoT (Internet of Things) and the spread of applications that were unthinkable until recently due to their low quality and high latency, such as high-resolution international video calls; or due to the low capacity of the wireless access network and its geographical deployment, necessary for the increasingly widespread autonomous car or critical applications such as remote surgery, where the remote handling of robotic equipment required minimum latencies that are now becoming possible. [4]

To meet these digital needs, several solutions have been offered to the market. One of them is the improvement in signal processing to increase the quality of service (QoS), which allows high-priority data packets such as those corresponding to voice communications and, above all, real-time video to be unaffected by the congestion produced by the exponential increase in global traffic. In addition to advances in signal processing, one parameter that improves this QoS is the maximum point-to-point latency offered by the network. This is achieved, among other things, by moving more and more of the network's intelligence and data processing from the backbone (Core) to the access nodes. [5]

However, the electromagnetic spectrum is a limited resource, and its availability by telecommunications operators is limited not only by administrative but also by technical regulations. Therefore, another solution to increase the bandwidth available to each user is through broadband techniques and modulations such as OFDM, spectrally efficient multi-carrier techniques (SC-FDMA, FBMC) or multi-antenna techniques (MIMO, networking MIMO, massive MIMO).

But these solutions face the limitation of the maximum frequency available in the transmission channel. Therefore, it is essential to develop technologies with good performance at higher frequencies to support the rest of the solutions described above.

Since, as discussed earlier, the paradigm that the consumer market is trending towards is broadband, high capacity, ubiquitous and minimum latency wireless com-

munications, the components that make up the transceivers used in RF equipment as well as antennas need to be adapted to higher frequencies, typically above 30 GHz while keeping the manufacturing cost low for mass adoption and commercially profitable. The blockchain of a classic transceiver or RF frontend can be seen in Fig. 1.1.

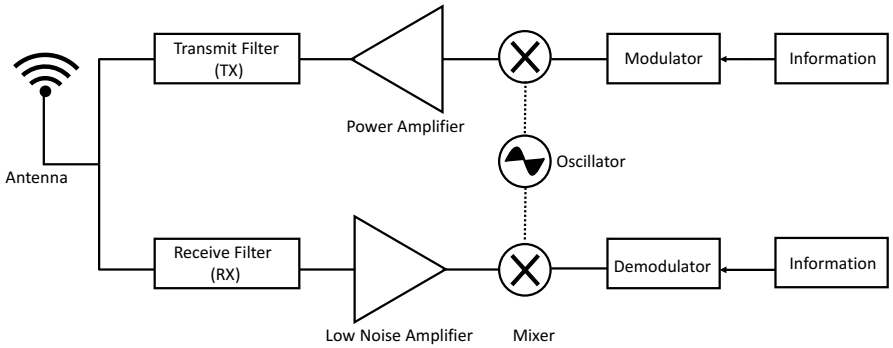

Figure 1.1: *Block diagram of a generic wireless communications system.*

If we are talking about high bandwidths, optical fiber is one of the best options. However, although great advances are being made, for the moment, at the ends of the transmission chain it always needs to be integrated with electrical circuits, whose most efficient and economical design would be working at optical frequencies without employing modulators from THz to the low operating frequencies of these electrical circuits. [6]–[10]

Ideally, the guiding technology on which this thesis is based would allow the manipulation of signals directly at the transmission frequency of these high-frequency systems. As a leading-edge technology in high-frequency electromagnetic energy guidance, the so-called Gap-Waveguide presented in 2009 [11], and later patented [12], solves two major problems encountered with commercially available waveguides. The technology is so promising that a Swedish-based company, Gapwaves

AB was created some years ago and it is now commercializing the technology.

One of them is the losses of existing planar technologies based on dielectric substrates, which become more pronounced with increasing frequency [13]–[15]. After its presentation to the scientific community in 2001 by Ke Wu [16], Substrate Integrated Waveguide (SIW) [17]–[20] based PCB solutions and applications with metallized vias making walls have been proposed that significantly improve the ohmic and radiation losses at high frequencies while maintaining a moderate cost. However, still requiring a substrate through which the energy propagates, their losses remain a limiting factor for the development of very high frequency solutions.

On the other hand, those related to the machining of metallic hollow guides whose diameter is reduced with the increase in frequency, and therefore, the manufacturing tolerances are inversely proportional to their profitability for large-scale production. In addition to the disadvantage of having to manufacture them in two pieces that, even if the manufacturing tolerances are very high, there are always power leaks with variations of 20%-35% with respect to the theoretical values of the simulations [21]. Ensuring a good electrical contact between the two parts that allows a continuity of currents is a technical problem widely studied but still poorly solved. [11], [22]–[26].

In addition, there is the fact that essential components in many devices such as narrow band (high Q) filters suffer a lot from manufacturing tolerances and small imperfections can lead to large frequency deviations. Not to mention the insertion losses that substrate-based filters present at mm-wave band frequencies. [27]

The physical principle of this new guiding technology stems from the fundamentals of hard and soft surfaces, which, depending on various parameters such as periodicity, height and orientation of the corrugations arranged longitudinally (*hard*) or transversely (*soft*), allow (*hard*) or block (*soft*) the propagation of electromagnetic energy [28], [29]. However, this technology makes use of an EBG (Electromagnetic Bandgap) surface that blocks propagation in all directions without regard to the orientation of the corrugations since they are designed as two-dimensional periodic

surfaces in the form of PMC (Perfect Magnetic Conductor). There have been previous studies [30]–[32] focusing on open surfaces and guides. The novelty of this technology is the possibility to create guides and transmission lines locally between two parallel metal plates by controlling the propagation of parallel plate modes [11].

The principle of operation can be seen in Fig. 1.2, where if we have a PEC and a PMC boundary condition, separated from each other less than $\lambda/4$, there is not any solution of Maxwell´s Equations (no propagation between this boundary condition plates) [33]. So with this in mind, we can create a waveguide with a PEC path between the two bottom PMC surfaces. The problem is how we can make a PMC surface, because no natural material exists with PMC properties, but we can synthesize a Metasurface, that functions as an "Artificial Magnetic Conductor" within a frequency range.

To date, numerous high-impedance periodic surfaces have been proposed that replicate the PMC boundary conditions [32], [34]. From the first ones made with rectangular metallic pins, where in [35] have been mathematical characterized, passing through pyramid-shaped pins [36], mushroom-type surface [32], [37], spring-shaped pins [38], or with the novel technique of employing perforations in the metal to create the required EBG [39]–[43]. A new Half-Groove Gap Waveguide for rapid prototyping, lowering its cost for mass production has also been recently presented to the community [44].

The performance of this EBG structure is determined by the dimensions of the periodic elements we use to build these high impedance surfaces. Particularly for the general case with pins (width, period, height), the height is the most determinant parameter to fix the frequency at which the propagation blocking is observed [45]. But not only does this principle work at frequency f_0, but in a range of these, which we call "stop-band". The PMC boundary condition is created in a plane over the pins.

There are works with in-depth parametric studies on various types of unit cells

and their influence on bandwidth, stop-band and propagation modes as in [45] and in [46] as co-author, where higher symmetries are studied and interesting design conclusions are provided.

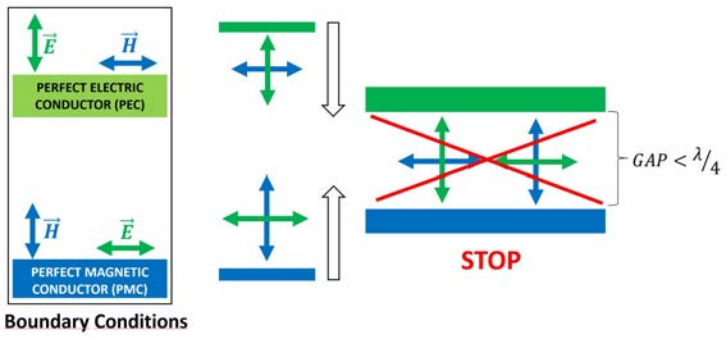

(a) *Each of the boundary conditions represented as PMC (blue) and PEC (green) plates forces a polarization of the electric and magnetic field. If these plates are gradually brought closer together, there will come a time when the distance (gap) between PEC and PMC is less than λ/4, at which point all electromagnetic propagation is blocked. This gap height determines the stopband of the Gap Waveguide.*

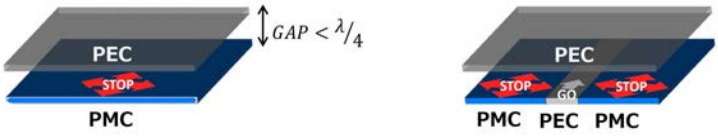

(b) *Guiding mechanism between parallel PEC and PMC plates with the propagation blocking zones marked until another PEC zone is included through which the energy can be propagated.*

Figure 1.2: *Operating concept of the Gap Waveguide technology.*

From the theoretical conception of this new guidance technology, different versions have been proposed and their operating principles and devices have been experimentally validated at frequencies as high as 320 GHz [47] by simply scaling the dimensions and modifying the manufacturing methods and technologies.

Up to now, Groove Gap Waveguide (GGW) [48], Ridge Gap Waveguide (RGW) [49], Inverted Microstrip Gap Waveguide (IMGW) [50] and a printed variation of the Ridge have been proposed, denoted, Microstrip Ridge Gap Waveguide or Printed Ridge Gap Waveguide (PRGW) [51]. The cross section of each of them along with their fundamental propagation mode are shown in Fig. 1.3.

Each of these versions stands out from the others in terms of losses, cost, ease of manufacture or integration with existing commercial planar technologies. Thanks to their concept of parallel metallic plate-to-plate guidance, they are a highly recommended option for integration with aperture antennas.

An advantage of the Inverted Microstrip Gap Waveguide (IMGW) and Ridge Gap Waveguide technologies is that they allow propagation of quasi-TEM modes, which makes them easily integrated with printed technologies and other transmission lines, while the Groove Gap version propagates TE/TM modes, much like rectangular waveguides.

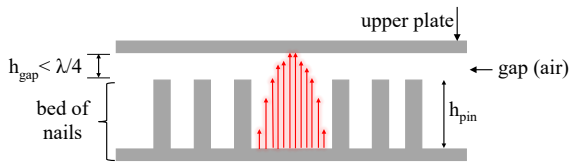

(a) *Groove Gap Waveguide cross section with plotted field distribution (TE/TM modes propagation).*

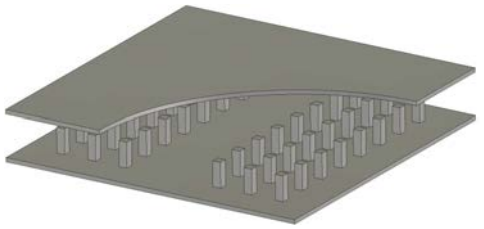

(b) *Groove Gap Waveguide 3D model.*

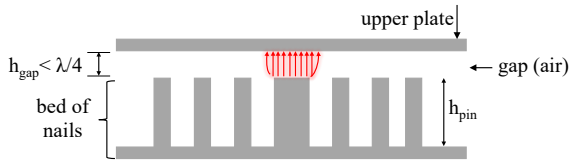

(c) *Ridge Gap Waveguide cross section with plotted field distribution (QTEM mode propagation).*

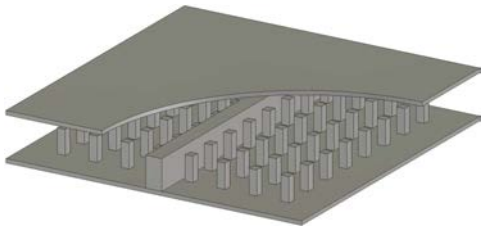

(d) *Ridge Gap Waveguide 3D model.*

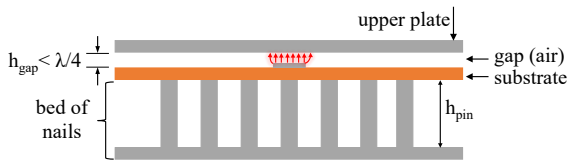

(e) *Inverted Microstrip Gap Waveguide cross section with plotted field distribution (QTEM mode propagation).*

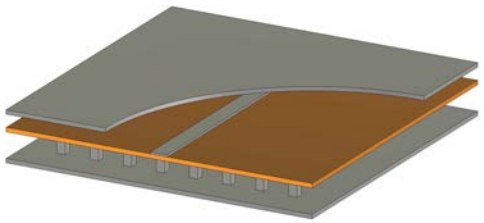

(f) *Inverted Microstrip Gap Waveguide 3D model.*

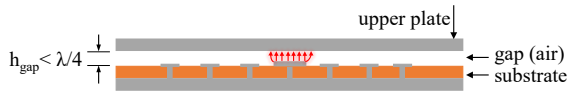

(g) *Microstrip Ridge Gap Waveguide cross section with plotted field distribution (QTEM mode propagation).*

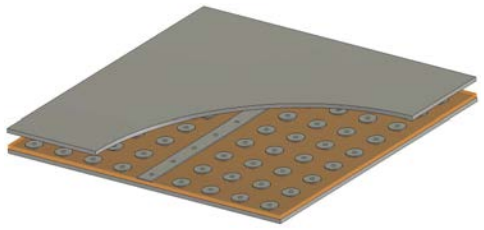

(h) *Microstrip Ridge Gap Waveguide 3D model.*

Figure 1.3: *The different versions of the Gap Waveguide technology developed and researched to date, highlighting their propagation modes.*

The first experimental verification of the Gap Waveguide technology in [49] has been followed to date by numerous circuit and antenna designs based on it. For example, filters are already available [52]–[59], couplers [60]–[66], diplexers [67]–[73], aperture antennas [74]–[81] and their corresponding feed networks [82]–[86] or the

various transitions needed to connect to conventional connectors and guides [87]–[100].

Focusing on the Inverted Microstrip Gap Waveguide version, we can start by looking at the advantage of using it even at frequencies as low as X-band. The simulated transmission coefficient $|S_{21}|$ between different microstrip versions is shown in Fig. 1.4. For this example of a double bend 90° line, we see how the conventional microstrip versions suffer from much higher losses, mainly due to radiation at the bend discontinuities, as well as because they use the substrate as the energy propagation medium. Whereas in the *gap* version the field travels largely through the air and confined along the transmission line as we see in Fig. 1.5.

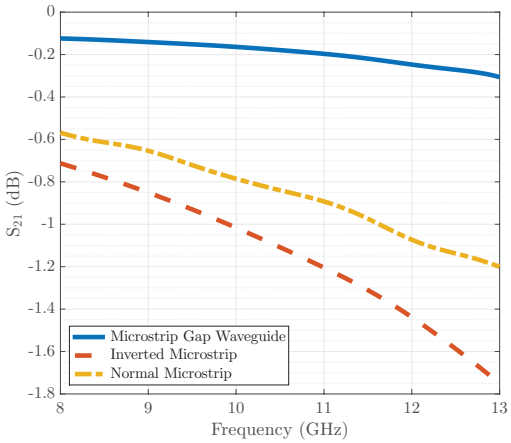

Figure 1.4: *Comparison of $|S_{21}|$ parameter for a double bent line: Conventional Microstrip, Inverted Microstrip and Inverted Microstrip Gap.*

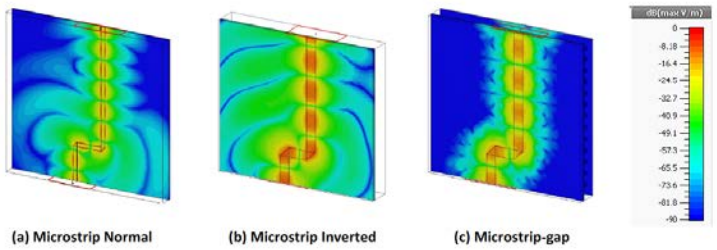

Figure 1.5: *Representation of the E field for the three microstrip versions.*

We must shed light on some delicate aspects of this Inverted Microstrip Gap Waveguide version. Despite all the works already published on devices that use it, we find that there is a lack of practical design guides in the literature, which clearly analyze the influence of the various parameters that make up this technology such as pin density or substrate thickness on aspects that are necessary to take into account for the design such as impedance value and losses suffered.

Previous studies have found that this technology suffers greatly with the density of the pin bed, as it can alter the relative location of the printed lines with the pins under the substrate, and with it, the characteristic impedance, greatly complicating circuit design. In addition, as higher frequencies are used, the substrates necessarily become thinner and susceptible to bending which can also cause disturbances in propagation across the air gap, as this also modifies the impedance.

1.2 Study of the Line Impedance

Since the appearance of the Gap Waveguide technology, one of the challenges has been to characterize and obtain its characteristic impedance [101]. Something that prevents its calculation in the traditional way of a conventional inverted microstrip line is the use of metamaterials made with periodic surfaces. Different ways of calculating its value have been proposed in the literature. Beginning with the approximation of [102] to the more accurate one of [103], or based on the use of variational methods [104]. In [105] some first sensitivity analyses were already proposed with respect to some elements that define this technology.

The objective of this section is to investigate the sensitivity of the characteristic impedance of the inverted microstrip gap waveguide line according to design parameters such as the dielectric thickness and the period of the pinned surface.

For these cases, where lines loaded with periodic elements are involved, we need to deal with their Bloch impedance [106]–[110]. These waves analyses in periodic

structures are based on the study of the propagation of forward and backward waves existing in each unit cell, mathematically modeled as a cascaded lattice of unit cells, defined by a matrix of amplitudes [106]. It can then be particularized for symmetric 2-port terminated and truncated networks. Or, in other words, one way to proceed is to start from an infinite number of these elements which, subsequently, must be truncated and add input/output ports; together with the corresponding impedance transformers to adapt them to the input impedance of these ports [111].

Therefore, in order to perform the necessary parametric studies, we will use a set of circuital parameters that are perfectly adapted to ladder network topologies. For this, we start from the definition of the ABCD parameters, where we can obtain the characteristic impedance of a homogeneous transmission line. Since, as we know from basic high frequency circuit theory [112], we can define these ABCD parameters of an ideal lossless line with characteristic impedance Z_0, length l and propagation constant $\gamma = j\beta$ as in Eq. 1.1:

$$\begin{pmatrix} A & B \\ C & D \end{pmatrix} = \begin{pmatrix} \cos\beta l & jZ_0 \sin\beta l \\ jY_0 \sin\beta l & \cos\beta l \end{pmatrix} \tag{1.1}$$

that, particularizing for the reciprocal and symmetric case, we can obtain Z_0 as in Eq.1.2:

$$Z_0 = \sqrt{\frac{B}{C}} \tag{1.2}$$

From this, we can concatenate more two-port networks with $N-1$ periods in order to iteratively reduce the size to that of a unit cell as proposed in the publications [113] and [114] in order to avoid mathematical instabilities related to the complex quadratic solution of Eq. 1.2.

And so, we combine the parameters to have:

- 3 widely used impedance transmission lines, whose widths are shown in parentheses for the nominal ideal case with PMC surface under the inverted microstrip line substrate: 35 Ω ($w = 3.6$ mm), 50 Ω ($w = 2.19$ mm) and 70 Ω ($w = 1.25$ mm).
- 2 substrate thicknesses: $h_{sub} = 0.508$ mm and $h_{sub} = 0.762$ mm.
- 2 pin periods: $p = 1.6$ mm and $p = 2.5$ mm.
- 2 positions of the line w.r.t. the rows of pins. (See Fig. 1.6).

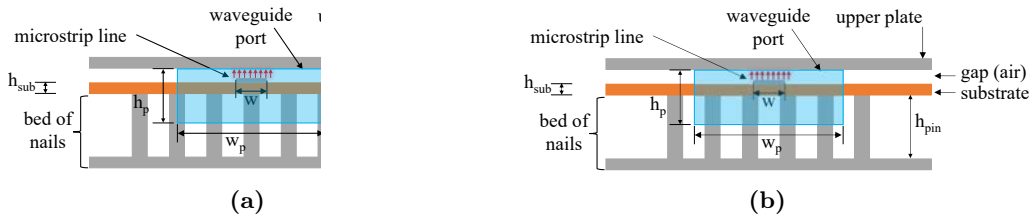

Figure 1.6: *Cross section of Inverted Microstrip Gap Waveguide with its most important parameters and the CST Studio Waveguide port dimensions, showing the differences between routing: a) over one row of pins or b) between two rows of pins. Air gap must be* $h_{gap} < \lambda/4$.

We keep constant in all calculations the pin width (0.8 mm) and air gap (0.508 mm) on the ideal RO4003C substrate without losses. The frequency used is 30 GHz and the number of stages $N = 6$.

Regarding the feeding port configuration, the procedure followed to adequately size the waveguide ports in CST [1] should be highlighted. An analysis with ideal boundary conditions (PEC, PMC) was performed to determine the most suitable size to excite the periodic structure since the size has a significant influence on the simulations. Fig. 1.7 shows that from a port size of 4 times the microstrip line width, the values are already sufficiently accurate by covering the quasi-TEM mode of the line cross section. Moreover, as already discussed in depth in [115] for the practical

realization of the PMC with a bed of pins, the ports are extended to cover half of the pin height; and towards the top plate part until it contacts the top plate (see Fig. 1.6).

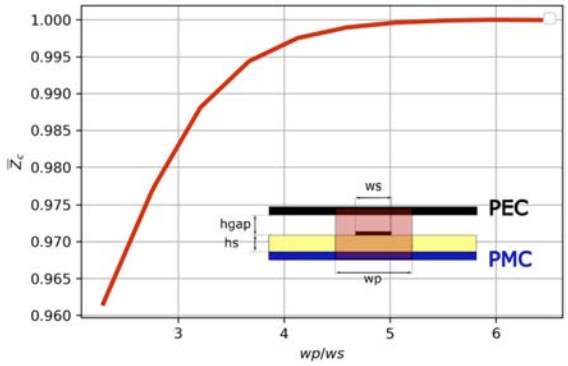

Figure 1.7: *Normalized characteristic impedance vs. wp/ws simulated with ideal boundary conditions PMC and PEC.*

Results

The results obtained with the parameter combinations described above are presented in Fig. 1.8.

Although in these graphs we see an overview of the variations for each linewidth case with respect to the nominal case with PMC, to improve their visualization and to obtain better conclusions, it is convenient to normalize these values and show them as a function of the "impedance relative error" with respect to this nominal case as in Eq. 1.3. All these simulated and normalized results are shown in Fig. 1.9.

$$IRE(\%) = \frac{Z_{pin} - Z_{PMC}}{Z_{PMC}} * 100 \tag{1.3}$$

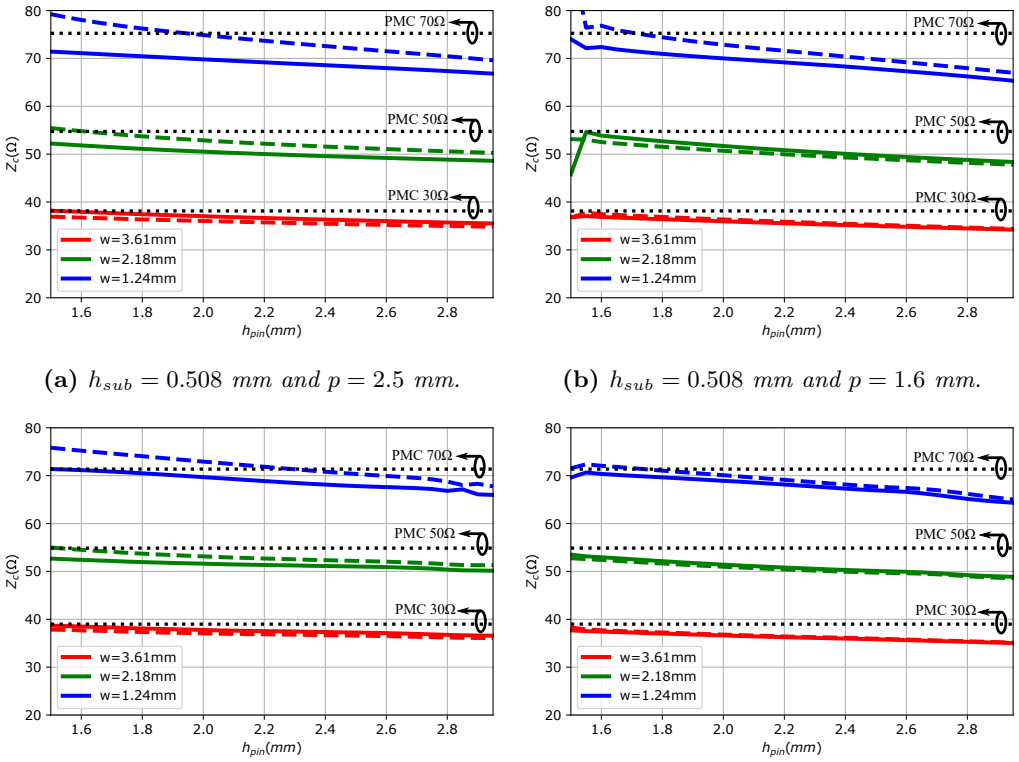

(a) $h_{sub} = 0.508\ mm$ *and* $p = 2.5\ mm$.

(b) $h_{sub} = 0.508\ mm$ *and* $p = 1.6\ mm$.

(c) $h_{sub} = 0.762\ mm$ *and* $p = 2.5\ mm$.

(d) $h_{sub} = 0.762\ mm$ *and* $p = 1.6\ mm$.

Figure 1.8: *Simulated results obtained from the characteristic impedance according to the proposed calculation method for various combinations of parameters as a function of pin height (i.e., influence within the stopband), substrate thickness and pin period. Depending on the relative position w.r.t. to the pin row, they are shown in solid lines (between 2 pins) or dashed lines (over the pin row).[116]*

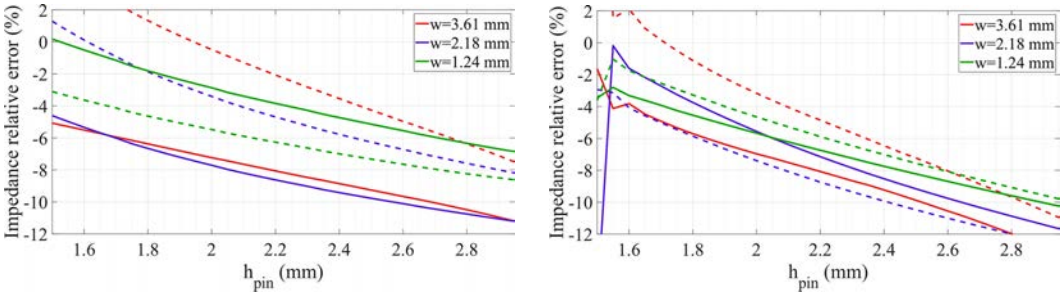

(a) $h_{sub} = 0.508$ *mm and* $p = 2.5$ *mm.* **(b)** $h_{sub} = 0.508$ *mm and* $p = 1.6$ *mm.*

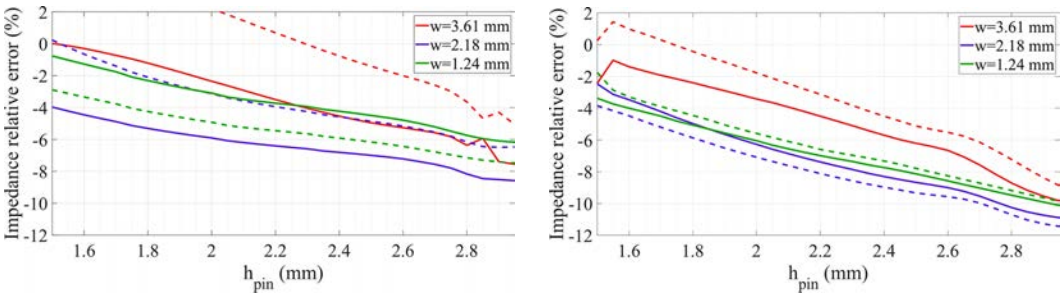

(c) $h_{sub} = 0.762$ *mm and* $p = 2.5$ *mm.* **(d)** $h_{sub} = 0.762$ *mm and* $p = 1.6$ *mm.*

Figure 1.9: *Relative error to the nominal case for the different cases shown in Fig. 1.8. Data obtained for a frequency of 30 GHz, $N = 6$ versus the nominal case with PMC, for different pin heights, different substrate thickness, and depending on the position relative w.r.t. to the pin row, are shown in solid lines (between 2 pins) or dashed lines (above the pin row).[116]*

Some conclusions we can be drawn from these results:

- **Using the thicker substrate ($h_{sub} = 0.762$ mm) results in the impedance being maintained with less variation as a function of pin height.**
- **For denser bed of nails ($p = 1.6$ mm), the difference between the impedance between pins and over pins is smaller**, as already advanced in [105], [117].
- As the height of h_{pin} increases, the variation with respect to the nominal case with PMC also increases both in absolute terms and in terms of relative error.
- Except for the case $w = 3.61$ mm with the smallest pin heights h_{pin}, in all cases the impedance is always lower than the nominal case.
- The anomalies observed in plots b) and d) for the smaller pin heights are

explained by the closeness of the frequency to the lower limit of the lid of pins stop-band. Fig. 1.10 shows the different stopbands for various study cases.

- On the impedance variation as a function of the relative position of the line with respect to the rows of pins, there is no clear conclusion in general terms. However, for the case $h_{sub} = 0.508$ mm we conclude that the relative error is larger when the line is located between two rows of pins.

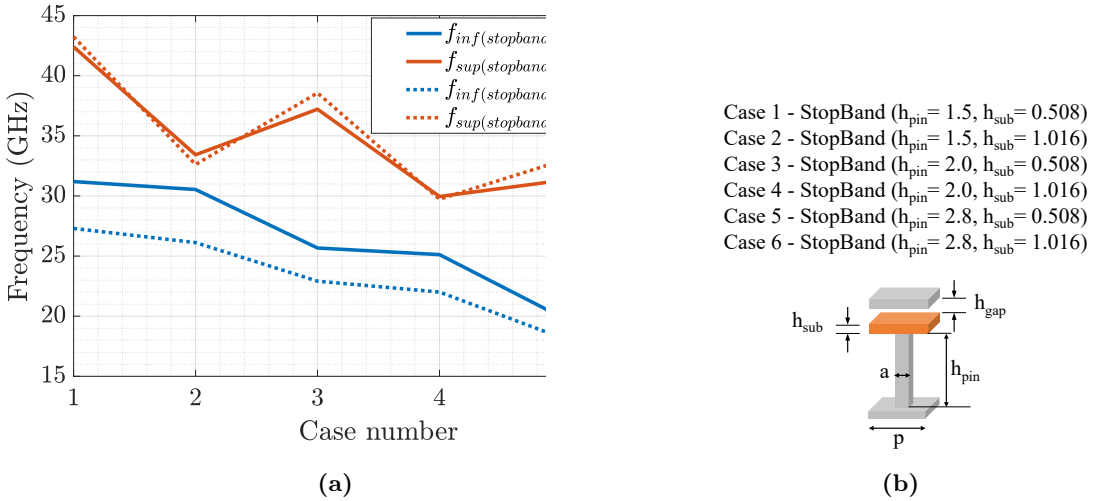

(a) **(b)**

Figure 1.10: *Lower and upper limits of the stopbands as a function of the case analyzed, together with the corresponding unit cell dimensions in mm.*

1.3 Study of the Line Attenuation

In addition to impedance, another important factor to consider when designing high-frequency devices are the losses. This is specially relevant in the case of this version of Gap Waveguide where, although most of the energy propagates through the air, still needs a substrate to support the printed circuit boards.

1.3.1 Method 1 : Through Resonators

There are several methods to calculate the losses of these transmission lines. One of them is by studying the Q factors in resonator circuits. This quality factor measures the ratio between dissipated energy and stored energy. We know from [112], that for transmission lines with TEM type propagation modes the attenuation can be calculated as:

$$\alpha = \frac{\beta}{2Q_U} \tag{1.4}$$

with β as the propagation constant.

$$\frac{1}{Q_L} = \frac{1}{Q_U} + \frac{1}{Q_E} \tag{1.5}$$

And where according to [118], [119] for 2-port networks, the external quality factor Q_E is given by Equation 1.6:

$$Q_E = 10^{-S_{21}/20} Q_L \tag{1.6}$$

And so, according to [120] one can rewrite Q_U as a function of S_{21} as:

$$Q_U = \frac{Q_L}{1 - S_{21}} \tag{1.7}$$

For this purpose, and following the method of [121] where it had already been studied for the Groove and Ridge versions, but not for Inverted Microstrip, X-band resonators were designed for convenience in order to perform the measurements with SMA connectors.

We know that if the ports are weakly coupled, Equation 1.7 can be approximated as $Q_U \approx Q_L$, and this Q_L can be defined as follows in 1.8. [112]:

$$Q_L = \frac{f_o}{\Delta f_{3dB}} \tag{1.8}$$

So, at this point, a first approach is made by modeling a short-circuit resonator with inverted microstrip gap on a low-cost bed of nails in order to be able to perform numerous tests and variations. For this purpose, M2 metric screws are chosen as cylindrical pins and the full-wave simulator CST Studio Suite is configured with PEC as boundary conditions on the sidewalls. The stopband created by the unit cell loosely covers this frequency band. In Fig. 1.11 we see the simulated results for different commercial standard substrate thicknesses and as a function of the relative position of the printed line with respect to the central row of screws.

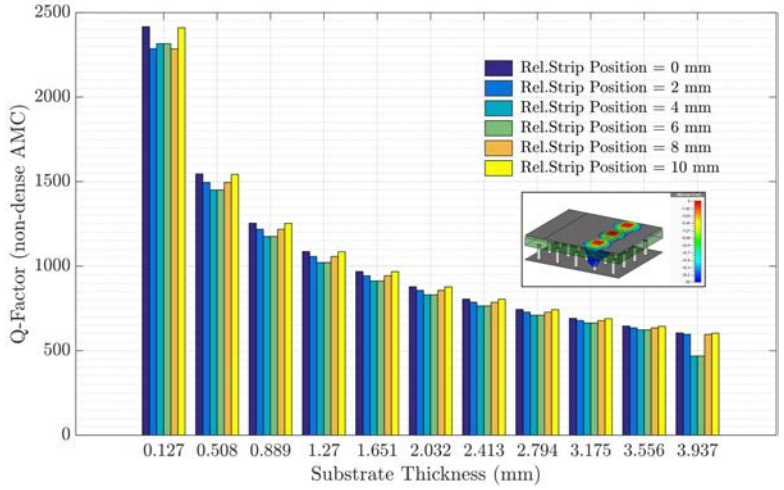

(a) *Low Density AMC (Pin Period=10 mm)*

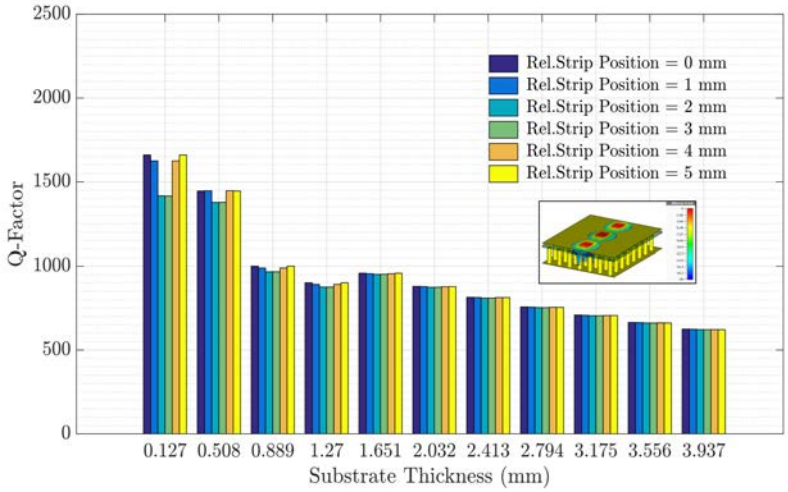

(b) *High Density AMC (Pin Period=5 mm)*

Figure 1.11: *Comparison of the Q factor of a third order short-circuit resonator as a function of the 11 standardized thicknesses of the lossy dielectric RO4003C with ideal metals PEC; and 5 positions of the resonator line with respect to the row of pins under it.*

From this preliminary analysis, it is clear that the losses increase with the substrate thickness in all cases. On the other hand, the location of the microstrip w.r.t. the pins has a very small effect on the losses. Finally, the periodicity of the pins that is critical in order to achieve a more independent line impedance is practically not affecting the losses.

However, it is necessary to verify the data experimentally. To this aim, from

the aforementioned work [121], we know that open-circuit resonators present less discrepancies between simulation and measurement than short-circuited ones, so the models were made in this way from here on; particularizing only for 2 thicknesses and 2 periodicities of the bed of nails as we see in Fig. 1.12 and 1.13. Note that when obtaining the Q values using the 3dB width of the resonance seen in S_{21} (Equation 1.8), the "Transient" solver of CST in the time domain is not valid due to its low resolution and extremely long simulation time in highly resonant circuits, being necessary to make a tetrahedral mesh and use the frequency domain solver (Fig. 1.14 and 1.15).

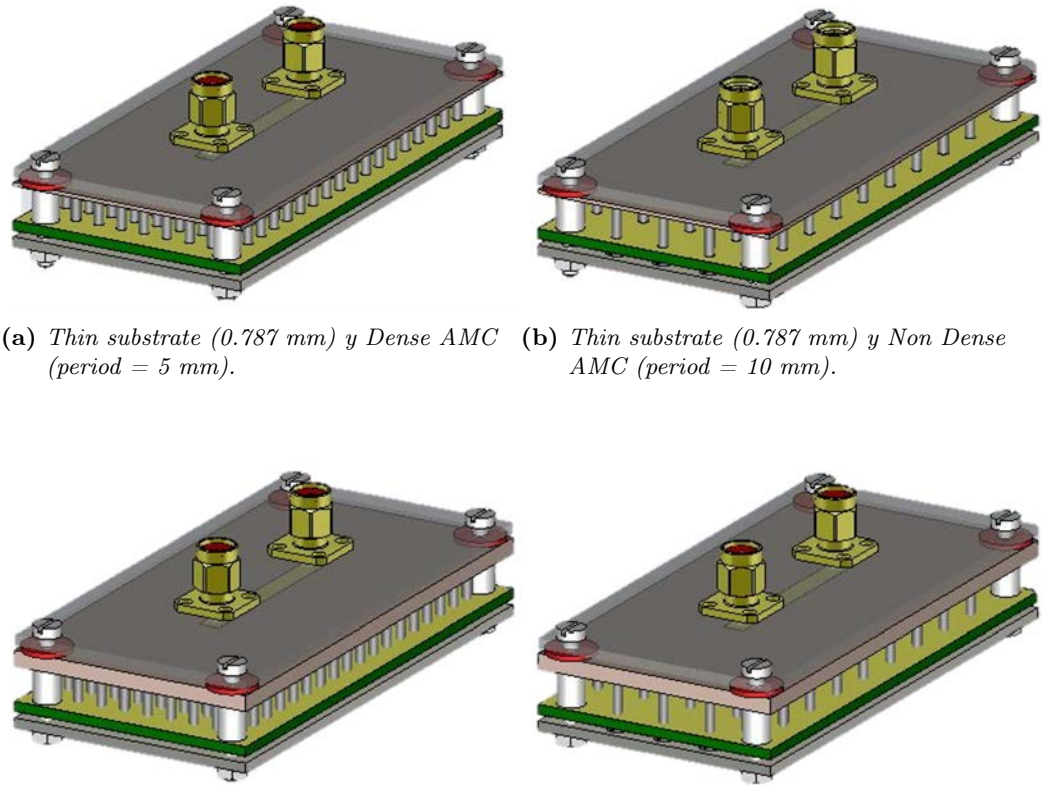

(a) *Thin substrate (0.787 mm) y Dense AMC (period = 5 mm).*

(b) *Thin substrate (0.787 mm) y Non Dense AMC (period = 10 mm).*

(c) *Thick substrate (3.175 mm) y Dense AMC (period = 5 mm).*

(d) *Thick substrate (3.175 mm) y Non Dense AMC (period = 10 mm)*

Figure 1.12: *3D models of built open-circuit resonators.*

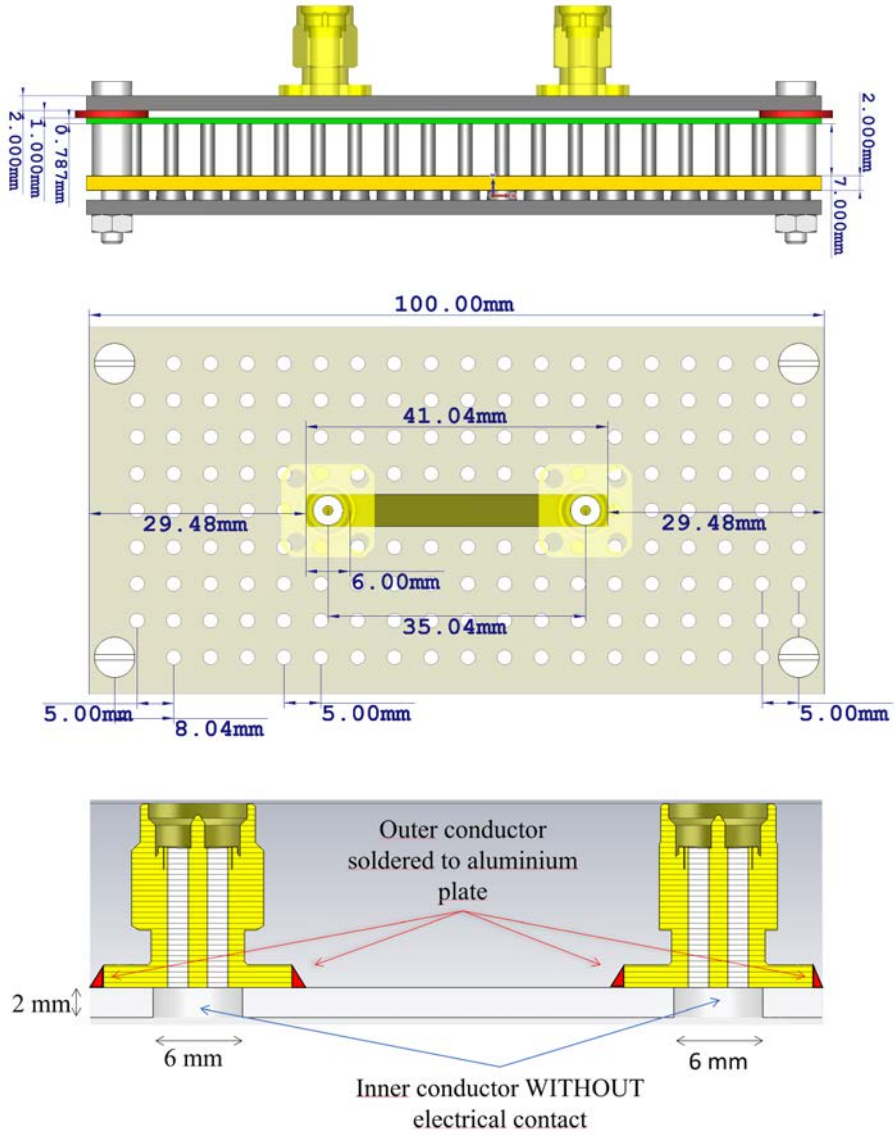

Figure 1.13: *Dimensions and assembly scheme of the model made with thin substrate (0.787 mm) and with dense bed of nails (período=5 mm). Note the way of fastening the screws vertically on the metal plate with a perforated FR4 substrate embracing the heads and giving rigidity to the whole together with nylon spacers (white) and Teflon spacers (red) for the 1 mm gap.*

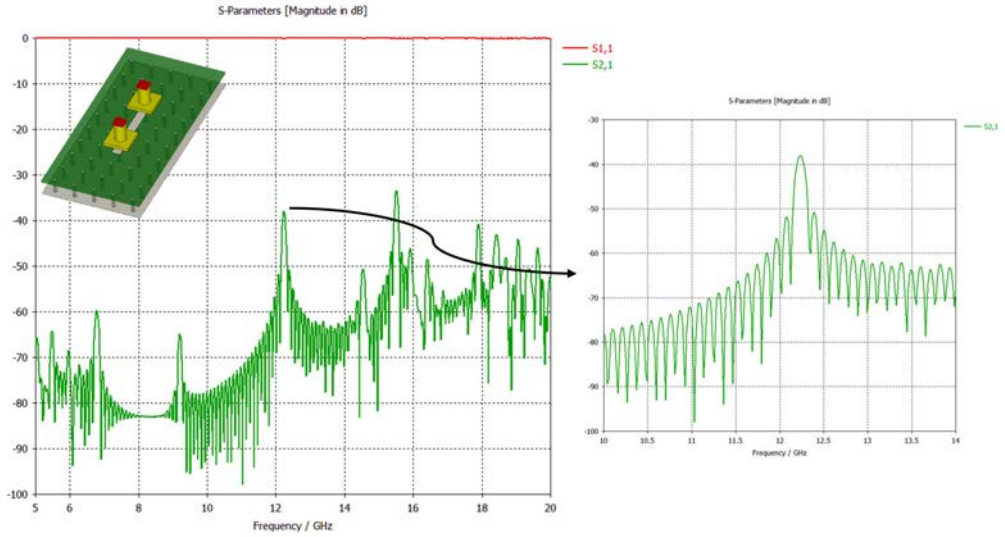

Figure 1.14: *Resonances simulated using the Transient solver of CST Studio Suite for open-circuit resonator.*

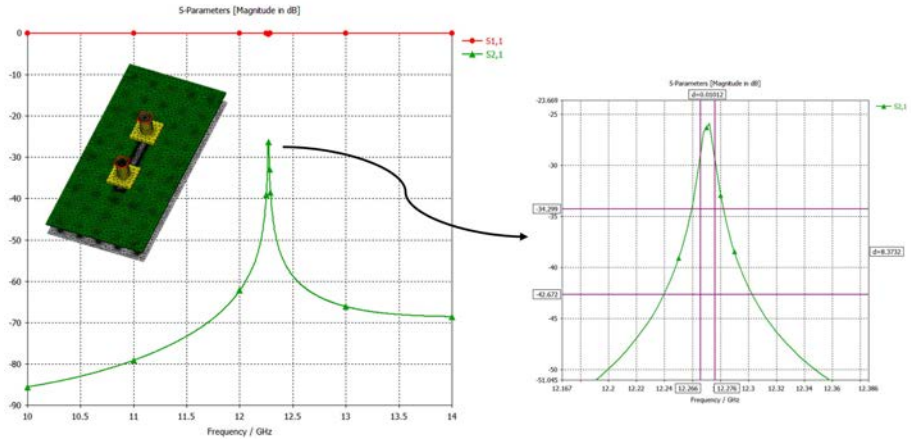

Figure 1.15: *Resonances simulated using the Frequency solver of CST Studio Suite for open-circuit resonator.*

However, the first Q tests in the laboratory gave an erratic result, probably due to the poor electrical contact in the way the screws forming the bed of nails were arranged, or perhaps their low conductivity, even though they were made of metal. Therefore, a milled plate with metal pins was used for the following tests, although its cost was considerably higher. In Fig. 1.16 we see the difference between the two bed of nails solutions and in Fig. 1.17 the detail of the weakly coupled ports that allow us to make the approximation $Q_U \approx Q_L$.

Figure 1.16: *Low cost bed of nails with screws vs. new bed of nails machined with metal pins.*

Figure 1.17: *Detail of weakly coupled ports in the resonators.*

The measurement process of the resonators with the VNA Rohde & Schwarz ZVA40 after calibration with the Rosenberger RPC-2.92 02CK010-150 kit is shown in Fig. 1.18. The results obtained from the measurements versus the simulated values are presented in Fig. 1.19. These simulated values were calculated with the CST F-solver with the following options: 3rd variable order, Adaptive Meshing (to refine the meshing in the parts where there is more energy) and the rest of the options were left as default. Table 1.20 compiles all the values obtained after measurements versus simulated ones.

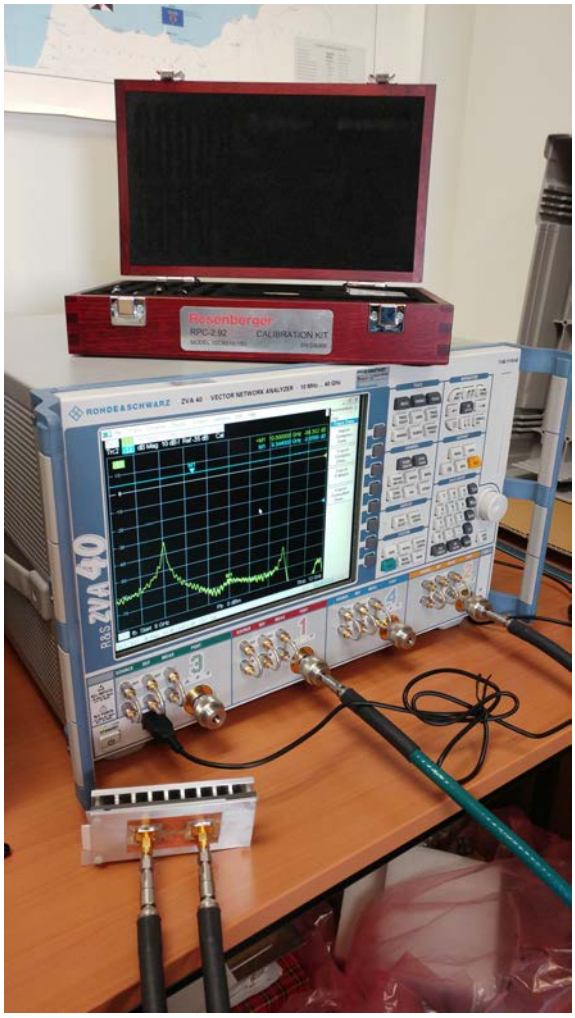

Figure 1.18: *Measurement process of open-circuit resonators in Inverted Microstrip Gap Waveguide technology.*

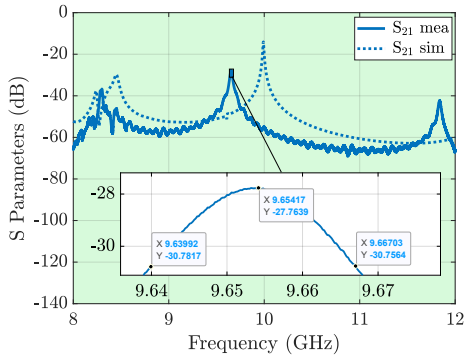

(a) *Thin substrate (0.787 mm) and Dense AMC (period = 5 mm).*

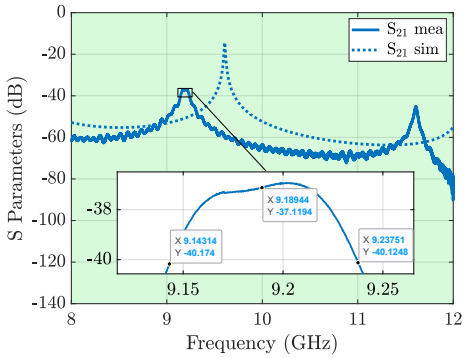

(b) *Thin substrate (0.787 mm) and Non Dense AMC (period = 10 mm).*

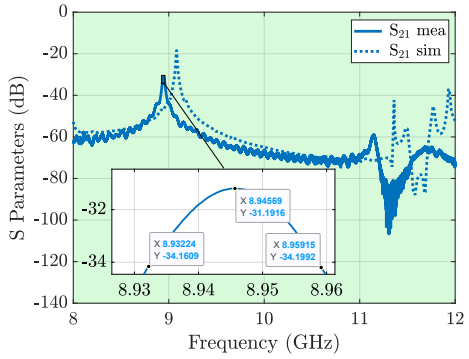

(c) *Thick substrate (3.175 mm) and Dense AMC (period = 5 mm).*

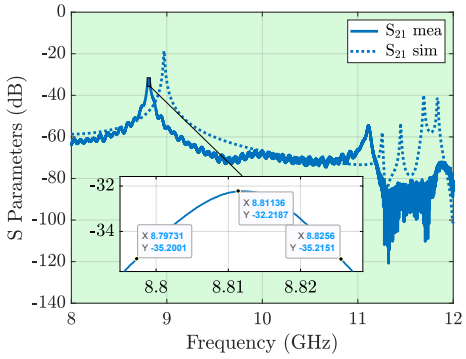

(d) *Thick substrate (3.175 mm) and Non Dense AMC (period = 10 mm)*

Figure 1.19: *Simulated vs. measured results for obtaining the Q of open-circuit resonators.*

	SIMULATIONS			MEASUREMENTS			DIFFERENCES, %		
	$Q_U(S_{21})$	f (GHz)	α (dB/m)	$Q_U(S_{21})$	f (GHz)	α (dB/m)	$Q_U(S_{21})$	f	α
t=10 mm H=3.175 mm	844	8.9712	0.111310	304	8.811	0.303515	**63.98**	1.786	63.3
t=5 mm H=3.175 mm	855	9.0818	0.111233	331	8.946	0.283028	**61.28**	1.495	60.7
t=10 mm H=0.787 mm	889	9.6062	0.113156	**96**	9.189	1.002364	**89.20**	4.343	**88.7**
t=5 mm H=0.787 mm	928	9.9906	0.112738	357	9.654	0.283183	**61.53**	3.369	60.2

Figure 1.20: *Simulated and measured attenuation values for the 4 types of open-circuit resonators in Inverted Microstrip Gap Waveguide.*

1.3.2 Method 2 : Transmission Through Long lines

As the differences between the simulated and measured values were too large to draw conclusions, an alternative method was considered to study how the different design parameters of the Inverted Microstrip Gap Waveguide technology influence its losses as well as the influence of the operating frequency within the stopband.

For sufficiently high frequencies in the region of 30 GHz, it is feasible to measure the attenuation of sufficiently long lines of at least 10λ as in the work of [122], [123]. To this aim, different parameters have been combined based on a 50 Ω line with 2.18 mm width and 10 cm length, on a Rogers substrate RO4003C^{TM} (ε_r = 3.55, tanδ=0.0027). The air gap value is kept at the same 0.508 mm of the previous impedance section; as well as the pin width at 0.8 mm. The thickness of the substrate takes values of 0.508 mm and 1.016 mm (to be named as "thick" in the plots). The periodicity of the pins will range between these 2 values: 1.6 mm and 2.5 mm. The height of these pins will take values of 1.5 mm, 2.0 mm and 2.8 mm. Regarding the position of the line w.r.t. to the rows of pins we will take into account two possible cases: between two rows of pins and when the line is centered on a row of these pins (Fig. 1.21). Finally, regarding the material of the pins, two versions are examined: one, modeled as perfect electric conductor (PEC); and the other, with aluminum, with a finite conductivity.

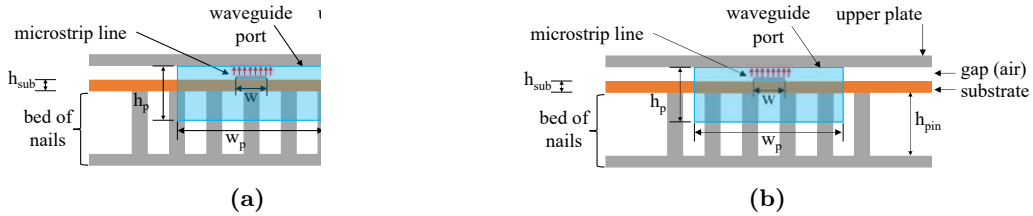

Figure 1.21: *Cross section of Inverted Microstrip Gap Waveguide with its most important parameters and the CST Studio Waveguide port dimensions, showing the differences between routing: a) over one row of pins or b) between two rows of pins. Air gap must be $h_{gap} < \lambda/4$.*

Table 1.1: *Combinations of parameter values used in the simulations for the study of influence on losses.*

Description	**Parameter**	**Values**		
Gap	gap	0.508 mm		
Pin Width	a	0.8 mm		
Substrate thicknesses	h_{sub}	0.508 mm	1.016 mm ("thick")	
Pin periodicity	p	1.6 mm	2.5 mm	
Pin height	h_{pin}	1.5 mm	2.0 mm	2.8 mm
Line position w.r.t. pines	pos	In between pins rows	Over pins row ("shifted")	
Pin metallic material	material	PEC	Aluminium ("lossy")	

In Fig. 1.22 we see a compilation of the simulated results for the combinations of values mentioned in Table 1.1. The "nominal" case refers to a substrate $h_{sub} = 0.508$ mm, pins modeled as ideal and the line placed centered between two rows of pins (not "shift") (see Fig. 1.21).

From the plots we can conclude that the losses are higher whenever a thicker h_{sub} substrate is used, as well as with the use of pins with finite aluminum conductivity. The periodicity of the pins p and the relative position of the line on them hardly affect the simulated losses. The height h_{pin} modifies the stopband of the bed of nails, producing distortions especially at frequencies close to the lower limit of the bed of nails, so it is not advisable to operate in these areas.

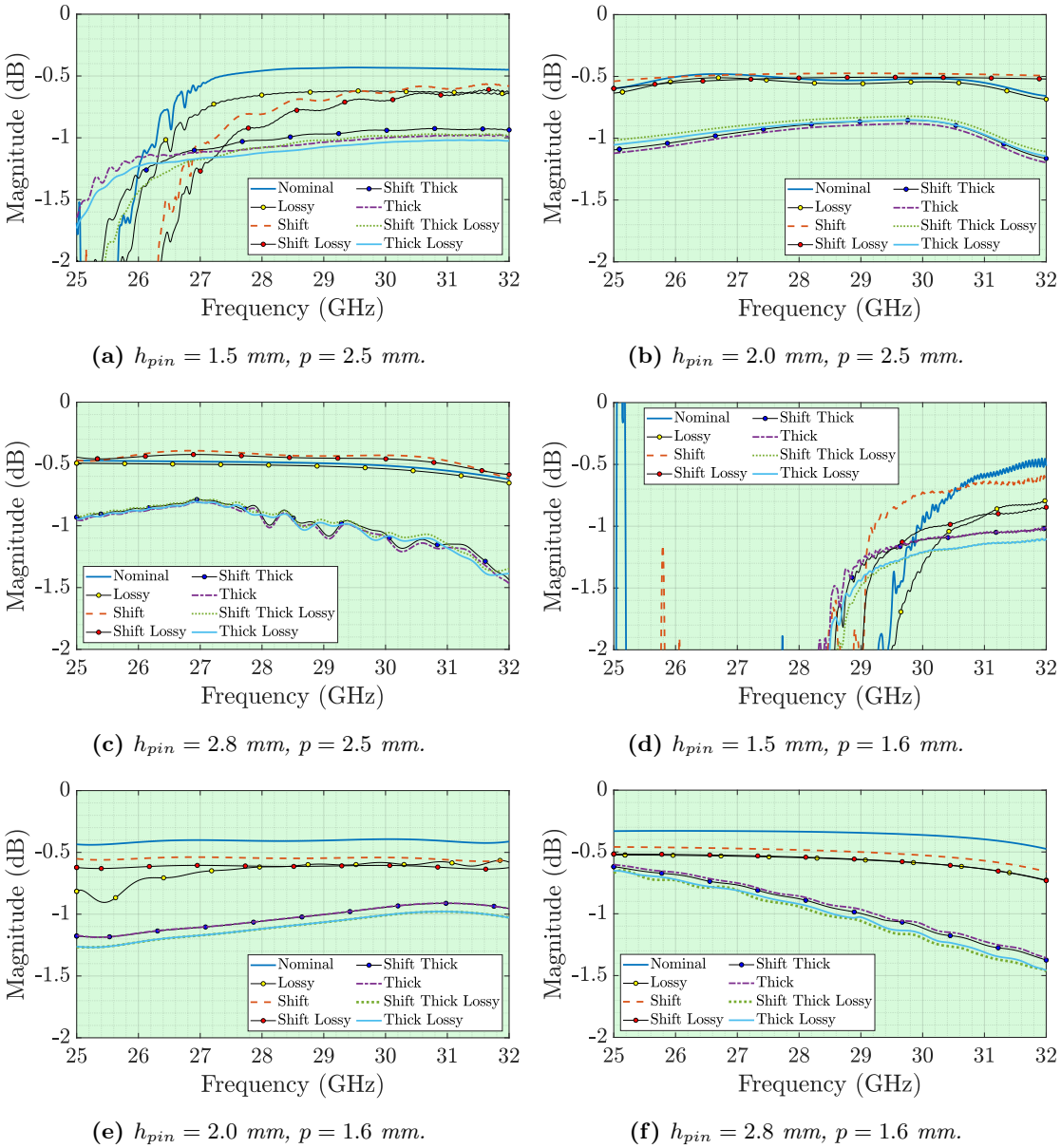

(a) $h_{pin} = 1.5\ mm,\ p = 2.5\ mm.$ **(b)** $h_{pin} = 2.0\ mm,\ p = 2.5\ mm.$

(c) $h_{pin} = 2.8\ mm,\ p = 2.5\ mm.$ **(d)** $h_{pin} = 1.5\ mm,\ p = 1.6\ mm.$

(e) $h_{pin} = 2.0\ mm,\ p = 1.6\ mm.$ **(f)** $h_{pin} = 2.8\ mm,\ p = 1.6\ mm.$

Figure 1.22: *Simulated losses as attenuation of the transmission factor $|S_{21}|$ for different cases of pin heights, periods between pins from a) to f). Each figure contemplates different cases of study: Two substrate thicknesses and two relative positions of the Inverted Microstrip Gap Waveguide line (on pins or offset between two rows).[116]*

Results

To experimentally test the hypotheses obtained with simulations, two bed-of-nails prototypes are built with the values from Table 1.2. In Fig. 1.24 we see the fabricated model together with a transition to conventional 50Ω microstrip to place the Southwest 1092-04A-5 End-Launch connectors. As usual, to eliminate the influence of the connectors on the measurements, a TRL calibration kit has also been engineered and built.

To design the transition, we follow the indications of [124], where they use the same dielectric material for this transition as for the inverted circuit. In Fig. 1.23a we can see the corresponding geometry of this transition. This is designed starting from the inverted microstrip gap line with the width to obtain a characteristic impedance of 50 Ω with this RO4003C substrate and air gap dimension, *i.e.*, w = 2.2 mm. At the end, this width is reduced to that corresponding to an impedance of 50 Ω for the same frequency in RO4003C substrate (w = 1.24 mm). Finally, over these reduced width sections, the air gap is used to insert inverted sections of conventional microstrip line of the same line width with the ground plane in contact with the metallic top cover. Fig. 1.23b shows the good results achieved in matching (below −15 dB) and its low losses (about −0.5 dB) in the band of interest. Simulated S-parameters include lossy materials: aluminum pins, copper lids and metallizations, and Rogers substrate. Fig. 1.23c shows the normalized E field distribution in this transition.

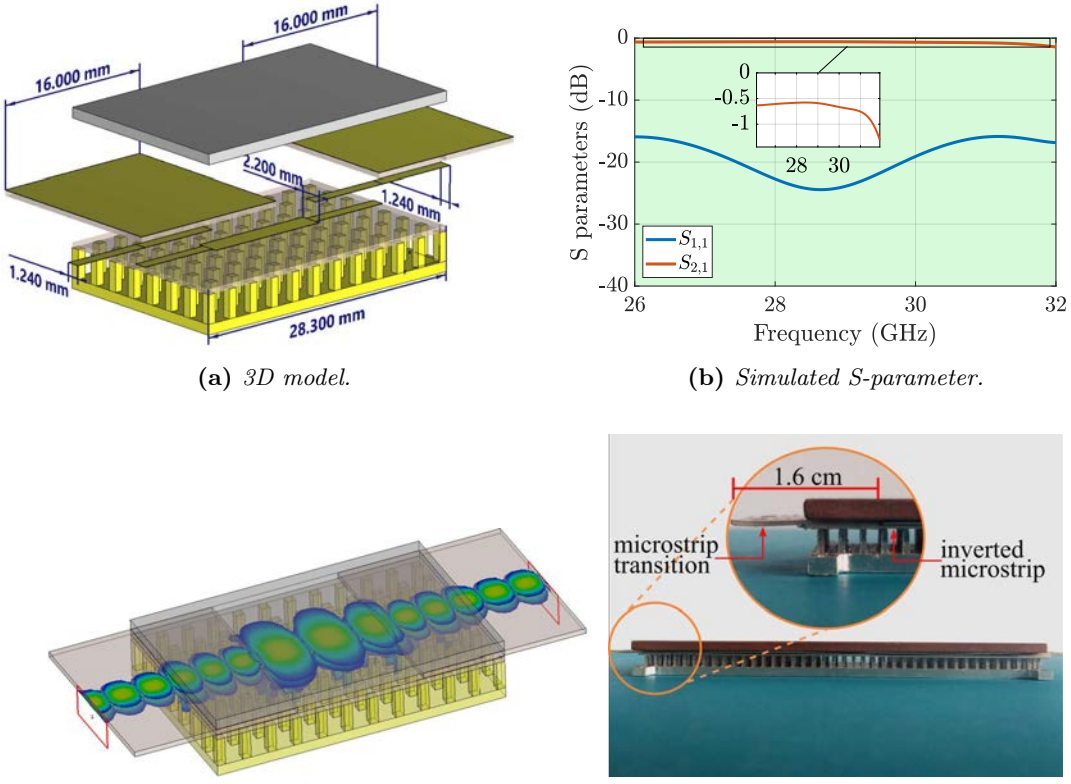

(a) *3D model.*

(b) *Simulated S-parameter.*

(c) *E field distribution (3D view).*

(d) *Detail of the manufactured prototype.*

Figure 1.23: *B2B transition from Inverted Microstrip Gap Waveguide to conventional Microstrip.*

The results of the measurements compensating for the effect of the connectors for the four parameter combinations are shown in Fig. 1.25. The equipment used to perform them was an ANRITSU MS46122B VNA.

As expected, **the losses increase with the use of thicker substrates and with increasing frequency**. The f_{sup} marks in the figure indicate the frequency that restricts the stopband in each case where distortions similar to those simulated can be seen.

Table 1.2: *Selection of selected parameters for the loss study prototypes.*

Description	Parameter	Values		
Gap	gap	0.508 mm		
Pin Width	a	0.8 mm		
Substrate thicknesses	h_{sub}	0.508 mm	1.016 mm ("thick")	
Pin periodicity	p		2.5 mm	
Pin height	h_{pin}		2.0 mm	2.8 mm
Line position w.r.t. pines	pos	In between pins rows		
Pin metallic material	material		Aluminium ("lossy")	

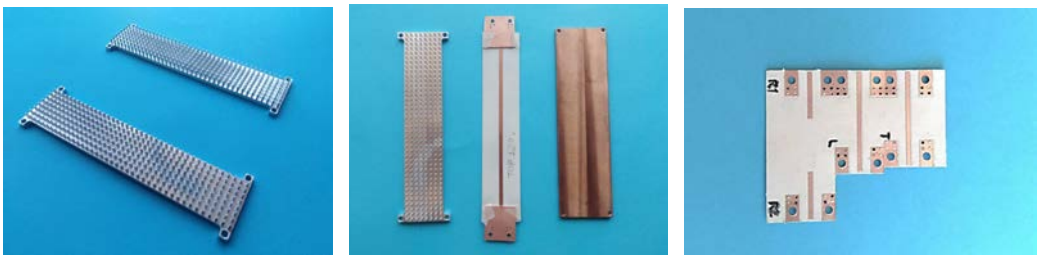

(a) **(b)** **(c)**

Figure 1.24: *Prototype of 10 cm transmission line built in Inverted Microstrip Gap Waveguide with Rogers RO4003C substrate: a) The 2 bed of nails used for the measurements, both of period $p = 2.5$ mm and heights $h_{pin} = 2.8$ mm and 2.0 mm. b) Final assembly of the prototype. c) TRL calibration kit used to eliminate the influence of the End-Launch connectors.*

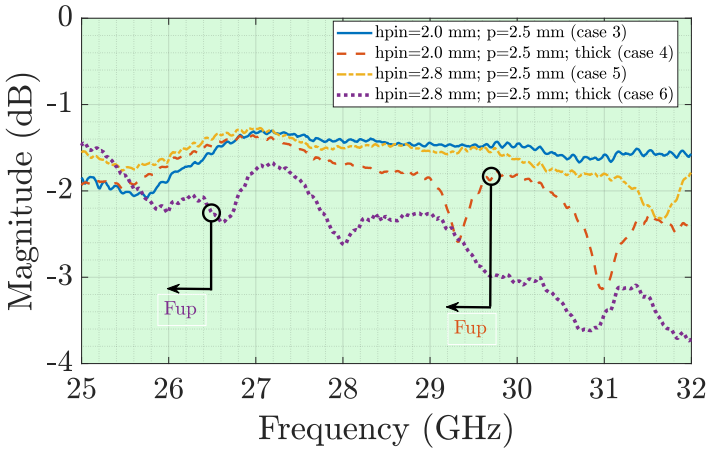

Figure 1.25: *Measured $|S_{21}|$ parameter for the manufactured models for the cases chosen from the Table 1.2.*

1.4 Conclusions

This chapter provides an in-depth study of the influence of the parameters required for the design of Inverted Microstrip Gap Waveguide lines and how they influence the characteristic impedance and losses in order to give a basis for design considerations that are useful from the practical point of view of the design of devices based on this technology. The first part analyzes how the impedance of the inverted microstrip gap line varies as a function of the periodicity of the bed of pins.

The first conclusions we can draw are that using thicker substrates means that the impedance is maintained with less variation depending on the height of the pins. In addition, for denser bed of nails, the difference between the impedance between pins and over pins is smaller. Another fact that we can conclude is that working at frequencies near the lower limit of the stopband, can cause anomalies in the calculations. These cases bring the practical realization of the BoN closer to the ideal case with PMC.

Regarding losses, it has been experimentally demonstrated that the use of thicker substrates will produce more losses; and that the other design parameters such as the relative position of the line on the pins or the periodicity of the BoN have hardly any influence. However, these losses will always be much lower than those of solutions with conventional microstrip or inverted microstrip.

Chapter 2

Ka-band Diplexer in Inverted Microstrip Gap

In this chapter, the design of a diplexer in Inverted Microstrip Gap Waveguide technology is presented. This device is widely used in transceivers. [125]

2.1 Diplexer Design

When designing circuits in this technology, the first thing to consider is the metamaterial in the form of periodic pins to be used. In addition, it is necessary to choose the most suitable bandpass filter topology for this application.

In a first phase of the design process, parallel coupled line filters were chosen as those employed in [117]. However, although previous studies have been conducted in which the performance at frequencies as low as 10 GHz is as expected [67], for Ka-band, parallel coupled line filters suffer from large tolerance issues due to their position with respect to the pins under the substrate.

In-depth studies on these tolerances have already been detailed in the previous chapter. For this reason, End-Coupled bandpass filters have been chosen, following

the methodology described in [126]. In this type of filters there is much less influence on the impedance due to the location of the lines with respect to the pins under the substrate. The diplexer will be used to separate the frequency bands of 24 and 28 GHz.

2.1.1 Bed of nails selection

As explained above, the Gap Waveguide technology needs to emulate a Perfect Magnetic Conductor (PMC) surface, which does not exist in nature, with an Artifical Magnetic Conductor (AMC) in the form of a bed of nails for its simplicity of fabrication. With the stopband in mind covering both operating bands of both filters (24 GHz and 28 GHz), a unit cell is designed with the dispersion diagram shown in Fig. 2.1. Because of its availability, in a first phase of the design, a Rogers RO4003C^{TM} (ε_r = 3.55, tanδ=0.0027) substrate was chosen. From the following unit cell dimensions, we obtain a stopband from 18.10 to 29.66 GHz: substrate thickness = 0.508 mm; pin height = 3 mm; gap = 0.5 mm, period = 2 mm and side = 1 mm. However, due to the poor results obtained with the diplexer using this substrate, the very low loss RO5880^{TM} substrate (ε_r = 2.2, tanδ = 0.0009) is finally chosen. The dispersion diagram for this material is added to Fig. 2.1.

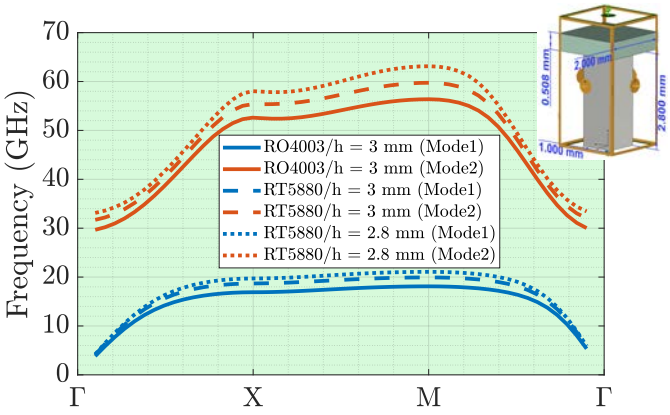

Figure 2.1: *Stopbands for substrate 4003C vs 5880 in 2 different pin heights (2.8 mm and 3 mm). The dispersion diagram is included for the 5880 substrate on which the diplexer will be finally designed, constructed and measured.*

2.1.2 Filters Design

For the design of circuits in Inverted Microstrip Gap it is advisable to start with the PMC ideal boundary condition under the substrate for its simplification and computational cost savings. Afterwards, we have to add to the preliminary design with PMC, the bed of nails. Here, we will have to perform more computationally expensive adjustments and simulations but predictably in smaller number.

A good approach to the filter design process is the one followed in [127]. In order to add precision we must handle the discontinuity by including the effect of the pins under the microstrip lines. This is done with the considerations of [126] as a π-network of capacitances as presented in Fig. 2.2a,b. For different values of the discontinuity gap we obtain different values of the Y-parameters for this 2-port network.

Subsequently, by means of Equation (2.1) we obtain the associated capacitances.

$$C_g = -\frac{Im(Y_{21})}{\omega_0};\ C_p = -\frac{Im(Y_{11}+Y_{21})}{\omega_0} \tag{2.1}$$

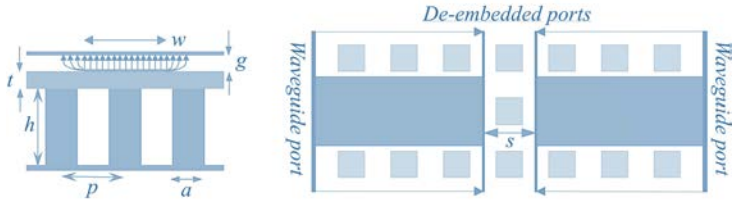

(a) *End-coupled lines discontinuity effect in Inverted Microstrip Gap Waveguide technology.*

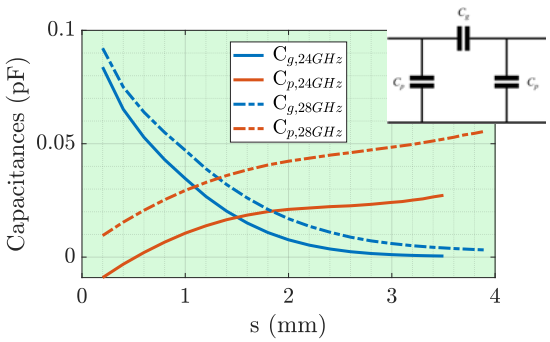

(b) *Simulation of the capacitances for different gap sizes. Discontinuity model with π-network capacitors inset*

Figure 2.2: *Discontinuity model with capacitors in Inverted Microstrip Gap Waveguide technology.*

From these initial data, we can make modifications with the CST full-wave simulator. Following the classical procedure, two Chebyshev End-Coupled fifth order band pass filters are designed, with a bandwidth of 3.3% and 0.5 dB of ripple in the passband at center frequencies of 24 GHz and 28 GHz, but by subsequent adjustments, the highest possible flatness in the passband was sought. The starting dielectric material is RO4003C$^{\text{TM}}$ (ε_r=3.55;tanδ=0.0027).

The result is shown in Fig. 2.3. We see three versions of the design: the first one, with the PMC boundary condition, and the remaining ones with pins either considering substrate and metal losses or not. Passband losses of about 1.6 dB are achieved. We can highlight the great similarity between the models with PMC and with pins.

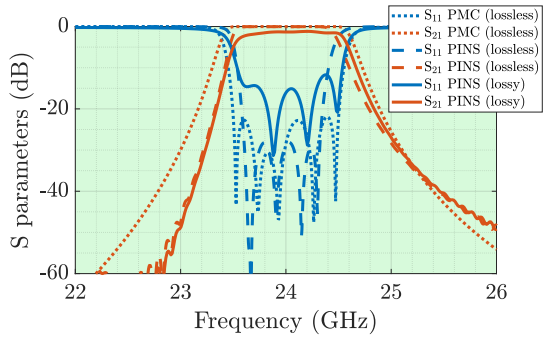

(a) *24 GHz inverted microstrip gap filter.*

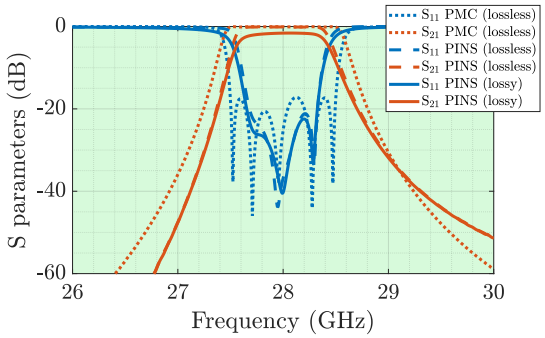

(b) *28 GHz inverted microstrip gap filter*

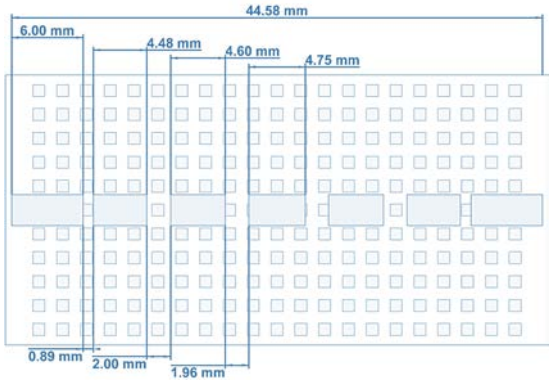

(c) *24 GHz inverted microstrip filter with pins and dimensions*

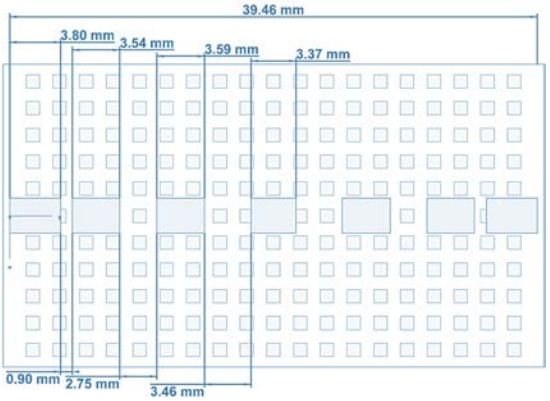

(d) *28 GHz inverted microstrip filter with pins and dimensions*

Figure 2.3: *Simulated S-parameters of PMC and AMC designed filters (with pins).*

Additionally, a study was carried out to determine the origin of the losses appearing in our filter with pins. In Fig. 2.4 we see the comparison between the case without losses ('Lossless'), and for the cases of only losses in the 'pins', the 'lid', the 'circuit', the 'substrate' or in the case of all components having losses ('Lossy'). We note that most of the losses are originated in the substrate, at least in this frequency band.

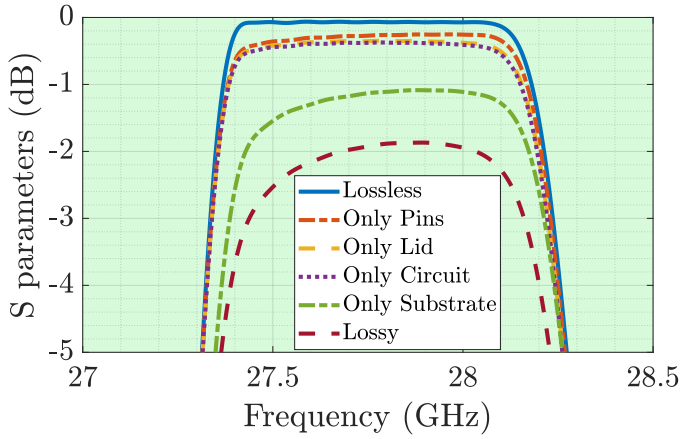

Figure 2.4: *Loss study in Ka-band End-Coupled lines passband filter in Inverted Microstrip Gap technology (RO4003C, substrate thickness = 0.508 mm).*

2.1.3 Power Splitter Design

Once we have the two filters designed with pins under the substrate we need a way to distribute the power that is frequency dependent. To do this, we need a po put arr 28]. As rm acc

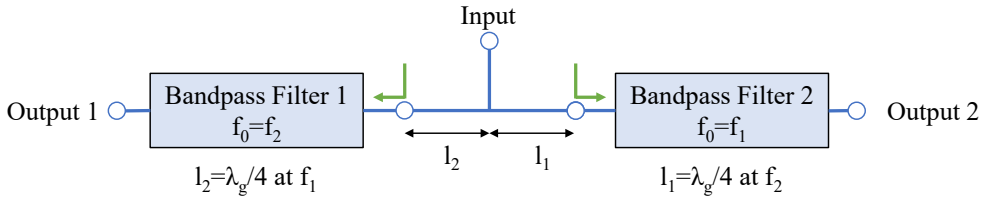

Figure 2.5: *Block diagram explaining the operation of the diplexer as a function of frequency.*

The power divider uses a conventional T-junction, where we start from a design with the PMC boundary condition and then add the bed of nails. The length of the symmetrical branches are calculated with the distance $\lambda_{g,24}/4$ and $\lambda_{g,28}/4$ as shown in Fig. 2.6.

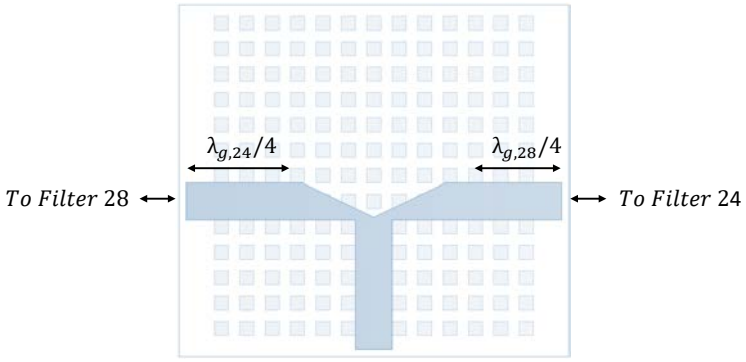

(a) *Power divider model.*

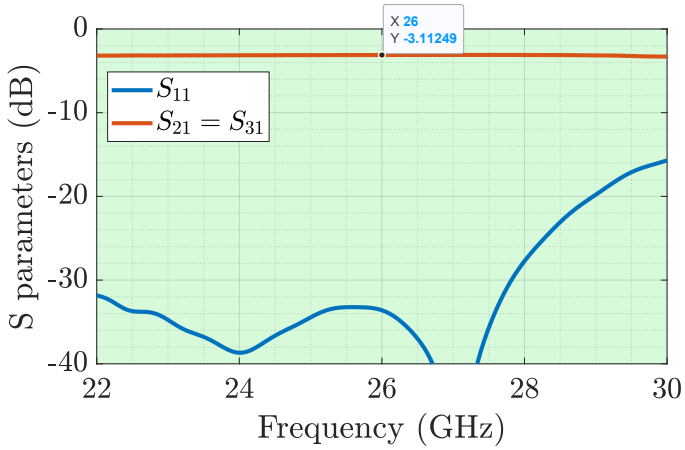

(b) *Simulated S-parameters of the model. S_{11} is the common port matching. .*

Figure 2.6: *Designed 1 to 2 power divider in Inverted Microstrip Gap Waveguide.*

These initial values of the length of the power divider branches need to be adjusted with full-wave simulations after including the previously designed filter stages. In Fig. 2.7a we have the simulated diplexer where the common port appears in the central part along with the filters. The simulated S-parameters with ideal pins and materials without losses are shown in Fig. 2.7b, where we appreciate an excellent performance and the flatness of the passband of each channel (24 GHz and 28 GHz). We can even observe the stopband limits that create the pin surface, where they broadly cover the working bands of the device until couplings appear at the extremes (below 22 GHz and above 31.5 GHz). In Fig. 2.8 we can see the transmission losses that occur when real materials are included in the simulation. The losses are about -2 and -2.3 dB, for 24 and 28 GHz, respectively.

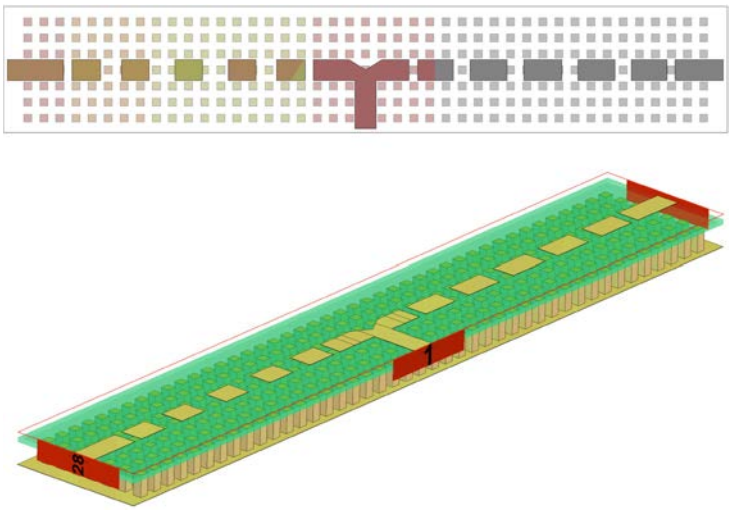

(a) *Diplexer: 3D model with semi-transparent upper metal.*

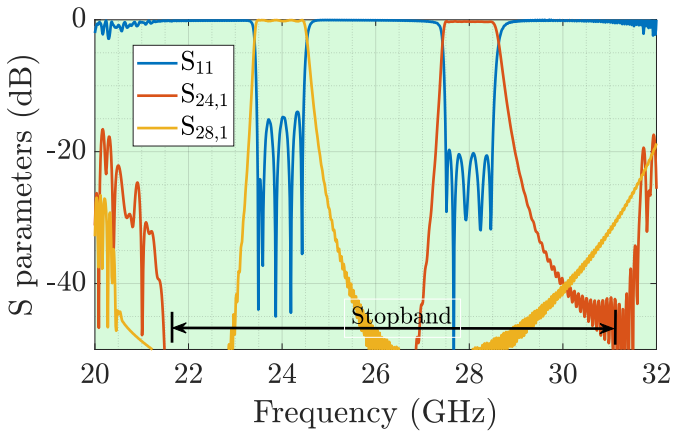

(b) *Diplexer Simulated S-parameters with pins as AMC and ideal lossless materials.*

Figure 2.7: *Design result of the Inverted Microstrip Gap Waveguide diplexer in Ka-band with ideal RO4003C^{TM} materials without losses.*

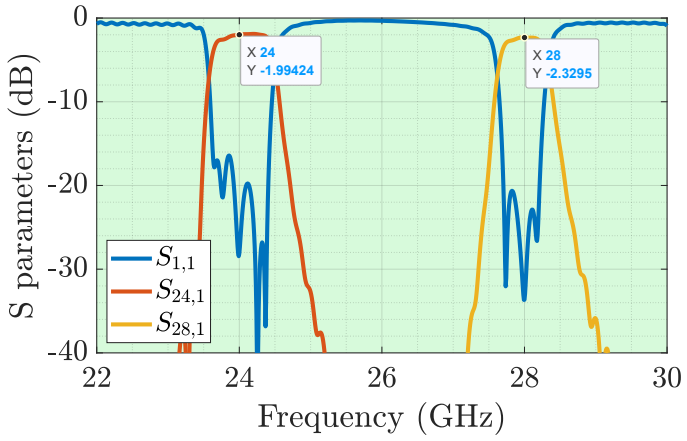

Figure 2.8: *Diplexer simulated S-parameters with pins and lossy RO4003C substrate.*

2.1.4 Microstrip to Inverted Microstrip Gap Transition

With the aim of integrating this technology with conventional connectors with which to perform the measurements of the prototype built in a reliable, robust and consistent way, we need to design a transition with conventional microstrip output, where the various End-Launch connectors appropriate for these bands will be placed.

To this aim, we follow the indications of [124], where they use the same dielectric material for this transition as for the inverted circuit. In Fig. 2.9a we can see the corresponding geometry of this transition. This is designed starting from the inverted microstrip gap line with the width to obtain a characteristic impedance of 50 Ω with this RO4003C substrate and air gap dimension, *i.e.*, w = 2.6 mm. At the end, this width is reduced to that corresponding to an impedance of 50 Ω for the λ_g in RO4003C substrate (w = 1 mm). Finally, over these reduced width sections, the air gap is used to insert inverted sections of conventional microstrip of the same line width with the ground plane in contact with the metallic top cover. In Fig. 2.9b we can see the good results achieved in matching (below -14 dB) and its low losses (about -0.25 dB) in the band of interest.

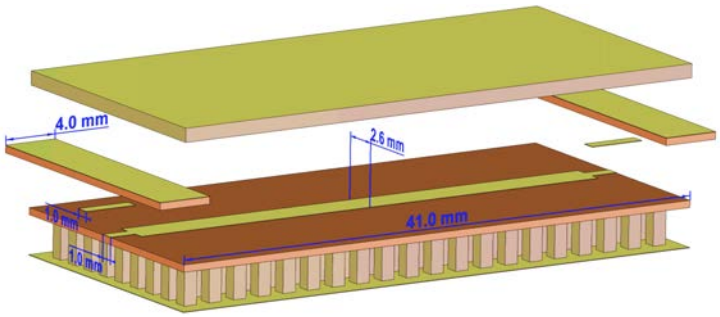

(a) *3D view.*

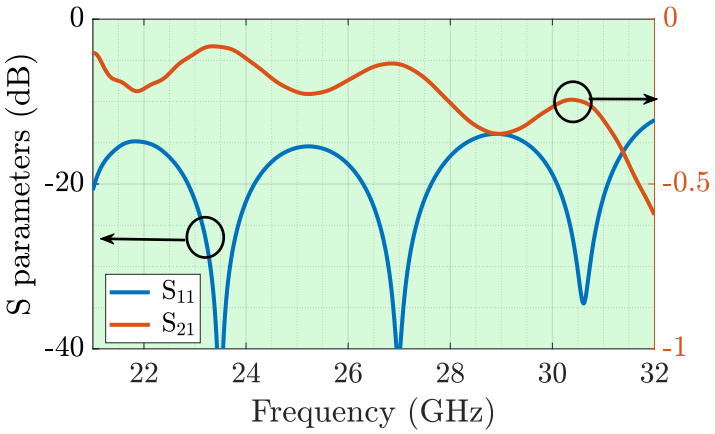

(b) *Simulated S parameters.*

Figure 2.9: *B2B transition from Inverted Microstrip Gap Waveguide to conventional Microstrip.*

In Fig. 2.10 we can see the result of the simulated S-parameters when these transitions are added to the 3 ports of the above lossy diplexer. We see that the losses remain in the order of -2 dB and -2.3 dB at the 24 and 28 GHz frequencies.

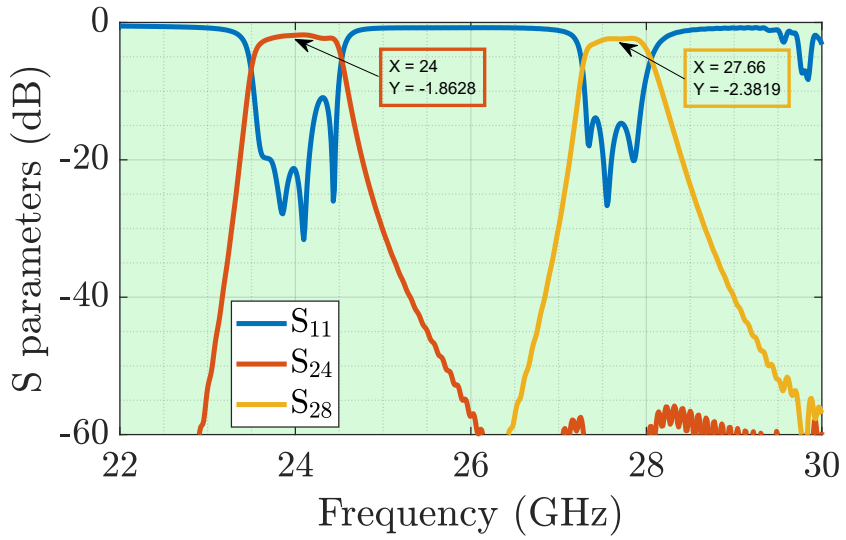

Figure 2.10: *Final diplexer design in Inverted Microstrip Gap Waveguide including RO4003C™ real materials and transition to conventional Microstrip.*

2.1.5 Losses Analysis in Materials

However, although the simulated losses are much lower than those of other microstrip filters at similar frequencies [129]–[133], it is worth finding out where the different contributions of losses come from, therefore a study was conducted.

From the analysis of absorbed losses in each of the diplexer materials (substrate, aluminum for the pins and the top lid, and copper for the lines) shown in Fig. 2.11 we conclude that most of these losses are due to the substrate used Rogers RO4003C™, so we proceeded to the **complete** redesign of the diplexer and transitions with a new substrate of very low losses such as **Rogers RO5880™** whose parameters are $\varepsilon_r = 2.2$ and $\tan\delta = 0.0009$. It should be noted that this new substrate is more expensive because of its excellent properties in this respect.

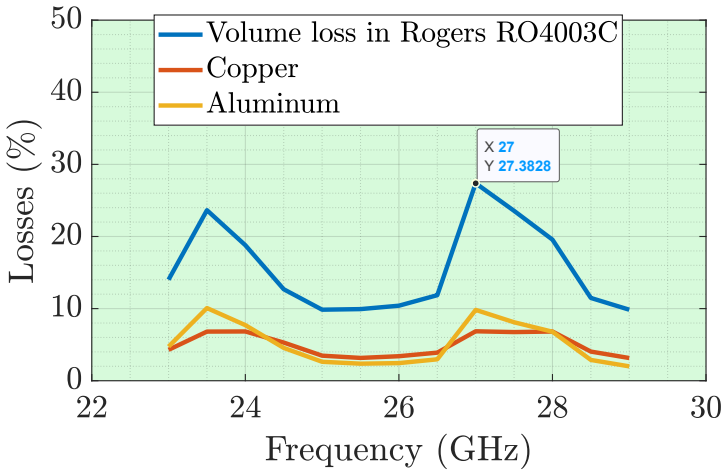

Figure 2.11: *Percentage of absorbed losses in each of the diplexer materials.*

2.1.6 Design with Low Loss Rogers RO5880 Substrate

At this point, we recalculated the values of the inverted microstrip gap model between lines on pins with the new RO5880$^{\text{TM}}$ substrate, and subsequently, the same process with the filters independently and with the diplexer power divider as a whole.

As seen in Fig. 2.12, which is reproduced here again for the reader's convenience, the dispersion diagram remains very similar when changing the unit cell substrate, however, a modification of the pin height from 3 mm down to 2.8 mm was considered, since the proximity of the stopband at the top to the 28 GHz channel disturbed both matching (S_{11}) and transmission (S_{21}) performance.

A lower pin height shifts the stopband to higher frequencies as shown in Fig. 2.12. A summary of the exact stopband frequency values for the different substrate versions and heights considered is given in Table 2.1.

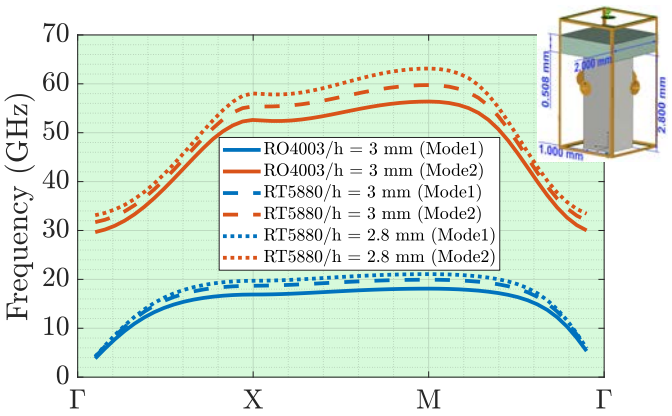

Figure 2.12: *Stopbands for substrate 4003C vs 5880 for two different pin heights.*

Table 2.1: *Changes in the stopband as a function of the substrate under consideration and the unit cell pin heights.*

Substrate	**Pin height**	**Freq. inf (GHz)**	**Freq. sup (GHz)**
RO4003C	3 mm	18.1	29.7
RT5880	3 mm	19.9	31.7
RT5880	2.8 mm	21.1	33.1

We see in Fig. 2.13 the distortion produced by the proximity of the stopband for the above mentioned case and the reason why this height has been modified. In Fig. 2.14 we see the final diplexer design with the new very low loss substrate and 2.8 mm pins along with a detail of the low insertion loss achieved. Fig. 2.15 shows the frequency-dependent operation of the diplexer showing the absolute electric field distribution across the diplexer circuit.

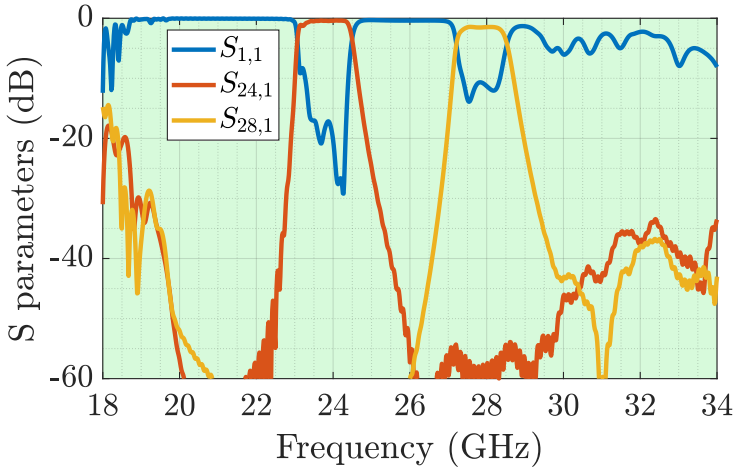

(a) *Pin Height 3.0 mm.*

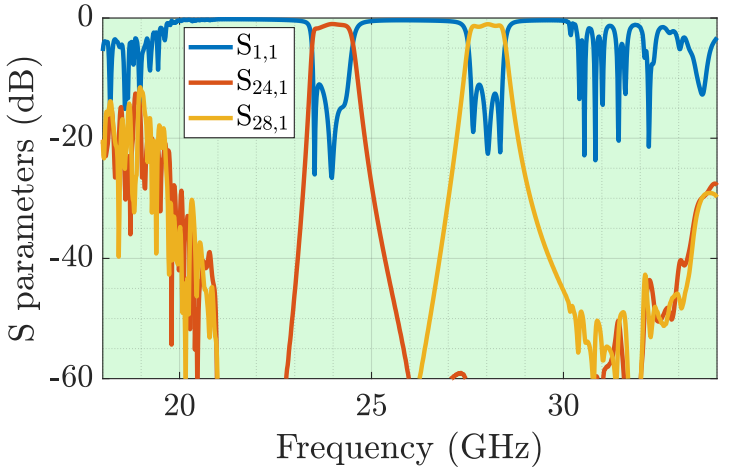

(b) *Pin Height 2.8 mm.*

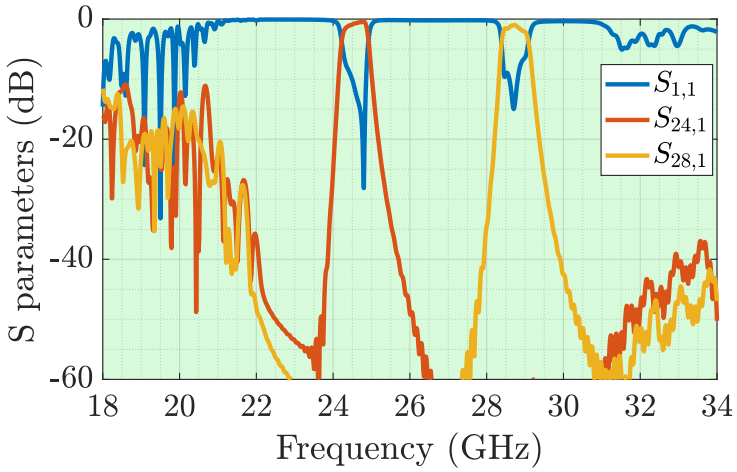

(c) *Pin Height 2.6 mm.*

Figure 2.13: *Variation of diplexer response as a function of pin height (stopband).*

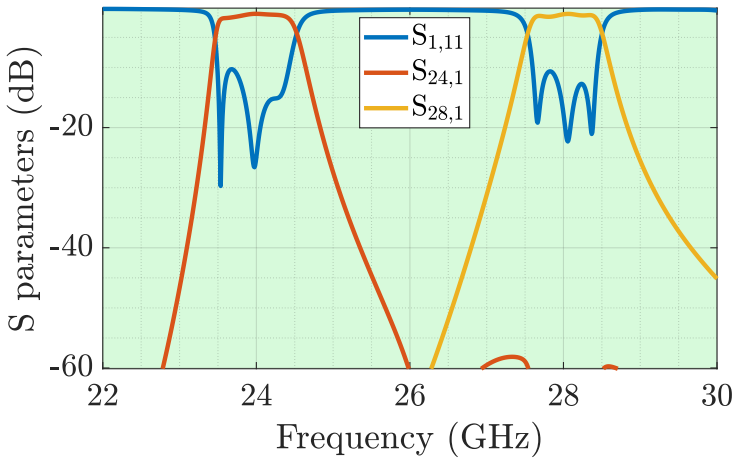

(a) *General view.*

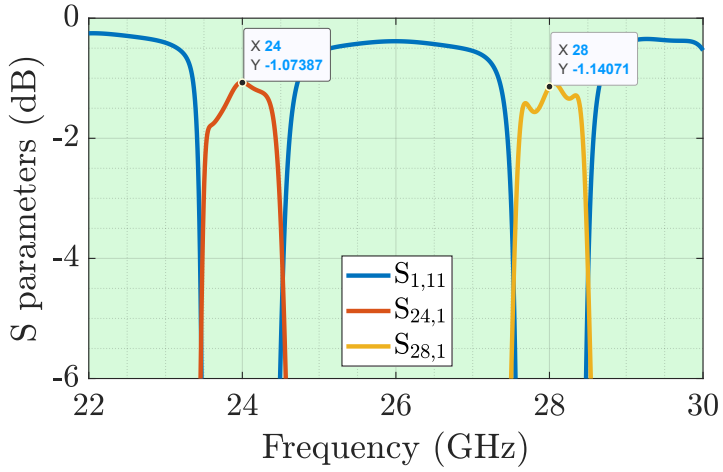

(b) *Zoom.*

Figure 2.14: *Simulated S-parameters of the diplexer with very low loss substrate 5880 including actual losses, plus those corresponding to the metals, for pin height = 2.8 mm.*

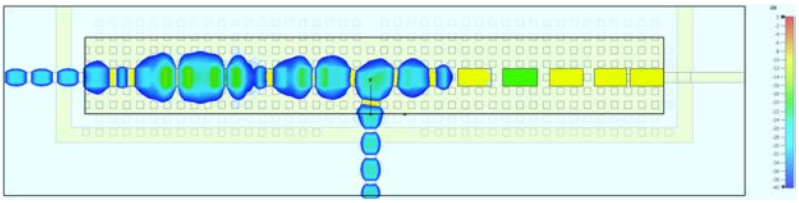

(a) *E field @28 GHz channel visualization.*

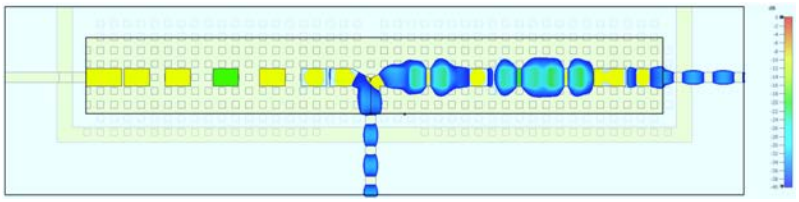

(b) *E field @24 GHz channel visualization.*

Figure 2.15: *Normalised E-field as a function of frequency for RO5880 substrate and pin height = 2.8 mm.*

2.2 Mechanical Fabrication

Once the full-wave simulation results are in accordance with the specifications, we move to the mechanical design phase for fabrication. The fabricated prototype consists of several parts shown in Fig. 2.16a, along with the dimensions of the two bandpass filters and power divider in 2.16b. It should be noted that the diplexer is not symmetrical due to the difference in size of the filters, with the 28 GHz one being shorter than the one resonating at 24 GHz. Fig. 2.16c shows the transition from inverted microstrip to microstrip, where the End-Launch connectors will be placed. Finally, in Fig. 2.16d the 3D model of the pin bed with its dimensions is shown. It should be noted that in the common port part of the diplexer several pins were removed for reasons of space with the connector, without affecting the simulated performance. Fig. 2.17 shows the built prototype and separated into the different parts that form it.

2.3 Results

To obtain measurements without the influence of the connectors, it is common to make TRL (Thru, Reflect, Line) calibration kits. This TRL kit is shown in Fig. 2.18. In the result of these measurements shown in Fig. 2.19, we see that we obtain insertion losses of -1.4 dB in the 24 GHz channel and -2 dB for the 28 GHz channel. Although these are higher than those simulated (-1.07 dB at 24GHz and -1.14 dB at 28 GHz), they are still acceptable. Note also that these losses include the transition from inverted microstrip gap to microstrip.

The slight frequency shift of the measurements with respect to the simulations is highly likely to be due to variations in the permittivity of the substrate. To check this, we have run a simulation changing the permittivity of the dielectric from the reference 2.2 to 2.0 and in Fig. 2.20 we can see the shifting in frequency. This decrease of the permittivity of the material with the frequency has been reported in the datasheet by the manufacturer.

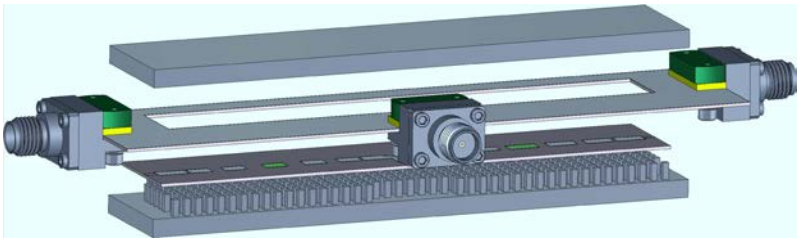

(a) *3D Inverted Microstrip Gap Diplexer geometry.*

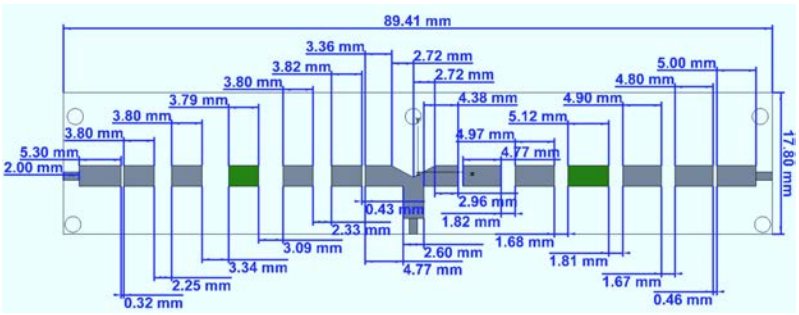

(b) *Diplexer dimensions.*

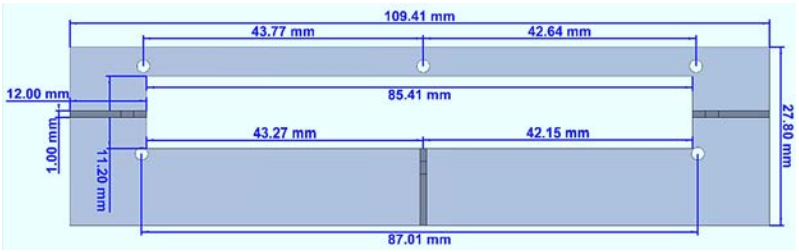

(c) *Transition dimensions.*

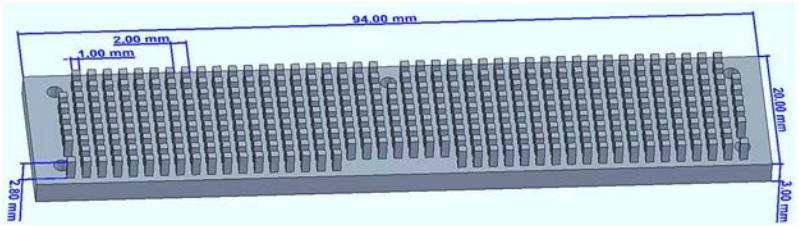

(d) *Bed of nails dimensions.*

Figure 2.16: *Inverted Microstrip Gap Waveguide Diplexer: Geometry and Dimensions.*

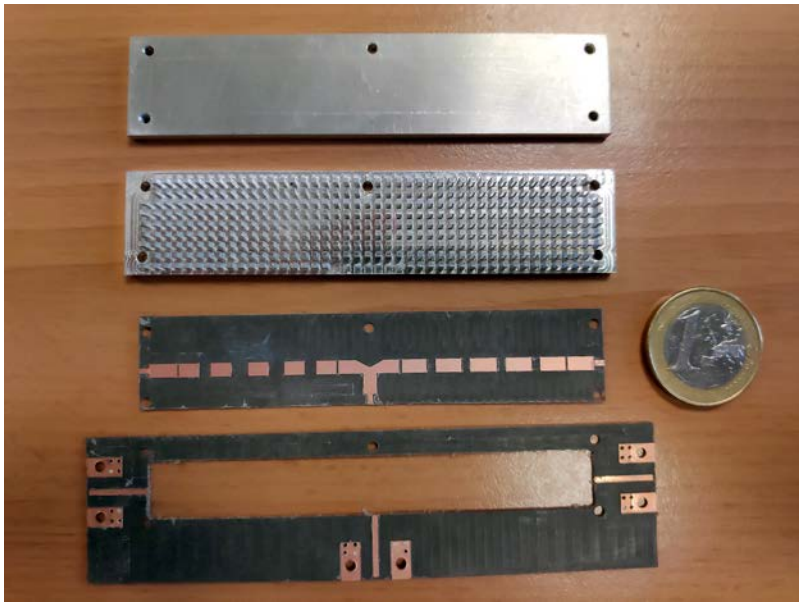

(a) *Parts breakdown of diplexer.*

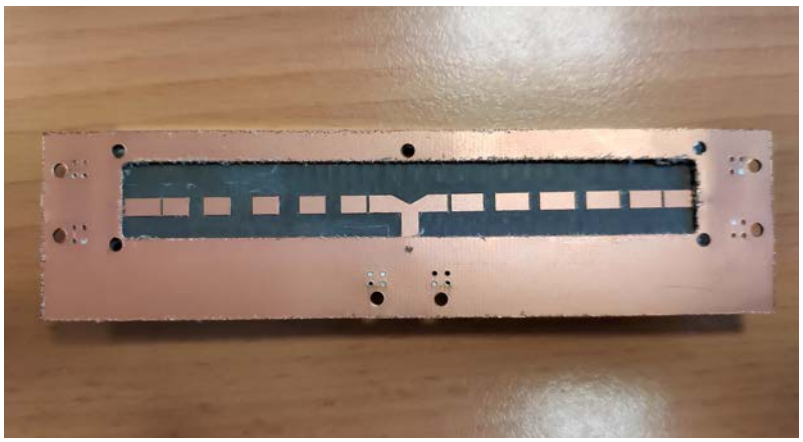

(b) *Intermediate assembly.*

(c) *Top of assembled diplexer with transition and connectors.*

Figure 2.17: *Inverted Microstrip Gap Waveguide Diplexer: Mounting and Assembly.*

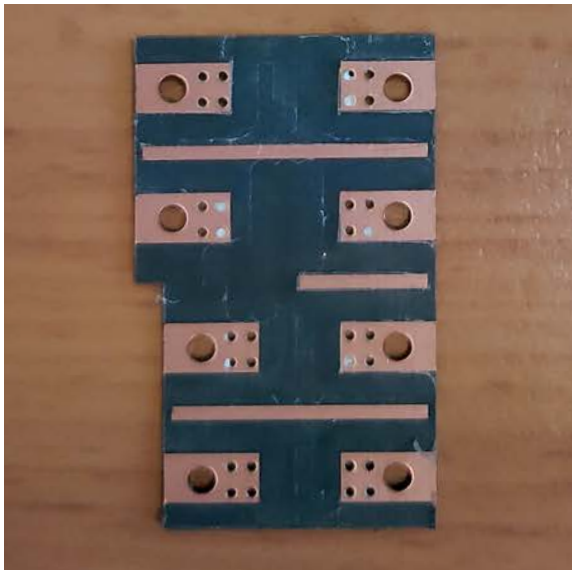

Figure 2.18: *TRL kit for eliminating the effect of End-Launch connectors.*

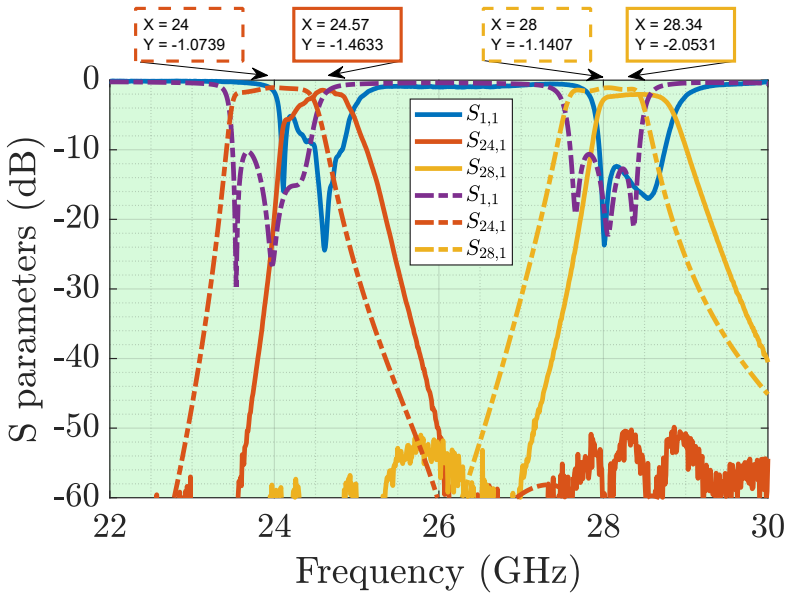

Figure 2.19: *Measured S-parameters of the diplexer built in Inverted Microstrip Gap Waveguide with the low loss RO5880 substrate.*

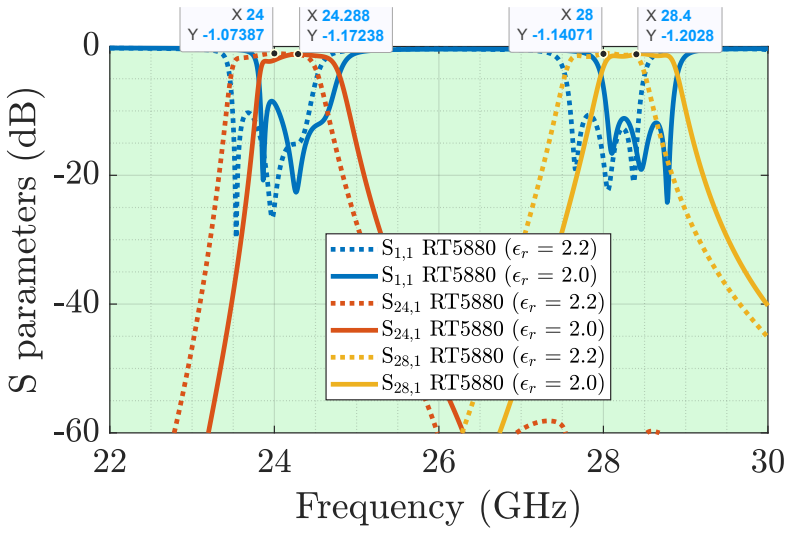

Figure 2.20: *Simulated S-parameters for 2 permittivities of RO5880 substrate.*

2.3.1 Comparative study with other diplexers

If we compare the most important parameters of other diplexers in similar frequency bands as presented in Table 2.2, we can see that the designed diplexer has insertion losses of the order or even lower than some of them while maintaining a "Low" cost characteristic. A classification has been made of the various existing technologies in this comparison so that we give a "Very Low" cost for conventional microstrip; those based on waveguide, as "High", and other more complex versions as "Very High". So this technology is a good competitor with SIW, improving isolation by 30 dB.

Table 2.2: *Comparative study with other diplexers [125].*

	f_0 (GHz)	IL (dB)	Isol (dB)	BW (%)	Cost	Type
[134]	35	0.35	NA	1.7	High	Waveguide
[135]	66	1.5	50	59	Very High	Waveguide + SSL
[136]	20	4	50	2.4	Very High	Cryo-Microstrip
[137]	30	1.4	35	5	Very High	Membrane coupled microstrip
[138]	60	2.5	25	8.8	Very High	LCP (Liquid Crystal Polymer)
[54]	60	0.9	60	1.7	High	Groove Gap WG
[139]	35	3.5	30	3.7	Very Low	Classic Microstrip
[140]	60	6	30	6.25	Low	SIW
Our	28	2	60	3.5	Low	Inverted Microstrip Gap WG

2.4 Conclusions

In this chapter, a must-have device type in RF front-ends has been presented. The operation of the diplexer in inverted microstrip gap waveguide (IMGW) technology has been demonstrated for the lower part of the mm-wave spectrum, where it can be employed for future uses in 5G technologies and beyond. Although this diplexer has been designed along classical lines of coupled line filters, there are more complex devices [141], [142] that could be adapted to this technology without any problems.

The concept of this diplexer was initially formed by two Chebyshev type filters centred at 24 GHz/28 GHz, with a bandwidth of 1 GHz and a ripple of 0.5 dB, but, by subsequent adjustments, the highest possible flatness in the passband was sought. Initially, following a more classical concept, the problem of the filters was approached as parallel coupled line bandpass filters, although various problems of the lines with respect to the position on the pins placed under the substrate led to a change to End-Coupled passband filters. The substrate on which the design was carried out was RO4003C^{TM}, although in order to improve the insertion losses,

acceptable as they already were, the diplexer was completely redesigned with a very low loss substrate RT5880^{TM} with a change of permittivity from 3.38 to 2.20 in the latter.

The measurements are in accordance with the simulations except for a slight increase in losses and a slight frequency shift. The insertion loss in the 24 GHz passband is 1.5 dB and 2 dB for the 28 GHz passband. Regarding the slight band offset we have shown that it is due to a discrepancy with the permittivity value of the material, something easily correctable if necessary and with high reproducibility in terms of mass production. When we compare this proposed diplexer with others published in similar bands, we see that we get similar or even better insertion losses than some of them, keeping the cost relatively low, especially when comparing with other variants of the Gap Waveguide technology (Ridge and Groove), which also do not allow such a simple integration of amplifier elements and aperture antennas.

Chapter 3

Hybrid Splitter-Diplexer for Dual Band Array Antenna Compact Module in Inverted Microstrip Gap

This chapter deals with the development of a Hybrid Splitter-Diplexer in Inverted Microstrip Gap Waveguide technology compatible with low-profile array antennas, and based on the diplexer proposed in the previous chapter. Much of this work was carried out during a stay at Concordia University in Montreal, Canada, under the supervision of Prof. Ahmed Kishk.

For this purpose, the diplexer designed in groove gap waveguide technology presented in [70] was taken as reference to build the diplexer function.

3.1 Hybrid Splitter-Diplexer Design

The work in this section is a direct continuation of the previous chapter.

From the model that includes the conventional microstrip transition, one of the first steps in the design of this device has been to extend the common port sym-

metrically with respect to the axis containing the End-Coupled line filters to create a second common port and check the obtained result. In Fig. 3.1a we can see the preliminary result of the simulated device. We check that, to the insertion loss we already had in the previous model of the diplexer with only one common port, -3 dB more is added, since we are dividing the power between the two common ports.

The next step, and given that the number of meshcells in this model reaches 17 million and results in very long simulations, is to reduce the complexity of the model as far as possible without losing accuracy in the results.

For this purpose, it is evaluated how much the distortion is in the simulations of the model without transitions with respect to the simulations that include the transition from inverted microstrip gap to conventional microstrip. We see in Fig. 3.1d that the result is acceptable, and the computing cost savings is remarkable, decreasing the number of meshcells to 3 million (83% reduction). There is also a slight offset in frequency towards lower frequencies, but it is sufficient to take into account the new center frequency in future adjustments so that when the transition is added, the center frequencies return to 24 GHz and 28 GHz, respectively.

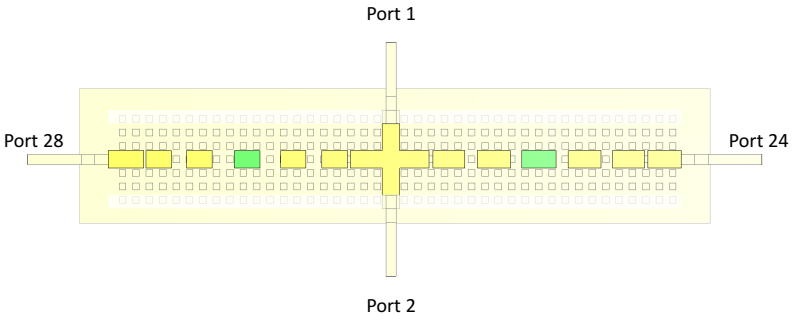

(a) *Model WITH transition without the metal covers for better visualization.*

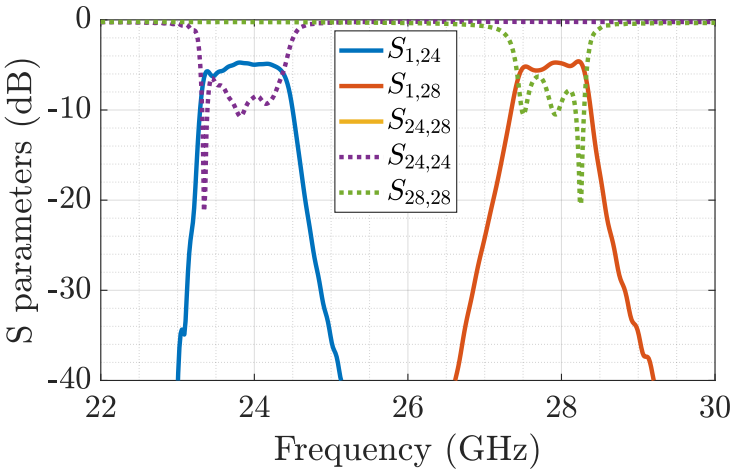

(b) *Simulated S-parameters of the model with transition.*

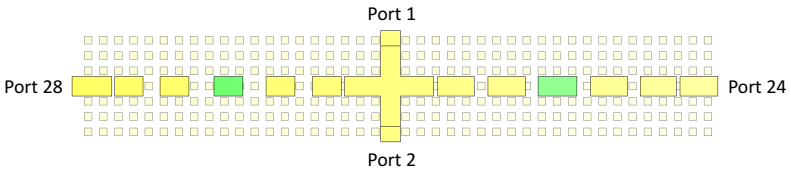

(c) *Model WITHOUT transition without the metal covers for better visualization.*

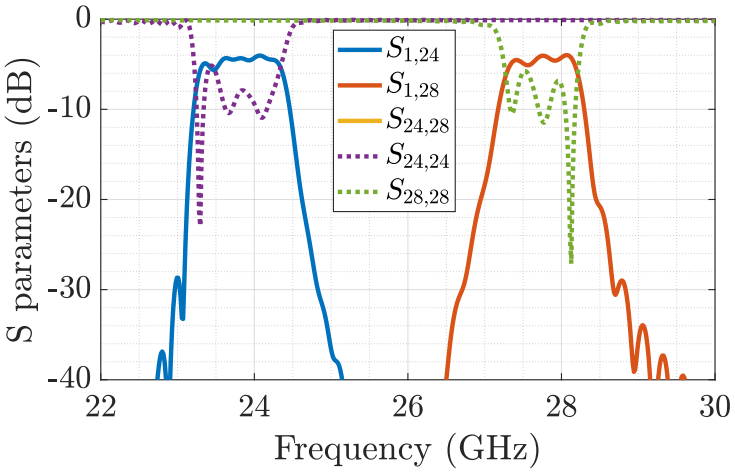

(d) *Simulated S-parameters of the model without transition.*

Figure 3.1: *Simulated models and S-parameters for the version with and without transition.*

In addition, after several similar analyses and similar electric field distribution in the structure, it is concluded that the complexity of the model can be further reduced by taking into account that from the 2nd resonator counted from the common ports, the energy is negligible, so that much of the opposing filter can be omitted to simulate each channel band separately. That is, to simulate the 28 GHz channel, the opposed filter can be removed from the computational domain of the CST solver, as seen in Fig. 3.2, decreasing the number and complexity of the computational domain by another 30% to 1.8 million meshcells. The same is done with the 24 GHz filter.

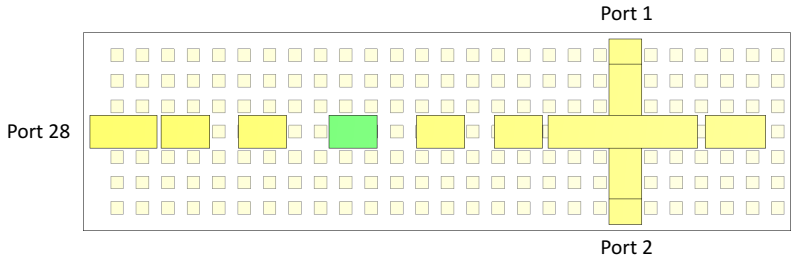

(a) *Non-transition model without the metal covers for better visualization with the 24 GHz counter filter removed up to the first resonator.*

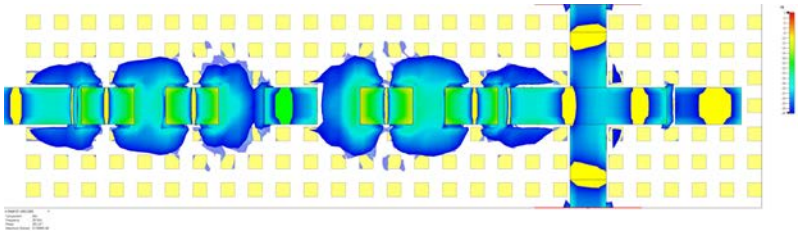

(b) *E field distribution at 28 GHz in absolute value.*

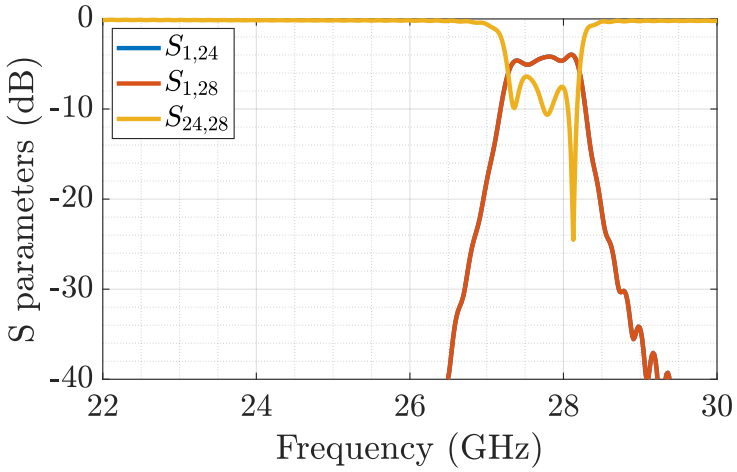

(c) *Simulated S-parameters of the model with the opposite filter at 24 GHz removed.*

Figure 3.2: *Methodology for the simplification of the filter model up to the 2nd resonator.*

Now, taking the above mentioned reference work in groove gap technology [70] and making some assumptions by establishing parallelisms with the "zero" resonator of this reference, a diamond shaped power divider is proposed. In Fig. 3.3 the best result achieved after adjusting the 10 resonators that form the 2 filters and the power divider is shown. We see that the reflection coefficients ($|S_{11}|$) in each of the bands is less than -10 dB, however, the insertion loss presents some distortions at the extremes of each of the passbands. The isolation between the filters is more than 40 dB, being out of the graph.

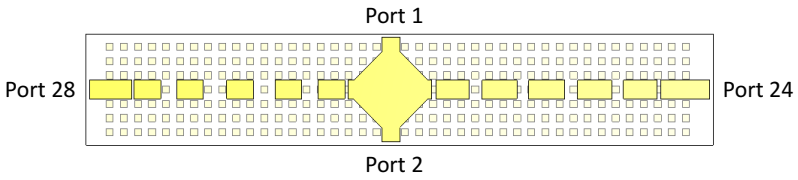

(a) *Model with symmetrical diamond shape power divider.*

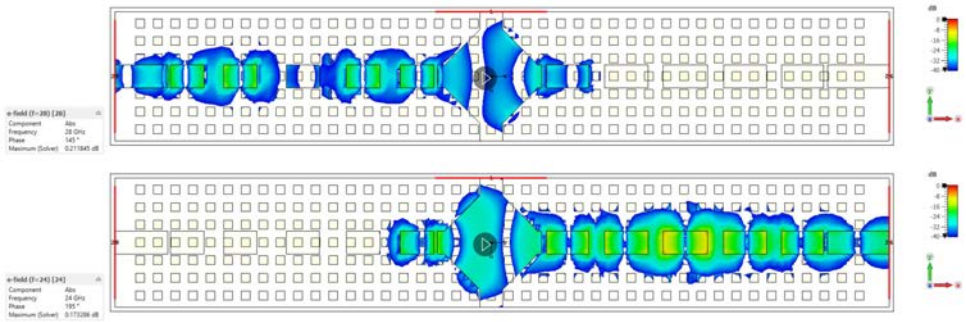

(b) *E field distribution feeding from 28 GHz and 24 GHz filter, respectively.*

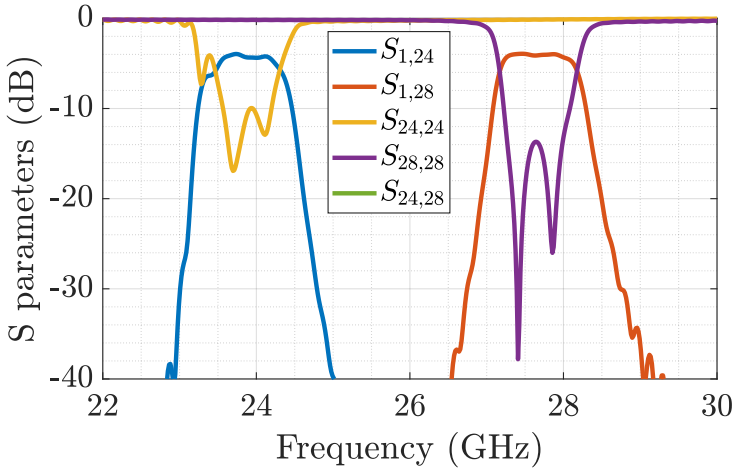

(c) *Simulated S-parameters.*

Figure 3.3: *Model of the diplexer-splitter with symmetrical diamond-shaped power divider.*

After analyzing the propagation of the electric field through each of the branches, the asymmetry in the response as a function of frequency is observed, so it is proposed to consider this dispersive behavior by adding a modification in the power divider in the form of an asymmetry. This change forces to readjust all model parameters. In Fig. 3.4 we see the achieved result. The response is now flatter and more balanced throughout the passband, after adjusting the poles of the filter resonators to the impedance seen by them. It is possible to observe the frequency offset of 300 MHz because we are not including the transition in the simulations. The insertion loss is 4 dB, which corresponds to 3 dB due to the ideal power divider and 1 dB from the losses in the conductive and dielectric materials (aluminum and Rogers RT5880$^{\text{TM}}$, respectively). The isolation between the filters is, again, more than 40 dB, falling outside the graph.

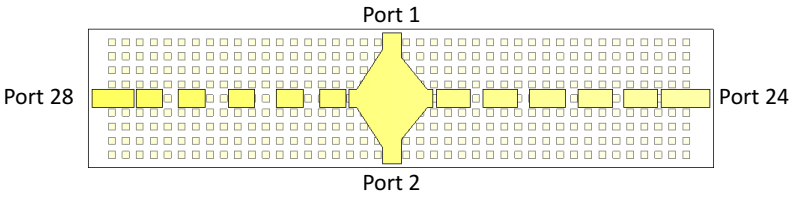

(a) *Model with asymmetrical diamond shape power divider.*

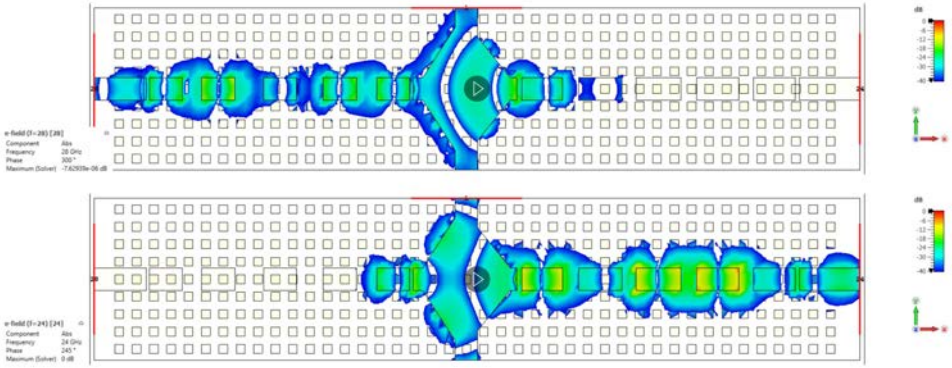

(b) *E field distribution feeding from 28 GHz and 24 GHz filter, respectively.*

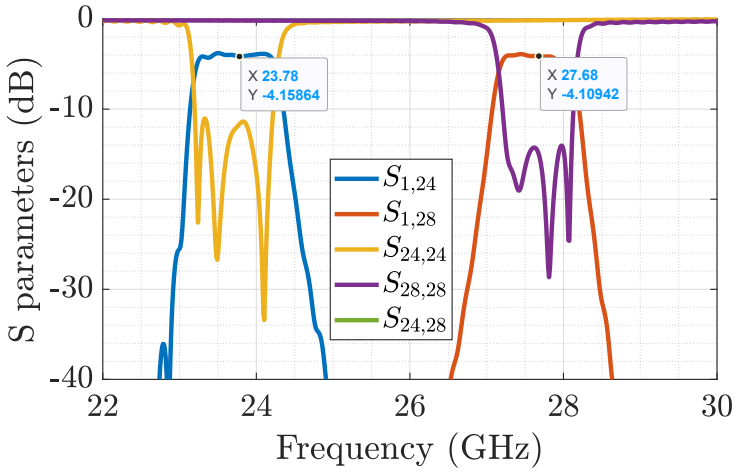

(c) *Simulated S-parameters.*

Figure 3.4: *Model of the diplexer-splitter with asymmetrical diamond-shaped power divider.*

3.2 Dual Band Radiating Elements Designs

Once the hybrid splitter-diplexer model has been adjusted, a study of different radiating elements compatible with dual-band aperture antennas is carried out. The determining factor is that it must allow matching to two bands at 24 GHz and 28 GHz. This can be achieved with a wide bandwidth design that covers these frequencies, or by making modifications to radiating elements with 2 resonant frequencies to separate them sufficiently to cover both.

3.2.1 Dual Band Off-Centered T-feed Slot

The first proposal was the design of a "Dual band off-centered T-feed Slot" type antenna as shown in Fig. 3.5. In Fig. 3.6, we present the simulation results after tuning. We see that each of the resonances creating this antenna loosely covers the two bands with matching values below -10 dB. The slots include rounded corners thinking in the fabrication with conventional machining on a 1 mm thick metal plate.

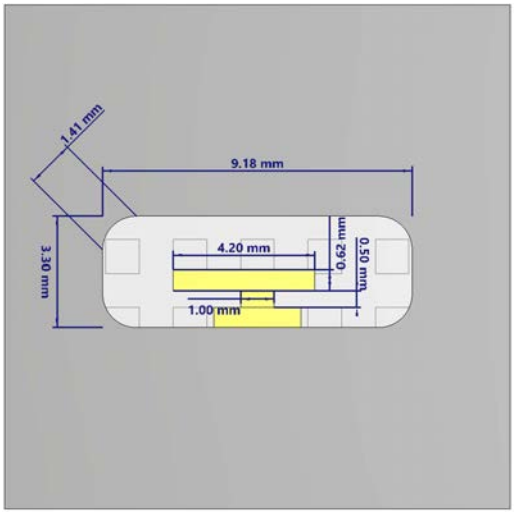

(a) *Dual band off-centered T-feed Slot in Inverted Microstrip Gap Waveguide model (details of the dimensions).*

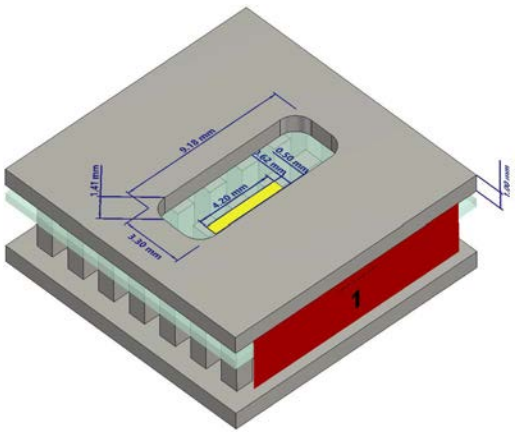

(b) *Dual band off-centered T-feed Slot in Inverted Microstrip Gap Waveguide (3D).*

Figure 3.5: *Dual band off-centered T-feed Slot in Inverted Microstrip Gap technology with 1 mm thickness aluminium lid.*

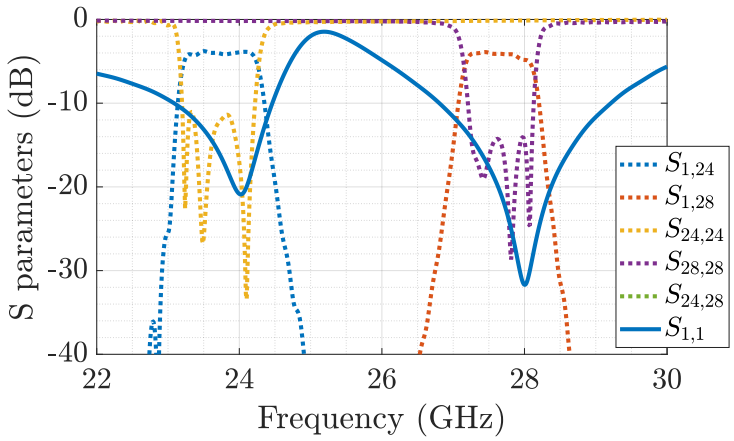

Figure 3.6: *Dual band off-centered T-feed Slot simulated S-parameters superimposed on the result of the hybrid splitter-diplexer designed in the previous section.*

3.2.2 Dual Band Off-Centered T-feed Slot (printed technology)

A second model is proposed in which this metal plate supporting the slot is of the thickness of the metallization of a typical substrate (35 µm), in order to machine it with technologies for printed circuit boards. Fig. 3.7 and Fig. 3.8 contain the designed model and the S-parameters simulation results, respectively.

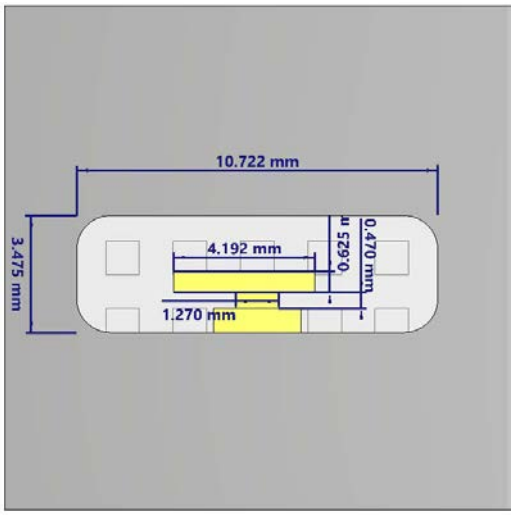

(a) *Printed model for the Dual band off-centered T-feed Slot (details of the dimensions).*

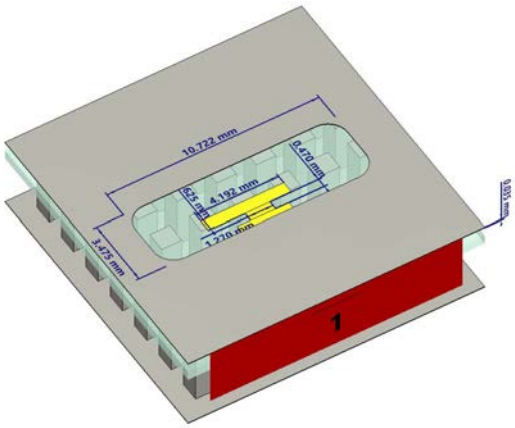

(b) *Printed model for the Dual band off-centered T-feed Slot (3D).*

Figure 3.7: *Dual band off-centered T-feed Slot in Inverted Microstrip Gap Waveguide with lid prepared for printed technology.*

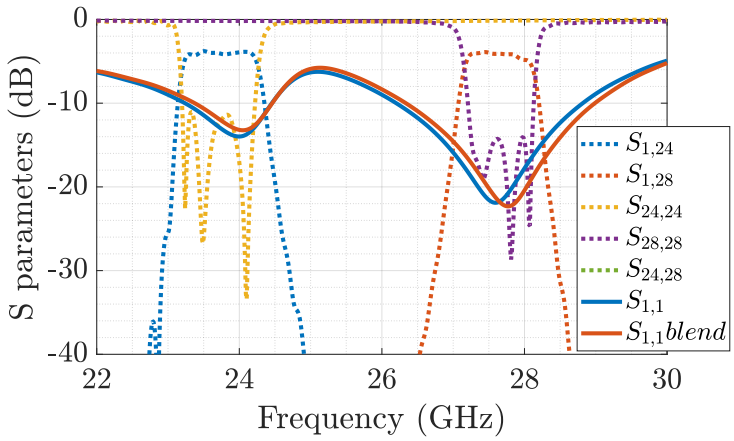

Figure 3.8: *Dual band off-centered T-feed Slot simulated S-parameters superimposed on the result of the hybrid splitter-diplexer designed in the previous section. The figure shows the difference between the result for rounded slots ('blend') and those with straight corners.*

However, something to take into account when designing antennas is the cross polarization generated, so this issue is studied and shown in Fig. 3.9 and Fig. 3.10 for the two designed cases. We see that for both 24 GHz and 28 GHz frequencies, the 35 mm thick antenna has a very high cross-polarization level, consequently this model could be discarded.

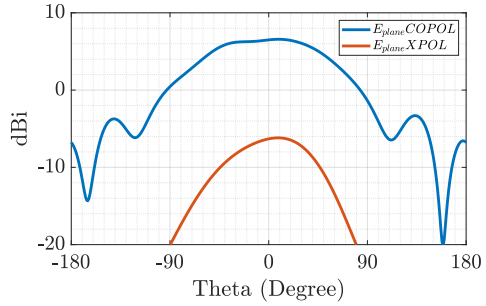

(a) *E-plane COPOL-XPOL at 24 GHz and 1mm upper metal plate.*

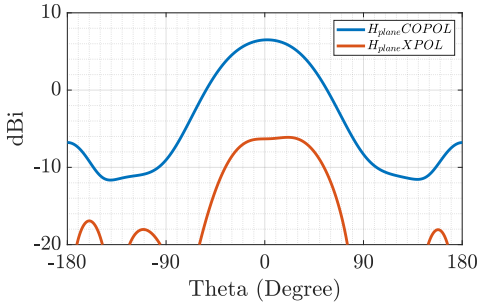

(b) *H-plane COPOL-XPOL at 24 GHz and 1mm upper metal plate.*

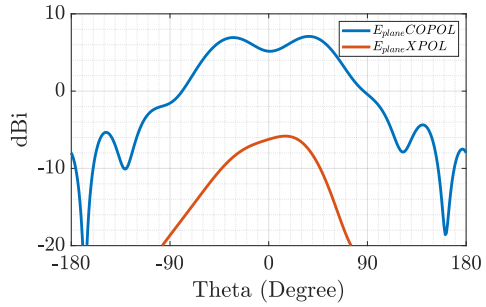

(c) *E-plane COPOL-XPOL at 28 GHz and 1mm upper metal plate.*

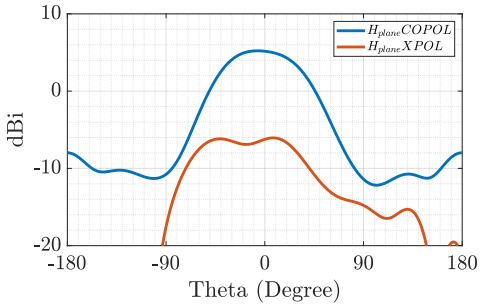

(d) *H-plane COPOL-XPOL at 28 GHz and 1mm upper metal plate.*

Figure 3.9: *COPOL-XPOL at 24 GHz / 28 GHz and 1mm upper metal plate.*

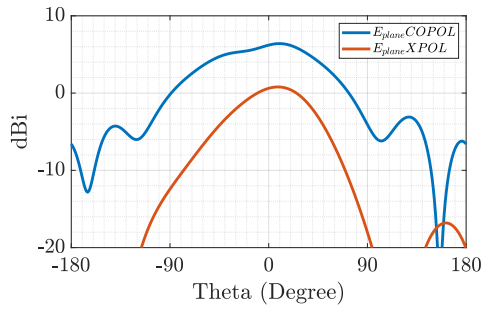

(a) *E-plane COPOL-XPOL at 24 GHz and 0.035mm upper metal plate.*

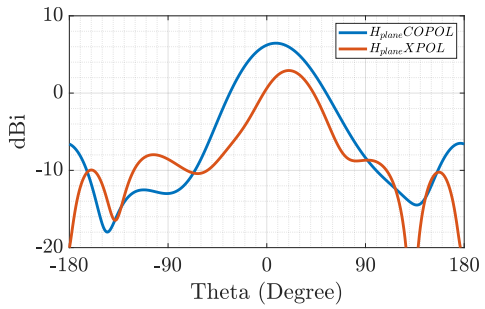

(b) *H-plane COPOL-XPOL at 24 GHz and 0.035mm upper metal plate.*

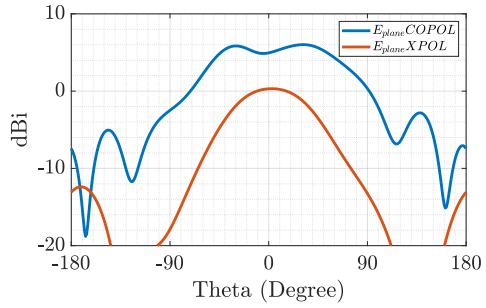

(c) *E-plane COPOL-XPOL at 28 GHz and 0.035mm upper metal plate.*

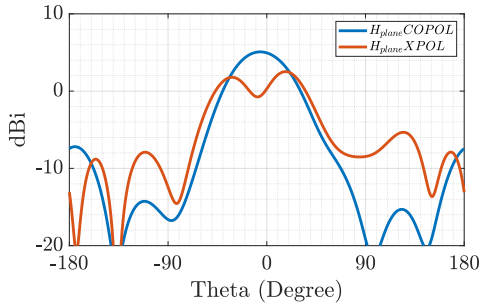

(d) *H-plane COPOL-XPOL at 28 GHz and 0.035mm upper metal plate.*

Figure 3.10: *COPOL-XPOL at 24 GHz / 28 GHz and 0.035mm upper metal plate.*

3.2.3 Centered Dual band T-feed Slot (printed technology)

A third variation studied is the same slot with T-feed as in the previous section but without offset. In this case, it is designed to have sufficient bandwidth to cover both bands. Fig. 3.11 shows the best obtained model, together with the simulated S-parameters. As we can see, this model does not meet the specifications as it does not cover the lower band, but could be used for other designs with closer bands.

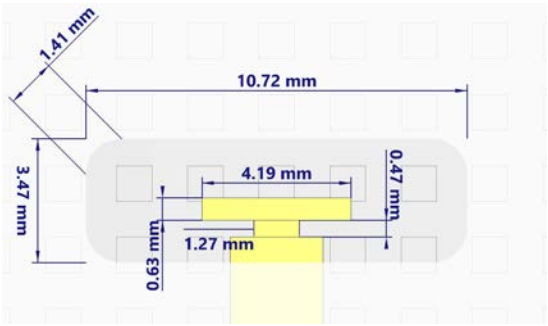

(a) *Centered Dual band T-feed Slot in Inverted Microstrip Gap Waveguide.*

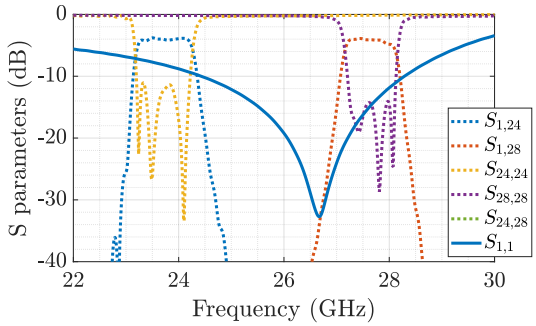

(b) *Simulated S-parameters superimposed on the result of the hybrid splitter-diplexer designed in the previous section.*

Figure 3.11: *Centered Dual band T-feed Slot in Inverted Microstrip Gap Waveguide.*

For this design, the cross-polarization is also calculated and, in Fig. 3.12, we see that only in the H-plane of each band do we obtain a cross-polarization level that is relevant. In the E-plane it has levels below −90 dB. This design was only made with the 35 µm lid model.

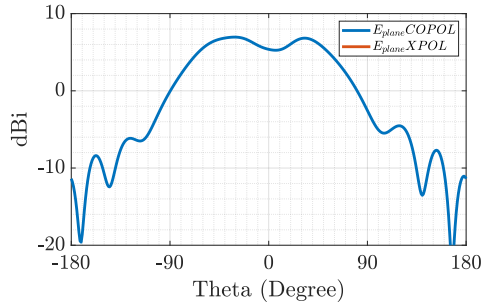

(a) *E-plane COPOL-XPOL at 24 GHz and 0.035 mm upper metal plate.*

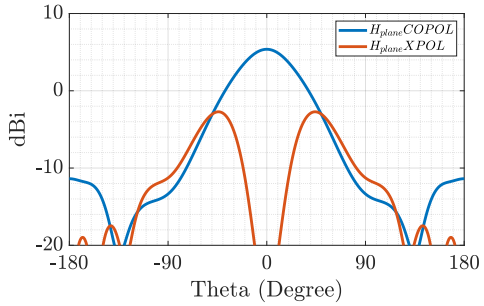

(b) *H-plane COPOL-XPOL at 24 GHz and 0.035 mm upper metal plate.*

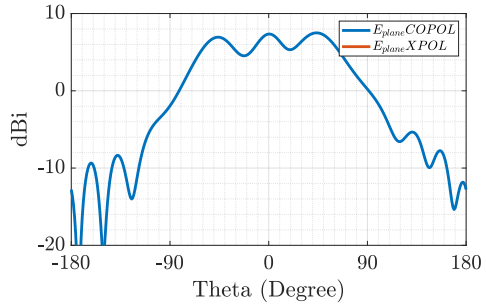

(c) *E-plane COPOL-XPOL at 28 GHz and 0.035 mm upper metal plate.*

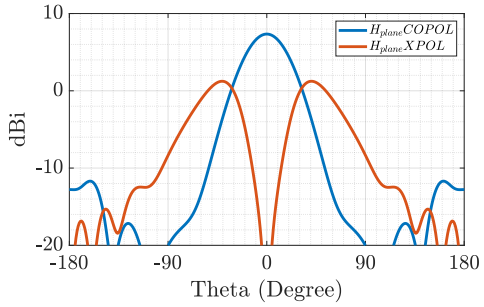

(d) *H-plane COPOL-XPOL at 28 GHz and 0.035 mm upper metal plate.*

Figure 3.12: *COPOL-XPOL at 24 GHz / 28 GHz and 0.035 mm upper metal plate.*

3.2.4 Wide-band T-feed Bowtie Slot

Using the metallization of a substrate as the ground plane of the antenna over the air gap required by the Inverted Microstrip Gap technology increases the difficulty in the assembly as it lacks sufficient robustness. Furthermore, it has been verified that the matching bandwidth is worse than in the case with a 1 mm metal lid (see Fig. 3.6 and Fig. 3.8), so the following designs will use this 1 mm thickness.

To extend the bandwidth, a model with a Bowtie-shaped slot is studied. However, although we managed to create a new resonance with which to have one more degree of freedom, it is still not enough to cover these two widely separated bands at 24 GHz and 28 GHz. Fig. 3.13 shows the model and S-parameters. The cross-polarization levels in H-plane are similar to the previous case, however in the E-plane these levels increase to −12 dB (Fig. 3.14).

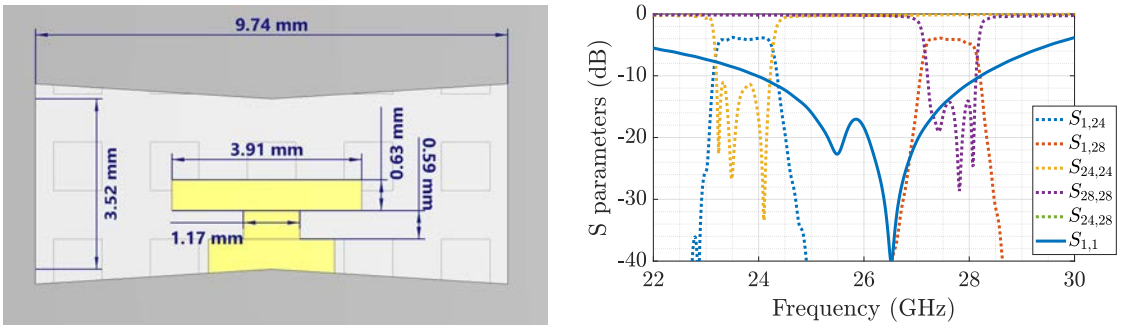

(a) *Wide-band T-feed Bowtie Slot model in Inverted Microstrip Gap Waveguide.*

(b) *Simulated S-parameters superimposed on the result of the hybrid splitter-diplexer designed in the previous section.*

Figure 3.13: *Wide-band T-feed Bowtie Slot model in Inverted Microstrip Gap Waveguide.*

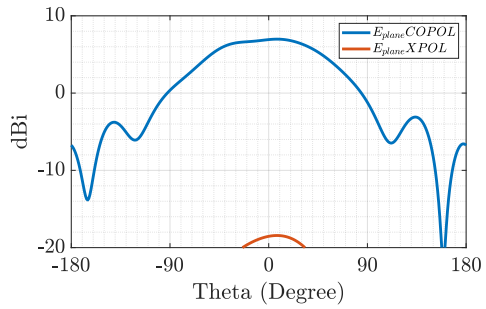

(a) *E-plane COPOL-XPOL at 24 GHz and 15 mm upper metal plate.*

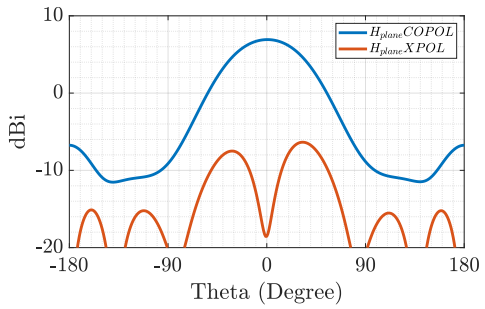

(b) *H-plane COPOL-XPOL at 24 GHz and 1 mm upper metal plate.*

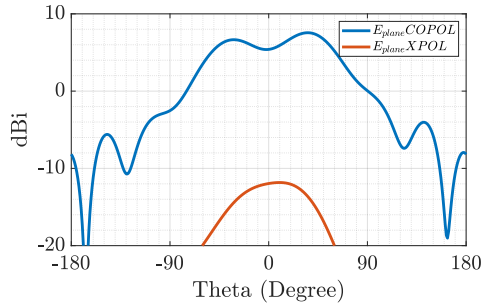

(c) *E-plane COPOL-XPOL at 28 GHz and 1 mm upper metal plate.*

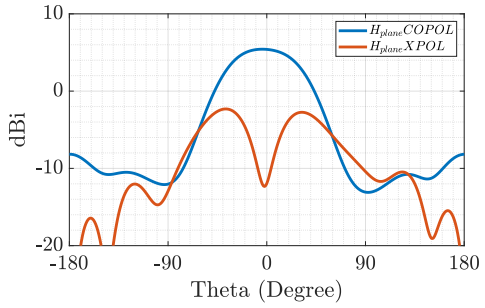

(d) *H-plane COPOL-XPOL at 28 GHz and 1 mm upper metal plate.*

Figure 3.14: *COPOL-XPOL at 24 GHz / 28 GHz and 1 mm upper metal plate with Bowtie Slot.*

3.2.5 Hybrid Diplexer-Splitter Loaded with two Dual band off-centered T-feed Slot Antennas

After these preliminary analyses, the initial model "Dual band off-centered T-feed Slot" is chosen and only for the purpose of analyzing the influence of loading the hybrid splitter-diplexer designed in the previous section, two of these antennas are loaded in each common port and the 10 resonators and the diamond-shaped power divider are readjusted. From the splitter-diplexer design process we know that we can reduce the simulation time by almost half by designing the filters separately, truncating up to the 2nd resonator of the opposing filter. The same is done in this case. Fig. 3.15 shows this methodology along with the number of parameters that need to be adjusted. For the complete final design with the two filters and two antennas, the good result of the achieved matching is shown. It should be mentioned that the offset in the center frequency of the passbands is calculated to include the transitions to achieve more centered bands at 24 GHz and 28 GHz respectively.

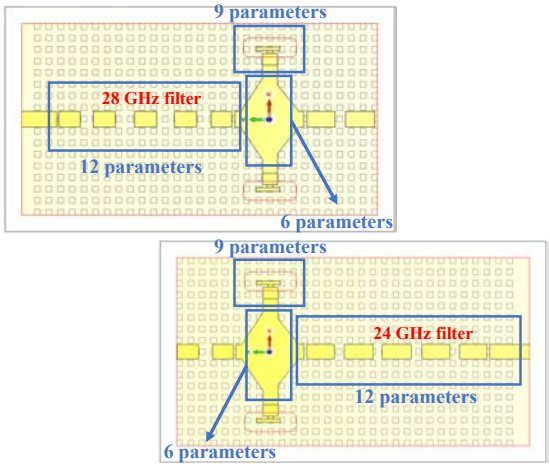

(a) *Hybrid Diplexer-Splitter Loaded with 2 Slot Antennas Design Methodology.*

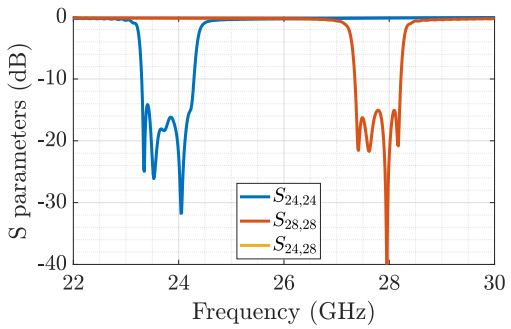

(b) *Simulated S-parameters of the COMPLETE Hybrid Diplexer-Splitter Loaded with 2 Slot Antennas.*

Figure 3.15: *Hybrid Diplexer-Splitter Loaded with 2 Slot Antennas S parameters.*

3.3 Corporate Feed Network and Subarray Design

Regarding the design of the corporate feed network, we started with the design of a 1:2 power divider using 1-section transformers of $\lambda/4$ to avoid taking up too much space and impairing the complete design of the corporate feed network of the array. Since that feed network will run over pins and pinless areas, we check by a sensitivity analysis on the relative position of the line w.r.t. the pins that in all cases the matching remains below -15 dB. (Fig.3.16).

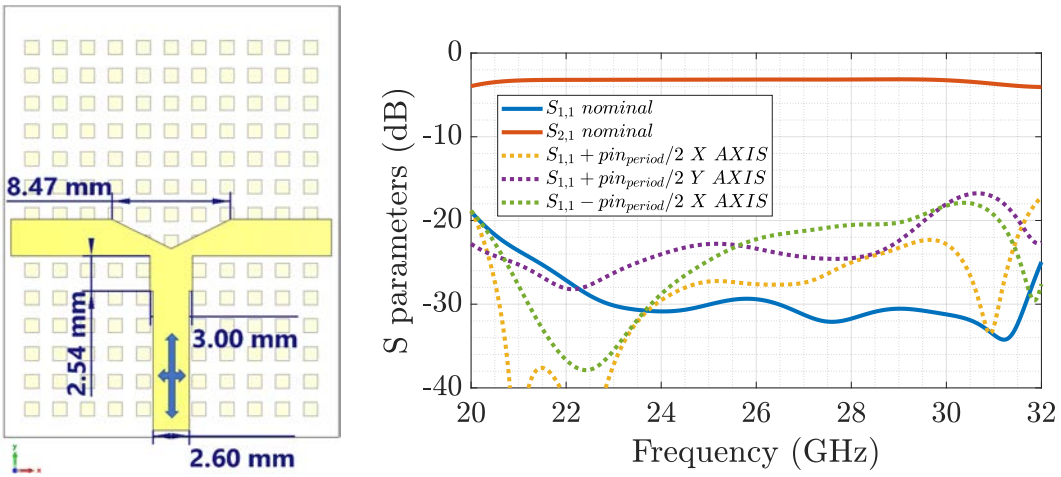

(a) *One section Quarter Wave power divider dimensions and axis.*

(b) *Simulated S-parameters of the power divider together with the result of the line sensitivity analysis w.r.t. the pins.*

Figure 3.16: *Wideband power divider in Inverted Microstrip Gap Waveguide Technology.*

Now that we have adjusted the splitter-diplexer to be matched to 2 antennas on the common ports, we study a 2-element subarray including the power divider. Unfortunately, we observe that the minimum dimensions between the 2 elements with a margin of 1 mm produces grating lobes at the upper frequency (28 GHz), since the separation between elements is $> \lambda$, specifically, 1.04λ. In Fig. 3.17, the S-parameters are presented and in Fig. 3.18 the radiation patterns with the grating lobes due to the spacing between array elements being greater than λ or very close can be observed.

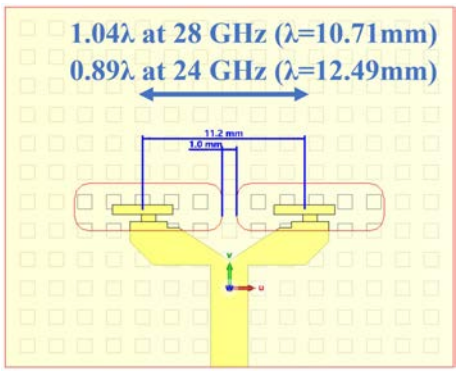

(a) *Two Slot Array Antenna with wideband power divider in Inverted Microstrip Gap Waveguide.*

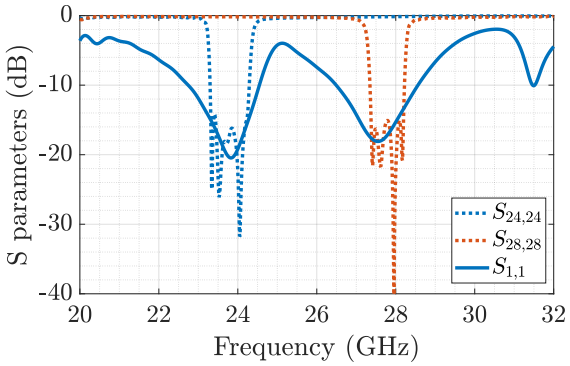

(b) *Simulated S-parameters of the 2 element subarray with the wideband power divider, superimposed on the response of the hybrid diplexer-splitter loaded with 2 slot antennas.*

Figure 3.17: *Two Slot Array Antenna with wideband power divider in Inverted Microstrip Gap Waveguide.*

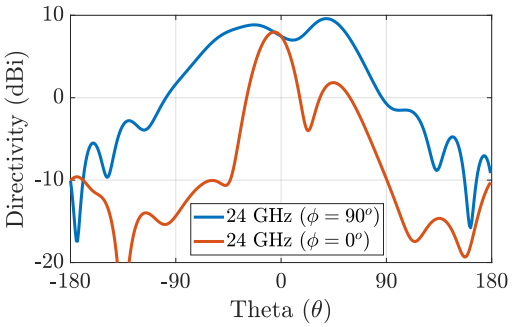

(a) *24 GHz radiation pattern.*

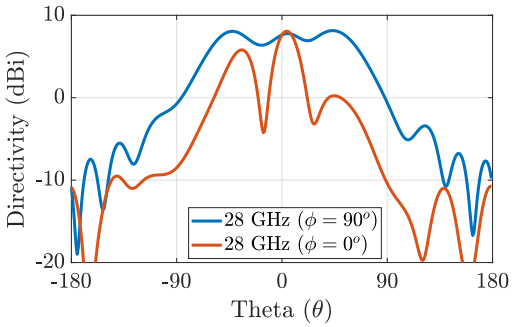

(b) *28 GHz radiation pattern.*

Figure 3.18: *Radiation pattern for the Dual Slot Array Antenna with wideband power divider in Inverted Microstrip Gap Waveguide.*

Following the same scheme, a 4-slot subarray was adjusted. Fig. 3.19b shows the best result achieved with 50 Ω impedance lines even with the modification of the input line to move it away from the lower left quadrant slot (see Fig. 3.19a). To avoid this coupling, half width lines are also tested (100 Ω), but the results are also unsatisfactory. In addition, this narrower line width, as already seen in the chapter on characteristic impedance, is very susceptible to the relative position of the line with respect to the pins under the substrate, complicating the design of the feed network.

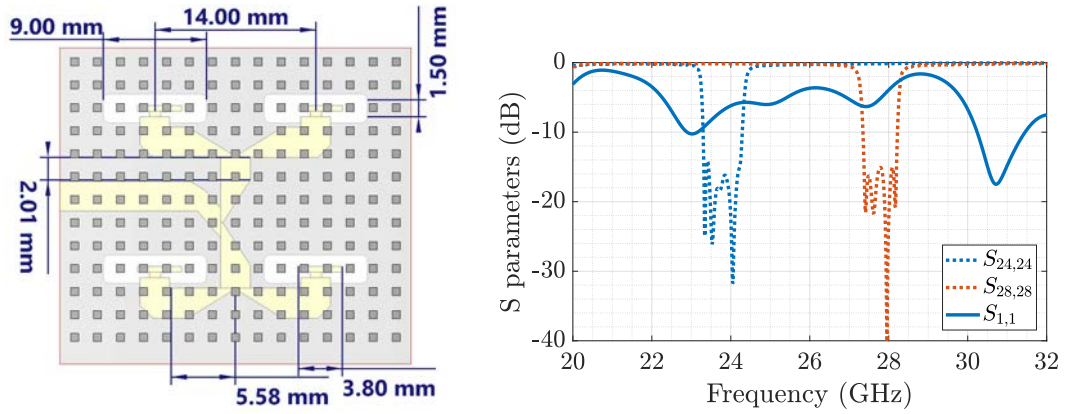

(a) *2D model without lids.*

(b) *Simulated S-parameters superimposed on the response of the hybrid diplexer-splitter loaded.*

Figure 3.19: *4 Slot Array Antenna with wideband power divider in Inverted Microstrip Gap Waveguide.*

3.4 Conclusions

This chapter presents the design of a hybrid splitter-diplexer device in Inverted Microstrip Gap technology with RO5880 substrate, based on an similar design made in Groove Gap Waveguide technology.

The starting point of the design is the diplexer obtained in the previous chapter with the addition of a power divider. Given the computational cost of this model, the first task to do is reducing its complexity as much as possible, analysing the loss in accuracy of the results when the transition from microstrip to inverted microstrip gap is removed. This causes a slight frequency shift of 300 MHz that will define our new working central frequencies. By integrating the transition afterwards, these frequencies will return to 24 and 28 GHz. After analysing the electric field distribution exciting from the 24 GHz filter port, it is observed that the energy does not propagate beyond the second resonator of the filter, so it can be removed from the simulation further reducing the computational cost. The behaviour is similar with the filter at 28 GHz.

From the aforementioned reference work, parallelisms of the central resonator in

groove gap waveguide technology are established to model our power divider as a 4-port diamond-shaped element. The results obtained in simulation are satisfactory both in matching and in transmission losses (about 4 dB), of which 3 dB correspond to the power divider function. The isolation between the filters is more than 40 dB.

After analysing the propagation of the electric field through the structure, an asymmetry is observed depending on whether the energy comes from the 24 GHz filter or the 28 GHz filter. This leads us to consider adding an asymmetry in the diamond shape to avoid this dispersive behaviour. The performance improves at the extremes of the passbands, achieving a more uniform response while maintaining the same level of losses and isolation.

After adjusting this splitter-diplexer, different dual-band radiating elements compatible with the diplexer bands are studied. We start with a dual band off-centered T-feed slot antenna in inverted microstrip gap that achieves a good matching of less than -10 dB at 24 and 28 GHz. The 1 mm thick metal lid is replaced by the thickness of the metallization of a typical substrate (35 µm) in order to study its suitability for fabrication with low cost printed technologies. Unfortunately, its matching and level of cross-polarisation are not as good as in the previous case and this path is discarded. In addition, this form of assembly presents robustness problems over the air gap. A wide-band centered T-feed bowtie slot was also designed, but it did not achieve sufficient bandwidth, so the element finally chosen was the dual band off-centered T-feed Slot. Subsequently, the hybrid splitter-diplexer is readjusted when the splitter-diplexer output ports are loaded by two of these antennas.

Next, a broadband 1:2 power divider is designed, which will be a key element in the corporate feed network. This design employs a conventional T-junction to which only one $\lambda/4$ transformer is added to avoid taking up too much space. Given the known problems of impedance sensitivity of the inverted microstrip gap line impedance with its position w.r.t. the pins, a study is carried out. This study

confirms that in all cases the matching will be below -15 dB.

For the subarray design, we start with only two elements to study the minimum distance at which they can be placed without generating mutual coupling problems and grating lobes. Unfortunately, the minimum distance is of the order of λ for the upper frequency (28 GHz). Similarly, a 4-element subarray is designed with poor results.

We can conclude that the use of broadband T-feed antennas requires the use of large slots, making it impossible to design arrays without creating grating lobes. Some solutions that can be proposed in order to demonstrate the performance of the device are the use of frequency bands less separated from each other, e.g. 26 GHz and 28 GHz, in fact, the reference paper on which this chapter is based works on 28 GHz and 29 GHz. Another possible solution is to use another layer for the subarray feed structure, although this complicates and makes the final design much more expensive.

Part II

Design of Groove-Gap Waveguide Components

Chapter 4

K-Band Monopulse Antenna with Sum and Difference Pattern in Groove Gap Waveguide technology implemented with Modified Glide Symmetric Holey EBG

This part of the thesis presents the design challenges and results of an K-band antenna for monopulse RADAR designed in Groove Gap Waveguide technology at 24 GHz, which, instead of being implemented with conventional rectangular pins, is implemented with a modification of the Glide Symmetrical Holey EBG structure.

4.1 Introduction to Monopulse Tracking Radar

The most intuitive way to detect and track targets using RADAR systems, defined as those in which the transmitter emits a signal and expects to receive the echo

in the form of backscattering, is by means of the azimuth/elevation angle sweep, mechanically or electronically, of a high directivity antenna that detects the maximum amplitude of this echo, thus obtaining its angular position. Among the errors of this system are the accuracy of azimuth detection, which depends on the antenna beamwidth, thermal noise, and scintillation (fluctuations in the cross-section of the target that distort the echo signal).

However, a monopulse system avoids interference between other echo signal pulses, reducing the error in the position indeterminacy. In these systems it is common to use slot array antennas fed with uniform amplitude and phase, which, adding phase shifters and couplers allow generating sum (Σ) and difference (Δ) radiation patterns. The sum pattern is used in the transmission mode (Tx) and the difference pattern for the reception mode (Rx). [143]. In these systems, the radiation lobe of the sum pattern is reoriented by means of servomotors (or electronics) controlled by closed-loop control systems so that it is always illuminating the target, which allows the signal to noise ratio in detection to be superior to other methods used in moving target localization.

To calculate the angle of arrival in azimuth, called OBA (Off-Boresight Angle), the monopulse function defined in Eq. 4.1 compares the signals of both channels.

$$OBA = \varphi_{Az} = \frac{\Delta_{Az}(\varphi)}{\Sigma_{Az}(\varphi)} \tag{4.1}$$

Monopulse systems, however, are not without drawbacks such as increased complexity and cost. In their conventional implementation, one of the slotted antennas is connected to a 90° phase shifter and the other to a rectangular waveguide without phase shifter. Then, both subsystems are fed through a hybrid coupler that equally splits the power and adds an additional 90° to the waveguide including the phase shifter, resulting in 180° or 0° depending on whether we excite through one port or the other as we see in Fig. 4.1a. For 3D monopulse systems (azimuth + elevation) it

is necessary to use 4 arrays of antennas to obtain in addition the $\Delta_{El(\theta)}$, which implies duplicating all the components to be able to make the comparisons of Fig. 4.2.

This system is designed to perform amplitude comparisons as the antennas of both channels share the same phase center (Fig. 4.1). In this case, the Eq. 4.2 would be particularized to the amplitude or absolute value of the ratio of these values X_Δ and X_Σ.

In ca[illegible] they are sepa[illegible] tions RADAR [illegible] of the signals (

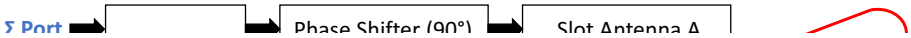

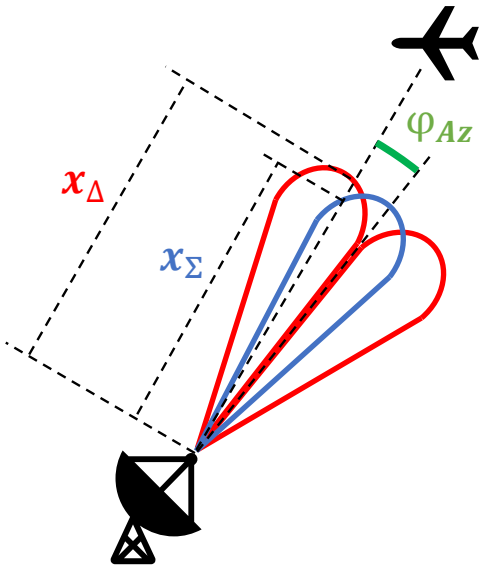

(b) *Amplitude comparison monopulse principle.*

Figure 4.1: *Monopulse antenna system.*

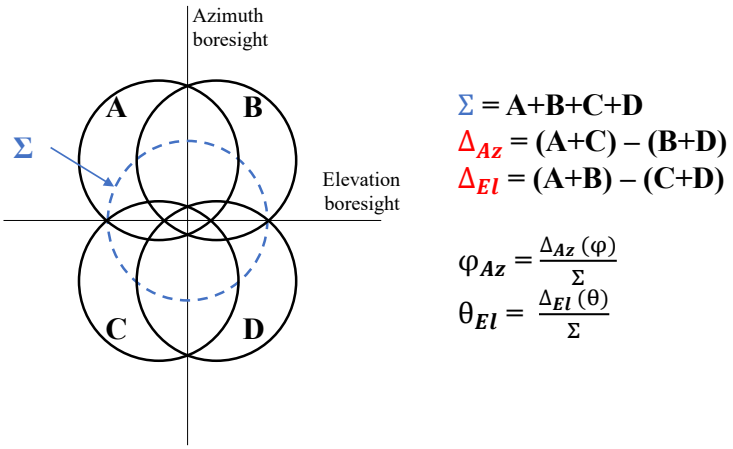

Figure 4.2: *Signal processing of the 3D monopulse system consisting of 4 antennas.*

$$\varphi_{Az} = \frac{|\Delta_{Az}(\varphi)|}{|\Sigma(\varphi)|} \tag{4.2}$$

$$\varphi_{Az} = \angle\Delta_{Az}(\varphi) - \angle\Sigma(\varphi) \tag{4.3}$$

4.2 Groove Gap Waveguide Implementation with Glide Symmetric Holey EBG

As we saw in the "Gap Waveguide Technology Background" section, there are several ways to implement the Gap Waveguide technology.

To date, numerous high-impedance periodic surfaces have been proposed that replicate the PMC boundary condition [32], [34]. From the first ones made with rectangular metallic pins, that were mathematical characterized in [35], passing through pyramid-shaped pins [36], mushroom-shaped pins [32], [37], spring-shaped pins [38], or with the novel technique of employing perforations in the metal to create an EBG structure [39]–[43]. A new Half-Groove Gap Waveguide for rapid prototyping, lowering its cost for mass production has also been recently presented to the community [44], here again using pins.

Great progress has also been made so far in the understanding and mathematical analysis of holey implementation of the Groove Gap Waveguide technology, [39], [145]–[152]. In particular, details such as the modeling of the conical shape of the bottom of the drilled holes in [146]. The fact is that the biggest advantage of this new form of implementation over CNC machined pins is the ease of fabrication by drilling. In addition, to achieve a stop-band in a given frequency range, the size of the holes is much larger than that of the pins [153], [154]. This advantage starts to become considerable from millimeter-wave bands and above. Also it is frequent that larger stopbands are achieved with this implementation compared to the version with pins [145]. Some very important considerations on the design of gap waveguide structures with glided-symmetrical holey are presented in [155].

Fig. 4.3 shows a unit cell designed with Glide Symmetrical Holey EBG structure for different gaps. It is observed that only with gap = 0.01 mm the stopband matches with our working frequency (24 GHz). This exposes us to be outside the stopband due to the manufacturing tolerances and the roughness of the metal plates in case

the gap is bigger. Furthermore, due to the complexity of the device we are going to design, we cannot use larger holes or periods. As a consequence, we propose a new combination of holes as shown in Fig. 4.4, which do have the forbidden band at our frequency even until a gap of 0.1 mm.

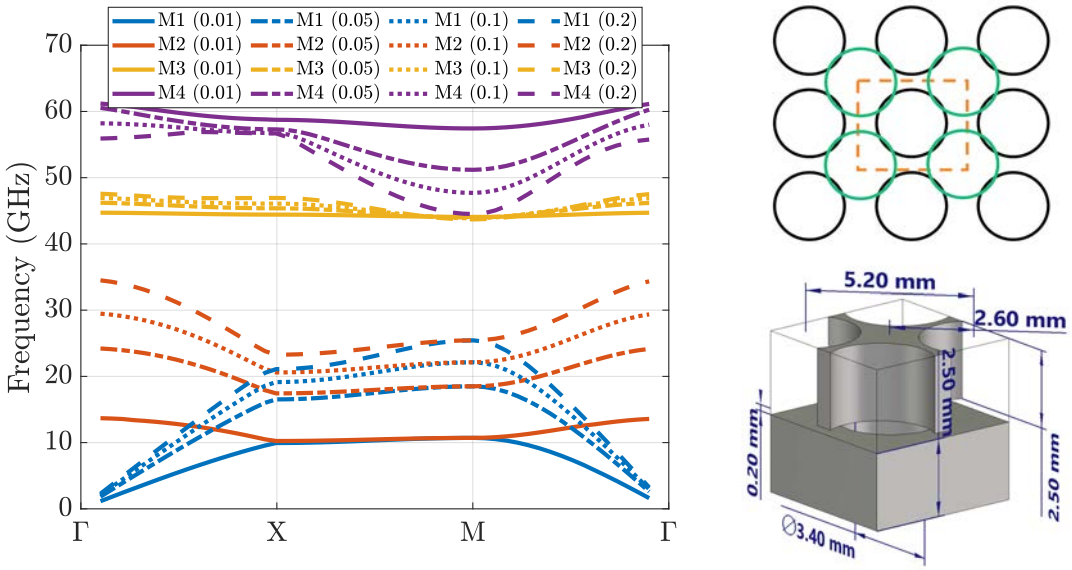

(a) *Dispersion diagram comparison for Conventional Holey Glide Symmetric EBG.*

(b) *Unit cell dimensions.*

Figure 4.3: *Conventional Holey Glide Symmetric EBG with period=5.2 mm, hole radius=1.7 mm, hole deep=2.5 mm and variable gap.*

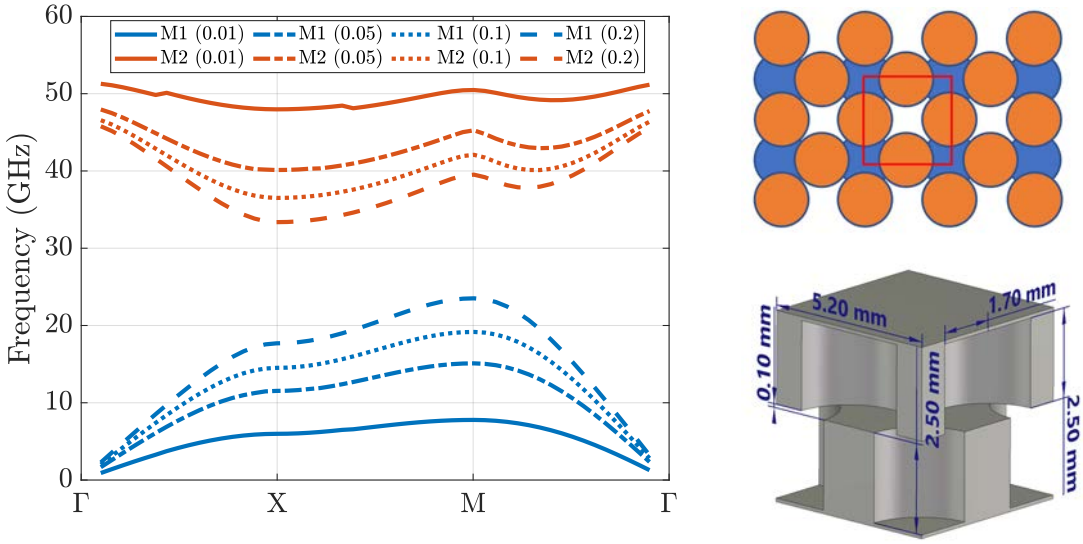

(a) *Dispersion diagram comparison for Modified Holey Glide Symmetric EBG.*

(b) *Unit cell dimensions.*

Figure 4.4: *Modified Holey Glide Symmetric EBG with period=5.2 mm, hole radius=1.7 mm, hole deep=2.5 mm and variable gap.*

An example of qualitative comparison of the stopband and 4x4 unit cell size between the implementation with pins and with holes for a similar frequency band can be seen in Fig. 4.5, Fig. 4.6 and Fig. 4.7.

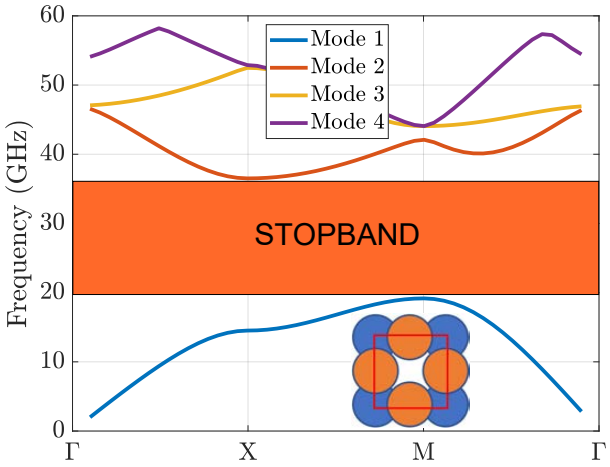

(a) *Dispersion diagram with inset for glide symmetric holey structure (orange=top, blue=bottom).*

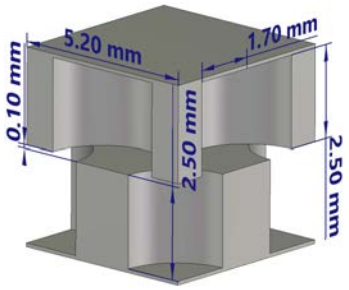

(b) *Unit cell dimensions.*

Figure 4.5: *EBG stopband achieved with Modified Glide-Symmetric Holey Unit Cell from 19.17 GHz to 36.51 GHz with period=5.2 mm, hole radius=1.7 mm, hole deep=2.5 mm and gap=0.1 mm.*

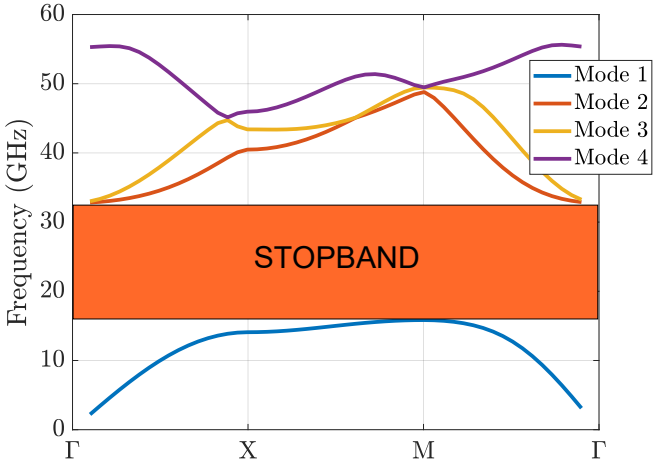

(a) *Dispersion diagram for Inverted Microstrip GW (orange=top, blue=bottom).*

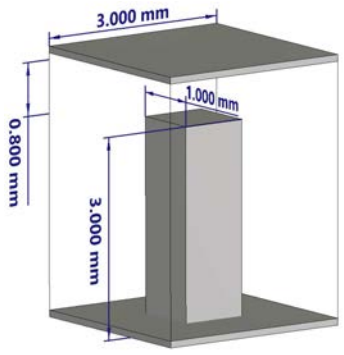

(b) *Dimensions of the inverted microstrip gap unit cell.*

Figure 4.6: *EBG stopband achieved with pins from 15.8 GHz to 32.8 GHz with period=3 mm, pin=1 mm, height=3 mm and gap=0.1 mm.*

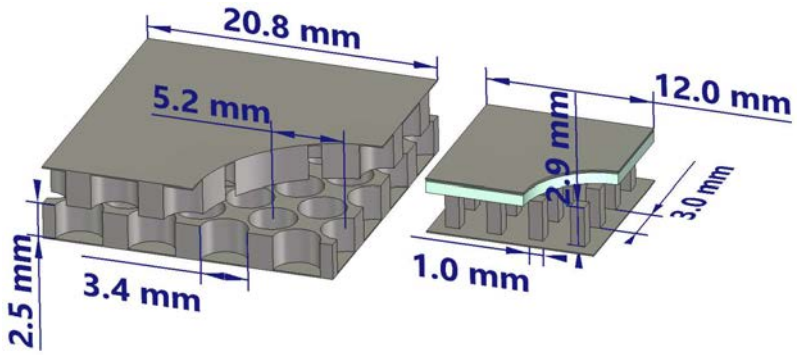

Figure 4.7: *Example of equal scale comparison between 4 unit cells with Modified Glide Symmetry and 4 cells with Inverted Microstrip Gap Waveguide pins for similar EBG stopband.*

However, this new combination can also present problems in some specific designs, in particular with the antenna that is the subject of this chapter, as we will see in the following.

4.3 Riblet Coupler Design

Now, we can consider the design of the antenna components for the monopulse design. The first one is the most critical and consists of a "Riblet Short-Slot coupler", chosen for its compact size and good performance over a moderate bandwidth [156]–[158]. This type of coupler is a 3 dB hybrid in which the power is equally splitted between the "coupled" and the "through" outputs with a 90° phase shift between them. The operating principle of this coupler is to allow the TE_{20} and TE_{10} modes to be propagated simultaneously in the middle part of it where the central wall of 2 longitudinally juxtaposed guides is eliminated. The size of the central septum determines the frequency at which this power splitting between the 2 output branches occurs. This size must be bigger than $\lambda_g/2$ [159].

4.3.1 Rectangular Waveguide Design

To facilitate the design and subsequent parameter setting, we start by making this Riblet coupler in standard rectangular waveguide technology with lossy metals (aluminum), and closed, *i.e.*, **without gap between the 2 parallel plates**. In Fig. 4.8 we show the ideal case with the approximate dimensions that will serve as a starting point for the design with holes. We can see the coupler and its dimensions (Fig. 4.8a and b), the S parameters with equal power distribution between the outputs (-3 dB in each port) (Fig. 4.8c), and the distribution of the electric field in absolute value for 24 GHz in Fig. 4.8d. Here, it is qualitatively appreciated the phase difference between the output ports corresponding to 90.47° obtained from the simulation.

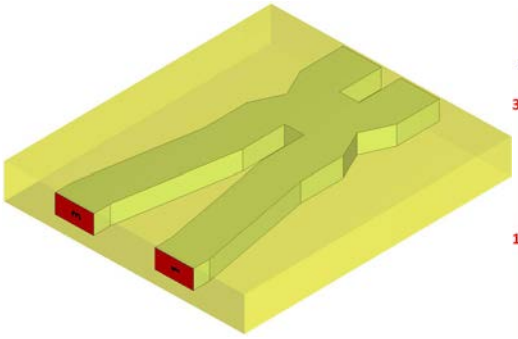

(a) *3D view.*

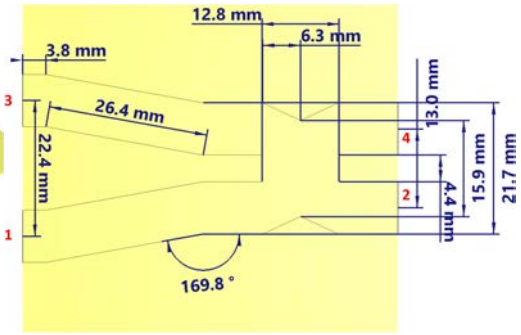

(b) *Dimensions.*

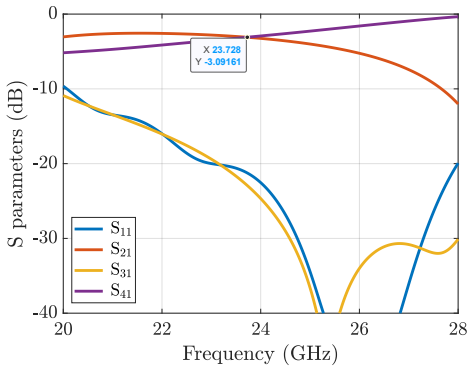

(c) *Simulated S-parameters.*

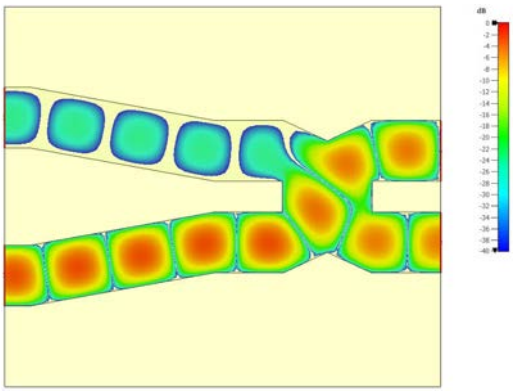

(d) *Electric field distribution in absolute value for 24 GHz.*

Figure 4.8: *Riblet Coupler design in conventional Rectangular Waveguide Technology.*

4.3.2 Holey Glide Groove Gap Waveguide Design

With these initial parameters of the coupler in RWG technology, we proceed as with the other designs based on Gap Waveguide, determining the dimensions of the holes (unit cell) to achieve the stop-band in the working band. In Fig. 4.9 we reproduce again for the reader's convenience the dispersion diagram of the comparison of the initial part of the chapter with the final design parameters of the chosen periodic structure with holes with modified glide symmetry.

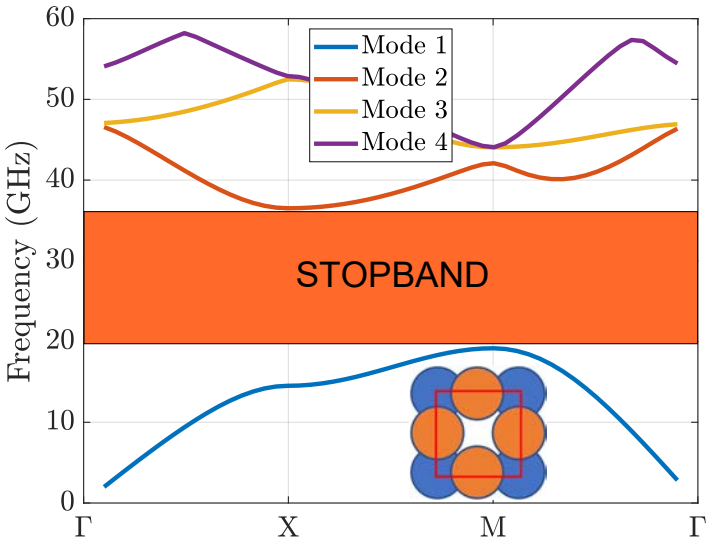

(a) *Dispersion diagram with inset for modified glide symmetrical holey structure (orange=top, blue=bottom).*

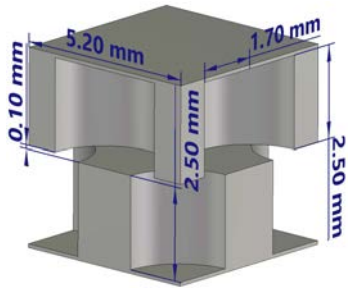

(b) *Unit cell dimensions.*

Figure 4.9: *EBG stopband achieved from 19.17 GHz to 36.51 GHz with period=5.2 mm, hole radius=1.7 mm, hole deep=2.5 mm and gap=0.1 mm.*

It should be noted that thinking about the antenna part and to avoid separating the 2 slot antennas by more than λ to avoid grating lobes, the distance between the outputs should be adjusted to the minimum possible; and, in this way, only one row of holes displaced in one direction fits. Therefore, in this part of the component we would have a "soft" surface with propagation blocking in the direction perpendicular to it, instead of an EBG with blocking in the entire 2D plane. Still this structure has been successfully used in previous designs such as [160], [161].

This part of the component must be designed to allow the assembly of WR34 transitions to perform the measurements with VNA. To this aim, the input has the ports separated to accommodate them, producing a conformal hole repositioning following the profile of the guides.

It should be noted that in this design we do not use "matching posts" [160], in order to make the device easier and cheaper to be manufactured. These pins allow phase rebalancing in the odd mode in addition to improving matching [159], although in our case they were not necessary. Only mechanical alignment pins on the outside of the circuit are used to match the two lids.

The model in Fig. 4.10a shows the final design with its dimensions, where the holes in the upper part have been marked with a thicker line and those in the lower metal plate with a thinner line. A 3D view and the front view of the model are shown in Fig. 4.10b and c.

To see the phase shift between the outputs we can look at Fig. 4.11a where the electric field distribution at 24 GHz is shown and in Fig. 4.11b it is shown the exact value calculated as a function of the frequency. This achieved phase shift is 80° at the frequency of interest.

Finally, Fig. 4.12 shows the simulated S-parameters of this coupler, where the transmission losses we obtain with this model considering in the simulations the losses of the materials (aluminum) are -0.91 dB at most, since -3 dB are due to the symmetrical power split between the outputs at 24 GHz.

If we wish to go a little deeper into the origin of these losses in order to improve the structure, we can carry out a study of the absorbed power with CST, discriminating by type of material and propagation characteristics. The nomenclature used by this software is summarized in Fig. 4.13a, where it is shown that the power stimulated to the structure is composed of outgoing power through all ports, plus the power accepted by the structure. This, in turn, is divided into power absorbed

(losses) by metals and dielectrics and radiated power. CST normalizes the excitation power to 1 W, and we observe in Fig. 4.13b,c that the losses are mainly due to lossy metals, aluminum in this case, with values of 55.5 mW at the frequency of interest, and to a lesser extent, radiation losses, with 30.7 mW at the same frequency of 24 GHz, whose sum (86.2 mW) corresponds to the power accepted by the structure of 88.3 mW with an error of 2 mW, possibly due to rounding errors of the simulation algorithm or modes not considered in the port excitation. A radiation loss peak is also observed at 21 GHz.

Note that in the designed complete model, a wedge-shaped taper in the coupler septum is added to improve matching when coupling the antenna.

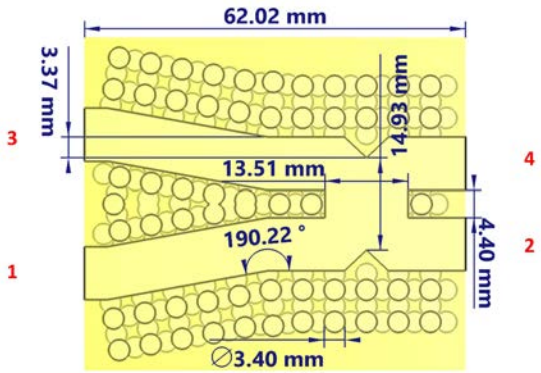

(a) *Designed model with dimensions and detailed ports.*

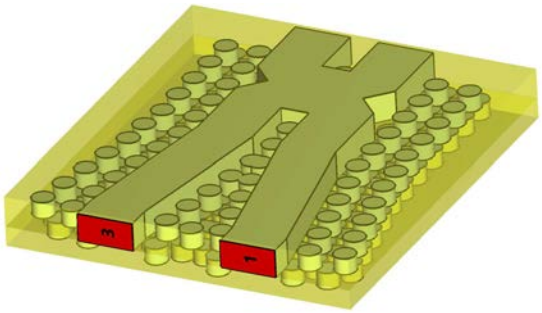

(b) *Designed model in 3D.*

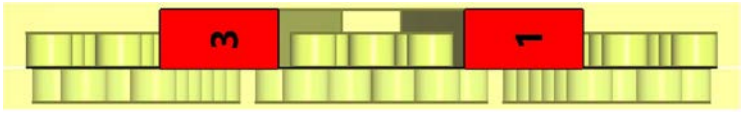

(c) *Frontal view of the Riblet Coupler.*

Figure 4.10: *Designed Riblet Coupler in modified Glide Symmetrical Holey Groove Gap Waveguide Technology.*

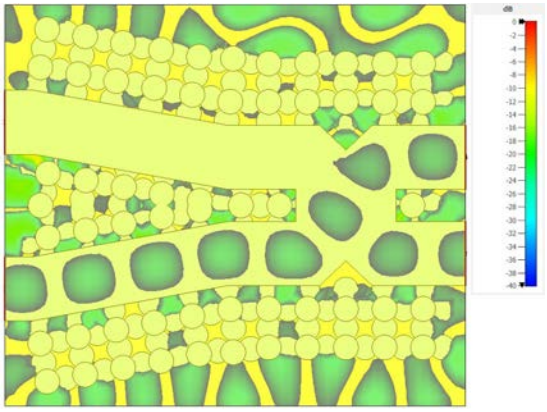

(a) *E field (absolute value) distribution @ 24 GHz.*

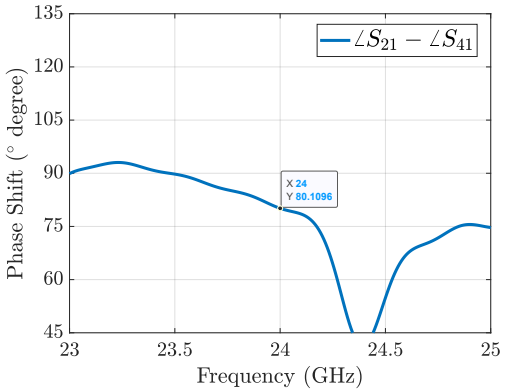

(b) *Phase offset between outputs in the designed Riblet Coupler.*

Figure 4.11: *Phase offset in Riblet Coupler with modified Glide Symmetrical Holey Groove Gap Waveguide Technology.*

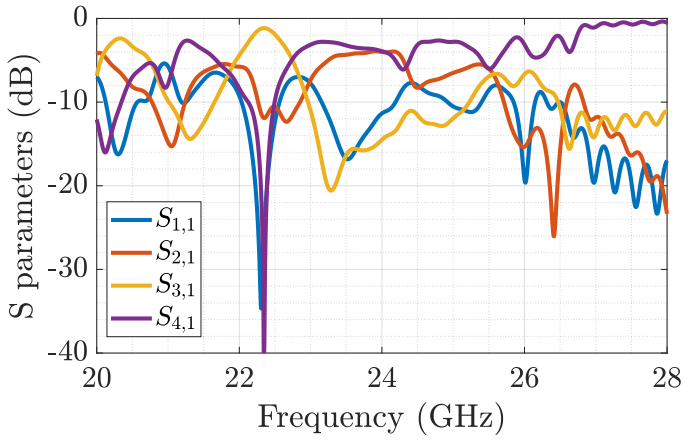

(a) *S parameter.*

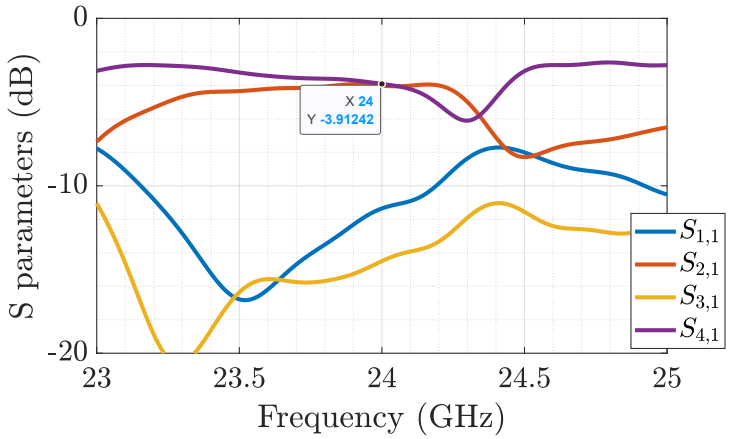

(b) *S parameter (Zoom).*

Figure 4.12: *S parameters for the Riblet Coupler in modified Glide Symmetrical Holey Groove Gap Waveguide Technology.*

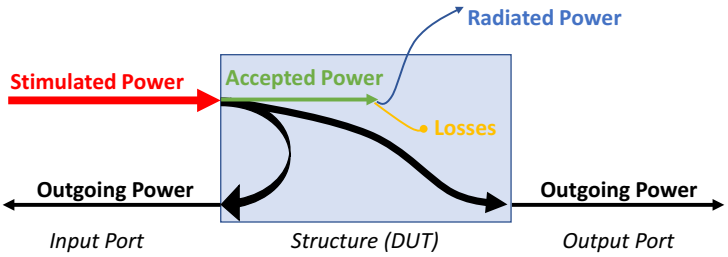

(a) *Nomenclature used by CST in power analysis through structure.[1]*

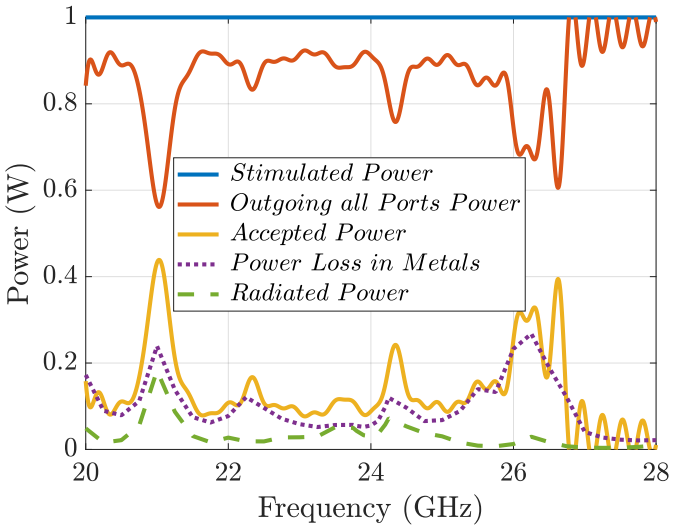

(b) *Power Analysis.*

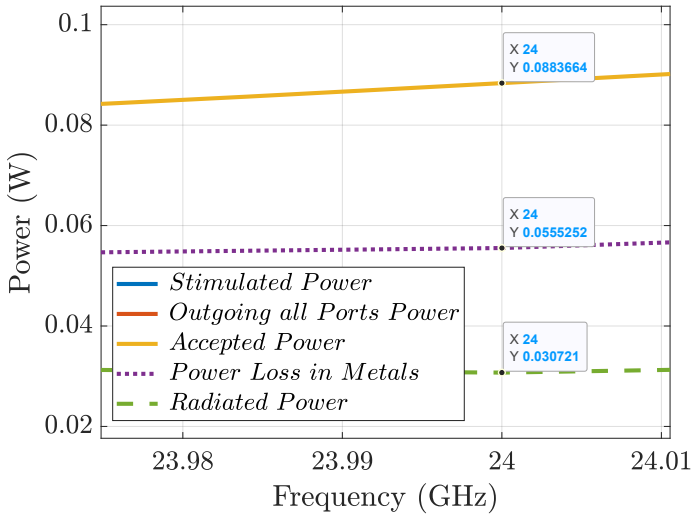

(c) *Power Analysis (zoom at 24 GHz).*

Figure 4.13: *Power Losses Analysis according to materials or radiated power for the Riblet Coupler in modified Glide Symmetrical Holey Groove Gap Waveguide Technology.*

4.4 Phase Shifter Design

In order to radiate with a sum or difference pattern, we need to place a 90° Phase Shifter after the Riblet Coupler to achieve a phase shift of 180° or 0° between the outputs, depending on the port from which we excite the structure.

One way to phase shift a signal of one channel with respect to that of another is by means of **differential phase shifters**, modifying the electrical length of one of them. The disadvantage of this solution with rectangular waveguides is the size, added complexity and, therefore, cost. Another solution is with **insertion phase shifters**, where the phase shift occurs between the output and input signal of an internally modified waveguide, taking as a reference the phase at the output of the one that remains unmodified.

Within the insertion phase shifters, in rectangular waveguides we can choose to increase the width (a) of one of the guides, which decreases the cutoff frequency, and therefore increases the propagation constant β (decreases the λ_g), as we see in Eqs. 4.4 and 4.5. The cutoff frequency of the TE_{10} mode is shown since after the Riblet coupler it is the only mode that would propagate.

$$f_C(TE_{10}) = \frac{c}{2a} \tag{4.4}$$

$$\beta = \frac{2\pi\sqrt{1-(\frac{f_c}{f})^2}\sqrt{\varepsilon_r}}{\lambda_0} \tag{4.5}$$

Another insertion method widely used in phase shifters is the use of dielectric slabs with which we can modify the effective electrical permittivity of the waveguide, being the one that has been chosen in this work for its good results.

To achieve this, a dielectric sheet has been used in the center of the guide, where the TE_{10} mode is maximum, and whose length determines the phase shift achieved.

In some cases with groove gap waveguide (GGWG) technology, such as the work presented in [162] it is necessary to widen the part of the waveguide that coincides with the slab to contribute to the phase shift and to improve the matching avoiding power reflections, although it was not necessary in this case and the two waveguides were kept straight in parallel, facilitating and simplifying the design and, therefore, reducing the manufacturing cost.

As with the Riblet coupler design, a design was first made with rectangular waveguides to estimate the sheet length and then the holes were added.

The dielectric used for the phase shifter slab is a very low loss Rogers RT5880^{TM} ($e_r = 2.2,\ tan\delta = 0.0009$), with 0.51 mm thickness, for which we need a length of 30 mm to obtain 90° phase shift with respect to the other guide. We have used a low permittivity material to avoid reflections.

Fig. 4.14 shows the designed phase shifter model with its most relevant dimensions and a 3D view. Fig. 4.14c shows the simulated S-parameters where the insertion loss is -0.34 dB and the obtained matching is below -15 dB in the band of interest. This good matching and low losses are achieved due to the small thickness of the film and its low permittivity as mentioned.

In Fig. 4.15a the distribution of the electric field in absolute value normalized to the maximum value for a simultaneous excitation of the two input ports is presented. Note the same amplitude level is observed inside the waveguides and in the external frame as the holes do not extend to the edge to simplify the fit of the model in simulation. In Fig. 4.15b we can appreciate the obtained phase shift of 89°.

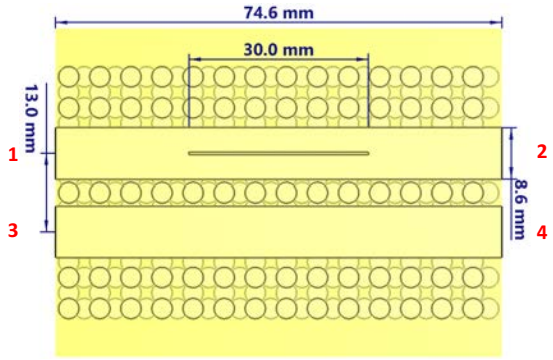

(a) *Designed Phase Shifter with dimensions and detailed ports.*

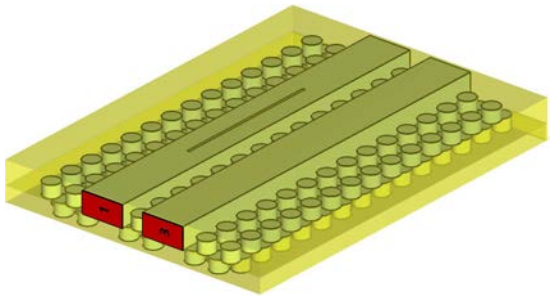

(b) *Designed Phase Shifter (3D view).*

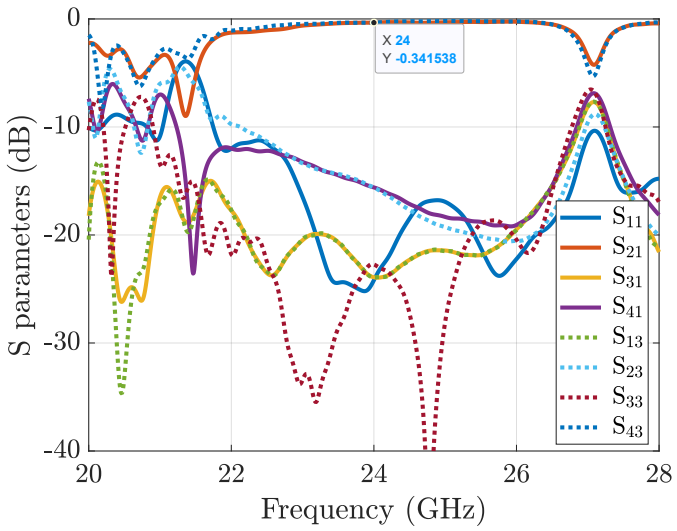

(c) *Simulated S parameters for Phase Shifter.*

Figure 4.14: *Designed Modified Glide Symmetrical Holey 90° Phase Shifter.*

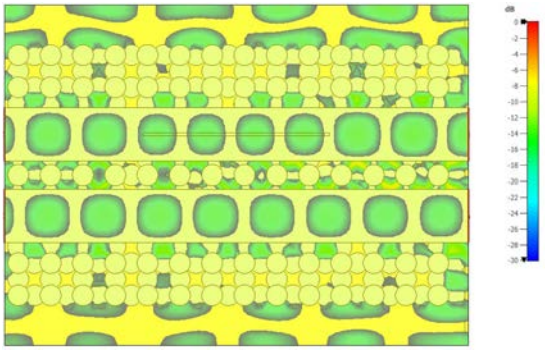

(a) *E field (absolute value) distribution @ 24 GHz for simultaneous excitation of ports 1 and 3.*

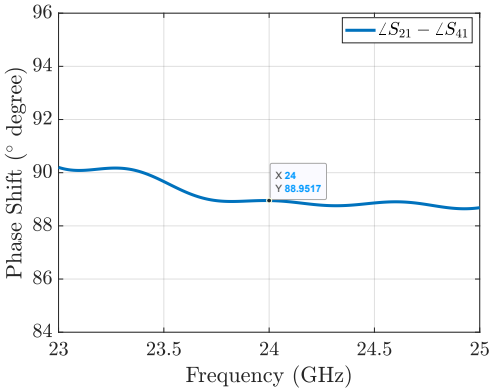

(b) *Simulated Phase Shift.*

Figure 4.15: *Designed Modified Glide Symmetrical Holey 90° Phase Shifter: Model and simulated results.*

4.5 Riblet Coupler and Phase Shifter Integration

4.5.1 Central Row of Holes Design

Having calculated the dimensions of the phase shifter, the next logical step is to add it next to the Riblet coupler while maintaining the periodicity of holes on both sides of the waveguides and in the center row in the propagation direction. However, doing so produces a large power imbalance between the outputs as we see in Fig. 4.16, with port 2 having a value of -10.49 dB and port 4 having -1.14 dB. Modifications to the Riblet coupler septum were tried without success by modifying the straight wall to a more progressive wedge-shaped bifurcation (V-shape taper central walls) that would reduce reflections.

After many modified designs it was discovered that the absence of the second coupler septum hole exactly leaving one period from the first one was very critical. In the following figures, Fig. 4.16, 4.17, 4.18 and 4.19, the differences between some solutions designed in order to equalize the output power when extending the coupler waveguides, all still without the phase shifter sheet, are shown. The most plausible explanation for this behavior after analyzing the electric field distribution through the structure is that this area without holes allows the filtering of energy towards the other waveguide decreasing the impedance seen by the wave, acting as a "matching no-hole".

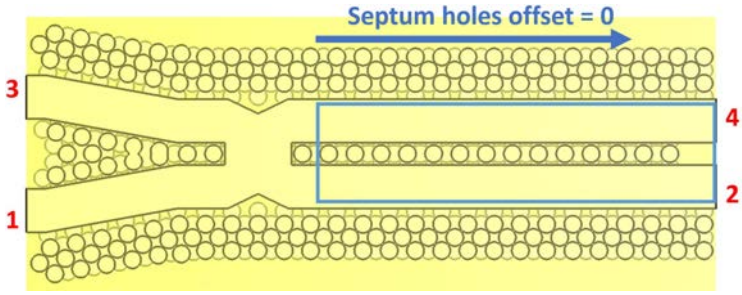

(a) *Waveguide extended coupler model #0 with detailed ports.*

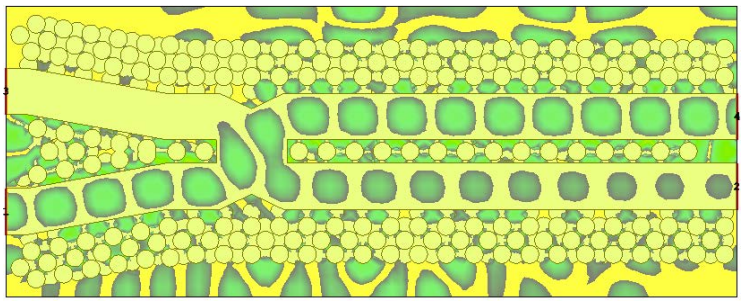

(b) *E field distribution (absolute value @ 24 GHz) for port 1 excitation. Model #0.*

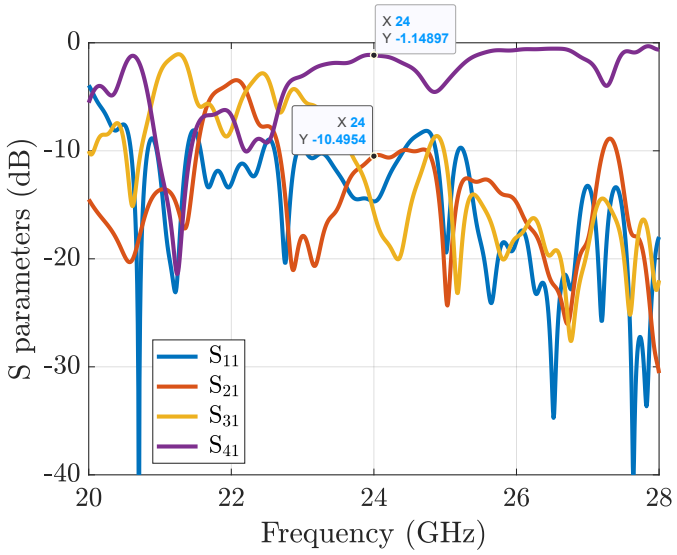

(c) *Simulated S parameters of the Extended Riblet Coupler model #0.*

Figure 4.16: *Waveguide Extended Riblet Coupler Model #0 with continuous center row of holes.*

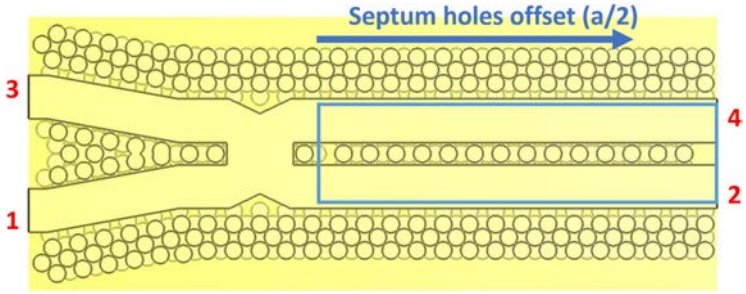

(a) *Waveguide extended coupler model #1 with detailed ports.*

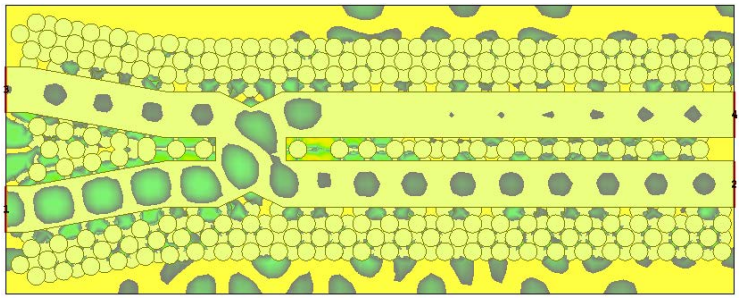

(b) *E field (absolute value) distribution @ 24 GHz for excitation port 1 for model #1.*

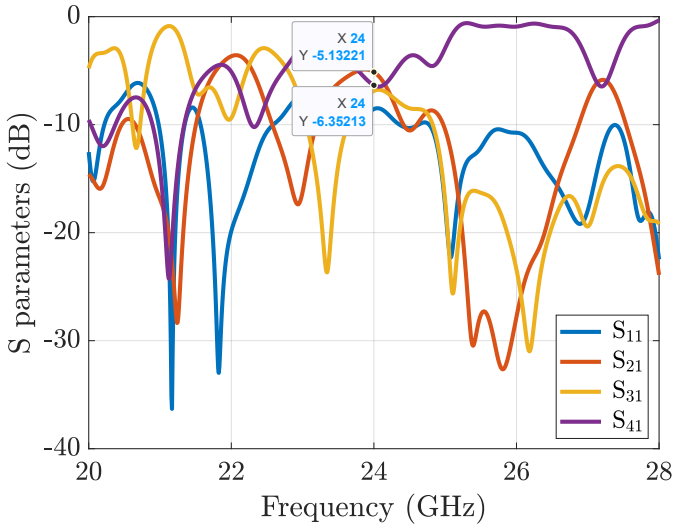

(c) *Simulated S parameters of the Extended Riblet Coupler model #1.*

Figure 4.17: *Waveguide Extended Riblet Coupler Model #1 leaving a half-period spacing (a/2) in the center row of holes.*

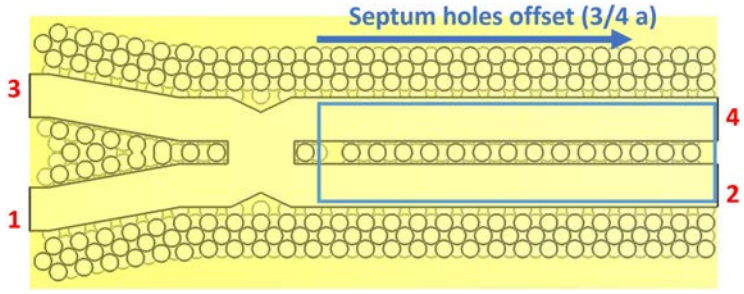

(a) *Waveguide extended coupler model #2 with detailed ports.*

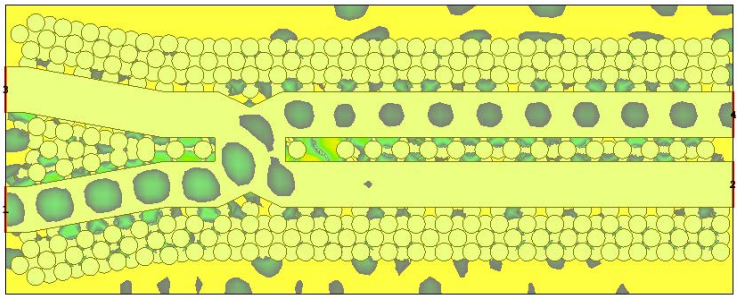

(b) *E field (absolute value) distribution @ 24 GHz for excitation port 1 for model #2.*

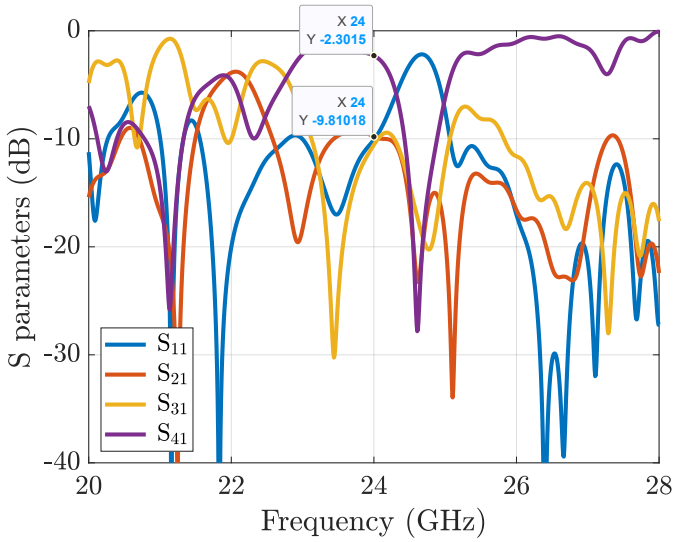

(c) *Simulated S parameters of the Extended Riblet Coupler model #2.*

Figure 4.18: *Waveguide Extended Riblet Coupler Model #2 leaving a space of three-quarters of a period (3/4 a) in the center row of holes.*

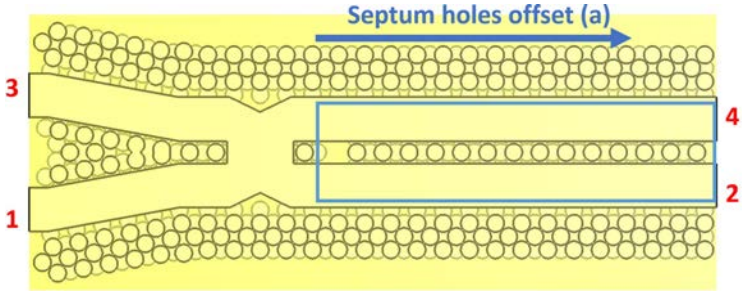

(a) *Waveguide extended coupler model #3 with detailed ports.*

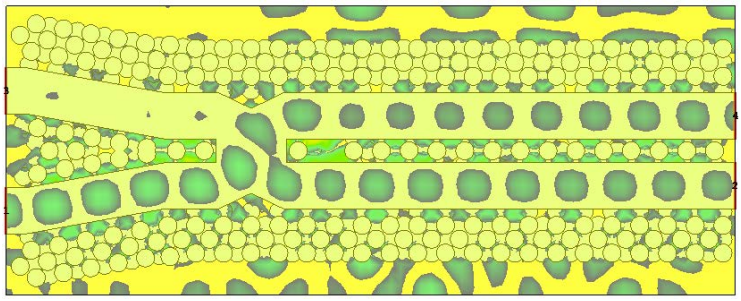

(b) *E field (absolute value) distribution @ 24 GHz for excitation port 1 for model #3.*

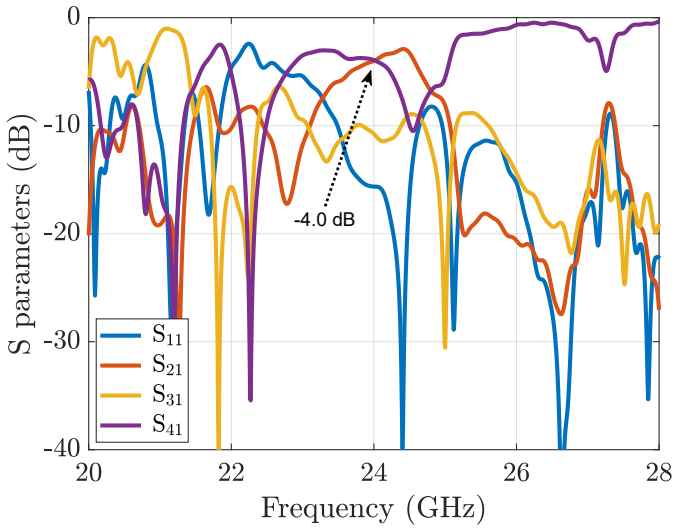

(c) *Simulated S parameters of the Extended Riblet Coupler model #3.*

Figure 4.19: *Waveguide Extended Riblet Coupler Model #3 leaving a one-period space (a) in the center row of holes.*

4.5.2 Dielectric Strip Position Design

After improving the power unbalance problem occurred after extending the guides in the Riblet coupler, we can now place the phase shifter slab to obtain an extra phase shift of 90°.

Although intuitively it would seem that the position of this dielectric slab should not affect the power unbalance of the outputs, the simulations indicate otherwise. Therefore, the distance at which we should place it with respect to the beginning of the phase shifter block was also adjusted.

In Fig. 4.20, we see for the case where the slab is located just at the beginning of the first hole in the phase shifter module, that the unbalance between the outputs is remarkably high (-2.6 dB vs -6.2 dB). In Fig. 4.21, this slab has been shifted one period (a), obtaining a power unbalance similar to the previous case. We must shift the slab at least 7.5 hole periods (7.5a) for the power to stop being affected and obtain balanced outputs of the order of -3.6 dB. The phase shift obtained in this model is 188° (See Fig. 4.22).

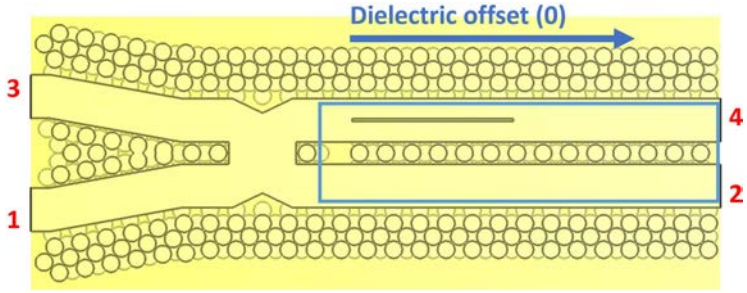

(a) *Waveguide extended coupler model with phase shifter slab and detailed ports.*

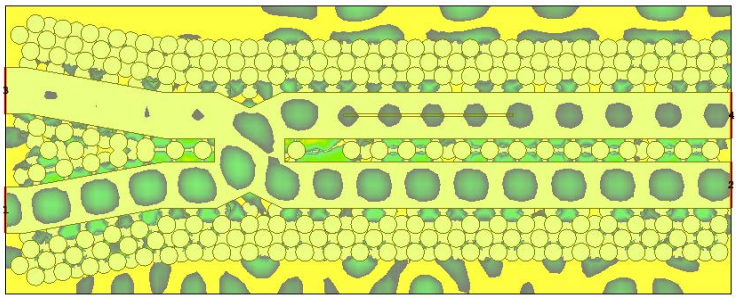

(b) *E field (absolute value) distribution @ 24 GHz for excitation port 1.*

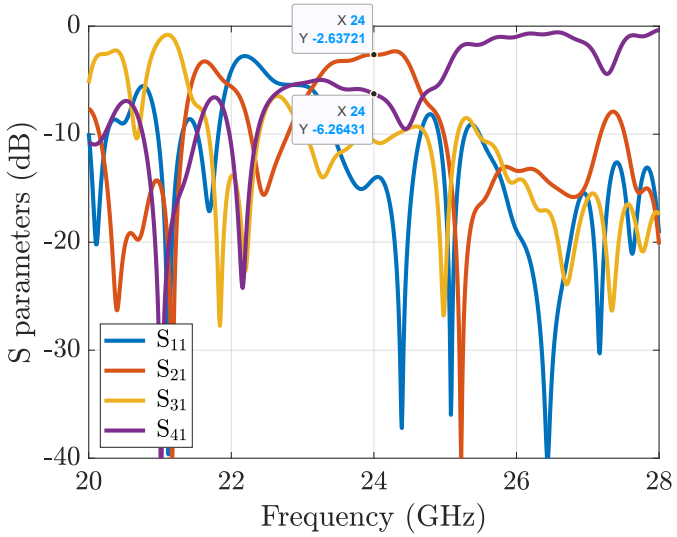

(c) *Simulated S parameters of the Extended Riblet Coupler model with phase shifter slab.*

Figure 4.20: *Riblet Coupler and Phase Shifter Model with the phase shifter slab at the beginning of the continuous row of holes.*

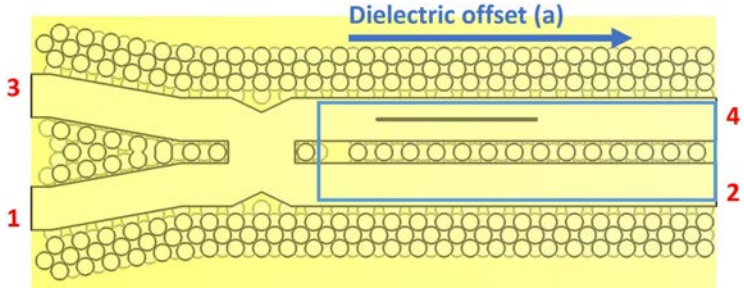

(a) *Waveguide extended coupler model with phase shifter slab and detailed ports.*

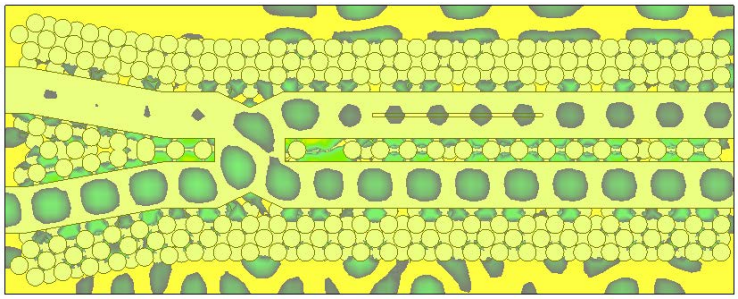

(b) *E field (absolute value) distribution @ 24 GHz for excitation port 1 .*

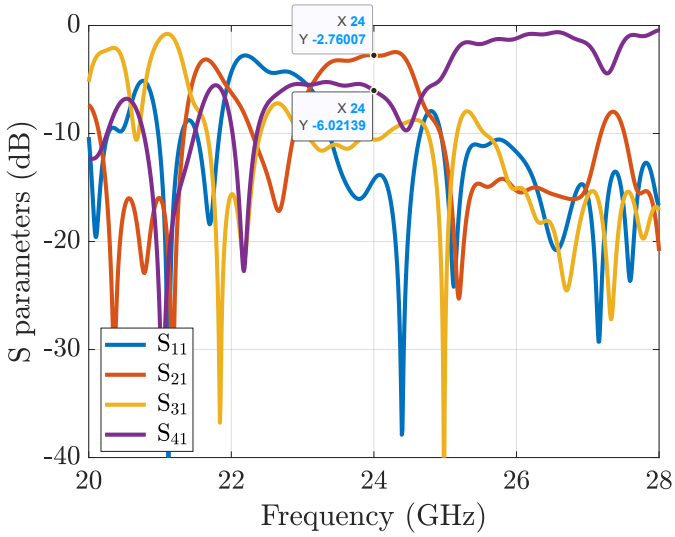

(c) *Simulated S parameters of the Extended Riblet Coupler model with phase shifter slab.*

Figure 4.21: *Riblet Coupler and Phase Shifter Model with the phase shifter slab at 1 period of the continuous row of holes.*

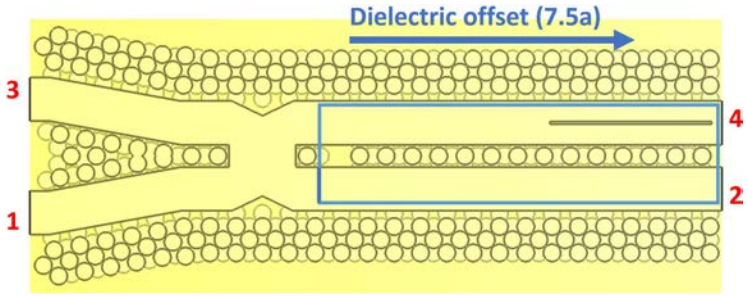

(a) *Waveguide extended coupler model with phase shifter slab and detailed ports.*

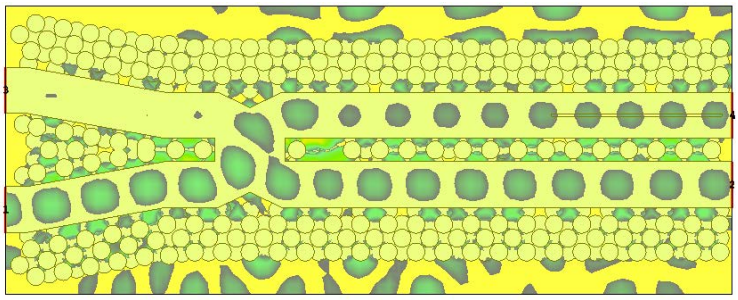

(b) *E field (absolute value) distribution @ 24 GHz for excitation port 1.*

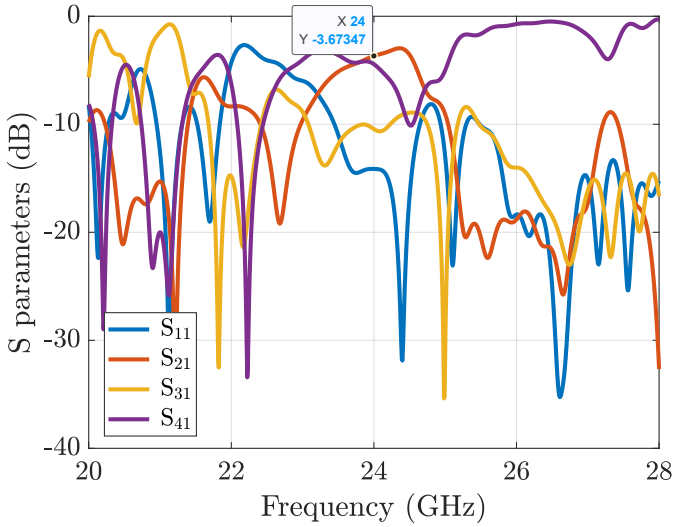

(c) *Simulated S parameters of the Extended Riblet Coupler model with phase shifter slab.*

Figure 4.22: *Riblet Coupler and Phase Shifter Model with the phase shifter slab at 7.5 periods of the continuous row of holes.*

Therefore, as we can see, at least a distance of 7.5 periods (7.5a) is needed for the slab to be undisturbed. The holes are also extended to the edge of the structure. After some minor adjustments, we see in Fig. 4.23 the final design of the Riblet coupler with the integrated phase shifter.

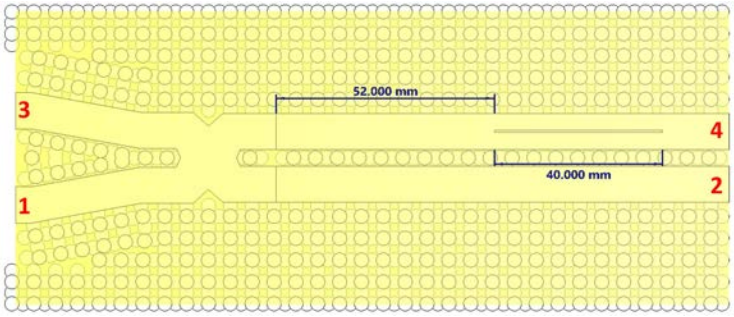

(a) *Waveguide extended coupler final model with integrated phase shifter and detailed ports.*

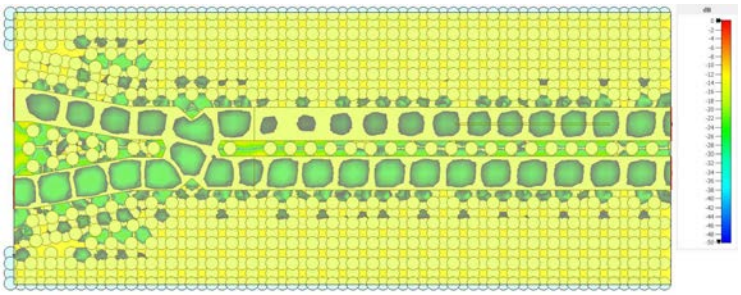

(b) *E field (absolute value) distribution @ 24 GHz for excitation port 1 (difference) for model with integrated phase shifter.*

Figure 4.23: *Riblet Coupler and Phase Shifter Final Model with integrated phase shifter.*

Fig. 4.24 shows the simulated S-parameters and the phase offset between the outputs for a excitation from port 1 (difference pattern). We note the identical power split between the outputs of -4.44 dB at the frequency of interest, indicating insertion losses of -1.44 dB in total.

The resulting phase shift after exciting the structure from port 1 (difference pattern) is 175° right at 24 GHz. This design also incorporates the wedge-shaped taper in the coupler septum because of improved matching when coupling the antenna described in the following section.

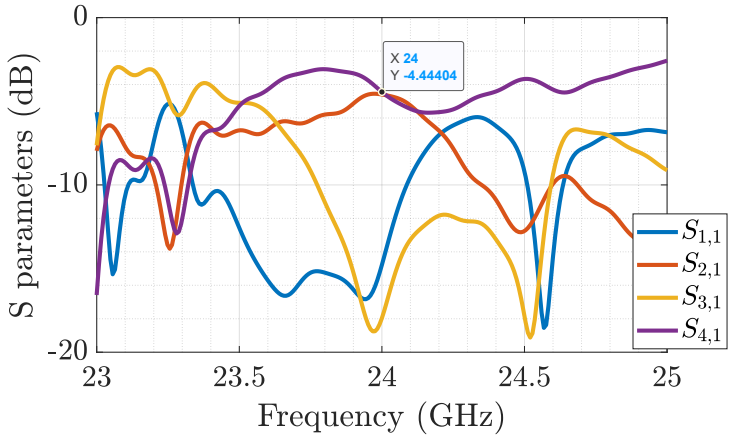

(a) *Simulated S parameter of the Riblet coupler with integrated phase shifter.*

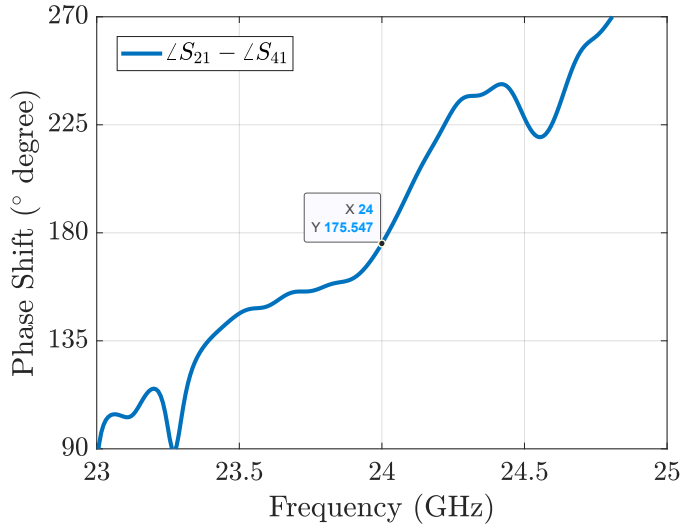

(b) *Phase offset between outputs in designed Riblet coupler with integrated phase shifter.*

Figure 4.24: *S parameters and phase offset for the Riblet Coupler with integrated phase shifter slab.*

4.6 Slot Array Antenna Design

It is observed that the optimum performance of the coupler array with the phase shifter is very narrow band, practically resonant. Now for radiating from these parallel plate waveguides we will integrate slot array antennas. Adding two narrowband elements in cascade may lead to incompatibilities, however, this type of antenna is chosen for its simplicity and ease of integration into the structure. As with the other two subsystems, this array was first designed with conventional rectangular waveguides.

For radiation to occur in a slotted hollow cavity, the propagating mode current lines must be disturbed by the slots. For this antenna, they are placed parallel to the guide axis all spaced an identical distance apart from the guide axis (X_{slot}) and spaced $\lambda_g/2$ apart, with λ_g the guided wavelength, to obtain the same amplitude and phase in all of them and thus increase directivity. By alternating the slots on opposite sides of the guide axis, we get the main lobe to radiate at 90° ('broadside'), as shown in Fig. 4.25. The slots should have an aspect ratio much longer than wide of at least 10:1, with an approximate value of the length of $L_{slot} = \lambda_0/2$. [163]

To excite the slots there are two methods: One is to feed the guide with a progressive wave by placing a matched load at the end to avoid reflections, and the other is to create a standing wave by placing a metal wall at the end of the waveguide, placing the closest slot to $\lambda_g/4$ where the first maximum of the standing wave is located. This 'resonant array' option is the one we will follow because of its eas

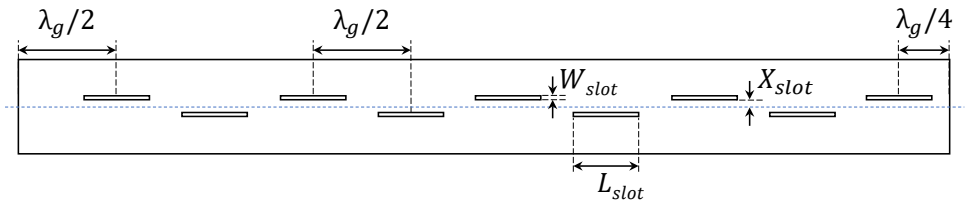

(a) .

Figure 4.25: *Rectangular waveguide resonant slotted array antenna design principle.*

The following parameters are taken as design specifications:

- Propagation mode: TE_{10}
- Operating frequency: $f_0 = 24$ GHz
- Number of slots: $N = 9$
- Rectangular waveguide size: WR34 ($a = 8.636\ mm,\ b = a/2$)

Although for the Riblet coupler and Phase Shifter not explicitly detailed in the previous sections, we must first check that the TE_{10} mode can propagate to the 24 GHz frequency in the WR34 guide, and we start by calculating the cutoff frequency of the fundamental mode in the waveguide with Eq. 4.6, with c as the speed of light in vacuum, ε_r as the permittivity of the dielectric filling the guide (air with $\varepsilon_r = 1$), $m = 1$ and $n = 0$.

$$f_c = \frac{c}{2\sqrt{\varepsilon_r}}\sqrt{(\frac{m}{a})^2 + \frac{n}{b})^2} \tag{4.6}$$

particularizing for the requested specifications, we obtain a $f_c = 17.37$ GHz, so it is mathematically demonstrated that it is a propagating mode.

To obtain the array design parameters, we start by calculating the wavelength in vacuum as $\lambda_0 = c/f_0 = 12.5$ mm and the guided wavelength according to Eq. 4.7:

$$\lambda_g = \frac{\lambda_0}{\sqrt{1 - (\frac{f_c}{f_0})^2}} = 18.11\ mm \tag{4.7}$$

With this, we obtain the length of the slotted guide as: $L_{total} = 9(\lambda_g/2) + \lambda_g/4 = 86.02\ mm$.

The only value left to calculate is the separation of the slots to the waveguide axis (X_{slot}), which we do by means of Eq. 4.8 of the conductance of each resonant

slot normalized to the admittance of the TE_{10} mode developed in [164]:

$$g_i = 2.09\frac{\lambda_g}{\lambda_0}\frac{a}{b}cos(\frac{\pi}{2}\frac{\lambda_0}{\lambda_g})^2 sin(\frac{\pi}{a}X_{slot})^2 \tag{4.8}$$

and knowing that the total conductance of the waveguide can be modeled as an equivalent circuit of N=9 conductances in parallel, where if they are fed from one end, we have $g_{total} = 1$, and, therefore, $g_i = 1/9$; we obtain $X_{slot} = 0.786\ mm$. [164]

In Fig. 4.26 we can see the radiation pattern of the designed rectangular waveguide antenna at 24 GHz. It has a directivity of 16.4 dBi and the SLL=−13 dB, as expected for a uniformly illuminated slot array. [164]

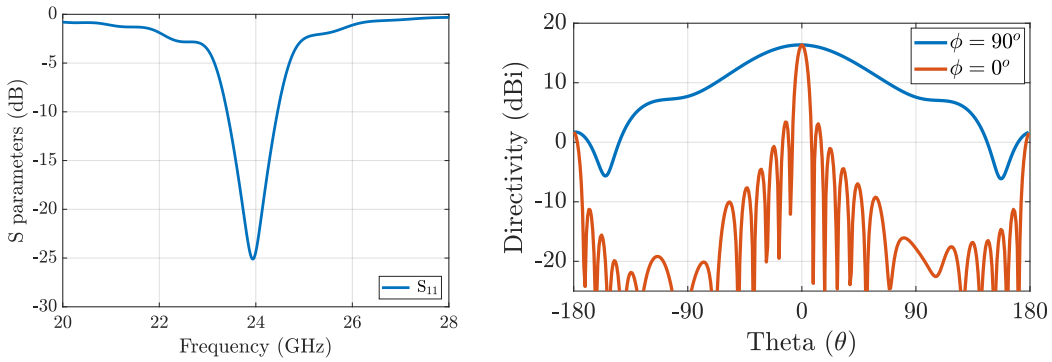

(a) *Simulated S parameters*

(b) *Radiation pattern in E-plane ($\phi = 90°$) and H-plane ($\phi = 0°$).*

Figure 4.26: *Simulated results for Slot Array in Rectangular Waveguide at 24 GHz.*

Once the correct operation of the array with conventional rectangular waveguide technology was verified by means of simulations, the model was modified to groove gap waveguide, replacing the metallic walls with the holey glide-symmetric version as shown in Fig. 4.27 with its final dimensions.

The disadvantage that exists in this design is the separation between the two arrays of slots, since the diameter of the holes located in the central row between the two guides determines the minimum distance at which they can be separated, the model being at the limit of producing grating lobes since its value is close to

$\lambda_0 = 12.5\ mm$. Therefore, the width of the separation wall is 3.9 mm and the diameter of the holes is 3.4 mm, with 0.2 mm of metal wall on each side. The top and bottom walls which form the waveguide, have 1.4 mm of metal up to the first row of holes.

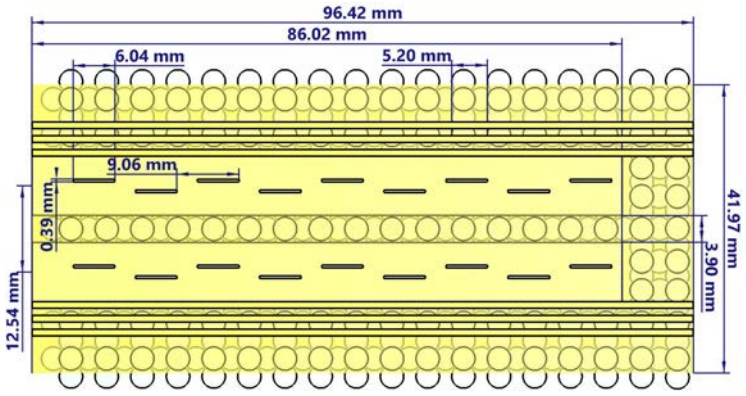

(a) *Top view.*

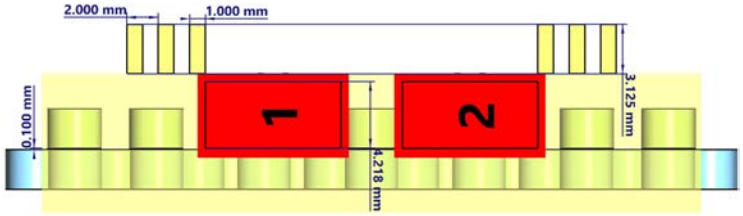

(b) *Frontal view.*

Figure 4.27: *Final dimensions of the slot array model in modified Glide-Symmetric Holey Groove Gap Waveguide technology.*

In Fig. 4.28 we see the model matching with this consideration having a lower value of -25 dB at the 24 GHz frequency for the 'sum' excitation. However, we observe that for the simultaneous excitation with one of the ports phase shifted 180° ('difference pattern') a frequency offset appears. It is found that this distortion will be compensated by including the antenna in the final monopulse array as we will see in the next section.

Fig. 4.29 shows the distribution of the electric field normalised to the maximum value for a simultaneous excitation of the two input ports in phase (sum pattern) and opposite phase (difference pattern). It is easy to see that the slots match the maxima of the standing wave created by the PEC boundary condition implemented

with holes.

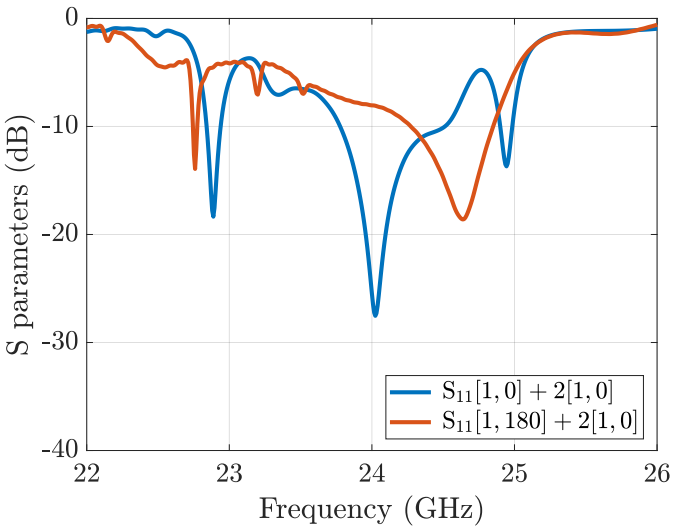

Figure 4.28: *S-parameters of the designed slot array antenna in modified Glide-Symmetric Holey Groove Gap Waveguide. Blue line for excitation of the 2 in-phase ports (amplitude = 1 V, phase = 0 °). Red line for excitation of 1 of the ports with amplitude = 1 V, phase = 180 °.*

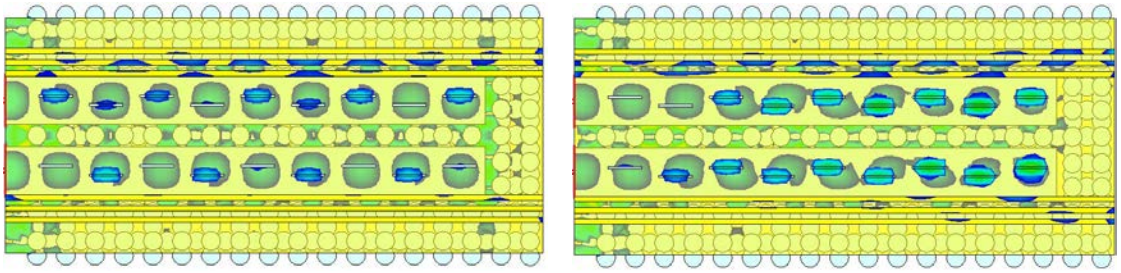

(a) *E field distribution for simultaneous in phase excitation port 1 and 2 for sum pattern.*

(b) *E field distribution for simultaneous opposite phase excitation port 1 and 2 for difference pattern.*

Figure 4.29: *E field distribution for designed slot array antenna in modified Glide-Symmetric Holey Groove Gap Waveguide.*

When simulating the radiation pattern, a directivity problem is observed given the small size of the antenna ground plane. Due to the small transverse size of the two antenna arrays of approximately 42 mm ($3.3\lambda_0$ in the E-plane), it is decided to add corrugations on both sides of the slots to increase the overall directivity of the antenna (see Fig. 4.27). These corrugations create a high impedance surface for a particular polarization and direction of propagation reducing the back radiation. [163]

The design values of these corrugations are: Height = 3.25 mm, period = 2 mm, width = 1 mm, number of corrugations = 3. The reason for adding this number of corrugations is to be able to compare on equal terms with another prototype made at the University of a monopulse antenna using Groove Gap waveguide technology implemented with pins. In Fig. 4.30 we see the difference in directivity before and after adding these elements. We get an improvement of almost 5 dBi, going from 16.8 dBi to 21.7 dBi, with SLL ('sum pattern') = −8.9 dB. In Fig. 4.31 we see the radiation pattern in polar coordinates for the model with corrugations.

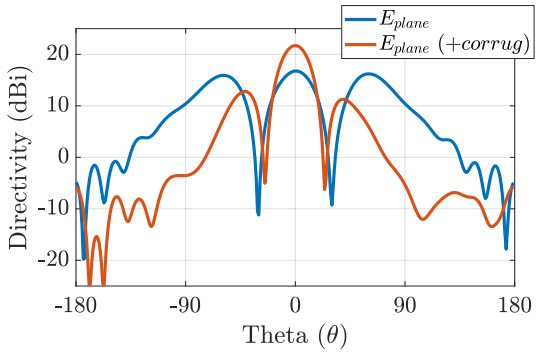

(a) *E-plane radiation pattern for simultaneous in phase excitation port 1 and 2 for sum pattern without (Dir=16.8 dBi) and with corrugations (Dir=21.7 dBi).*

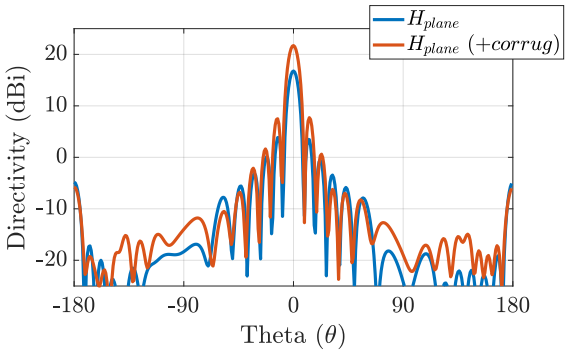

(b) *H-plane radiation pattern for simultaneous in phase excitation port 1 and 2 for sum pattern without (Dir=16.8 dBi) and with corrugations (Dir=21.7 dBi).*

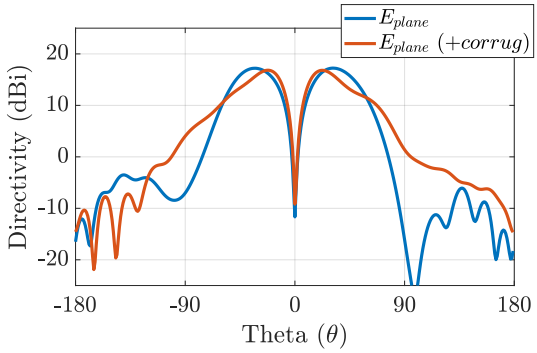

(c) *E-plane radiation pattern for simultaneous opposite phase excitation port 1 and 2 for difference pattern with/without corrugations.*

Figure 4.30: *Simulated radiation pattern for designed holey groove gap waveguide slot array antenna with/without corrugations.*

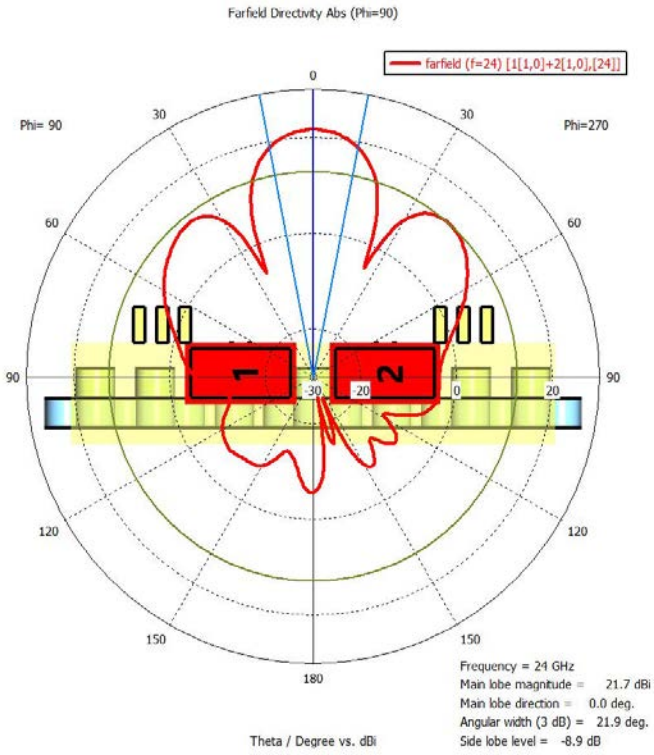

(a) *E-plane radiation pattern for simultaneous in phase excitation port 1 and 2 for sum pattern.*

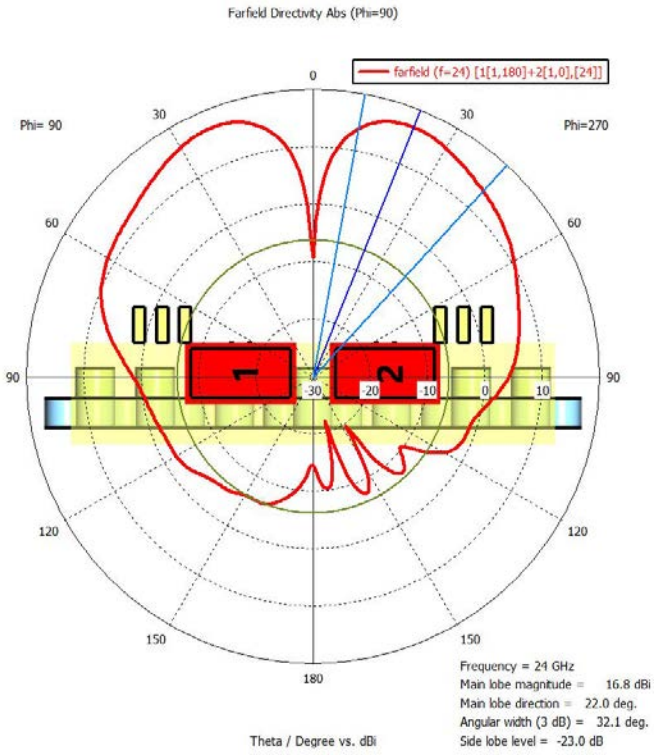

(b) *E-plane radiation pattern for simultaneous opposite phase excitation port 1 and 2 for difference pattern.*

Figure 4.31: *Simulated radiation pattern for designed holey slot array antenna model in polar coordinates.*

4.7 Complete Monopulse Antenna

After designing and checking the operation of the monopulse antenna subsystems in simulation environment, we proceeded to join and fine tune them to compensate for small reflections and distortions that the models of the components, separately, did not produce and which affected the parameters S_{11} and S_{22}. In Fig. 4.32 and Fig. 4.33 we see the model ready to manufacture with its most relevant dimensions.

The matching at the frequency of interest manages to be excellent and consistent for both the 'sum' port excitation (with $|S_{22}| = -17$ dB) and the 'difference' port excitation ($|S_{11}| = -23$ dB) as shown in Fig. 4.34a.

Although the theoretical stopband of the chosen unit cell ranges from 19.17 GHz to 36.51 GHz (Fig. 4.9), we can see in Fig. 4.34a the large number of resonances outside the 23.5 GHz - 25 GHz band in which the monopulse antenna components are tuned to operate. In Fig. 4.34b we can see in detail the excellent matching and moderate inter-channel isolation of the antenna.

Fig. 4.35 shows the distribution of the electric field normalised to the maximum value for both the excitation by the port generating the sum pattern (2, up) and the excitation by the port generating the difference pattern (1, down). To see the radiation patterns we have to look at Fig. 4.36.

In the final version, despite including the corrugations of the previous section and extending the width of the monopulse antenna to 70 mm from the previous 42 mm to include the WR34 transitions, the simulated directivity for the sum pattern is 20 dBi versus almost 22 dBi for the separate slot array. This is due to small distortions throughout the system that prevent getting the exact same amplitude and phase in all slots. Radiation efficiency is 71% and the SLL (sum pattern) is -5.3 dB. Note that, for the previously designed slot array, SLL ('sum pattern') was -8.9 dB.

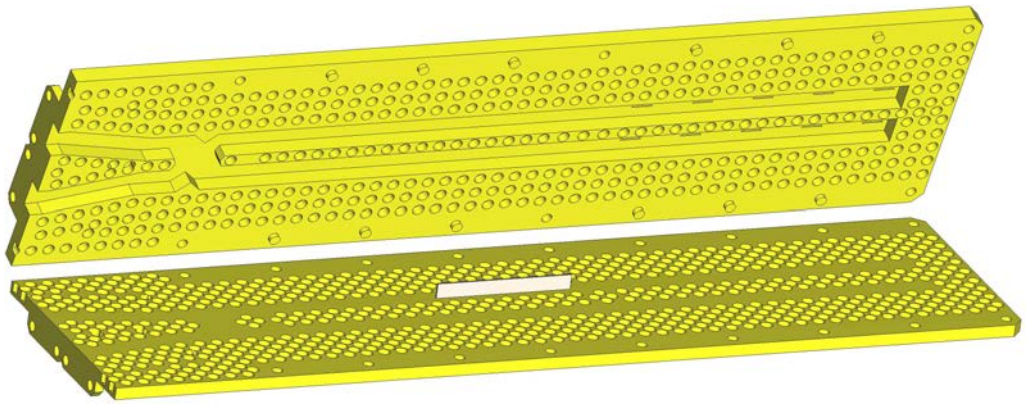

(a) *3D view of the monopulse antenna consisting of two machined metal parts with detail in the centre of the Rogers 5880 phase shifter slab.*

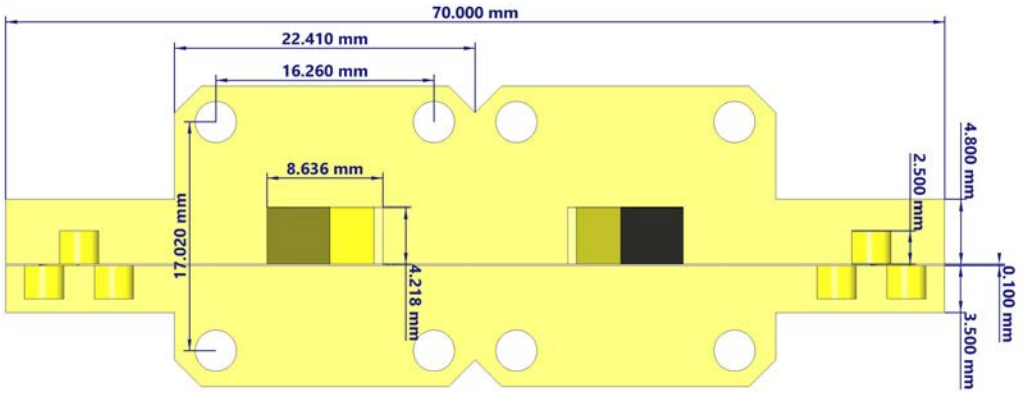

(b) *Front detail of WR34 flanges for connection to VNA and other measuring equipment.*

Figure 4.32: *Monopulse antenna model with details of the most relevant dimensions.*

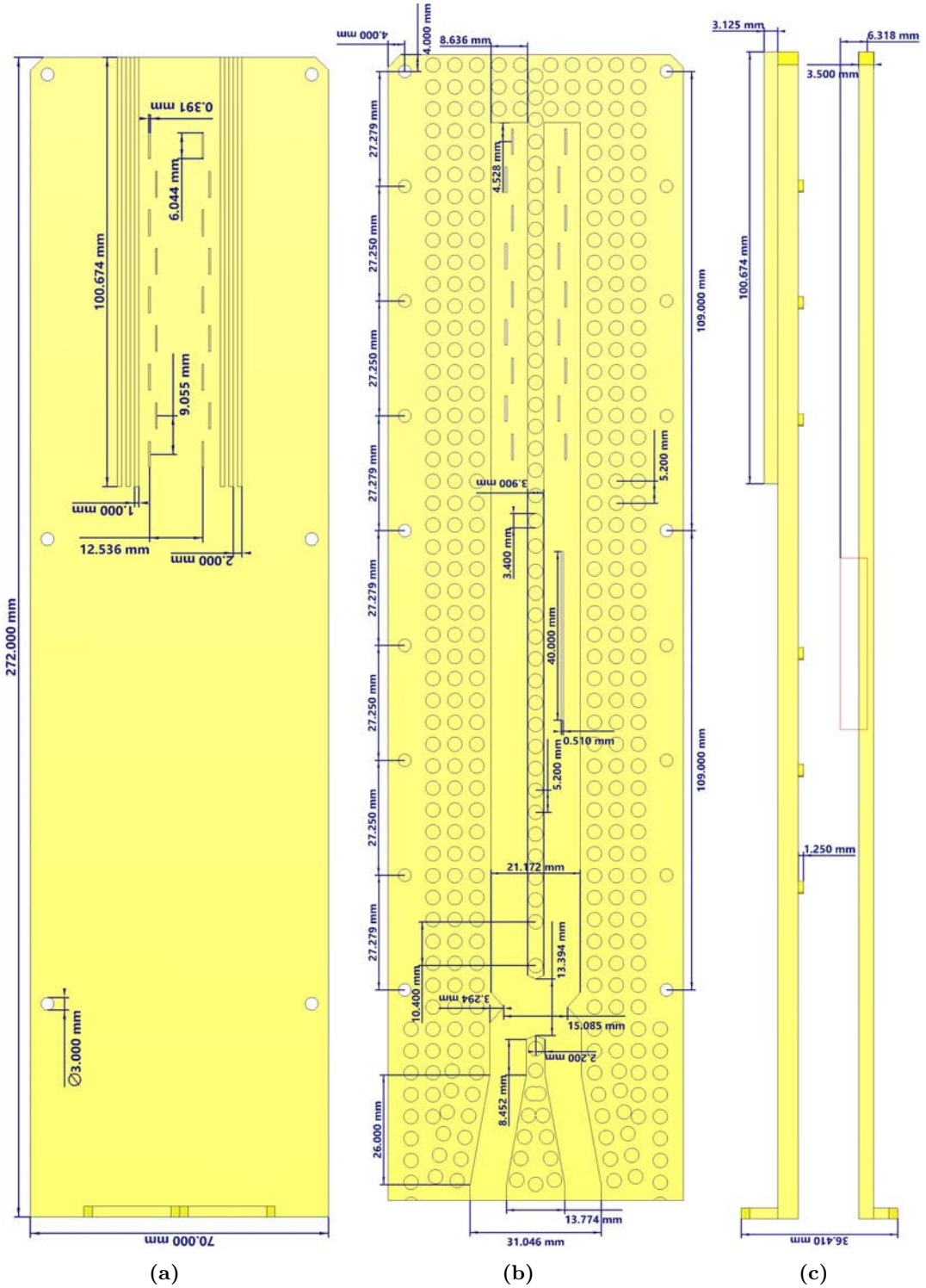

Figure 4.33: *Monopulse antenna model with details of the most relevant dimensions. Top, bottom and side views.*

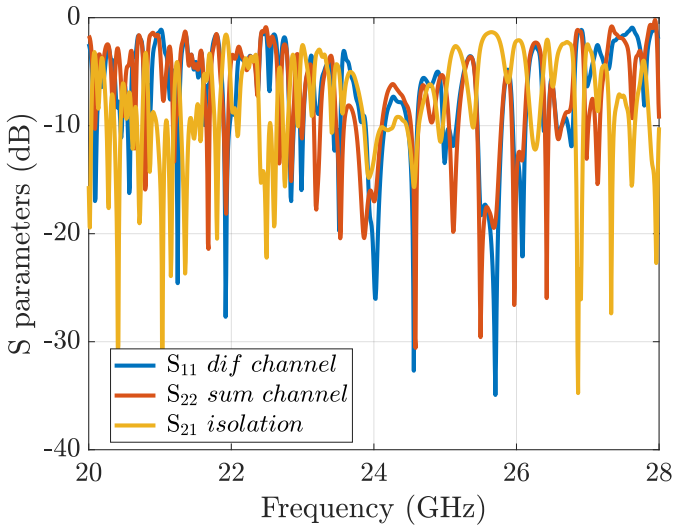

(a) *S-parameters of the full monopulse antenna.*

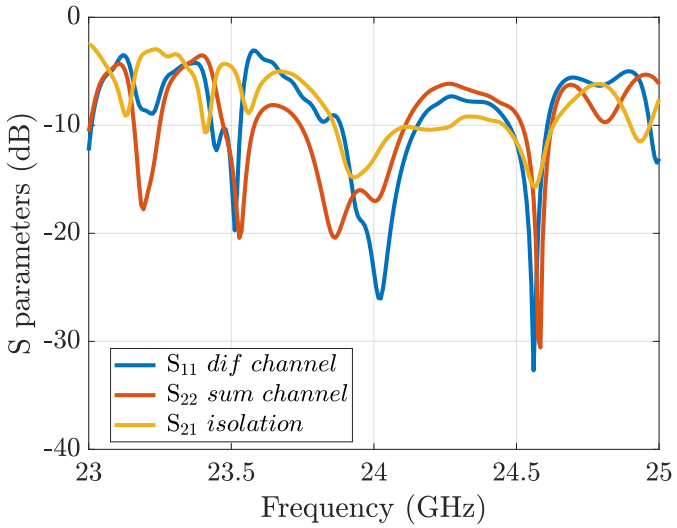

(b) *S-parameters of the full monopulse antenna (zoom).*

Figure 4.34: *Simulated S-parameters of the complete monopulse antenna array with coupler, phase shifter and slot arrays.*

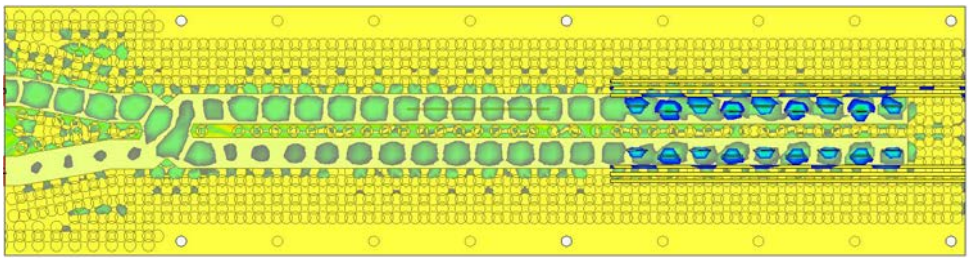

(a) *With excitation for sum pattern from port 2 (up).*

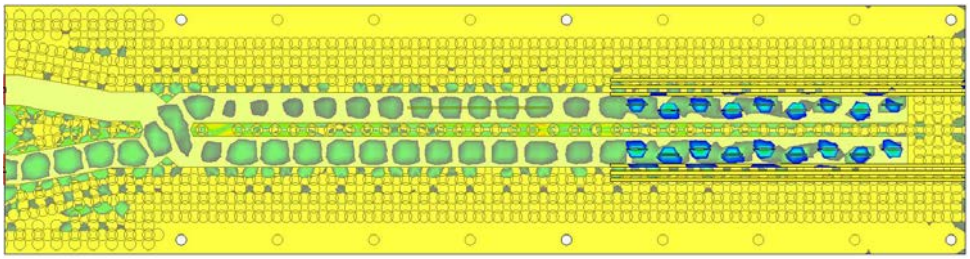

(b) *With excitation for difference pattern from port 1 (down).*

Figure 4.35: *E field distribution for monopulse antenna in modified Glide-Symmetric Holey Groove Gap Waveguide technology.*

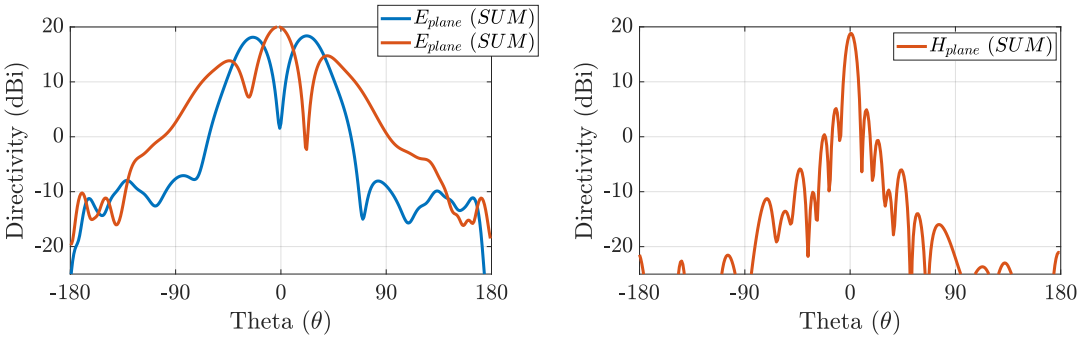

(a) *E-plane.* **(b)** *H-plane.*

Figure 4.36: *Simulated radiation pattern for designed monopulse antenna in modified Glide-Symmetric Holey Groove Gap Waveguide technology at 24 GHz.*

The results of the sum pattern are not good enough and are due to problems with the feed system and this is observed as asymmetries in the pattern and high side lobes different directions ($\theta = +43.17°$ and $\theta = -40.8°$).

4.8 Manufacturing and Measurements

4.8.1 Implemented Monopulse Antenna in Groove Gap Waveguide Technology with Holey Structure

Fig. 4.37 shows the built aluminum CNC machined monopulse antenna designed with this new implementation of Groove Gap Waveguide technology. Due to the unavailability of the 0.51 mm thickness RT5880^{TM} ($\epsilon_r = 2.2$), the metallization of **two** 0.25 mm thickness RT5880^{TM} strips was eliminated with ferric acid. To avoid changing the total permittivity of the phase shifter, and thus altering the designed phase between the channels, cyanoacrylate glue ($\epsilon_r = 3.3$) to attach these two strips was considered.

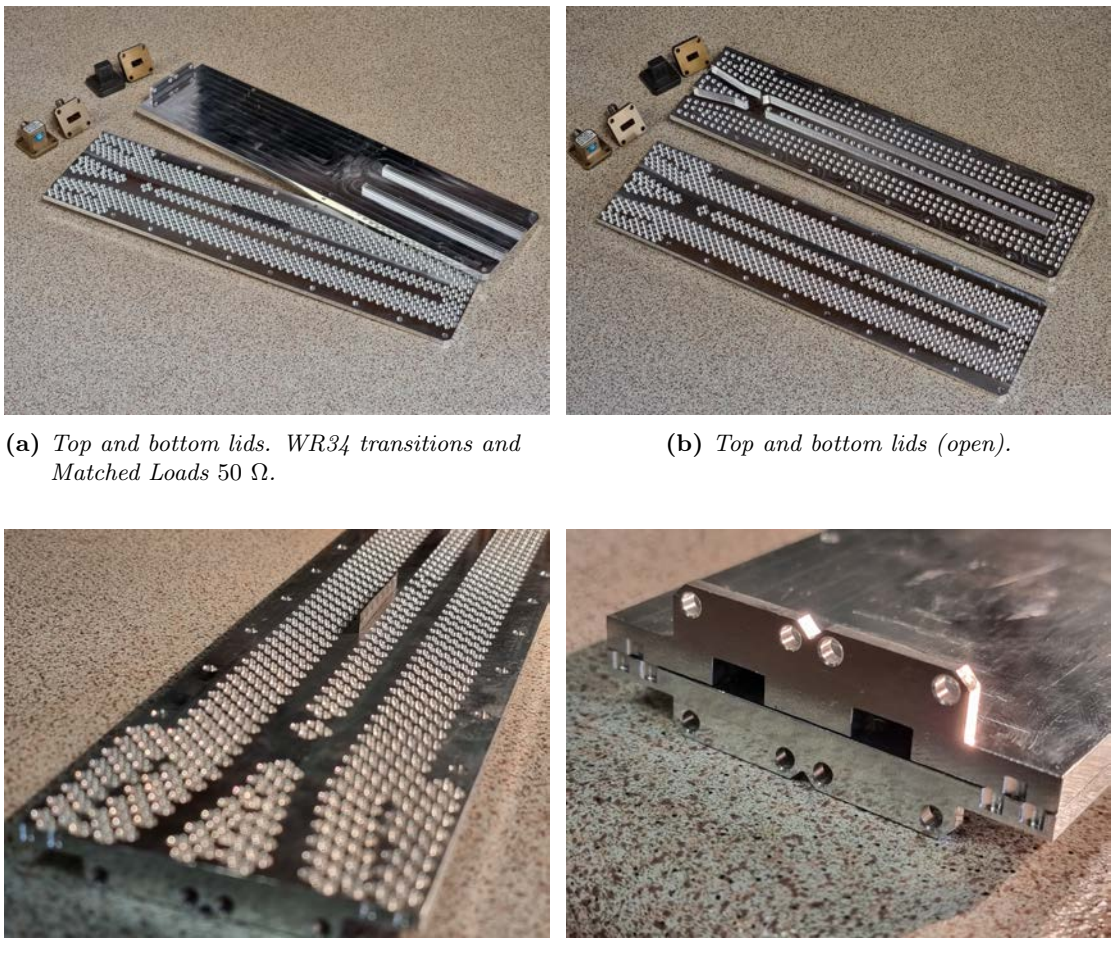

(a) *Top and bottom lids. WR34 transitions and Matched Loads* 50 Ω.

(b) *Top and bottom lids (open).*

(c) *Detail of the phase shifter RO5880 strip.*

(d) *Detail of the WR34 input ports.*

Figure 4.37: *Glide-Symmetric Holey Implemented Monopulse Antenna in Groove Gap Waveguide Technology: Mounting and Assembly.*

S-parameters of the monopulse antenna implemented with glide symmetric holey structure were measured with VNA Rohde & Schwarz ZVA40 after calibration with the Rosenberger RPC-2.92 02CK010-150 kit in each frequency range. Fig. 4.38 shows the results. It is observed that the antenna is matched for both sum and difference excitation between 23.8 GHz and 24.1 GHz.

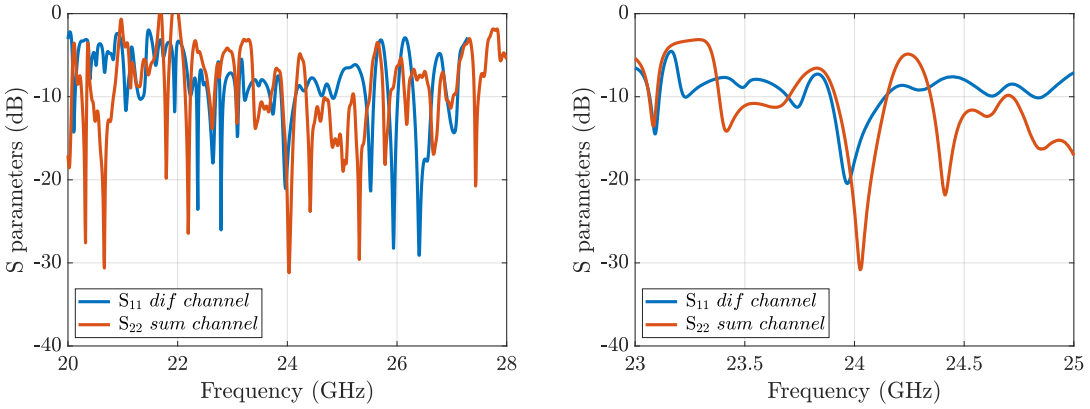

(a) *S-parameters of the full monopulse antenna.* **(b)** *S-parameters of the full monopulse antenna (zoom).*

Figure 4.38: *Measured with VNA S-parameters of the Glide-Symmetric Holey Structure Implemented Monopulse Antenna in Groove Gap Waveguide Technology. (Calibrated for each frequency range).*

The radiation pattern measurements were performed at the Centre for High Technology and Homologation (CATECHOM) at the University of Alcalá de Henares. A holder to attach the antenna to the anechoic chamber positioner was designed and built with 3D printing using PLA (polylactic acid) filament on a PRUSA i3 MK3 printer (see Fig. 4.39b). This holder must take into account the simulated antenna phase centre (Fig. 4.39a) to align it with the rotation axis of the chamber positioner. Fig. 4.39c and d show the installed antenna on the anechoic chamber positioner.

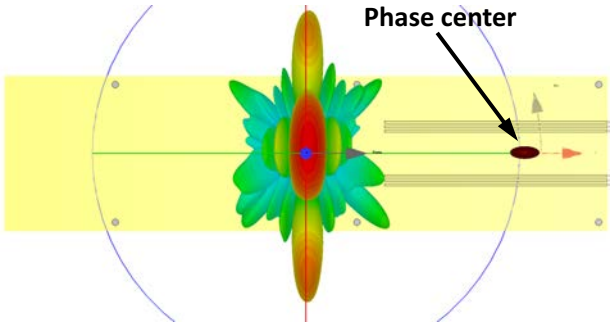

(a) *Simulated Phase Center for sum excitation.*

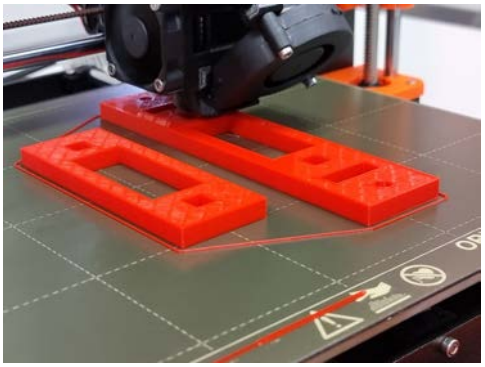

(b) *3D Printing Process.*

(c) *Installed antenna on the positioner (panoramic view).*

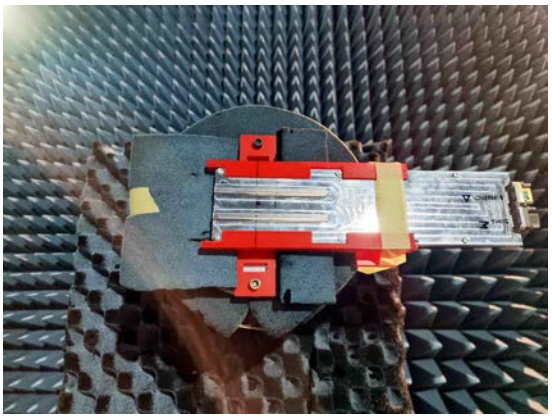

(d) *Installed antenna on the positioner (frontal view).*

Figure 4.39: *Glide-Symmetric Holey Implemented Monopulse Antenna in Groove Gap Waveguide Technology: 3D Printed Holder and installed antenna for the measurement of radiation patterns.*

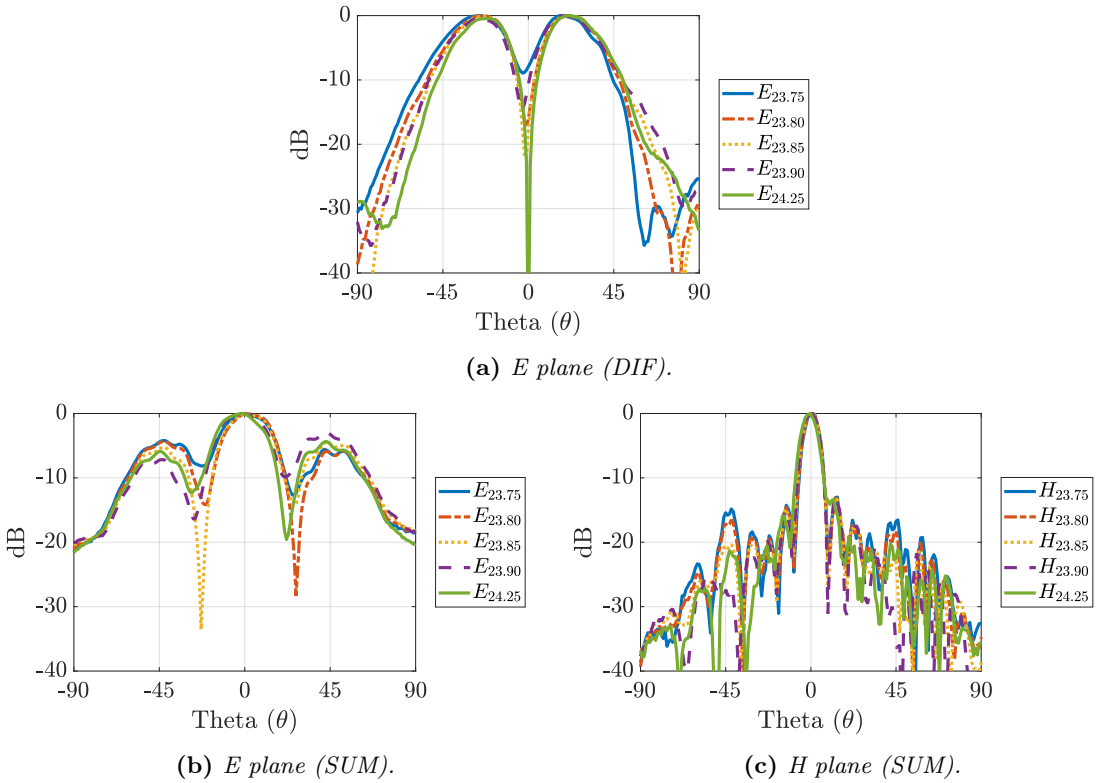

(a) *E plane (DIF).*

(b) *E plane (SUM).*

(c) *H plane (SUM).*

Figure 4.40: *Radiation pattern (measurement) of the Glide-Symmetric Holey Implemented Monopulse Antenna in Groove Gap Waveguide Technology.*

The measured radiation patterns are shown in Fig. 4.40. The results are in very good agreement with the obtained in simulation. E-plane sum and difference patterns are clearly seen. The SLLs of the sum pattern are similar to the simulated SLLs (-5 dB). This result of the sum pattern is not good enough and is probably due to problems with the feed system requiring further research. High side lobe levels have $\theta = +45°$ and $\theta = -44°$ directions.

4.8.2 Bed of Nails Implemented Monopulse Antenna in Groove Gap Waveguide Technology

The monopulse antenna developed with Modified Glide Holes could be compared with another project carried out at the University previously implemented with the conventional way of designing devices in Groove Gap (Bed of Nails). This design has similar dimensions as the design with holes.

The s-parameters were measured with VNA Rohde & Schwarz ZVA 40. Fig. 4.41 shows the result. We observe a bandwidth from 23.5 GHz to 24.5 GHz for the 'difference' excitation with matching below −10 dB and below −7 dB for 'sum' excitation from 23.5 GHz to 25 GHz. The manufactured prototype is shown in Fig. 4.42.

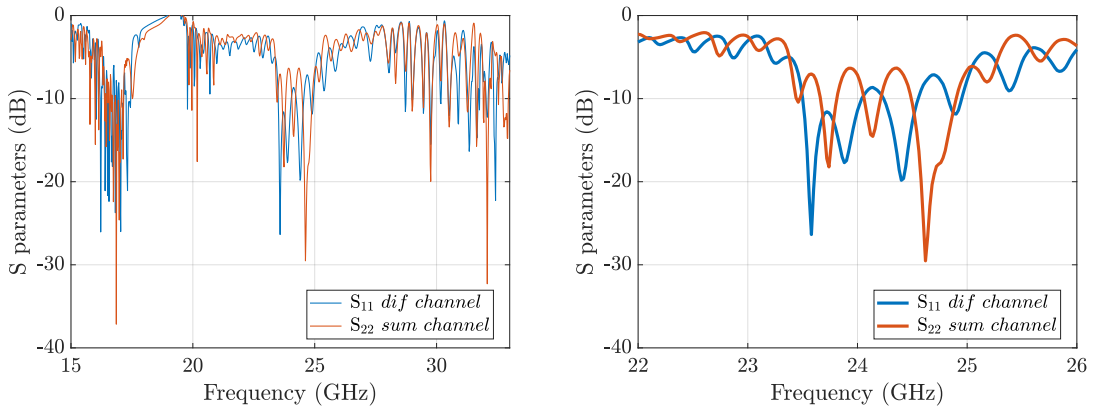

(a) *S-parameters of the full monopulse antenna.* **(b)** *S-parameters of the full monopulse antenna (zoom).*

Figure 4.41: *Measured S-parameters of the Bed of Nails Implemented Monopulse Antenna in Groove Gap Waveguide Technology. (Calibrated for each frequency range).*

(a) *Parts breakdown.*

(b) *Assembly of the two lids.*

(c) *Assembly of the two lids.*

(d) *Detail of the input ports for measurements. WR34 flange (port 1) + matched load (port 2).*

Figure 4.42: *Bed of Nails Implemented Monopulse Antenna in Groove Gap Waveguide Technology : Mounting and Assembly.*

As in the previous case, another holder to be used in the anechoic chamber was designed and 3D printed. The measured radiation patterns are shown in Fig. 4.43. In Fig. 4.43a the E-plane difference pattern is clearly seen, and in Fig. 4.43b and c the two main planes of the sum pattern are presented. This pattern has a SLL of −10 dB in E-plane as expected in simulation.

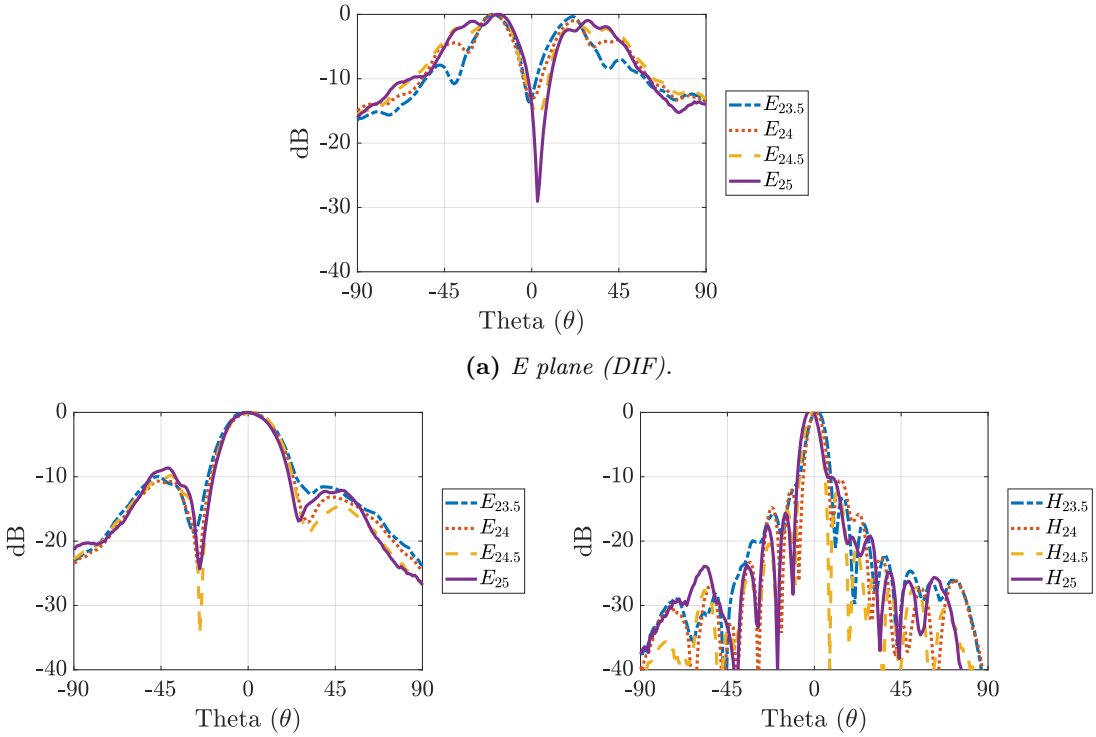

(a) *E plane (DIF).*

(b) *E plane (SUM).*

(c) *H plane (SUM).*

Figure 4.43: *Radiation pattern (measurement) of the Bed of Nails Implemented Monopulse Antenna in Groove Gap Waveguide Technology.*

4.8.3 Comparison

The first observed difference between the two measured antennas is the matching bandwidth. The monopulse antenna designed with Groove Gap Waveguide implemented with pins obtains a good matching that goes from 23.5 GHz to 25 GHz, although the excitation from the sum port presents some ripples that reach −7 dB. On the other hand, the antenna implemented with the modified glide-symmetrical holey structure has a smaller bandwidth. This antenna is matched from 23.9 GHz to 24.1 GHz for both sum and difference excitation.

The results of the radiation patterns are in good agreement in both cases with their respective simulations. The version with holes shows a non-good SLL level which requires further investigation of the origin of the non-uniform phase and amplitude illumination in the slots of the two arrays.

Finally, Fig. 4.44a shows the simulated and measured realized gain in the version with holes. We see that the measured gain in the version with holes is lower than expected. Fig. 4.44b shows the measured gain for both pin and hole versions.

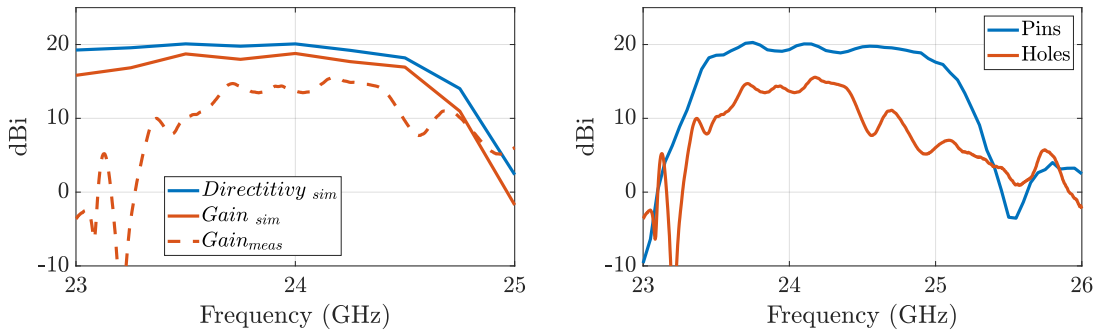

(a) *Measured vs simulated gain (Holes).*

(b) *Measured gain for Pins vs Holes implementation.*

Figure 4.44: *Comparison between gain measurements of the Bed of Nails and Glide-Symmetric Holey implemented monopulse antenna in Groove Gap Waveguide technology for excitation from sum port.*

4.9 Conclusions

This chapter presents a monopulse antenna in Groove Gap Waveguide (GGW) technology implemented with modified glide-symmetric holes. This way of realising the GGW has significant manufacturing and cost reduction advantages over the conventional machining of metal pins. However, the bigger hole size at equal bandgap, presents drawbacks in complex designs. In particular, in this monopulse antenna, where two channels run parallel to feed two arrays of slots, the separation between the antennas could not be less than 1 λ, which pushes the possible occurrence of grating lobes to the limit.

This monopulse antenna system consists of three blocks: a Riblet coupler, a phase shifter and two slot array antennas. First, a Riblet coupler is designed in conventional rectangular waveguide technology. This compact hybrid coupler splits equally the power into two channels by phase shifting the output of one channel by 90° with respect to the other. After verifying correct operation, the version with holes is implemented. The same procedure is used for the phase shifter. This phase shifter requires the use of a non-metallized RO5880 dielectric strip. It achieves 90° degrees between its outputs to achieve 0° or 180° degrees depending on whether we excite the input coupler through one port (sum) or the other (difference).

Several problems appeared during the integration of the Riblet coupler with the phase shifter. Also, when adding the dielectric slab in the centre of the guide, where the TE_{10} mode is maximum, to achieve the necessary phase shifter of 90°, we also obtained results that forced us to estimate the optimum distance of this slab with respect to the Riblet coupler block by trial and error. Failure to do so would have resulted in an imbalance in the power feeding the 2 slot arrays after the phase shifter, resulting in an squint of the main lobe in the sum pattern, which would distort the whole concept of the monopulse radar antenna.

The design of the slot array did not present any difficulties worth mentioning.

After the theoretical design for implementation with rectangular waveguide technology, and checking the result by simulation, the metal walls were replaced by holey walls. The distance between the two arrays was adjusted to the maximum allowed by the diameter of 1 hole, reaching almost 1 λ, which is at the limit of generating 'grating lobes'.

The small electrical size of these two slot array antennas (42 mm = $3.3\lambda_0$ in E-plane) limits the directivity that is not as high as it could be. To improve this drawback, corrugations are added on both sides of the antennas in E-plane to increase the directivity, resulting in a 5 dBi improvement.

Despite all the problems encountered during the development of this device, the results for both the sum and difference port excitation matched the specifications and were below $|S_{22}| = -17$ dB and $|S_{11}| = -23$ dB, respectively; with isolation between the two channels of 13 dB.

The radiation pattern shows a slight degradation of the monopulse antenna as a whole with respect to the individual block of slot array antennas, mainly due to distortions that prevent perfectly uniform illumination in amplitude and phase of the slots, reducing the maximum directivity of the total pattern from 21.7 dBi to 20 dBi.

Measured reflection coefficient and radiation patterns are in good agreement with the simulations. From 23.8 GHz to 24.1 GHz, both in sum and difference excitations, the $|S_{11}|$ is below -10 dB. The SLLs of the sum pattern are also similar to the simulated SLLs (-5 dB). This result of the sum pattern is not good enough and is probably caused by problems with the feed system requiring further research.

It was also possible to compare the performance of this antenna with holes with another one made at the university implemented with metal pins with the same dimensions. The measured gain with sum excitation for the version with pins is 20 dBi from 23.5 GHz to 24.5 GHz. However, for the holey version, the measured gain

was only about 15 dBi between 23.8 GHz and 24.2 GHz.

Chapter 5

Amplified Power Distribution Feed for Slot Array Antenna in Groove Gap Waveguide Technology

This chapter presents advances in Groove Gap technology implemented with conventional pins to explore distributed amplification solutions for feeding antenna arrays. Part of this work was presented at the 2017 EuCAP international conference [82].

5.1 Introduction

The work presented here is part of a more ambitious project to design a slot antenna array in which the power is amplified in a distributed manner. The motivation for employing spatial power combining/splitting methods lies in the limited ability of certain solid-state MMIC (Monolithic Microwave Integrated Circuit) amplifiers to handle high power, as their size is often inversely related to their ability to dissipate the heat produced by ohmic losses [165]. To this end, numerous works have been published in the literature to divide and combine EM fields in free space, with "quasi-

optical power combining" techniques based on lenses and reflectors [166], [167] in order to direct the distributed power towards an array of amplifiers whose joint capacity to handle power is greater than that which could be achieved individually; and subsequently recombine the amplified power. Among the problems encountered are, ohmic losses when the frequency is in the millimetre range or higher, low radiation efficiency, diffraction losses in lenses, etc. [168]–[174]

As one of the most promising technologies for millimetre band transceiver design, Gap Waveguide technology allows us to reduce the cost of waveguide fabrication by being modelled as two lids without the need for electrical contact and by not requiring as tight manufacturing tolerances as its competitors, while at the same time greatly reducing losses; aspects that have been detailed in the introduction chapter. This is why it is so interesting to study their ability to integrate active elements that allow us to build a complete transceiver in this technology.

However, as we saw in Fig. 1.3 in the first chapter, there is a discrepancy between the propagation modes in Groove guides (TE/TM) and those used by amplifier circuits on PCB substrates ($QTEM$) or the Ridge Gap version ($QTEM$); therefore, it is necessary to use transitions that manage to transform the energy in the cavity of the metal guide and confine it in the substrate on which the MMICs are mounted. There are already numerous publications of transitions using Gap Waveguide at one of its ends such as [51], [90], [175]–[177] and we will use some of them in this part of the work.

Hence, the block diagram of the targeted X-band slot array antenna with distributed amplified power is shown in Fig. 5.1.

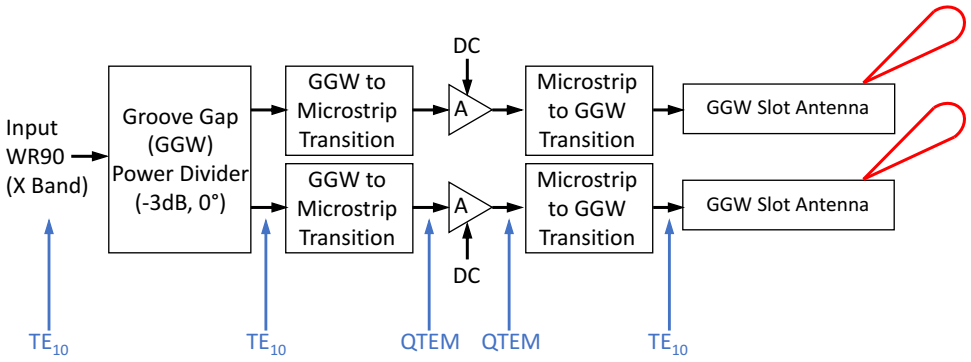

Figure 5.1: *Block diagram of the slot array antenna with distributed amplified power, with details of mode conversion and DC supply lines.*

5.2 1:2 Groove Gap Waveguide Power Divider Design

We must start with a Groove Gap Waveguide that is dimensionally consistent with rectangular guides at the desired band. In this case, as a proof of concept, the X-band, *i.e.*, WR90 (22.86 mm, 10.16 mm) will be selected. In this way we will use MMMIC amplifiers operating at 10 GHz and and we will use the bed of nails as packaging. Another requirement of the specifications is that the amplifier DC bias network must be easily accessible from outside the device.

As we have already seen, the first thing to calculate when working with Gap Waveguide is the dimensions of the unit cell that will provide the desired stopband in the band of interest. Fig. 5.2 shows the result of the dispersion diagram centered at 10 GHz (X-Band) with a stopband ranging from 7.2 GHz to 14.8 GHz. We see that the unit cell has a gap = 1.9 mm, making this the maximum height that our amplifier MMIC can have if we use the same structure for packaging.

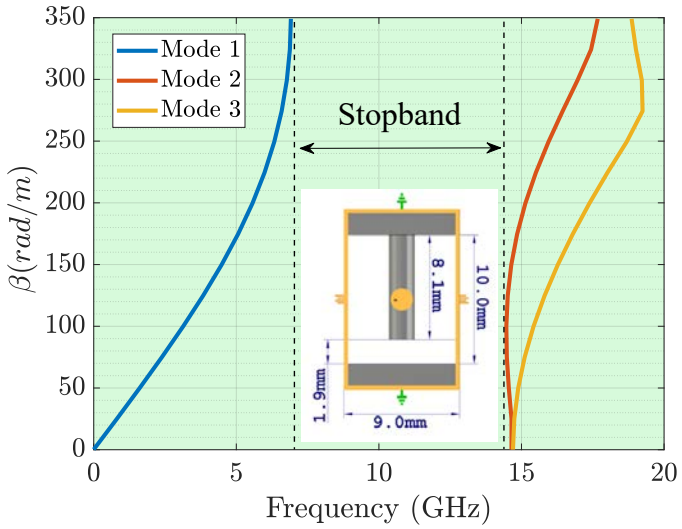

Figure 5.2: *Dispersion diagram for the designed unit cell with detailed dimensions in the inset. Stopband: 7.2 GHz to 14.8 GHz.*

According to published electric field attenuation studies and experimental tests with this technology ([11], [178]), for the GGW power divider design, it is sufficient to place 2 rows of pins acting as sidewalls so that the energy is confined and does not leak. 1:2 Y-junction power divider is the chosen topology. Here, the septum has only one row per output channel, but this is sufficient, since the power of each output channel is 2 rows apart. The septum and the dimensions of the power divider are shown in Fig. 5.3 and Fig. 5.4. Note the chamfered pin at the beginning of the septum and the optimisation of the position of several pins.

The simulated S-parameters of this divider are shown in Fig. 5.5, where we see the expected -3 dB transmission losses. We can see in Fig. 5.6 the electric field distribution at 11 GHz normalised to its maximum value.

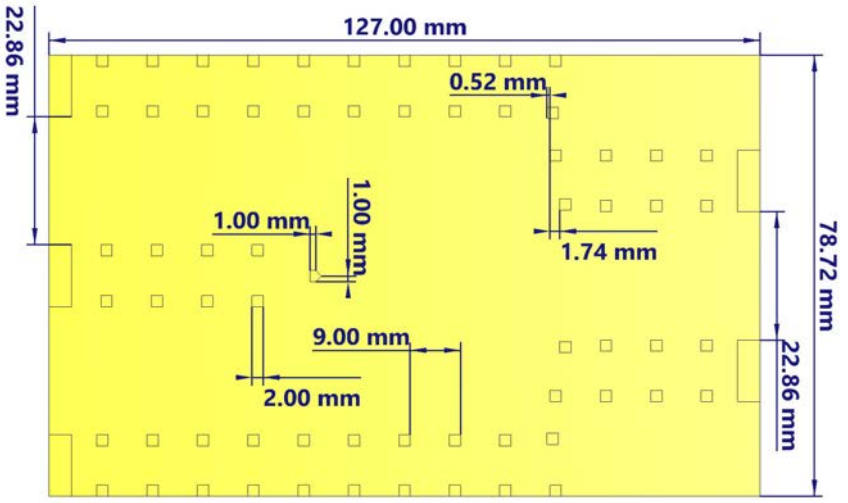

Figure 5.3: *Top view of the designed Groove Gap Waveguide splitter with detail of the pins that have their position modified and the dimensions of the chamfered pin..*

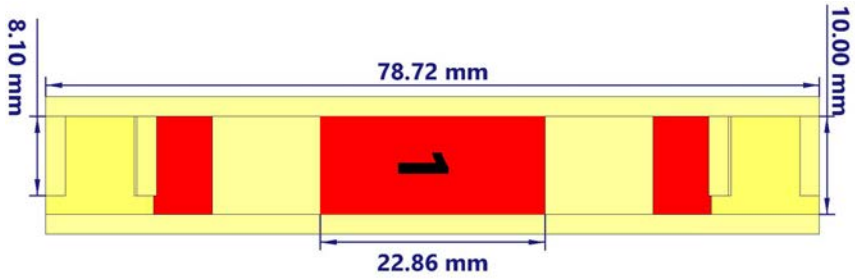

Figure 5.4: *Front view (from the input port) with detail of the dimensions of the splitter designed in Groove Gap Waveguide technology.*

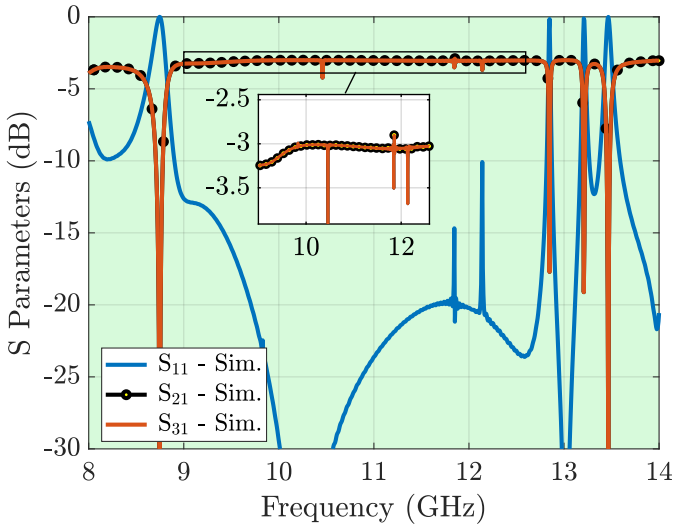

Figure 5.5: *Simulated S-parameters of the 1:2 power divider in Groove Gap Waveguide technology.*

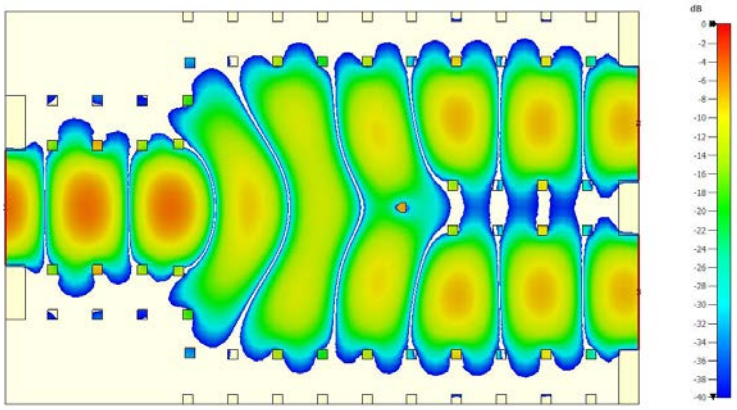

Figure 5.6: *11 GHz power divider 1:2 electric field distribution in Groove Gap Waveguide technology.*

5.3 Transition from Groove Gap to Microstrip Design

Classic wirebonding technology is not suitable at frequencies above 100 GHz, and above 40 GHz it has reduced performance because we need to compensate the low pass filter response of wirebonding with extremely low values of capacitance (of the order of femtofarads). Although a paper with integrated active device into gap waveguide technology through wirebonding at frequencies of the order of 30 GHz was published [179], at long-term, with higher frequencies, this approach is not suitable.

Therefore, we need a transition that converts the TE mode to QTEM, preferably with an inline topology that allows easy integration with planar technologies. Following the indications in [176], a non-contact back-to-back (B2B) transition is designed that transforms from Groove Gap to Ridge Gap, with which we would already have the QTEM mode compatible with MMICs confined in a plane. Then, through non-contact couplings, the field propagates from Ridge Gap to microstrip, with an intermediate step in SIW (Substrate Integrated Waveguide) as shown in the schematic in Fig. 5.7, where the energy propagates mainly along the 50 Ω microstrip line. The bed of nails above the transition from SIW to microstrip is used as circuit packaging to avoid coupling and resonances that can distort the operation of the MMIC amplifier.

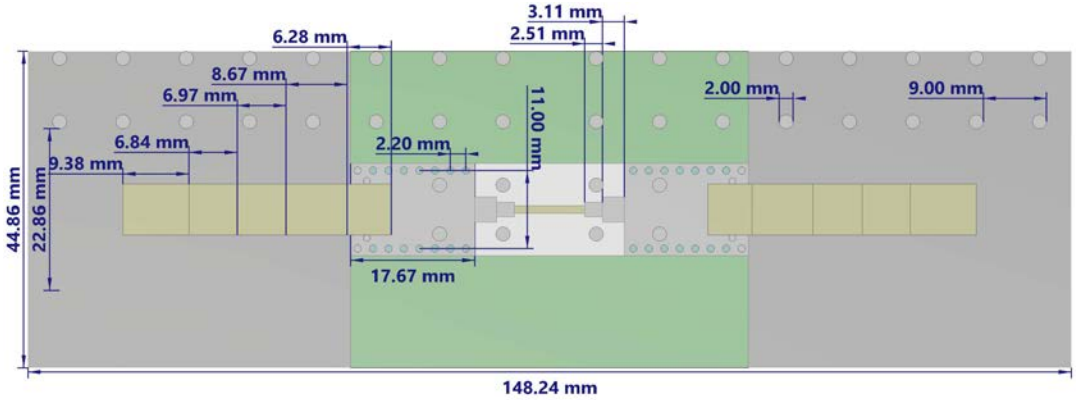

(a) *Top view with dimensions.*

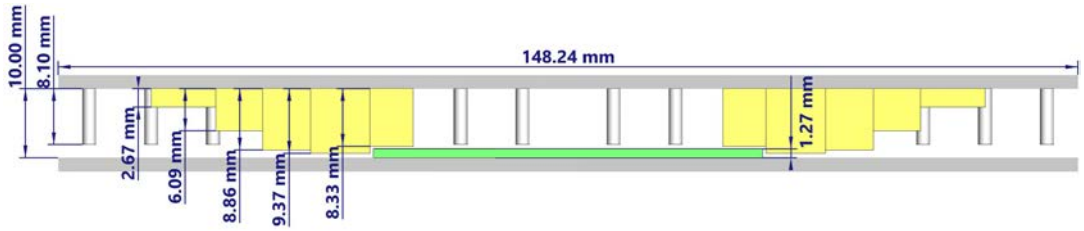

(b) *Lateral view with dimensions.*

(c) *Contactless zone with detailed dimensions.*

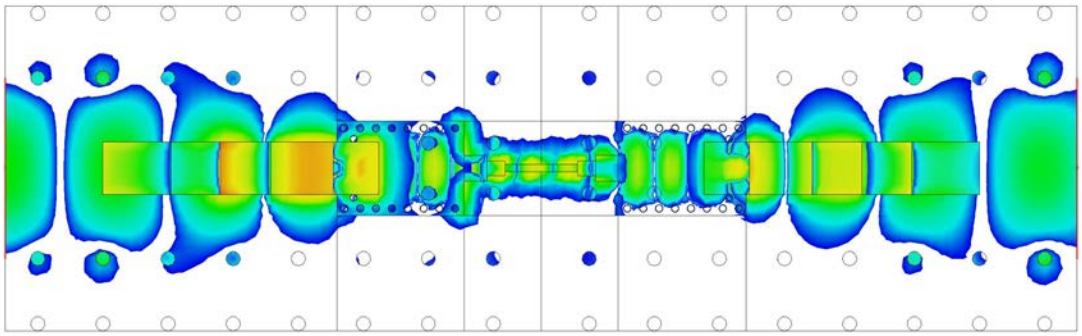

(d) *Normalised E field distribution, top view.*

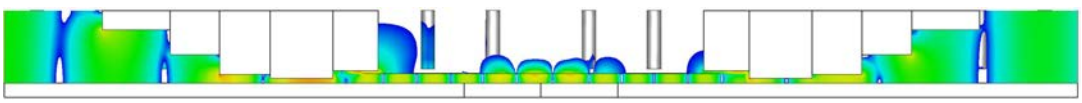

(e) *Normalised E field distribution, lateral view.*

Figure 5.7: *B2B Groove Gap Waveguide to conventional Microstrip Transition.*

A 34 parameters fine tuning optimization was carried out using CST Time domain solver and a genetic algorithm. The simulated S-parameters of the back-to-back transition "Groove-Ridge-SIW-Microstrip-SIW-Ridge-Groove" are shown in Fig. 5.8. The relative bandwidth at the centre frequency (11 GHz) is 31%, with about 0.5 dB insertion loss (B2B). The substrate used is Rogers TMM 10i ($\varepsilon_r = 9.9, tan\delta = 0.0020$).

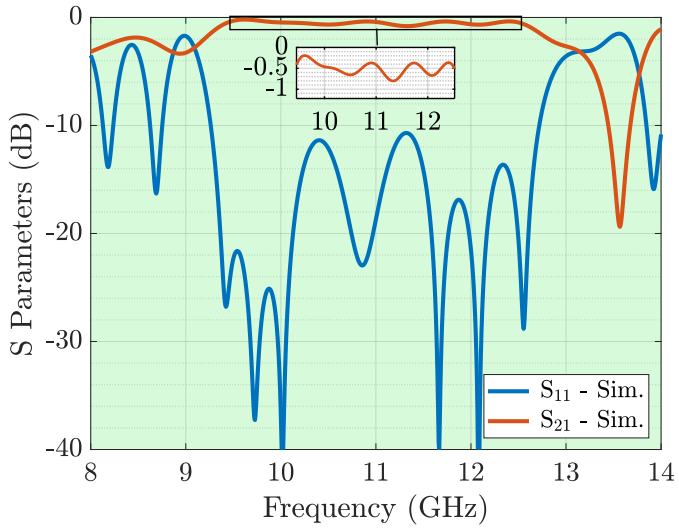

Figure 5.8: *Simulated S-parameter of the B2B Groove Gap Waveguide to conventional Microstrip Transition.*

With the B2B transition operation verified, the previously designed 1:2 power divider is added to obtain the simulated S-parameters shown in Fig. 5.9, where we verify that the same matching bandwidth is maintained, and the transmission losses remain in the -0.5 dB range. In Fig. 5.10 the distribution of the 1:2 distributed and 2:1 recombined electric field at 11 GHz is depicted.

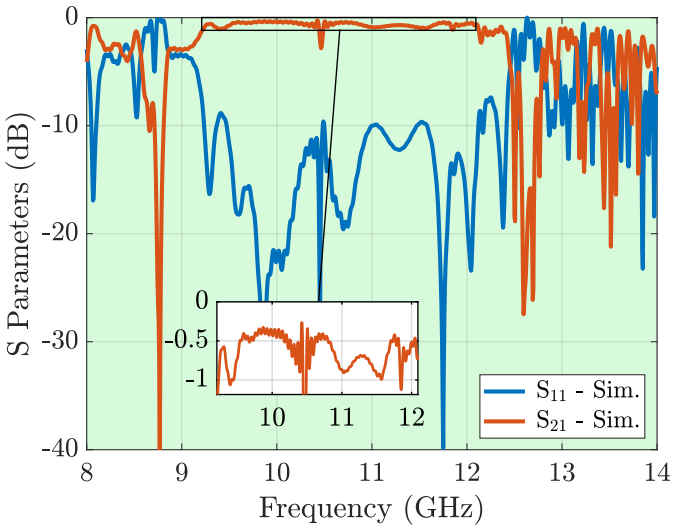

Figure 5.9: *Simulated S-parameters B2B transition with power divider 1:2 in Groove Gap Waveguide.*

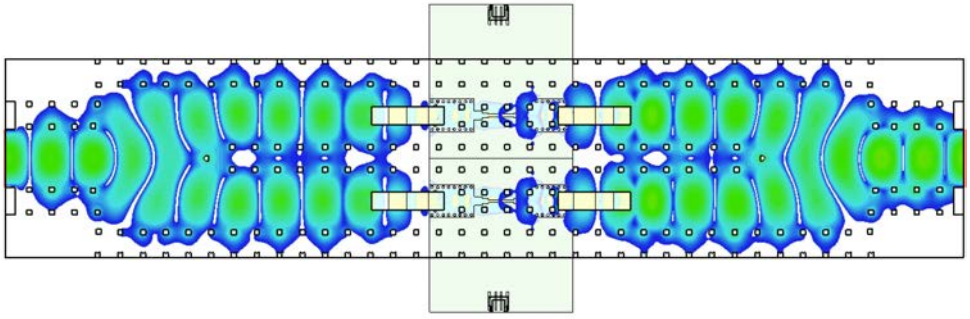

Figure 5.10: *E field distribution along the B2B transition with power divider 1:2 in Groove Gap Waveguide at 11 GHz.*

5.4 Active MMIC Integration Feasibility

Now, with the power properly distributed and confined along the microstrip lines, it is time to study the feasibility of integrating MMIC amplifiers in this band as a proof of concept.

To do this, we model and extract a 4-port model to the B2B transition without the power divider at this point. We do this by adding two discrete ports (50 Ω) (2 & 3) at the points where the amplifier is to be inserted maintaining the waveguide input and output ports (1 & 4) because we need to find out which is the maximum value of the unwanted positive feedback there (Port 3 to Port 2 loop) which is given by the parameter $|S_{23}|$. This will influence the amplifier gain we can use without cause oscillations as seen in Fig. 5.11a, *i.e.*, amplifier gain must be $< |S_{23}|$.

Doing this, we can see with the 4-port model S-parameters in Fig. 5.11b that the maximum amplifier total gain could have is 12 dB. With this in mind, we can choose a commercial device according to its RF band, gain, dimensions and a simple amplifier bias network. The Macom™ MAAM-011101 amplifier with TFDN6 package [180] meets these specifications. A lumped capacitor (Murata GRM0335C1E101 100 nF) and an inductor (Murata BLM15GG471 470 Ω) (See Fig. 5.12) are sufficient to bias the amplifier and its height is 0.75 mm (our gap is 1.9 mm).

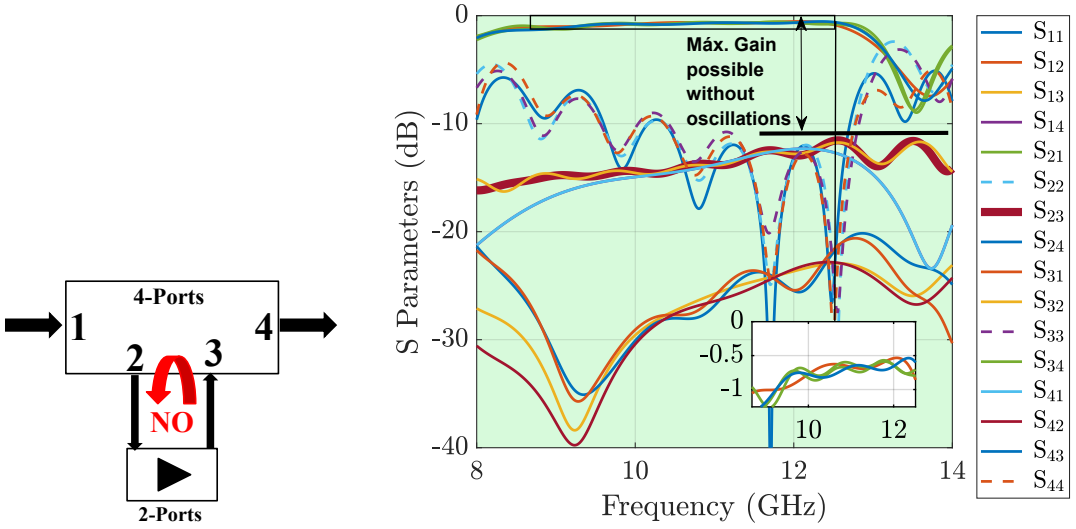

(a) *Block diagram of the amplified B2B transition with with detail in red of the feedback to be avoided (port 3 to 2).*

(b) *S-parameters of the B2B Groove-Microstrip transition modelled as a 4-port system with detail of maximum gain possible.*

Figure 5.11: *MMIC integration feasibility blocks model and B2B with 4-ports S-parameters sim-*

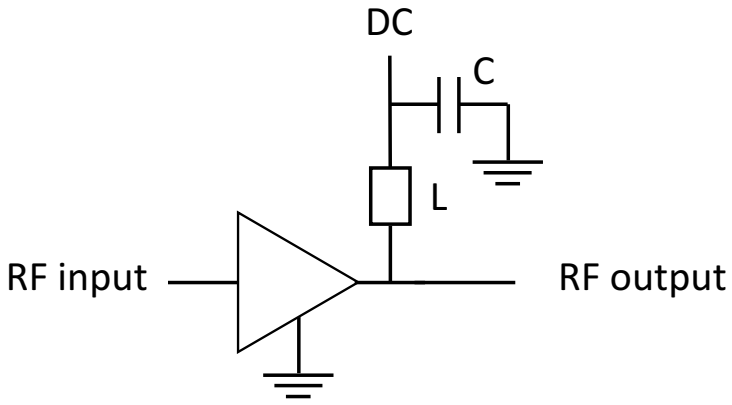

Figure 5.12: *Recommended MACOM MAAM-011101 amplifier mounting schematic. [180]*

5.5 Integration into Back to Back Transition

With the extracted 4-port model (.sp4 Touchstone file) and the 2-port S parameter matrix from the amplifier manufacturer for DC bias = 8 V, we modelled the assembly by two connected subsystems as in Fig. 5.11b using CST Design Studio™. The result of the S-parameters is shown in Fig. 5.13. We obtain a design where the

relative bandwidth is 30% (approximately from 9.6 to 12.6 GHz) and the resulting gain is 10 dB with a flatness of 1 dB.

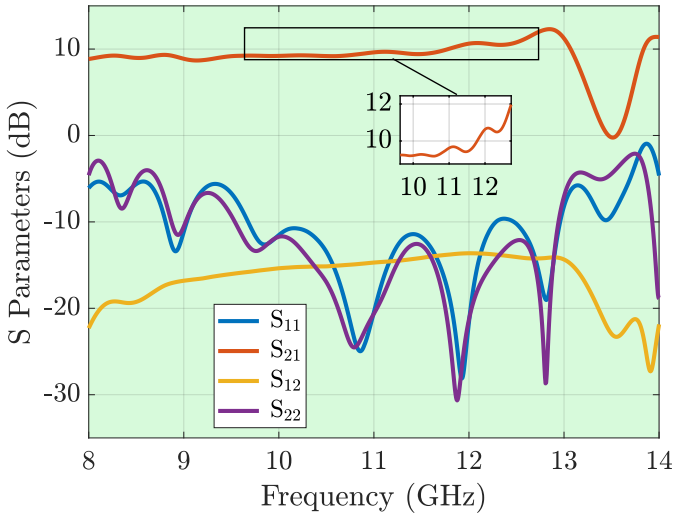

Figure 5.13: *Simulated S-parameters of the B2B Groove Gap Waveguide to conventional Microstrip Transition including MACOM amplifier. Zoom in the frequency band where matching exists ($|S_{11}| < -10$ dB).*

5.6 Manufacturing

5.6.1 Metallic block

For the experimental verification of the simulated results, 3 different prototypes with increasing complexity are proposed for the agile localisation of manufacturing and measurement problems.

The first prototype consists of the B2B Groove-Microstrip transition amplified with the MACOM chip. In the second prototype, the groove 1:2 power divider will be added to the previous one; and in the third prototype, the recombinant 2:1 part of the B2B transition with divider will be replaced by 2 arrays of slots as shown in Fig. 5.14.

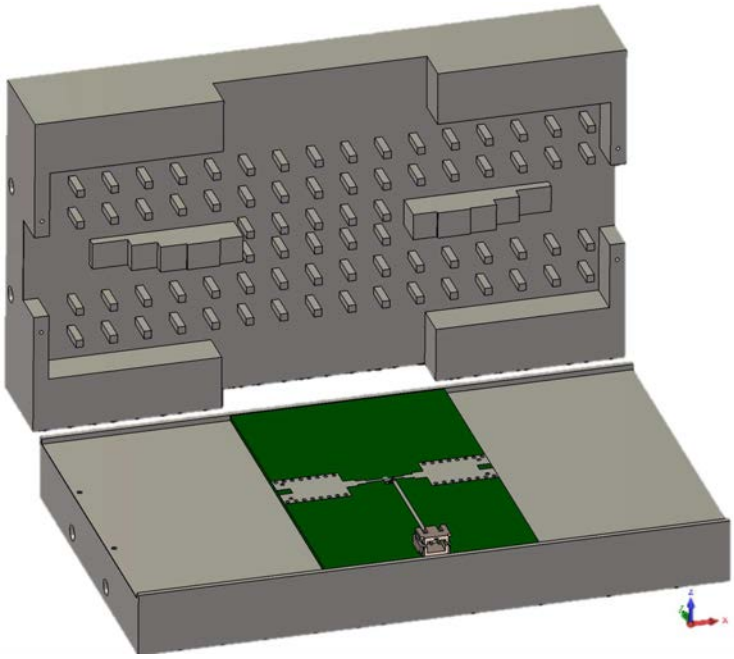

(a) *Prototype #1: Back to back Groove Gap Waveguide to Microstrip transition including amplifier.*

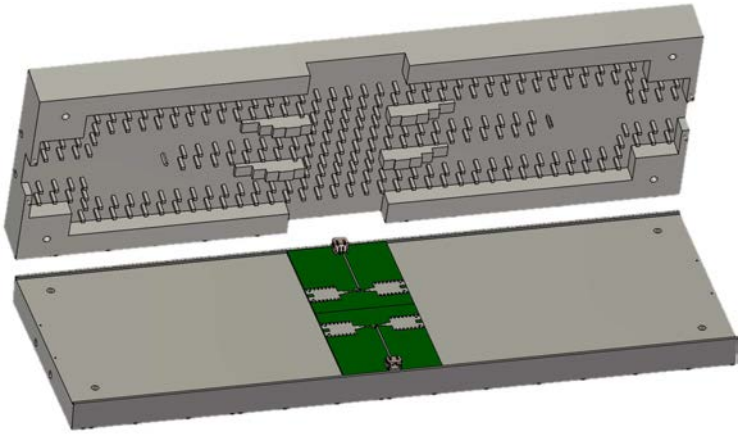

(b) *Prototype #2: Back to back Groove Gap Waveguide to Microstrip transition including amplifier and 1:2 splitter and 2:1 power recombiner.*

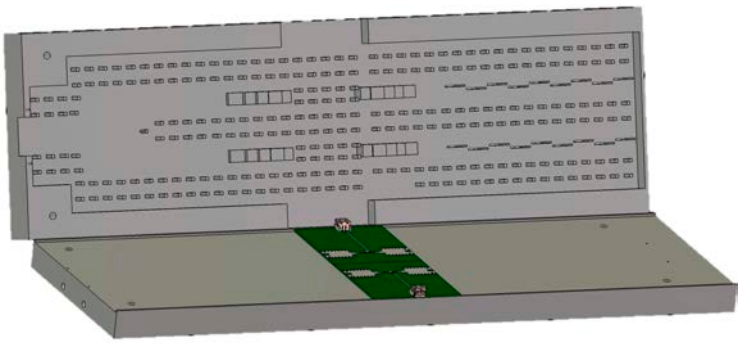

(c) *Prototype #3: Transition Groove Gap Waveguide to Microstrip with 1:2 power divider including amplifier with slot array antennas at output.*

Figure 5.14: *Manufacturing phases of the prototypes to be made in metal.*

In order to determine the ideal manufacturing technology for the construction of the metal blocks, an analysis of the manufacturing tolerances is carried out by means of a parametric study of the most critical values of the contactless coupling zone (t_g and t_v). It is determined that in order not to compromise B2B transition matching below -10 dB, these values must be within the values shown in the Fig. 5.15. The analysis is carried out with the rounded values to facilitate and reduce the manufacturing cost without losing accuracy.

$$tg = 480\mu m \pm 200\mu m$$

$$tv = 400\mu m \pm 200\mu m$$

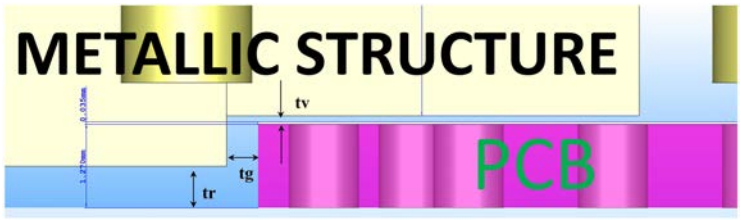

Figure 5.15: *Cross-section of the non-contact coupling area between ridge and PCB.*

With this data, the possibility of manufacturing the metal blocks by 3D metal printing (DMLS, Direct Metal Laser Sintering) or with 5-axis CNC (Computer numerical control) under standard "DIN ISO 2768-1 fine" is considered and it is concluded that the cost of DMLS printing is 10 times higher than CNC and its resolution is not much better. The result of the fabricated metal block can be seen in Fig. 5.16, note the centered stepped ridge and the periodic structure.

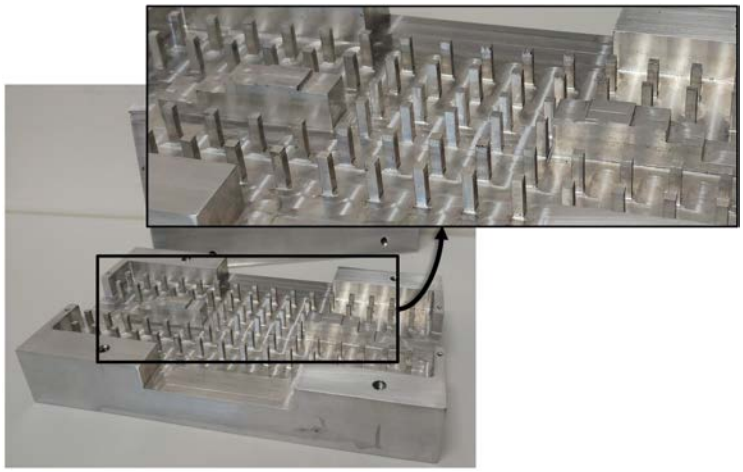

Figure 5.16: *Back to back Groove Gap Waveguide to Microstrip transition: Metal part manufactured by 5-axis CNC machining.*

5.6.2 PCB

In terms of PCB fabrication technology, we determined that it is a class 4 PCB (limited to 0.20 mm), given that the minimum spacing between conductive tracks we need is 0.21 mm (see Fig. 5.17b). Given its dimensions (1.5 x 1.2 mm 6-Lead TDFN package), the MMIC must be mounted using a vapour chamber. Access to the external DC power supply needs to be lateral through a connector.

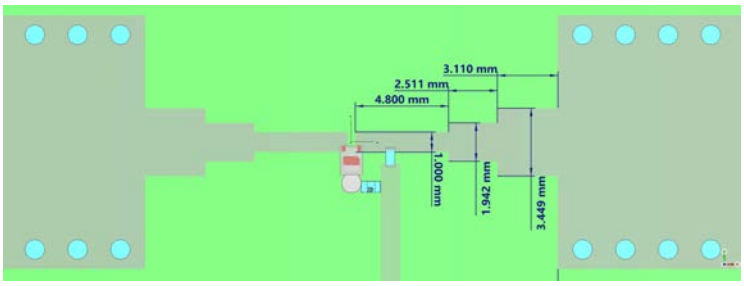

(a) *B2B Groove Gap Waveguide to Microstrip transition area with amplifier mounting detail.*

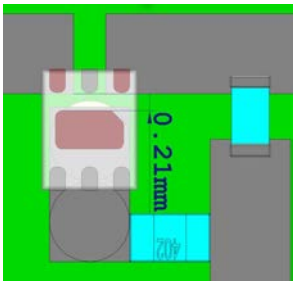

(b) *Detail of the minimum spacing between conductive tracks, which determine the PCB fabrication category.*

Figure 5.17: *Implementation of the MMIC amplifier in the microstrip part (50 Ω) according to the manufacturer's recommendation for use.*

With these considerations, the PCB shown in Fig. 5.18c is designed. To evaluate

the performance of the amplifier independently with conventional SMA inputs, an evaluation PCB (Fig. 5.18b) is also designed. The way to experimentally test the performance of the B2B transition without using amplification is by means of the PCB in Fig. 5.18a.

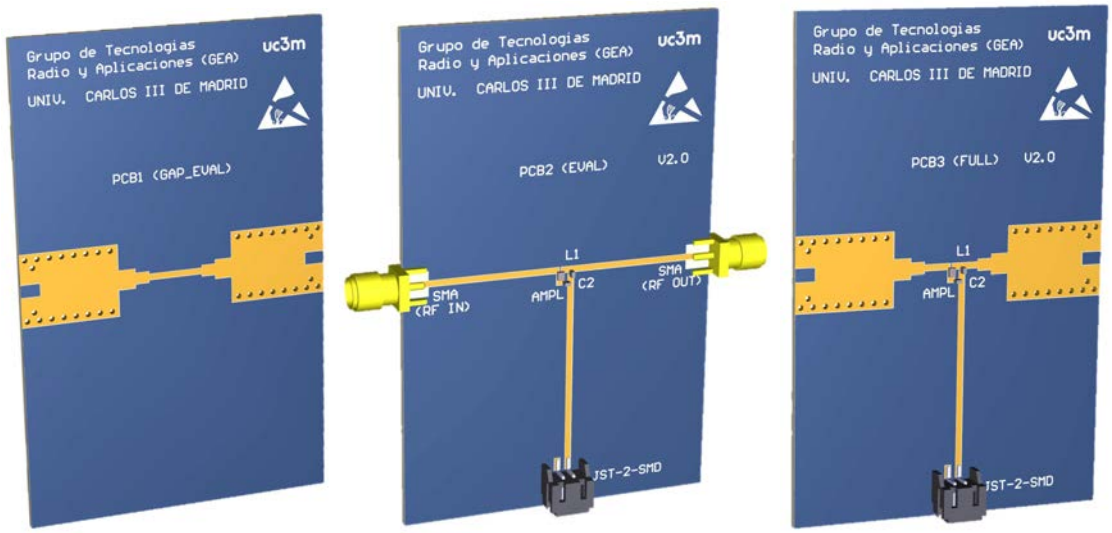

(a) *B2B Groove Gap Waveguide to Microstrip transition Evaluation PCB.*

(b) *MACOM amplifier performance evaluation PCB.*

(c) *PCB for amplified B2B transition.*

Figure 5.18: *Necessary PCB types that have been designed for the different project phases.*

Using the VNA ZVA40 and 2.92 mm transitions (K connectors), it has been possible to measure the prototype #1 without amplification, obtaining the results shown in Fig. 5.20. We observe that the transmission loss of the whole back-to-back transition is around -2 dB. $|S_{11}|$ parameter fully matches the simulated one reaching a bandwidth from 9.5 GHz to 12.2 GHz. These higher than expected losses may be due to the manufacturing and mounting tolerances of the PCB in the metal structure, since its position determines the non-contact coupling of this component. Furthermore, we see that the losses are proportional to the frequency, which is compatible with the losses due to the substrate. Fig. 5.19 shows details of the fabricated prototype and the measurement process.

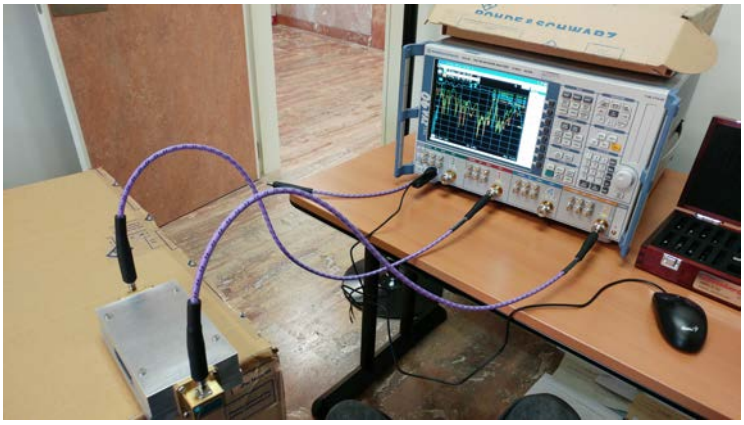

Figure 5.19: *Prototype #1 (B2B Groove Gap Waveguide to Microstrip transition without amplification): Measurement process with VNA ZVA40.*

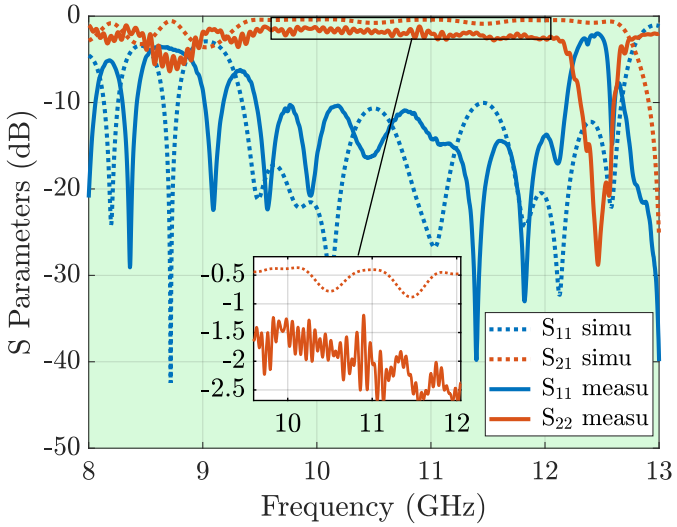

Figure 5.20: *Simulated and measured S-parameters for the B2B Groove Gap Waveguide to Microstrip transition.*

5.7 Conclusions and Future Lines

In this chapter, the ability to integrate active devices with Gap Waveguide technology has been explored, in particular with the Groove version. The design starts by designing a 1:2 power divider in order to distribute the power into two different branches in which to place an amplifier in each. Since the propagation modes must be converted from TE (Groove) to QTEM (Microstrip), a transition is used that confines the field via intermediate stages through Ridge Gap and SIW to Mi-

crostrip.

Once the operation of the back-to-back transition has been checked, the feasibility of integrating active elements is analysed by extracting a 4-port model in which the maximum gain value of the amplifier to be used to avoid feedback loops is obtained. With this data, a MACOM model is chosen that meets the specifications of bandwidth, gain and dimensions compatible with the air gap that the encapsulation with pins in the area above the microstrip allows. This packaging is an additional advantage of the use of this technology.

On the manufacturing side, the metal block is made by CNC machining as metal 3D printing does not offer better resolution and its cost is 10 times higher. In addition to the PCB that includes the amplifier with the power supply network recommended by the manufacturer, two more PCBs are designed to evaluate the operation of the B2B transition and another one for the evaluation of the amplifier separately with inputs with a 50 Ω connector.

Initial results measured with the transition with the PCB without the amplifier show higher losses than expected and future analyses of manufacturing and assembly tolerances will have to be carried out.

Experimental verification of the prototype with the B2B transition amplified with the built-in 1:2 power divider (#2 prototype) and the prototype with the slot antenna array (#3 prototype) are also proposed as future lines of research. Furthermore, it would be easy to extend this project by using 1:4 and 1:8 power dividers for radiating or recombining.

In addition, the work in this chapter was made at low frequencies (X band) as an initial proof of concept. Its extension to the millimeter-wave band is also a future research line, although the concept to be used will be the same.

Part III

Conclusions and Future Work

Conclusions

Part I: Design of Inverted Microstrip Gap Waveguide Components

This thesis is structured in two main parts. The first part focuses on the Inverted Microstrip Gap Waveguide technology. This part begins with a chapter on essential aspects that must be considered when designing components in this technology, such as the **characteristic line impedance** and its **attenuation**.

In order to perform the necessary parametric studies for impedance analysis, ABCD matrices are used. The considered frequency is 30 GHz and different combinations are chosen between: a) the three most frequent line widths corresponding to: 35 Ω (w = 3.6 mm), 50 Ω (w = 2.19 mm) and 70 Ω (w = 1.25 mm), all cases implemented with RO4003C^{TM} substrate and gap=0.508 mm; b) two substrate thicknesses: h_{sub} = 0.508 mm and h_{sub} = 0.762 mm, c) two pin periods: $p = 1.6$ mm and $p = 2.5$ mm, and d) two positions of the line w.r.t. the row of pins.

The following conclusions can be drawn:

1) **Using the thicker substrate results in the impedance being maintained with less variation as a function of pin height.** 2) **For denser bed of nails (p = 1.6 mm), the difference between the impedance between pins and over pins is smaller**, as already advanced in [105], [117].

The study of the **attenuation** is especially relevant in this version of the substrate based Gap Waveguide technology. The first method used is by means of open-circuit resonators. However, as the differences between the simulated and measured values were too large to draw conclusions, an alternative method using long lines (10 λ) was considered.

With this method, the design of a transition using the same substrate from inverted microstrip to microstrip is needed together with a TRL calibration kit to eliminate the influence of the End-Launch connectors that are mounted on the microstrip part. From the measurements, we observed that, as expected, **the losses increase with the use of thicker substrates and with increasing frequency**. The other design parameters such as the relative position of the line on the pins or the periodicity of the BoN practically do not affect the losses. In any case, these losses will always be much lower than those of solutions with conventional microstrip or inverted microstrip lines.

After that, the design of a critical device of RF front-ends has been presented. The operation of the **Diplexer in Inverted Microstrip Gap Wveguide (IMGW) Technology** has been demonstrated for the lower part of the mm-wave spectrum, where it can be employed for future uses in 5G technologies and beyond. This diplexer was designed with coupled line filters. Other more complex devices [141], [142] could be also easily translated to this technology.

The diplexer is formed by two Chebyshev type filters centred at 24 GHz/28 GHz, with a bandwidth of 1 GHz and a ripple of 0.5 dB, although, by subsequent adjustments, the highest possible flatness in the passband was sought. The filters were made with End-Coupled line resonators using initially RO4003C^{TM}, and redesigned afterwards with a very low loss substrate RT5880^{TM} to reduce the insertion losses.

The measurements shown a good agreement with the simulations except for a slight increase in losses and a slight frequency shift. The insertion losses in the 24 GHz passband were 1.5 dB and 2 dB for the 28 GHz passband. Regarding the slight

band offset we have shown that it is due to a discrepancy with the permittivity value of the material, something easily correctable if necessary and with high reproducibility in terms of mass production. When we compare this proposed diplexer to others published in similar bands, we see that we get similar or even better insertion losses than some of them, keeping the cost relatively low, especially when comparing to other versions of the Gap Waveguide technology (Ridge and Groove), which also do not allow such a simple integration with active components.

Based on the work done with this diplexer, the next chapter proposes a **Hybrid Diplexer-Splitter for Dual Band Array Antennas** by adding a power divider to the common port of the diplexer. The design was inspired in the work made with Groove Gap Waveguide presented in [70], using as power divider a 4-port diamond-shaped element. The results obtained in simulation are satisfactory both in matching and in transmission losses (about 4 dB), of which 3 dB correspond to the ideal power divider function. The isolation between the filters is more than 40 dB. An asymmetry in the behavior was observed depending on whether the energy comes from the 24 GHz filter or the 28 GHz filter. This was solved by adding an asymmetry in the diamond shape. The performance improves at the extremes of the passbands, achieving a more uniform response while maintaining the same level of losses and isolation.

After adjusting this splitter-diplexer, different dual-band radiating elements compatible with the diplexer bands were studied. Among them, the use of a dual band off-centered T-feed slot antenna in inverted microstrip gap with 1 mm thick metal lid achieves a good matching of less than -10 dB at 24 and 28 GHz. As key element in the corporate feed network, a broadband 1:2 power divider is designed that has to be compact to avoid grating lobes and at the same time keep a moderate mutual coupling level. Unfortunately, the minimum required distance is of the order of one wavelength for the upper frequency (28 GHz). The design was extended to a 4-element subarray with poor results also in terms of cross-polarization levels, and some solutions are proposed to be studied as future lines.

Part II: Design of Groove-Gap Waveguide Components

The second part focuses on the advances made with the Groove Gap Waveguide technology. It begins with a chapter proposing a **K-band monopulse RADAR antenna using a modification of the holey glide symmetrical unit cell**. This two-port system obtains 'sum' and 'difference' radiating patterns depending on the excitation from one port or the other.

The implementation of groove gap waveguide with periodic holes instead of pins has significant manufacturing and cost reduction advantages over the conventional machining of metal pins. However, the bigger hole size required to produce the same bandgap, presents drawbacks in complex designs. In particular, in this monopulse antenna, it was not possible to keep the separation between the two implemented antennas below one wavelength to avoid grating lobes.

This monopulse antenna consists of three blocks: a Riblet coupler, a phase shifter and two slot array antennas. First, a Riblet coupler was designed, initially in conventional rectangular waveguide technology. This compact hybrid coupler splits equally the power into two channels by phase shifting the output of one channel by 90° with respect to the other. After verifying its correct operation, the version with holes is implemented. The same procedure is used for the phase shifter. This phase shifter requires the use of a non-metallized RO5880 substrate strip. It achieves 90° degrees between its outputs to achieve 0° or 180° degrees depending on whether we excite the input coupler through one port (sum) or the other (difference).

After several partially solved problems appeared during the integration of the Riblet coupler with the phase shifter, the slot array antenna was designed. Following the same methodology, the metal walls in conventional rectangular waveguide design were replaced by holey walls. The distance between the two arrays was adjusted to the minimum imposed by the diameter of one hole, reaching almost one wavelength, which is at the limit of generating grating lobes. Corrugations are added on both

sides of the antennas to increase the directivity, resulting in a 5 dBi improvement in the sum pattern. The performance of the antenna in simulations shows well defined sum and difference patterns with a reasonable gain.

Measured reflection coefficient and radiation patterns agree well with the simulations. From 23.8 GHz to 24.1 GHz, both in sum and difference excitations, the $|S_{11}|$ is below -10 dB. The SLLs of the sum pattern coincide the simulated ones (-5 dB). This result of the sum pattern is not good enough and, probably, it is originated by problems with the feed system requiring also further research.

The performance of this antenna implemented with holes was compared to another similar one made at the University but implemented with metal pins. The measured gain with sum excitation for the version with pins is 20 dBi from 23.5 GHz to 24.5 GHz. However, for the holey version, the measured gain was only 15 dBi between 23.8 GHz and 24.2 GHz and the reason for this loss of gain compared to simulations is currently under study.

The following section proposes the **integration of active elements for distributed amplification in Groove Gap technology implemented with pins**. The design starts by designing a 1:2 power divider in order to distribute the power into two different branches where an amplifier will be placed (in each one of them). Since the propagation modes must be converted from TE_{10} (Groove) to QTEM (Microstrip), a transition is used that confines the field via intermediate stages through Ridge Gap and SIW to Microstrip. The design also considers the packaging of the amplifier using as well the gap waveguide concept.

With the operation of the back-to-back transition checked, the feasibility of integrating active elements is analysed by extracting a 4-port model in which the maximum gain value of the amplifier to be used to avoid feedback loops is obtained. With these data, a MACOM model is chosen that meets the specifications of bandwidth, gain and dimensions compatible with the air gap that the packaging with pins in the area above the circuit allows. This packaging is an additional advantage

of the use of this technology.

Initial results measured with the transition with the PCB version without the amplifier show higher losses than expected and future analyses of manufacturing and assembly tolerances will have to be carried out.

Finally, in the appendix, we present the development of a **slot array antenna based on microstrip in millimeter band**, in which a **PMC type packaging is added** to eliminate the back radiation typical of these antennas designed with microstrip. In particular, an 8x8 slot array antenna implemented in conventional microstrip technology at 28 GHz is designed. With this packaging, in addition to reduce the back radiation, the couplings between the corporate feed network lines are almost completely blocked, which favours the uniform illumination of the array, thus increasing its directivity. This PMC packaging, although made with metal parts, does not produce cavity modes making it a good solution for creating planar arrays of many more elements where the integrated active beam scanning electronics can be added. A prototype was manufactured and measured and a very good agreement with the simulated results was obtained.

Future work

As expected, the realization of this Thesis lets open several research lines. Some of them are related to the first part of the project as it is the case of the development of solutions for the hybrid splitter-diplexer. In particular, a solution to be explored is the use of frequency bands less separated from each other than the ones used in this Thesis. For instance, 26 GHz and 28 GHz can be considered. This, for sure, will generate a solution with good performance also for the antenna and could be manufactured and measured. Another possible solution and research line is to use another layer for the subarray feed structure, thus creating a multi-layer structure although this complicates and makes the final design more expensive. Finally, the

use of some kind of directive antenna instead of the slot, could be a solution that will allow a bigger separation among the array elements.

There are also opened research lines related to the second part of the Thesis. The first of them concerns the design of the monopulse antenna with the version of the groove gap waveguide implemented with the holey structure. The performance of the proposed design was not satisfactory and further studies on the origin of the non-uniform amplitude and phase illumination of the array slots are deserved. Additionally, the use of more corrugations both on the sides and in between the two arrays could be also studied with the purpose of reducing the side lobe level in the E-plane.

Another interesting future research line is the design of a monopulse antenna by extending the proposed design to the 3D case where both azimuth and elevation can be discriminated. To this aim, four slot array antennas allowing discrimination in two spatial coordinates (azimuth and elevation) simultaneously will be required in order to create the sum and difference radiation patterns, one for each plane. This design could be first made using conventional groove gap waveguide implementation with the bed of nails, and in a second phase, to implement it with a glide symmetrical holey EBG structure.

About the amplified distribution, the experimental verification of the prototype with the B2B transition amplified with the built-in 1:2 power divider and a prototype with the slot antenna array are also proposed as future lines of research. To extend this project by using 1:4 and 1:8 power dividers for radiating or recombining can be also considered. In addition, as the work in this chapter was made at low frequencies (X band) as an initial proof of concept, its extension to the millimeter-wave band is clearly an open research line.

Finally, concerning the implementation of the groove gap waveguide with holes, a new structure was proposed in this Thesis which is not the conventional glide symmetrical disposition of holes. The proposed structure is more compact and creates

big stopbands. These properties help to overcome the integration challenges that the holey structure presents when compared to the case with pins. The new proposed structure deserves a deeper analysis and characterization to fully understand its properties. Related to this, hybrid versions of groove gap waveguide combining pins and holes can be considered for study as a trade-off solution for some designs.

Appendix

Appendix A

PMC Packaging Application for Wideband mm-Wave Slot Array Antennas

This chapter presents another work published by the author of this thesis [181] related to Gap Waveguide technology, which highlights the excellent properties that this technology offers as a packaging solution for high frequency transceivers (circuits and antennas) designed in conventional, low cost and widely used technologies such as microstrip transmission lines.

A.1 Introduction

As described in the introduction of this thesis, the increasingly demanding need for bandwidth is pushing the state of the art of RF technology to work at higher and higher frequencies. The advent of 5G wireless technology has highlighted the urgent need to offer solutions in previously underused frequencies, such as the millimetre wave band.

Some of the advantages of using frequencies as high as 28 GHz is that the bandwidth of radio spectrum available to mobile operators can be licensed from 100 MHz to 800 MHz without much problem. However, for 700 MHz bands, bandwidth licences are typically around 5-10 MHz. This bandwidth conditions the data download speed and the number of simultaneous customers that can be served by each base station. For this reason, there is a growing trend to use frequencies as high as millimeter-wave in densely populated urban environments with large concentrations of users such as transport interchanges, airports, metro and train stations, sports stadiums, convention centres, etc.

However, the use of these frequencies is not without drawbacks. One of them is poor coverage due to its propagation and attenuation characteristics. Since this coverage is inferior to that offered by lower bands, the number of base stations needs to be increased, and interference control between nearby equipment sharing base station locations becomes more stringent.

On the other hand, printed technologies (based on dielectric substrates), which are the lowest cost, have high losses at 28 GHz, so it is preferred to design high efficiency and high directivity slot arrays based on all-metal technologies in order to dispense with the substrate, although this increases the cost significantly due to design complexity, which lengthens delivery times, and manufacturing tolerances.

If instead of conventional narrowband resonant antenna slot arrays the designs are wideband (>10 %), the fabrication becomes more complicated and expensive as additional layers and modules are needed [83], [122], [182], [183]. In Gap Waveguide technology [11], [29], [33], [34], [45], [49] there are already published papers that work with only a single layer [85], [184], but are still all-metal when using the 'Ridge' and 'Groove' versions, respectively; which makes it difficult their fabrication as low-cost, mass-produced solutions.

However, mixed designs can be made with Gap Waveguide concept where some part of the antenna that is less susceptible to losses is designed in printed tech-

nology as in [185] where only the corporate feed network is machined in a metal block. Arrays based on SIW technology, on the other hand, also allow for a certain compromise between losses and cost, [186], [187].

But, despite back radiation and other power leakage, microstrip slot or patch array antennas remain the preferred choice due to their ease of integration with active components.

A way to solve some of the problems of microstrip technologies is the use of Gap Waveguide technology as an effective packaging method as demonstrated in [188] and [189]. Regarding the type of unit cell used to form the structure, in this chapter the classical bed of nails is applied, although other structures can be used, such as pyramid-shaped pins [36], mushroom-shaped pins [32], [37] or even spring-shaped pins [38].

The packaging of microstrip feed networks reduces the coupling, the leakage and the radiation in bends or discontinuities.

This chapter describes the development of a PMC packaged bed of nails 8 x 8 wideband slot array made entirely of microstrip technology in which the back radiation and the couplings between the components forming the feed network are blocked as shown descriptively in Fig. A.1c.

With the classical topology shown in Fig. A.1a, the antenna has a strong back radiation and coupling between the feed network lines and the electronic components to be mounted under the substrate. Fig. A.1b solution with ground plane at a distance of $\lambda/4$ manages to avoid back radiation, but magnifies unwanted coupling between feed lines and active devices due to the excited cavity modes, so it is not a good option for beam scanning applications. One way to avoid this with microstrip technology is to isolate the different components on the different layers of the PCB, which increases the cost significantly due to its complexity, which can be uncompetitive for a company.

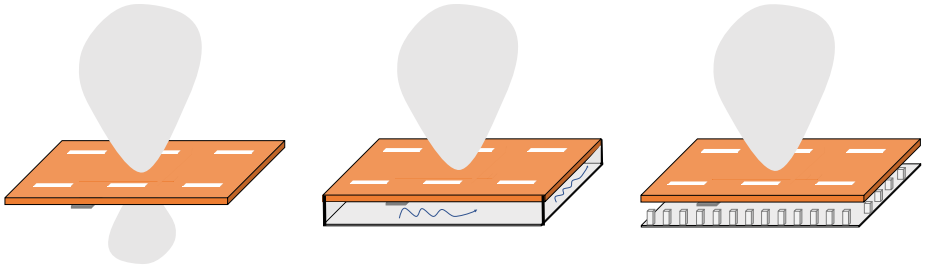

(a) *Classic (no packaging): Strong back radiation, unwanted coupling.*

(b) *With ground plane located at $\lambda/4$ forming a cavity: No back radiation, unwanted coupling and cavity modes.*

(c) *Bed of nails type PMC Packaging: No back radiation, No unwanted coupling and cavity issues.*

Figure A.1: *Types of radiation of a slot array antenna according to encapsulation (microstrip line feed under substrate).*

A.2 Feed Network Design

The design strategy followed was to obtain a 1:16 power divider on a 0.5 mm thick, very low loss Rogers RO5880$^{\text{TM}}$ substrate ($\varepsilon_r = 2.2$ and $\tan\delta = 0.0009$). For this purpose, an optimal distance between the output ports of 0.7 mm (0.65 λ_0) is determined for operation at 28 GHz avoiding grating lobes.

The corporate feed network strategy shown in Fig. A.2 is first designed with the PMC CST boundary condition on the circuit at a distance $g = 0.5$ mm from the substrate. In the T-junctions of the lines, the design includes 4 types of $\lambda/4$ impedance transformers to optimise the matching over as wide a bandwidth as possible. Fig. A.3 shows the simulated result for the 16-port S-parameters, with a loss of -0.3 dB since -12 dB is the ideal output power after 4 power dividers 1:2 (-3 dB). We can see that the matching ($|S_{11}|$) is better than -15 dB in a band from 26 GHz to 30.5 GHz.

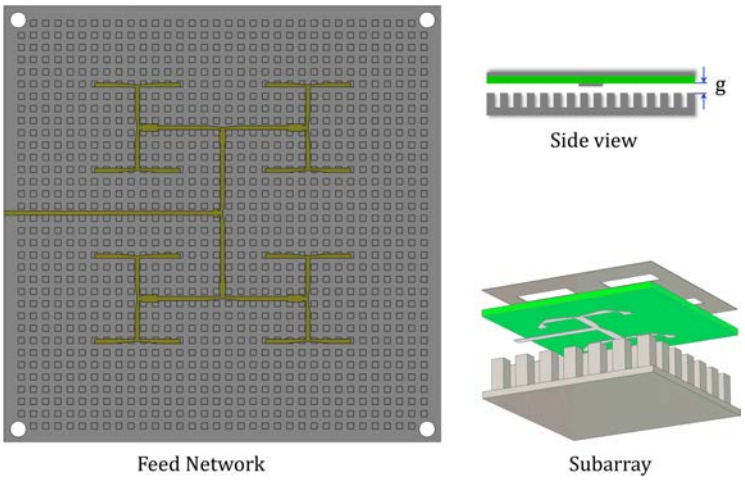

Figure A.2: *Descriptive view of the feed network over the bed of nails (left). Side view of the packaging located at a distance of g (gap) (top right). 3D view of the subarray components: Slots array, substrate, microstrip and bed of nails (bottom right).*

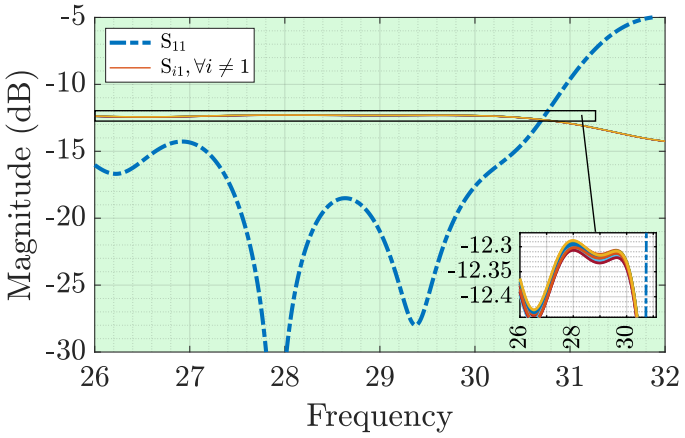

Figure A.3: *Simulated S-parameters of feed network 1:16 with PMC boundary condition.*

The next step is to replace the PMC boundary condition with the bed of nails. To do this, as with all Gap Waveguide designs, we must first adjust the unit cell whose stopband loosely covers the band of interest. Fig. A.4 shows the dispersion diagram together with the dimensions of the metal pin used. The stopband achieved ranges from 25.6 GHz to 37.7 GHz.

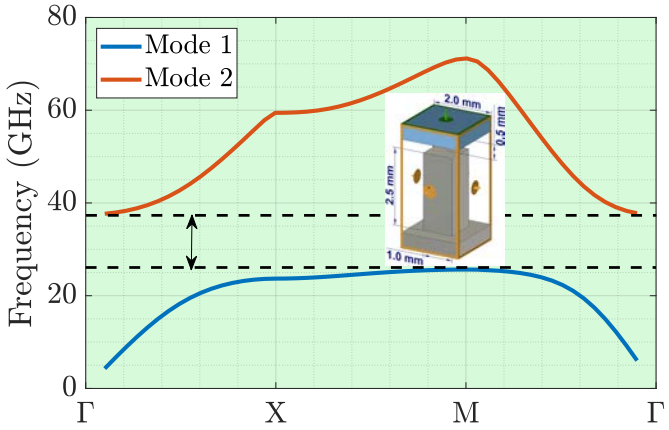

Figure A.4: *Unit cell´s dispersion diagram needed to implement the PMC boundary condition as a bed of nails. Inset with its dimensions. The stopband ranges from 25.6 GHz to 37.7 GHz.*

After placing this bed of nails on the 1:16 power divider and making adjustments with full wave simulations, we achieve the simulated S-parameters in Fig. A.5. It is observed that the losses have increased slightly from −0.3 dB to −0.6 dB when using real aluminium materials. The dimensions of the final design are presented in Fig. A.6 where the 4 types of 1:2 power dividers used are shown.

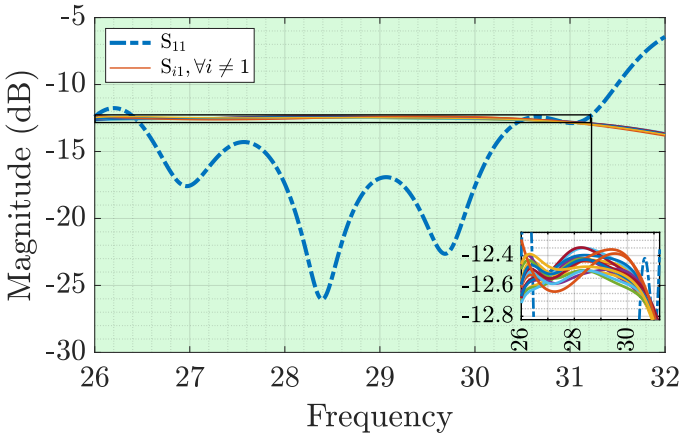

Figure A.5: *Simulated S-parameters of feed network 1:16 with pins.*

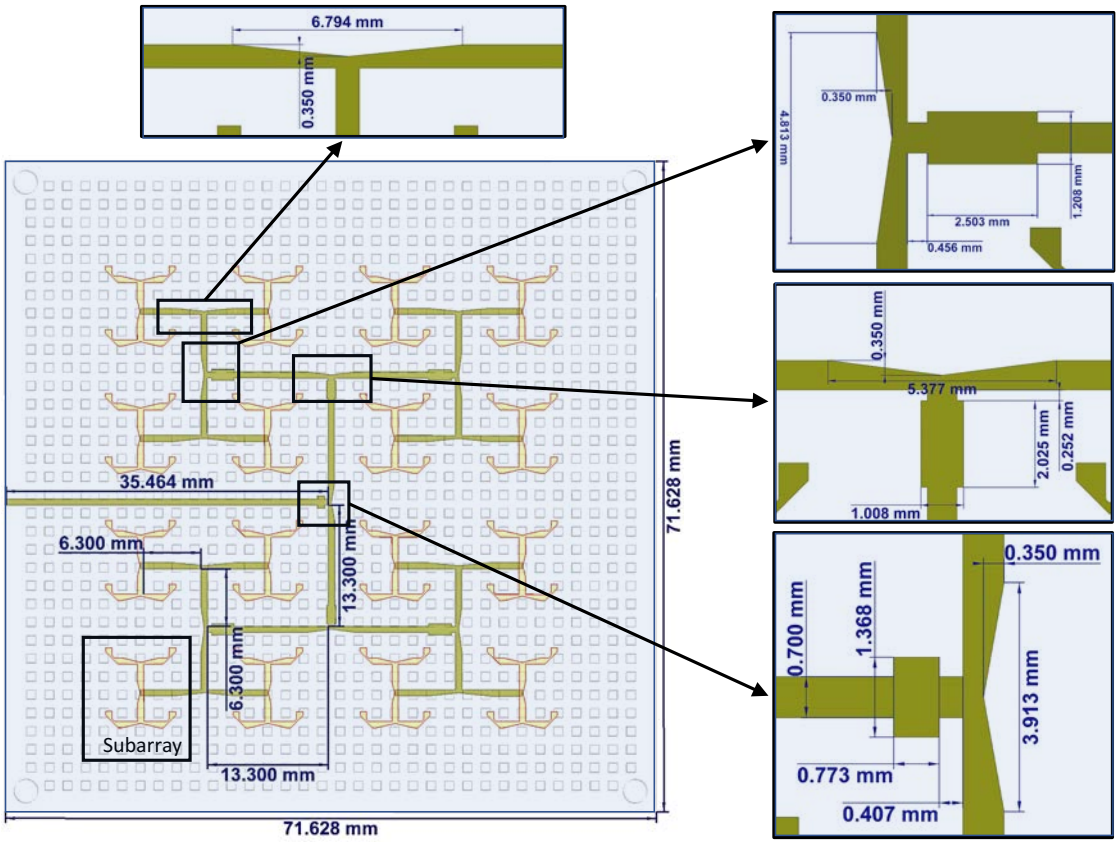

Figure A.6: *Feed network designed with pins, with details of their dimensions and those of the 4 types of power dividers that compose it.*

For ease of manufacturing and assembly with more robust pins and to study the influence of extending the pin dimensions from 2.5 mm to 3 mm, the S-parameter simulation of Fig. A.7 is performed, where we find that they still cover the band loosely from 21.8 GHz to 33.4 GHz and the feed design is not affected.

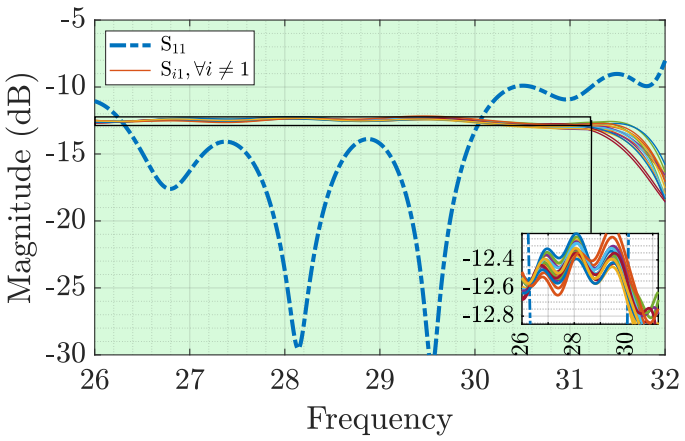

Figure A.7: *Simulated S-parameters of feed network 1:16 with pins ($h = 3$ mm).*

Additional simulations are performed with the pin-optimised feed, in which the encapsulation is removed, which would be equivalent to an 'open' boundary condition (Fig. A.1a) and whose results are shown in Fig. A.8a; and another, in which a metal plane is placed at a distance $\lambda_0/4$, which would be equivalent to placing a 'PEC' boundary condition (Fig. A.1b). It can be seen that in the case of not placing the encapsulation, the losses start to be significantly higher than in the case with packaging, even more above 28 GHz. In the case of the PEC surface, the cavity modes produced in this space distort the response and the transmission losses are no longer homogeneous among the 16 ports (Fig. A.8b) and again higher than in the case with packaging. This would inevitably lead to inhomogeneous feeding of the array slots and thus to a decrease in directivity.

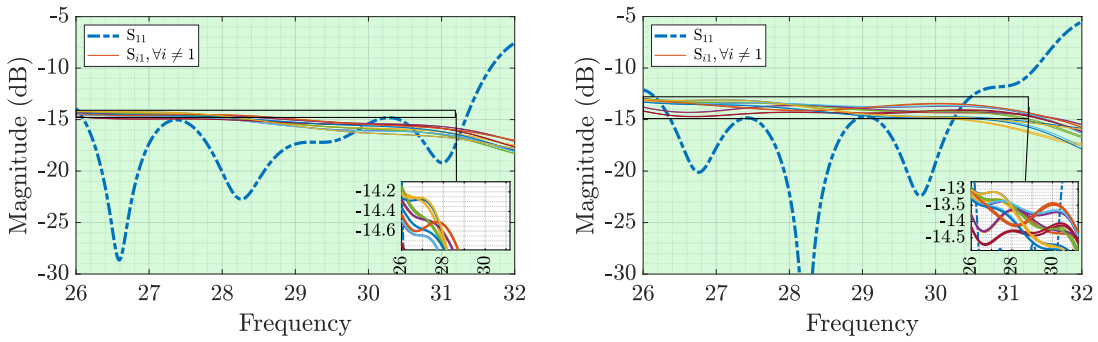

(a) *Open (No packaging)* **(b)** *PEC (reflector)*

Figure A.8: *Simulated S-parameters of feed network 1:16 (additional simulations).*

A.3 Subarray Design

Following the design strategy shown in Fig. A.2 it is now the turn of the subarray. First, a 2 x 2 slot array with microstrip feed is designed with the PMC condition located at distance $g =$ 0.5 mm.

The slots are placed at the distance between elements previously calculated for the corporate feed network of 7 mm, both in the $\hat{x}$ and in the $\hat{y}$ direction ($\hat{z}$ being the direction perpendicular to the plane containing the antenna). This determines the distance at which the slot can be placed closest to the feed line without causing

unwanted coupling. After the design with PMC, the dimensions are readjusted with the pins and the dimensions of the final subarray are shown in Fig. A.9. Fig. A.10 shows the simulated S-parameters for the two cases with PMC and with pins. A good matching is found from 27.4 to 30.2 GHz for the with pins case.

Unlike the feed network, and due to space constraints in the subarray, for the design of the 1:2 power dividers using $\lambda/4$ transformers is avoided and have only one taper across the width of the lines.

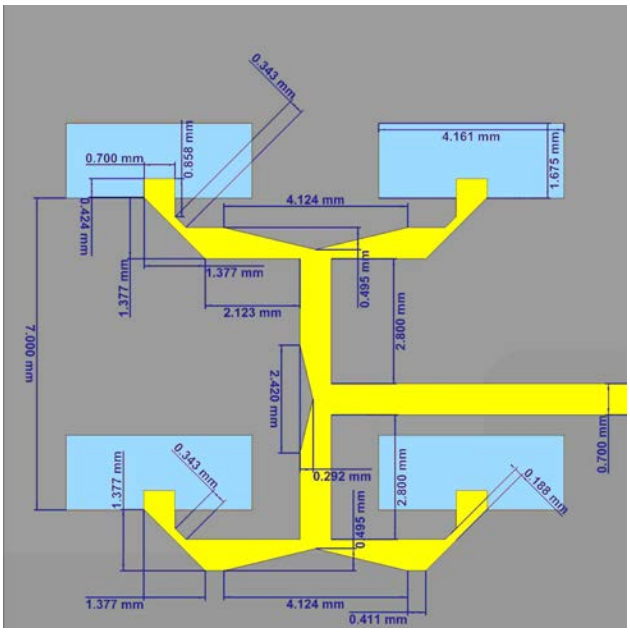

Figure A.9: *Dimensions of the designed subarray.*

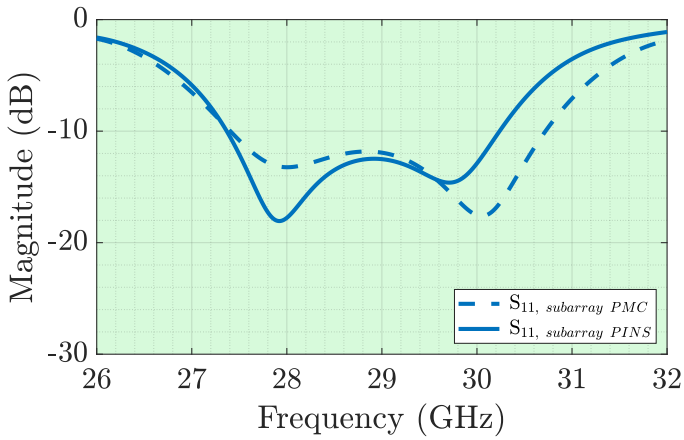

Figure A.10: *Simulated S-parameters of the designed subarray both with the PMC boundary condition and after pins replacement and fine tuning.*

To simulate the radiation pattern, we modelled the boundary conditions in CST with a periodic array to have 4 x 4 subarrays in its version with pins. Fig. A.11 details the radiation pattern for different frequencies between 27.5 GHz and 30 GHz in both the E- and H-plane. Directivity of approximately 25 dBi and SLLs below -12 dB are achieved in all cases. Note that due to periodic boundary conditions, only half of the space is considered.

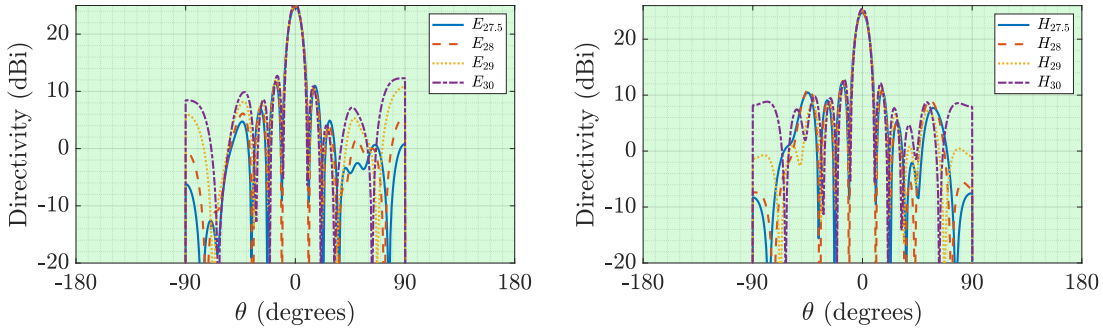

(a) *E plane.* **(b)** *H plane.*

Figure A.11: *Radiation pattern (simulation) of the designed subarray as a function of different frequencies.*

A qualitative way to demonstrate the performance of the PMC packaging is by plotting the electric field distribution of at least 4 subarrays with simultaneous excitations of the 4 ports to see the couplings. Fig. A.12 shows the comparison between the option of not using packaging (Open), of placing a metal plane at a distance of $\lambda/4$ or with PMC packaging implemented with pins. It is clear how the use of PMC packaging avoids couplings between slots and between subarrays.

Fig. A.12d shows the electric field distribution normalised to the maximum value for the full array design fed from a single port. We see that there are some slots with a small phase shift in their excitation, which will lead to a slight decrease in the directivity of the array, as we will see in the next section.

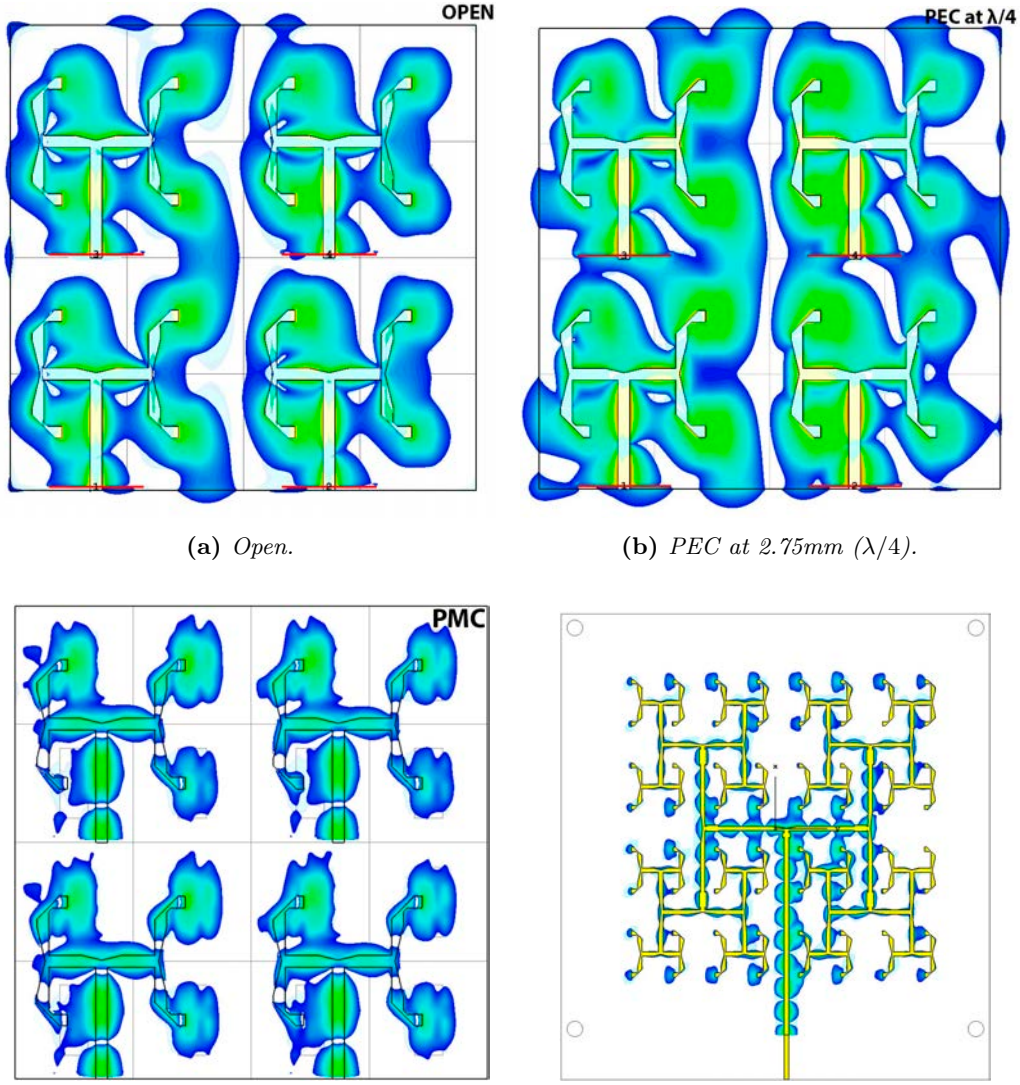

(a) *Open.*

(b) *PEC at 2.75mm (λ/4).*

(c) *Bed of Nails PMC implementation.*

(d) *Full microstrip slot array design with PMC packaging.*

Figure A.12: *Comparison between the electric field distributions for the cases (a) without encapsulation, (b) with the metal plane located at λ/4, (c) for the case with PMC packaging for the subarray with simultaneous feeding of the ports, and (d) for the final array design with the previously designed corporate feed network.*

A.4 PMC Packaged 8 x 8 Slot Array Antenna

Once we have verified the correct operation of the 2 x 2 subarray both in matching and in its radiation pattern, we add the 16 subarrays to the outputs of the previously designed 1:16 power divider and proceed to make fine adjustments with full wave simulations to improve the matching. Fig. A.13 shows the simulated S-parameters

for the final design with both PMC and pins with a bandwidth $> 11\%$ in the band of interest.

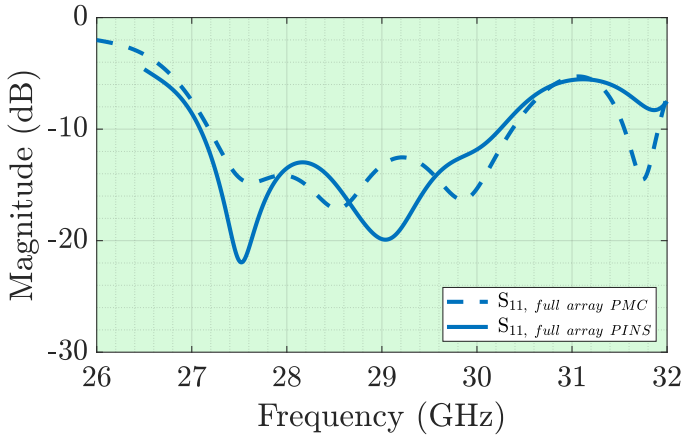

Figure A.13: *Simulated S-parameters of the designed array both with the PMC boundary condition and after replacement with pins.*

In Fig. A.14 the radiation patterns are shown for the same frequency cases and planes as for the subarray and in Table A.1 the obtained results are detailed. Now the obtained directivity ranges from 22.8 to 24.5 dBi compared to 25 dBi in the case of the 4 x 4 subarray model. This decrease is due to the slight phase differences between the aperture illuminations when the corporate feed network is used to feed them, due to small couplings of some lines with the nearest slots.

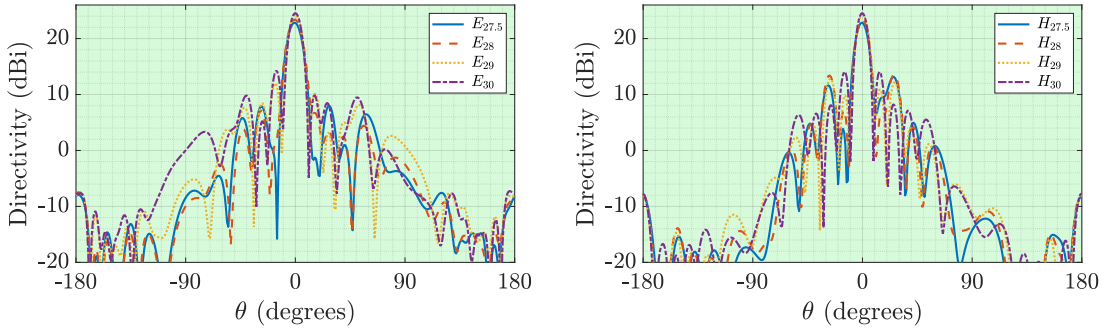

(a) *E plane.* **(b)** *H plane.*

Figure A.14: *Radiation pattern (simulation) of the designed complete array as a function of different frequencies.*

Table A.1: *Antenna parameters [181]*

Frequency [GHz]	**27.5**	**28**	**29**	**30**
Sim. Directivity [dB]	22.8	23.4	24.3	24.5
Sim. Gain [dB]	22.3	22.7	23.6	23.5
Meas. Gain [dB]	19.6	21.5	22.2	23.5
Sim. SLL (E)	-14.9	-16.2	-12.3	-10.3
Sim. SLL (H)	-9.7	-9.8	-11.5	-10.5
Meas. SLL (E)	-10.9	-13.5	-9.8	-11.7
Meas. SLL (H)	-13.6	-10.2	-10.3	-11.9

A.5 Manufacturing and measurement of the prototype

Fig. A.15 shows the fabricated prototype: It can be seen the slot array with an End-Launch connector, the feed network and the bed of nails acting as PMC packaging. Due to the use of this type of connector a transition from coplanar to microstrip is needed.

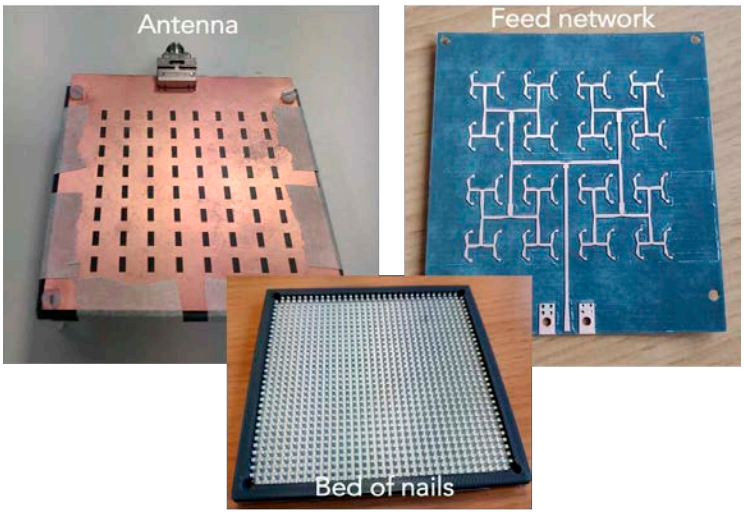

Figure A.15: *The 3 parts of the constructed prototype: Metal plane with the slots, corporate feed network and bed of nails. [181]*

To measure the prototype, it was necessary to create a TRL (Thru, Reflect, Line) kit to eliminate the effect of the connector, since the SOLT (Short-Open-Load-Thru) calibration gave unsatisfactory results. Except for a slight shift towards higher frequencies, we can see in Fig. A.16 the great similarity of the measurement with the simulated value after applying TRL, where we obtain a bandwidth of 3

GHz (27.5 GHz to 30.5 GHz).

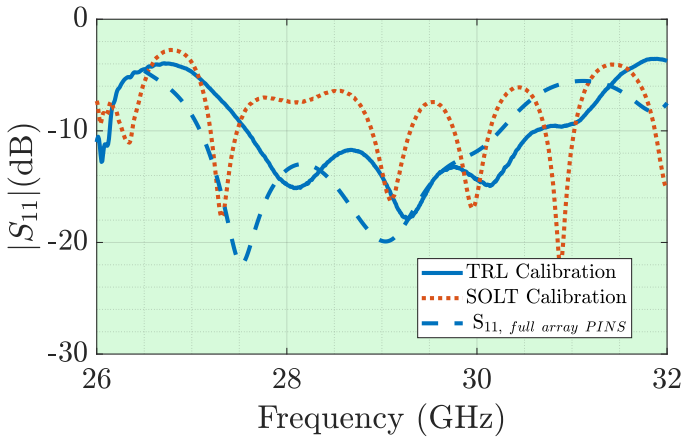

Figure A.16: *Comparison between the simulated S-parameters of the complete array with PMC packaging and the measured values by SOLT and TRL calibration.*

The normalised radiation patterns are shown in both planes and for different frequencies as they can be seen in Fig. A.17. The detailed measured values are listed in Table A.1.

We obtain even better back radiation suppression results than the simulated ones, since in the E-plane between $\theta = \pm 90^o$ and $\theta = \pm 180^o$ the levels are lower than -25 dB, in particular, for $\theta = 180^o$, the simulated front-to-back ratio was at -32 dB (24 dBi vs -8 dBi), while the measured value is lower than -50 dB.

In the H-plane we observe an even better behaviour because in the range between $\theta = \pm 90^o$ and $\theta = \pm 180^o$ the levels are lower than -35 dB, in particular for $\theta = 180^o$, the simulated front-to-back ratio was, again, approximately -32 dB (24 dBi vs -8 dBi), while the measured value is lower than -50 dB.

As for the measured side lobe level (SLL) the results around -12 dB are in line with what can theoretically be expected for a uniformly illuminated array (-13 dB). This shows that the PMC packaging manages to avoid coupling and distortions in the amplitude/phase of the field over the aperture.

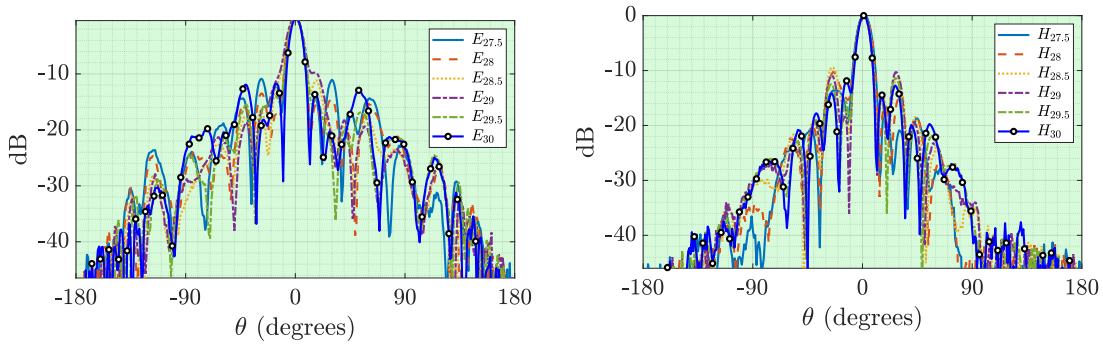

(a) *E plane.* **(b)** *H plane.*

Figure A.17: *Radiation pattern (measurement) of the designed complete array as a function of different frequencies.*

Additionally, Fig. A.18 shows the decomposition of the COPOL and CROSS components of the radiation pattern for 29 GHz where it can be seen that the cross-polarised component is −30 dB below the co-polar one in the direction of maximum directivity (broadside).

This is noteworthy, as such low cross-polarisation is more typical of very narrow slots, with very small bandwidths (resonant); and this array has used wide slots where much higher levels would be expected. This can be seen as one of the advantages of PMC packaging, which, overall, has achieved a high aperture radiation efficiency (79%) (estimated with the measured gain and the simulated directivity).

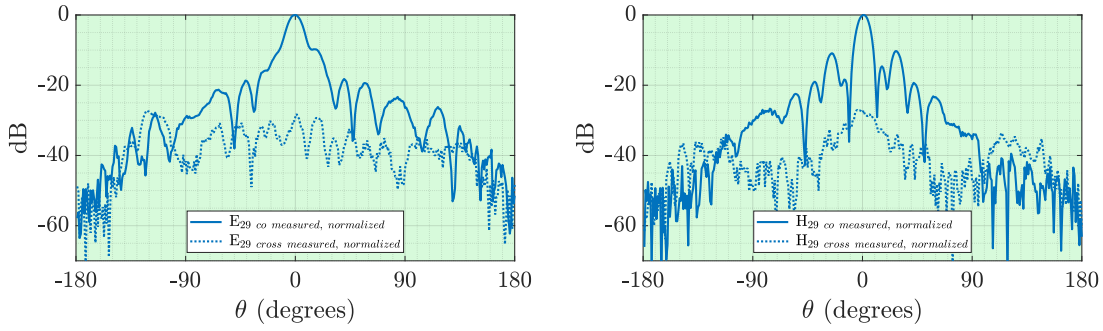

(a) *E plane.* **(b)** *H plane.*

Figure A.18: *Radiation pattern (measurement) of the complete designed array at 29 GHz with CROSS-COPOL decomposition.*

The last result to show is the comparison between simulated and measured gain

as a function of the frequency. Again, Fig. A.19 shows the good agreement between the two sets of values.

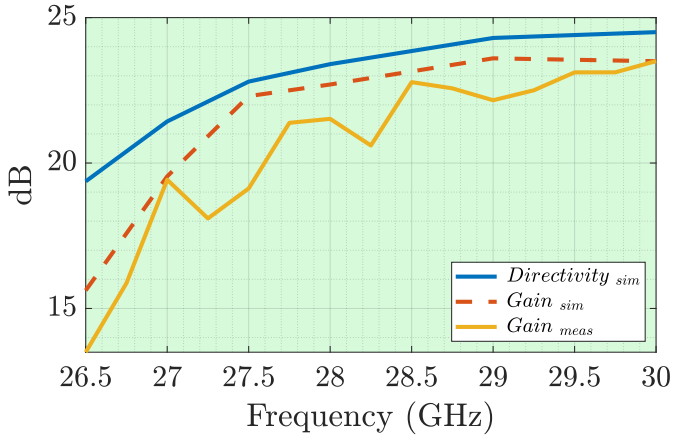

Figure A.19: *Simulated directivity and gain and measurements of slot antenna array with PMC packaging.*

To evaluate the performance of this design, it has been compared with other similar PCB-based planar arrays, the most important values of which are detailed in Table A.2. In it, a higher radiation efficiency is observed for the case with PMC packaging (efficiency is estimated with the measured gain and the simulated directivity).

Table A.2: *Comparison with other PCB-based planar arrays [181]*

	f_0 **(GHz)**	**#Els**	**#Lay**	**Size** (λ_0)	**BW** (%)	**Gain (dBi)**	**SLL (dB)**	**Rad.eff** (%)	**Type**
[187]	20	256	2	12x12.6	15	29.1	-17	76	SIW+Mstrip
[190]	60	50	1	7x7	12.5	25.2	-9	63.7	SIW+Mstrip
[191]	12.5	64	2	6.3x6.3	13	24	-12	NA	SIW
[192]	60	144	1	NA	4.16	22	-15	68	Mstrip
[193]	30	64	12	6x7.6	13.3	22.5	-12	57.8	Mstrip
This	**30**	**64**	**2**	**7.2x7.7**	**11.1**	**23.5**	**-11.7**	**79.4**	PMC+Mstrip

A.6 Conclusions

In this section we have presented the development of a slot array antenna based on microstrip in millimetre band, in which a PMC type packaging is added to eliminate the back radiation typical of these antennas designed with microstrip. In addition, the couplings between the corporate feed network lines are almost completely blocked, which favours the uniform illumination of the array, thus increasing its directivity. This PMC packaging, although made with metal parts, does not produce cavity modes that produce interference between amplifier elements that can be integrated, making it a good solution for creating planar arrays of many more elements with integrated active beam scanning electronic.

References

[1] *CST Computer Simulation Technology*, 2021. [Online]. Available: https://www.cst.com/.

[2] *AWR Microwave Office*, 2021. [Online]. Available: https://www.cadence.com/ko_KR/home/tools/system-analysis/rf-microwave-design/awr-microwave-office.html.

[3] D. Saha, A. Mukherjee, and S. Bandyopadhyay, *Networking Infrastructure for Pervasive Computing: Enabling Technologies and Systems*, en. Springer Science & Business Media, Jun. 2011, ISBN: 978-1-4615-1143-4.

[4] J. Song, *Council Post: Why Low Latency (Not Speed) Makes 5G A World-Changing Technology*, Link: https://bit.ly/3aXT2tJ. [Online]. Available: https://www.forbes.com/.../why-low-latency-not-speed-makes-5g-a-world-changing-technology/ (visited on 03/20/2022).

[5] *How 5G Low Latency Improves Your Mobile Experiences [video]*, en, May 2019. [Online]. Available: https://www.qualcomm.com/news/onq/2019/05/13/how-5g-low-latency-improves-your-mobile-experiences (visited on 03/20/2022).

[6] J. G. Huang, B. Dong, M. Tang, *et al.*, "All Optomechanical Signal Modulation in Photonic Circuits," in *2015 Transducers - 2015 18th International Conference on Solid-State Sensors, Actuators and Microsystems (TRANSDUCERS)*, ISSN: 2164-1641, Jun. 2015, pp. 2065–2068. DOI: 10.1109/TRANSDUCERS.2015.7181363.

[7] S. Corzine, P. Evans, and M. Kato, "Photonic Integrated Circuits for Phase Modulation Formats," in *LEOS 2008 - 21st Annual Meeting of the IEEE Lasers and*

Electro-Optics Society, ISSN: 1092-8081, Nov. 2008, pp. 334–335. DOI: 10.1109/LEOS.2008.4688626.

[8] S. Jin, L. Xu, V. Rosborough, J. Klamkin, and Y. Li, "RF Frequency Mixer Photonic Integrated Circuit," *IEEE Photonics Technology Letters*, vol. 28, no. 16, pp. 1771–1773, Aug. 2016, ISSN: 1941-0174. DOI: 10.1109/LPT.2016.2570520.

[9] K. Zhang, Q. Zhuge, H. Xin, H. He, W. Hu, and D. V. Plant, "Low-Cost WDM Fronthaul Enabled by Partitioned Asymmetric AWGR with Simultaneous Flexible Transceiver Assignment and Chirp Management," *Journal of Optical Communications and Networking*, vol. 9, no. 10, pp. 876–888, Oct. 2017, ISSN: 1943-0639. DOI: 10.1364/JOCN.9.000876.

[10] M. Luo, J. Li, T. Zeng, *et al.*, "Real-Time Coherent UDWDM-PON with Dual-Polarization Transceivers in a Field Trial," *Journal of Optical Communications and Networking*, vol. 11, no. 2, A166–A173, Feb. 2019, ISSN: 1943-0639. DOI: 10.1364/JOCN.11.00A166.

[11] P.-S. Kildal, E. Alfonso, A. Valero-Nogueira, and E. Rajo-Iglesias, "Local Metamaterial Based Waveguides in Gaps Between Parallel Metal Plates," *IEEE Antennas and Wireless Propagation Letters*, vol. 8, pp. 84–87, 2009, ISSN: 1548-5757. DOI: 10.1109/LAWP.2008.2011147.

[12] P.-S. Kildal, "Waveguides and Transmission Lines in Gaps Between Parallel Conducting Surfaces," US20110181373A1. [Online]. Available: https://patents.google.com/patent/US20110181373A1/en.

[13] J. Liu, J. Yang, and A. U. Zaman, "Study of Dielectric Loss and Conductor Loss among Microstrip, covered Microstrip and inverted Microstrip Gap Waveguide utilizing variational Method in Millimeter Waves," in *2018 International Symposium on Antennas and Propagation (ISAP)*, Oct. 2018, pp. 1–2.

[14] P. Sergienko, I. Golubeva, and Y. Prokopenko, "Loss in Tunable Microstrip Lines," in *2014 IEEE 34th International Scientific Conference on Electronics and Nanotechnology (ELNANO)*, Apr. 2014, pp. 97–100. DOI: 10.1109/ELNANO.2014.6873972.

[15] B. Young and T. Itoh, "Loss Reduction in Superconducting Microstrip-Like Transmission Lines," in *1988., IEEE MTT-S International Microwave Symposium Digest*, May 1988, 453–456 vol.1. DOI: 10.1109/MWSYM.1988.22072.

[16] D. Deslandes and K. Wu, "Integrated Microstrip and Rectangular Waveguide in Planar Form," *IEEE Microwave and Wireless Components Letters*, vol. 11, no. 2, pp. 68–70, Feb. 2001, ISSN: 1558-1764. DOI: 10.1109/7260.914305.

[17] J. Hirokawa and M. Ando, "Single-Layer Feed Waveguide Consisting of Posts for Plane TEM Wave Excitation in Parallel Plates," *IEEE Transactions on Antennas and Propagation*, vol. 46, no. 5, pp. 625–630, May 1998, ISSN: 1558-2221. DOI: 10.1109/8.668903.

[18] H. M. Hizan, Z. Ambak, A. Ibrahim, M. Z. Mohamed Yusoff, and T. Kanesan, "Effect of Insertion Losses on Millimeter-Wave SIW Filters Using LTCC Technology," in *2015 IEEE International RF and Microwave Conference (RFM)*, Dec. 2015, pp. 65–68. DOI: 10.1109/RFM.2015.7587714.

[19] Y. Ding, Y. Jin, G. Zhu, Z. Zou, E. Ren, and G. Yang, "A K-band Wideband Low Insertion Loss SIW-to-Waveguide Transition," in *2021 IEEE 4th International Conference on Electronics Technology (ICET)*, May 2021, pp. 692–695. DOI: 10.1109/ICET51757.2021.9451100.

[20] F. Parment, A. Ghiotto, T.-P. Vuong, J.-M. Duchamp, and K. Wu, "Air-Filled SIW Transmission Line and Phase Shifter for High-Performance and Low-Cost U-Band Integrated Circuits and Systems," in *Global Symposium on Millimeter-Waves (GSMM)*, May 2015, pp. 1–3. DOI: 10.1109/GSMM.2015.7175444.

[21] C. Kudsia, R. Cameron, and W.-C. Tang, "Innovations in Microwave Filters and Multiplexing Networks for Communications Satellite Systems," *IEEE Transactions on Microwave Theory and Techniques*, vol. 40, no. 6, pp. 1133–1149, Jun. 1992, ISSN: 1557-9670. DOI: 10.1109/22.141345.

[22] I. Corporation, *Waveguide and Method of Manufacture*, ko, Nov. 2002. [Online]. Available: http://scienceon.kisti.re.kr/srch/selectPORSrchPatent.do?cn=USP2007107280011 (visited on 03/21/2022).

[23] G. Bertin, B. Piovano, L. Accatino, and M. Mongiardo, "Analysis and Design of Circular Waveguide Polarizers with Elliptical Irises," in *2000 30th European Microwave Conference*, Oct. 2000, pp. 1–4. DOI: 10.1109/EUMA.2000.338646.

[24] X. Shang, M. J. Lancaster, M. Ke, and Y. Wang, "Measurements of Micromachined Submillimeter Waveguide Circuits," in *2010 76th ARFTG Microwave Measurement Conference*, Nov. 2010, pp. 1–4. DOI: 10.1109/ARFTG76.2010.5700055.

[25] C. Collins, R. Miles, J. Digby, *et al.*, "A New Micromachined Millimeter-Wave and Terahertz Snap Together Rectangular Waveguide Technology," *IEEE Microwave and Guided Wave Letters*, vol. 9, no. 2, pp. 63–65, Feb. 1999, ISSN: 1558-2329. DOI: 10.1109/75.755047.

[26] J. Digby, C. McIntosh, G. Parkhurst, *et al.*, "Fabrication and Characterization of Micromachined Rectangular Waveguide Components for Use at Millimeter-wave and Terahertz Frequencies," *IEEE Transactions on Microwave Theory and Techniques*, vol. 48, no. 8, pp. 1293–1302, Aug. 2000, ISSN: 1557-9670. DOI: 10.1109/22.859472.

[27] M. Brumos, V. E. Boria, M. Guglielmi, and S. Cogollos, "Correction of Manufacturing Deviations in Circular-Waveguide Dual-Mode Filters using Aggressive Space Mapping," in *2014 44th European Microwave Conference*, Oct. 2014, pp. 624–627. DOI: 10.1109/EuMC.2014.6986511.

[28] P.-S. Kildal, "Definition of Artificially Soft and Hard Surfaces for Electromagnetic Waves," *Electronics Letters*, vol. 24, no. 3, pp. 168–170, Feb. 1988, ISSN: 1350-911X. DOI: 10.1049/el:19880112.

[29] P.-S. Kildal, "Artificially Soft and Hard Surfaces in Electromagnetics," *IEEE Transactions on Antennas and Propagation*, vol. 38, no. 10, pp. 1537–1544, Oct. 1990, ISSN: 1558-2221. DOI: 10.1109/8.59765.

[30] Z. Šipuš, H. Merkel, and P.-S. Kildal, "Green's Functions for Planar Soft and Hard Surfaces Derived by Asymptotic Boundary Conditions," *IET Proceedings - Microwaves, Antennas and Propagation*, vol. 144, no. 5, pp. 321–328, Oct. 1997, ISSN: 1359-706X. DOI: 10.1049/ip-map:19971335.

[31] S. Skobelev and P.-S. Kildal, "Mode-Matching Modeling of a Hard Conical Quasi-TEM Horn Realized by an EBG Structure with Strips and Vias," *IEEE Transactions on Antennas and Propagation*, vol. 53, no. 1, pp. 139–143, Jan. 2005, ISSN: 1558-2221. DOI: 10.1109/TAP.2004.840417.

[32] D. Sievenpiper, L. Zhang, R. Broas, N. Alexopolous, and E. Yablonovitch, "High-Impedance Electromagnetic Surfaces with a Forbidden Frequency Band," *IEEE Transactions on Microwave Theory and Techniques*, vol. 47, no. 11, pp. 2059–2074, Nov. 1999, ISSN: 1557-9670. DOI: 10.1109/22.798001.

[33] A. U. Zaman and P.-S. Kildal, "GAP Waveguides," in *Handbook of Antenna Technologies*, Z. N. Chen, D. Liu, H. Nakano, X. Qing, and T. Zwick, Eds., Singapore: Springer, 2016, pp. 3273–3347, ISBN: 978-981-4560-44-3. [Online]. Available: https://doi.org/10.1007/978-981-4560-44-3_130.

[34] P.-S. Kildal and A. Kishk, "EM Modeling of Surfaces with STOP or GO Characteristics Artificial Magnetic Conductors and Soft and Hard Surfaces," *Applied Computational Electromagnetics Society Journal*, vol. 18, no. 1, pp. 32–40, 2003.

[35] M. G. Silveirinha, C. A. Fernandes, and J. R. Costa, "Electromagnetic Characterization of Textured Surfaces Formed by Metallic Pins," *IEEE Transactions on Antennas and Propagation*, vol. 56, no. 2, pp. 405–415, Feb. 2008, ISSN: 1558-2221. DOI: 10.1109/TAP.2007.915442.

[36] A. Uz Zaman, V. Vassilev, P.-S. Kildal, and A. Kishk, "Increasing Parallel Plate Stop-Band in Gap Waveguides Using Inverted Pyramid-Shaped Nails for Slot Array Application Above 60 GHz," in *Proceedings of the 5th European Conference on Antennas and Propagation (EUCAP)*, ISSN: 2164-3342, Apr. 2011, pp. 2254–2257. [Online]. Available: https://ieeexplore.ieee.org/document/5782024.

[37] E. Pucci, E. Rajo-Iglesias, and P.-S. Kildal, "New Microstrip Gap Waveguide on Mushroom-Type EBG for Packaging of Microwave Components," *IEEE Microwave and Wireless Components Letters*, vol. 22, no. 3, pp. 129–131, Mar. 2012, ISSN: 1558-1764. DOI: 10.1109/LMWC.2011.2182638.

[38] E. Rajo-Iglesias, P.-S. Kildal, A. U. Zaman, and A. Kishk, "Bed of Springs for Packaging of Microstrip Circuits in the Microwave Frequency Range," *IEEE Transactions on Components, Packaging and Manufacturing Technology*, vol. 2, no. 10, pp. 1623–1628, Oct. 2012, ISSN: 2156-3985. DOI: 10.1109/TCPMT.2012.2207957.

[39] Z. Sipus, M. Bosiljevac, and E. Rajo-Iglesias, "Higher Symmetries in Holey Structures Applied to Gap Waveguide Technology: Fundamentals and Considerations," in *2020 International Symposium on Antennas and Propagation (ISAP)*, Jan. 2021, pp. 585–586. DOI: 10.23919/ISAP47053.2021.9391106.

[40] M. Ebrahimpouri, O. Quevedo-Teruel, and E. Rajo-Iglesias, "Design Guidelines for Gap Waveguide Technology Based on Glide-Symmetric Holey Structures," *IEEE Microwave and Wireless Components Letters*, vol. 27, no. 6, pp. 542–544, Jun. 2017, ISSN: 1558-1764. DOI: 10.1109/LMWC.2017.2701308.

[41] M. Ebrahimpouri, O. Quevedo-Teruel, and E. Rajo-Iglesias, "Design of Microwave Components in Groove Gap Waveguide Technology Implemented by Holey EBG," in *2017 11th European Conference on Antennas and Propagation (EUCAP)*, Mar. 2017, pp. 746–748. DOI: 10.23919/EuCAP.2017.7928587.

[42] M. Ebrahimpouri, E. Rajo-Iglesias, and O. Quevedo-Teruel, "Wideband Glide Symmetric Holey Structures for Gap-Waveguide Technology," in *2017 11th European Conference on Antennas and Propagation (EUCAP)*, Mar. 2017, pp. 1658–1660. DOI: 10.23919/EuCAP.2017.7928356.

[43] Z. Sipus, K. Cavar, and E. Rajo-Iglesias, "Glide-Symmetric Holey Structures Applied to Waveguide Technology: Design Considerations," *Sensors*, vol. 20, no. 23, p. 6871, Dec. 2020. DOI: 10.3390/s20236871.

[44] M. Ferrando-Rocher, "Explorando las Prestaciones y Ventajas de la Half-Groove Gap Waveguide," Mar. 2022. [Online]. Available: http://rua.ua.es/dspace/handle/10045/122022.

[45] E. Rajo-Iglesias and P.-S. Kildal, "Numerical Studies of Bandwidth of Parallel-Plate Cut-Off Realised by a Bed of Nails, Corrugations and Mushroom-Type Electromagnetic Bandgap for Use in Gap Waveguides," *IET Microwaves, Antennas*

& *Propagation*, vol. 5, no. 3, pp. 282–289, Feb. 2011, ISSN: 1751-8733. DOI: 10.1049/iet-map.2010.0073.

[46] N. Memeletzoglou, C. Sanchez-Cabello, F. Pizarro-Torres, and E. Rajo-Iglesias, "Analysis of Periodic Structures Made of Pins Inside a Parallel Plate Waveguide," *Symmetry*, vol. 11, no. 4, p. 582, Apr. 2019, ISSN: 2073-8994. DOI: 10.3390/sym11040582.

[47] S. Farjana, A. U. Zaman, P. Lundgren, and P. Enoksson, "Micromachined Wideband Ridge Gap Waveguide Power Divider at 220–325 GHz," *IEEE Access*, vol. 10, pp. 27 432–27 439, 2022, ISSN: 2169-3536. DOI: 10.1109/ACCESS.2022.3156095.

[48] E. Rajo-Iglesias and P. Kildal, "Groove Gap Waveguide: A Rectangular Waveguide Between Contactless Metal Plates Enabled by Parallel-plate Cut-off," in *Proceedings of the Fourth European Conference on Antennas and Propagation*, Barcelona, Spain: IEEE, Apr. 2010, pp. 1–4, ISBN: 2164-3342. [Online]. Available: https://ieeexplore.ieee.org/document/5504912.

[49] P. .-. Kildal, A. U. Zaman, E. Rajo-Iglesias, E. Alfonso, and A. Valero-Nogueira, "Design and Experimental Verification of Ridge Gap Waveguide in Bed of Nails for Parallel-plate Mode Suppression," *IET Microwaves, Antennas & Propagation*, vol. 5, no. 3, pp. 262–270, Feb. 2011, ISSN: 1751-8733. DOI: 10.1049/iet-map.2010.0089.

[50] E. Pucci, A. U. Zaman, E. Rajo-Iglesias, and P.-S. Kildal, "New Low Loss Inverted Microstrip Line Using Gap Waveguide Technology for Slot Antenna Applications," in *Proceedings of the 5th European Conference on Antennas and Propagation (EUCAP)*, Apr. 2011, pp. 979–982, ISBN: 2164-3342. [Online]. Available: https://ieeexplore.ieee.org/document/5782604.

[51] H. Raza, J. Yang, P.-S. Kildal, and E. Alfonso Alós, "Microstrip-Ridge Gap Waveguide–Study of Losses, Bends, and Transition to WR-15," *IEEE Transactions on Microwave Theory and Techniques*, vol. 62, no. 9, pp. 1943–1952, Sep. 2014, ISSN: 1557-9670. DOI: 10.1109/TMTT.2014.2327199.

[52] L. Inclan-Sanchez, C. Sanchez-Cabello, J. Vazquez-Roy, and E. Rajo-Iglesias, "New EBG-Filter Design in Inverted Microstrip Gap Waveguide Technology," in *2017 IEEE International Symposium on Antennas and Propagation USNC/URSI*, Jul.

2017, pp. 1663–1664, ISBN: 1947-1491. DOI: 10.1109/APUSNCURSINRSM.2017.8072874.

[53] N. Castro, F. Pizarro, L. F. Herrán-Ontanón, and E. Rajo-Iglesias, "Evaluation of Inverted Microstrip Gap Waveguide Bandpass Filters for Ka-Band," *AEU - International Journal of Electronics and Communications*, vol. 134, p. 153 677, May 2021, ISSN: 1434-8411. DOI: 10.1016/j.aeue.2021.153677.

[54] M. Rezaee and A. U. Zaman, "Realisation of Carved and Iris Groove Gap Waveguide Filter and E-plane Diplexer for V-Band Radio Link Application," *IET Microwaves, Antennas & Propagation*, vol. 11, no. 15, pp. 2109–2115, 2017, ISSN: 1751-8733. DOI: 10.1049/iet-map.2017.0268.

[55] M. Shu, W. Xu, Z. Wu, C. Guo, J. Chen, and A. Zhang, "A Mixed Cross Coupling Gap Waveguide Bandpass Filter with Asymmetric Transmission Zeros," in *2019 International Symposium on Antennas and Propagation (ISAP)*, Xian, China, Oct. 2019, pp. 1–2.

[56] Z. Shaterian, A. K. Horestani, and M. Mrozowski, "Design Guidelines for Microwave Filters in Gap Waveguide Technology," in *2021 IEEE MTT-S International Microwave Filter Workshop (IMFW)*, Nov. 2021, pp. 182–184. DOI: 10.1109/IMFW49589.2021.9642373.

[57] Z. Liu, J.-Y. Deng, and D. Sun, "Slow-Wave Groove Gap Waveguide Bandpass Filter," *IEEE Access*, vol. 7, pp. 52 581–52 588, 2019, ISSN: 2169-3536. DOI: 10.1109/ACCESS.2019.2912496.

[58] A. del Olmo-Olmeda, M. Baquero-Escudero, V. E. Boria-Esbert, A. Valero-Nogueira, and A. J. Berenguer-Verdú, "A Novel Band-Pass Filter Topology for Millimeter-Wave Applications Based on the Groove Gap Waveguide," in *2013 IEEE MTT-S International Microwave Symposium Digest (MTT)*, ISSN: 0149-645X, Jun. 2013, pp. 1–4. DOI: 10.1109/MWSYM.2013.6697780.

[59] A. U. Zaman, P.-S. Kildal, and A. A. Kishk, "Narrow-Band Microwave Filter Using High-Q Groove Gap Waveguide Resonators With Manufacturing Flexibility and No Sidewalls," *IEEE Transactions on Components, Packaging and Manufacturing*

Technology, vol. 2, no. 11, pp. 1882–1889, Nov. 2012, ISSN: 2156-3985. DOI: 10.1109/TCPMT.2012.2202905.

[60] R. Yang, W. Ren, D. Shen, and X. Zhang, "Design of Integrated Substrate Gap Waveguide 3-dB Rectangular-Junction Couplers," in *2021 International Applied Computational Electromagnetics Society (ACES-China) Symposium*, Jul. 2021, pp. 1–2. DOI: 10.23919/ACES-China52398.2021.9581530.

[61] P. Mahdavi and S. E. Hosseini, "Ku-band Two-Section Branch-Line Coupler Based on Ridge Gap Waveguide Technology," in *2020 28th Iranian Conference on Electrical Engineering (ICEE)*, ISSN: 2642-9527, Aug. 2020, pp. 1–5. DOI: 10.1109/ICEE50131.2020.9261083.

[62] B. Halvaei, J. Ghalibafan, and M. Rezaee, "A Multi-Hole Groove Gap Waveguide Directional Coupler based on Glide-Symmetric Holey EBG for E-Band Application," in *2020 28th Iranian Conference on Electrical Engineering (ICEE)*, ISSN: 2642-9527, Aug. 2020, pp. 1–5. DOI: 10.1109/ICEE50131.2020.9260744.

[63] M. Taraji and M. Naser-Moghaddasi, "Design of Branch Line Coupler based on Ridge Gap Waveguide Technology for X-band Application," *IETE Journal of Research*, pp. 1–7, Jun. 2019, ISSN: 0377-2063. DOI: 10.1080/03772063.2019.1627916.

[64] M. Y. Soliman, M. M. M. Ali, S. I. Shams, M. F. A. Sree, D. E. Fawzy, and A. M. M. A. Allam, "Ridge Gap Waveguide Wideband Hybrid Directional Coupler for Ka-Band Applications," in *2020 7th International Conference on Electrical and Electronics Engineering (ICEEE)*, Apr. 2020, pp. 211–214. DOI: 10.1109/ICEEE49618.2020.9102609.

[65] D. Zarifi and A. R. Shater, "Design of a 3 dB Directional Coupler Based on Groove Gap Waveguide Technology," *Microwave and Optical Technology Letters*, vol. 59, no. 7, pp. 1597–1600, 2017, ISSN: 1098-2760. DOI: 10.1002/mop.30588.

[66] D. Sun and J. Xu, "Rectangular Waveguide Coupler with Adjustable Coupling Coefficient Using Gap Waveguide Technology," *Electronics Letters*, vol. 53, no. 3, pp. 167–169, 2017, ISSN: 1350-911X. DOI: 10.1049/el.2016.4039.

[67] C. Sánchez Cabello and E. Rajo-Iglesias, "Optimized Self-Diplexed Atenna in Gap Waveguide Technology," in *2015 IEEE International Symposium on Antennas and Propagation USNC/URSI National Radio Science Meeting*, ISSN: 1947-1491, Jul. 2015, pp. 460–461. DOI: 10.1109/APS.2015.7304616.

[68] C. S. Cabello and E. Rajo-Iglesias, "Low Cost Self-Diplexed Antenna in Inverted Microstrip Gap Waveguide Technology," in *2014 International Symposium on Antennas and Propagation Conference Proceedings*, Dec. 2014, pp. 169–170. DOI: 10.1109/ISANP.2014.7026584.

[69] E. A. Alós, A. U. Zaman, and P.-S. Kildal, "Ka-Band Gap Waveguide Coupled-Resonator Filter for Radio Link Diplexer Application," *IEEE Transactions on Components, Packaging and Manufacturing Technology*, vol. 3, no. 5, pp. 870–879, May 2013, ISSN: 2156-3985. DOI: 10.1109/TCPMT.2012.2231140.

[70] A. Vosoogh, M. S. Sorkherizi, A. U. Zaman, J. Yang, and A. A. Kishk, "An Integrated Ka-Band Diplexer-Antenna Array Module Based on Gap Waveguide Technology With Simple Mechanical Assembly and No Electrical Contact Requirements," *IEEE Transactions on Microwave Theory and Techniques*, vol. 66, no. 2, pp. 962–972, Feb. 2018, ISSN: 1557-9670. DOI: 10.1109/TMTT.2017.2757469.

[71] A. Vosoogh, M. Sharifi Sorkherizi, A. Uz Zaman, J. Yang, and A. A. Kishk, "An E-band Antenna-Diplexer Compact Integrated Solution Based on Gap Waveguide Technology," in *2017 International Symposium on Antennas and Propagation (ISAP)*, Oct. 2017, pp. 1–2. DOI: 10.1109/ISANP.2017.8229008.

[72] A. Vosoogh, M. S. Sorkherizi, A. U. Zaman, J. Yang, and A. A. Kishk, "Diplexer Integration into a Ka-band High-Gain Gap Waveguide Corporate-Fed Slot Array Antenna," in *2017 IEEE International Symposium on Antennas and Propagation USNC/URSI National Radio Science Meeting*, ISSN: 1947-1491, Jul. 2017, pp. 2667–2668. DOI: 10.1109/APUSNCURSINRSM.2017.8073376.

[73] M. Rezaee, A. U. Zaman, and P.-S. Kildal, "V-band Groove Gap Waveguide Diplexer," in *2015 9th European Conference on Antennas and Propagation (EuCAP)*, Apr. 2015, pp. 1–4.

[74] N. Memeletzoglou and E. Rajo-Iglesias, "Design of an Array of Stacked Groove Gap Waveguide Leaky-Wave Antennas in the Ka Band," in *2020 14th European Conference on Antennas and Propagation (EuCAP)*, Mar. 2020, pp. 1–5. DOI: 10.23919/EuCAP48036.2020.9135857.

[75] M. S. Ali and M. M. Tahseen, "Ka-Band Long Slot Antenna using Printed Ridge Gap Waveguide Technology," in *2021 1st International Conference on Microwave, Antennas Circuits (ICMAC)*, Dec. 2021, pp. 1–3. DOI: 10.1109/ICMAC54080.2021.9678252.

[76] W. Y. Yong, T. Emanuelsson, and A. A. Glazunov, "5G Wideband Magneto-Electric Dipole Antenna Fed by a Single-Layer Corporate-Feed Network based on Ridge Gap Waveguide," in *2020 14th European Conference on Antennas and Propagation (EuCAP)*, Mar. 2020, pp. 1–4. DOI: 10.23919/EuCAP48036.2020.9135588.

[77] R. Kon, W. Yan Yong, and A. Alayón Glazunov, "Wideband H-Slot Antenna Fed by Substrate Integrated Gap Waveguide for mmWave Arrays," in *2020 International Symposium on Antennas and Propagation (ISAP)*, Jan. 2021, pp. 577–578. DOI: 10.23919/ISAP47053.2021.9391511.

[78] L. F. Herran, A. A. Brazalez, M. N. M. Kehn, and E. Rajo-Iglesias, "Design of Antenna Arrays Using Groove Gap Waveguide Technology Implemented with Glide Symmetric Holes," in *2020 14th European Conference on Antennas and Propagation (EuCAP)*, Mar. 2020, pp. 1–4. DOI: 10.23919/EuCAP48036.2020.9135968.

[79] M. Guo and F. Yang, "W-Band Dual Polarized Array Antenna Based on Gap Waveguide Technology," in *2020 IEEE Asia-Pacific Microwave Conference (APMC)*, Dec. 2020, pp. 317–319. DOI: 10.1109/APMC47863.2020.9331476.

[80] X. Dong, H. Wang, F. Xue, and a. Y. Liu, "Design and Measurement of a Novel Seamless Scanning Leaky Wave Antenna in Ridge Gap Waveguide Technology," *Progress In Electromagnetics Research*, vol. 58, pp. 147–157, 2017, ISSN: 1937-8726. DOI: 10.2528/PIERM17051801.

[81] D. Zarifi, A. Farahbakhsh, A. U. Zaman, and P.-S. Kildal, "Design and Fabrication of a High-Gain 60-GHz Corrugated Slot Antenna Array With Ridge Gap Waveg-

uide Distribution Layer," *IEEE Transactions on Antennas and Propagation*, vol. 64, no. 7, pp. 2905–2913, Jul. 2016, ISSN: 1558-2221. DOI: 10.1109/TAP.2016.2565682.

[82] C. Sánchez-Cabello, L. Inclán-Sánchez, J. Vázquez-Roy, and E. Rajo-Iglesias, "Design of Antenna Feed with Amplified Power Distribution using Groove-Gap Waveguide Technology," in *2017 11th European Conference on Antennas and Propagation (EUCAP)*, Paris, France: IEEE, Mar. 2017, pp. 1661–1664. DOI: 10.23919/EuCAP.2017.7928449.

[83] A. Vosoogh and P.-S. Kildal, "Corporate-Fed Planar 60-GHz Slot Array Made of Three Unconnected Metal Layers Using AMC Pin Surface for the Gap Waveguide," *IEEE Antennas and Wireless Propagation Letters*, vol. 15, pp. 1935–1938, 2016, ISSN: 1548-5757. DOI: 10.1109/LAWP.2015.2510296.

[84] A. Jiménez Sáez, A. Valero-Nogueira, J. I. Herranz, and B. Bernardo, "Single-Layer Cavity-Backed Slot Array Fed by Groove Gap Waveguide," *IEEE Antennas and Wireless Propagation Letters*, vol. 15, pp. 1402–1405, 2016, ISSN: 1548-5757. DOI: 10.1109/LAWP.2015.2511139.

[85] M. Ferrando-Rocher, A. Valero-Nogueira, J. I. Herranz-Herruzo, and J. Teniente, "60 GHz Single-Layer Slot-Array Antenna Fed by Groove Gap Waveguide," *IEEE Antennas and Wireless Propagation Letters*, vol. 18, no. 5, pp. 846–850, May 2019, ISSN: 1548-5757. DOI: 10.1109/LAWP.2019.2903475.

[86] M. Ferrando-Rocher, A. Valero-Nogueira, and J. I. Herranz-Herruzo, "New Feeding Network Topologies for High-Gain Single-Layer Slot Array Antennas using Gap Waveguide Concept," in *2017 11th European Conference on Antennas and Propagation (EUCAP)*, Mar. 2017, pp. 1654–1657. DOI: 10.23919/EuCAP.2017.7928169.

[87] D. Zarifi and H. Oraizi, "A V-band Microstrip Line to Groove Gap Waveguide Transition," in *2016 16th Mediterranean Microwave Symposium (MMS)*, ISSN: 2157-9830, Nov. 2016, pp. 1–2. DOI: 10.1109/MMS.2016.7803803.

[88] U. Nandi, A. U. Zaman, A. Vosoogh, and J. Yang, "Novel Millimeter Wave Transition From Microstrip Line to Groove Gap Waveguide for MMIC Packaging and Antenna Integration," *IEEE Microwave and Wireless Components Letters*, vol. 27, no. 8, pp. 691–693, Aug. 2017, ISSN: 1558-1764. DOI: 10.1109/LMWC.2017.2723679.

[89] A. U. Zaman and P.-S. Kildal, "Packaging of MMIC by Using Gap Waveguide and Design of a Microstrip to Ridge Gap Waveguide Transition," in *2013 Asia-Pacific Microwave Conference Proceedings (APMC)*, ISSN: 2165-4743, Nov. 2013, pp. 10–12. DOI: 10.1109/APMC.2013.6695174.

[90] A. A. Brazález, E. Rajo-Iglesias, J. L. Vázquez-Roy, A. Vosoogh, and P.-S. Kildal, "Design and Validation of Microstrip Gap Waveguides and Their Transitions to Rectangular Waveguide, for Millimeter-Wave Applications," *IEEE Transactions on Microwave Theory and Techniques*, vol. 63, no. 12, pp. 4035–4050, Dec. 2015, ISSN: 1557-9670. DOI: 10.1109/TMTT.2015.2495141.

[91] A. Aljarosha, A. B. Smolders, M. Ivashina, and R. Maaskant, "Toward Wide Band Low Loss Gap Waveguide Integrated Grid Amplifiers," in *2017 International Symposium on Antennas and Propagation (ISAP)*, Oct. 2017, pp. 1–2. DOI: 10.1109/ISANP.2017.8228732.

[92] L. Yijing, H. Yanfei, D. Changjiang, Y. Weihua, and L. Xin, "Terahertz Broadband Ridge Gap Waveguide to Microstrip Line Transition Structure," in *2017 Sixth Asia-Pacific Conference on Antennas and Propagation (APCAP)*, Oct. 2017, pp. 1–3. DOI: 10.1109/APCAP.2017.8420610.

[93] A. A. Brazález, A. U. Zaman, and P.-S. Kildal, "Design of a Coplanar Waveguide-to-Ridge Gap Waveguide Transition Via Capacitive Coupling," in *2012 6th European Conference on Antennas and Propagation (EUCAP)*, ISSN: 2164-3342, Mar. 2012, pp. 3524–3528. DOI: 10.1109/EuCAP.2012.6206372.

[94] A. A. Brazález, E. Rajo-Iglesias, and P.-S. Kildal, "Design of Millimeter-Wave Wideband Gap Waveguide Transitions Considering Integration into the Antenna System," in *2015 9th European Conference on Antennas and Propagation (EuCAP)*, ISSN: 2164-3342, Apr. 2015, pp. 1–5.

[95] A. A. Brazález, E. Rajo-Iglesias, and P. Kildal, "Design of a Transition from WR-15 to Microstrip Packaged by Gap Waveguide Technology," in *2014 International Symposium on Antennas and Propagation Conference Proceedings*, Kaohsiung, Taiwan: IEEE, Dec. 2014, pp. 235–236. DOI: 10.1109/ISANP.2014.7026617.

[96] A. A. Brazález, E. R. Iglesias, and P.-S. Kildal, "Investigation of Transitions for Use in Inverted Microstrip Gap Waveguide Antenna Arrays," in *The 8th European Conference on Antennas and Propagation (EuCAP 2014)*, ISSN: 2164-3342, Apr. 2014, pp. 995–999. DOI: 10.1109/EuCAP.2014.6901932.

[97] B. Molaei and A. Khaleghi, "A Novel Wideband Microstrip Line to Ridge Gap Waveguide Transition Using Defected Ground Slot," *IEEE Microwave and Wireless Components Letters*, vol. 25, no. 2, pp. 91–93, Feb. 2015, ISSN: 1558-1764. DOI: 10.1109/LMWC.2014.2382658.

[98] D. Zarifi and A. Ashrafian, "A Broadband Transition From Microstrip to Groove Gap Waveguide For Ka-Band Applications," in *2020 14th European Conference on Antennas and Propagation (EuCAP)*, Mar. 2020, pp. 1–3. DOI: 10.23919/EuCAP48036.2020.9135460.

[99] Q. Ren, A. U. Zaman, J. Yang, V. Vassilev, and C. Bencivenni, "Millimeter-Wave Vertical Transitions Between Ridge Gap Waveguides and Microstrip Lines for Integration of MMIC with Slot Array," in *2021 15th European Conference on Antennas and Propagation (EuCAP)*, Mar. 2021, pp. 1–4. DOI: 10.23919/EuCAP51087.2021.9411273.

[100] M. Ferrando-Rocher, D. Sanchez-Escuderos, J. I. Herranz-Herruzo, and A. Valero-Nogueira, "Design of Broadband Gap Waveguide Transitions for Millimeter-Wave Antenna Arrays," in *2018 15th European Radar Conference (EuRAD)*, Sep. 2018, pp. 501–504. DOI: 10.23919/EuRAD.2018.8546608.

[101] A. Valero-Nogueira, M. Baquero, J. I. Herranz, J. Domenech, E. Alfonso, and A. Vila, "Gap Waveguides Using a Suspended Strip on a Bed of Nails," *IEEE Antennas and Wireless Propagation Letters*, vol. 10, pp. 1006–1009, 2011, ISSN: 1548-5757. DOI: 10.1109/LAWP.2011.2167591.

[102] H. Raza, J. Yang, and P.-S. Kildal, "Study of the Characteristic Impedance of Gap Waveguide Microstrip Line Realized with Square Metal Pins," in *2013 7th European Conference on Antennas and Propagation (EuCAP)*, Apr. 2013, pp. 3001–3005.

[103] A. Berenguer, M. Baquero-Escudero, D. Sanchez-Escuderos, and F. Vico, "Rigorous Method for Calculating Gap Waveguides Impedance Using Transmission Line Theory," in *The 8th European Conference on Antennas and Propagation (EuCAP 2014)*, ISSN: 2164-3342, Apr. 2014, pp. 2508–2512. DOI: 10.1109/EuCAP.2014.6902328.

[104] J. Liu, J. Yang, and A. U. Zaman, "Analytical Solutions to Characteristic Impedance and Losses of Inverted Microstrip Gap Waveguide Based on Variational Method," *IEEE Transactions on Antennas and Propagation*, vol. 66, no. 12, pp. 7049–7057, Dec. 2018, ISSN: 1558-2221. DOI: 10.1109/TAP.2018.2869204.

[105] A. Berenguer, M. Baquero-Escudero, D. Sánchez-Escuderos, and F. Vico, "Reduction of the Impedance Dependence on the Suspended-Strip Gap Waveguide," in *2014 USNC-URSI Radio Science Meeting (Joint with AP-S Symposium)*, Jul. 2014, pp. 151–151. DOI: 10.1109/USNC-URSI.2014.6955533.

[106] R. Collin, *Foundation of Microwave Engineering*. New York: McGraw-Hill Book Co., 1966.

[107] M. A. Eberspächer and T. F. Eibert, "Bloch Mode Analysis by Even-Odd-Mode Simulations," in *2013 7th European Conference on Antennas and Propagation (EuCAP)*, Apr. 2013, pp. 1021–1023.

[108] M. Smierzchalski and K. Mahdjoubi, "Asymmetric Bloch Impedance for Characterization Bi-Anisotropic Metamaterials," in *2013 7th International Congress on Advanced Electromagnetic Materials in Microwaves and Optics*, Sep. 2013, pp. 430–432. DOI: 10.1109/MetaMaterials.2013.6809076.

[109] E. Takagi, "Frequency Dependence of Bloch Impedance in a Periodic Transmission Line Structure," in *2001 IEEE MTT-S International Microwave Sympsoium Digest (Cat. No.01CH37157)*, ISSN: 0149-645X, vol. 2, May 2001, 779–782 vol.2. DOI: 10.1109/MWSYM.2001.967008.

[110] C. Sabah, F. Urbani, and S. Uckun, "High-Pass Filter Characteristic of Bloch Impedance in a Left-Handed Transmission Line," in *2007 19th International Conference on Applied Electromagnetics and Communications*, Sep. 2007, pp. 1–4. DOI: 10.1109/ICECOM.2007.4544445.

[111] M. E. Durán Zorrilla, "Diseño de Filtros Paso Bajo a Partir de Estructuras Periódicas EBG en Guía de Onda Rectangular con Inserciones Metálicas.," Final Master Thesis, Universidad de Alicante, Alicante, Sep. 2014.

[112] D. Pozar, *Microwave Engineering*, 4th. USA: John Wiley & Sons, Inc., 2011, ISBN: 978-1-118-21363-6.

[113] A. Mangan, S. Voinigescu, M.-T. Yang, and M. Tazlauanu, "De-Embedding Transmission Line Measurements for Accurate Modeling of IC Designs," *IEEE Transactions on Electron Devices*, vol. 53, no. 2, pp. 235–241, Feb. 2006, ISSN: 1557-9646. DOI: 10.1109/TED.2005.861726.

[114] F. Mesa, R. Rodríguez-Berral, and F. Medina, "On the Computation of the Dispersion Diagram of Symmetric One-Dimensionally Periodic Structures," *Symmetry*, vol. 10, no. 8, p. 307, Aug. 2018, ISSN: 2073-8994. DOI: 10.3390/sym10080307.

[115] J. Liu, A. U. Zaman, and P.-S. Kildal, "Optimizing the Numerical Port for Inverted Microstrip Gap Waveguide in Full-wave Simulators," in *2016 10th European Conference on Antennas and Propagation (EuCAP)*, Apr. 2016, pp. 1–5. DOI: 10.1109/EuCAP.2016.7481391.

[116] F. Pizarro, C. Sánchez-Cabello, J.-L. Vazquez-Roy, and E. Rajo-Iglesias, "Considerations of Impedance Sensitivity and Losses in Designing Inverted Microstrip Gap Waveguides," *AEU - International Journal of Electronics and Communications*, vol. 124, p. 153 353, Sep. 2020, ISSN: 1434-8411. DOI: 10.1016/j.aeue.2020.153353.

[117] A. Berenguer, M. Baquero-Escudero, D. Sanchez-Escuderos, and F. Vico, "Suspended-Strip Gap Waveguide Coupled-Line Properties for Ka-Band Component Design," in *2015 9th European Conference on Antennas and Propagation (EuCAP)*, ISSN: 2164-3342, Apr. 2015, pp. 1–5.

[118] J. Papapolymerou, J.-C. Cheng, J. East, and L. Katehi, "A Micromachined High-Q X-Band Resonator," *IEEE Microwave and Guided Wave Letters*, vol. 7, no. 6, pp. 168–170, Jun. 1997, ISSN: 1558-2329. DOI: 10.1109/75.585207.

[119] C. Chen-Yu, "Planar Microwave and Millimeter-Wave Components Using Micromachining Technologies," EN, Thesis, University of Michigan, USA, 1995. [Online]. Available: http://deepblue.lib.umich.edu/handle/2027.42/129676.

[120] D. Kajfez, *Q factor*, English. Oxford, Mississippi: Vector Fields, 1994, ISBN: 978-0-930071-06-6.

[121] E. Pucci, A. U. Zaman, E. Rajo-Iglesias, P. Kildal, and A. Kishk, "Study of Q-factors of Ridge and Groove Gap Waveguide Resonators," *IET Microwaves, Antennas & Propagation*, vol. 7, no. 11, pp. 900–908, Aug. 2013, ISSN: 1751-8733. DOI: 10.1049/iet-map.2013.0081.

[122] E. Rajo-Iglesias, M. Ferrando-Rocher, and A. U. Zaman, "Gap Waveguide Technology for Millimeter-Wave Antenna Systems," *IEEE Communications Magazine*, vol. 56, no. 7, pp. 14–20, Jul. 2018, ISSN: 1558-1896. DOI: 10.1109/MCOM.2018.1700998.

[123] A. A. Brazález, E. Rajo-Iglesias, and P. Kildal, "Design of Millimeter-wave Wideband Gap Waveguide Transitions Considering Integration into the Antenna System," in *2015 9th European Conference on Antennas and Propagation (EuCAP)*, Lisbon, Portugal: IEEE, Apr. 2015, pp. 1–5, ISBN: 2164-3342. [Online]. Available: https://ieeexplore.ieee.org/document/7228420.

[124] E. Rajo-Iglesias and A. A. Brazález, "5G Antenna in Inverted Microstrip Gap Waveguide Technology Including a Transition to Microstrip," in *2016 International Symposium on Antennas and Propagation (ISAP)*, Okinawa, Japan: IEEE, Oct. 2016, pp. 1042–1043. [Online]. Available: https://ieeexplore.ieee.org/document/7821321.

[125] C. Sanchez-Cabello, L. F. Herran, and E. Rajo-Iglesias, "Ka-Band Diplexer for 5G mmWave Applications in Inverted Microstrip Gap Waveguide Technology," *Electronics*, vol. 9, no. 12, p. 2094, Dec. 2020. DOI: 10.3390/electronics9122094.

[126] A. Vosoogh, A. A. Brazález, and P.-S. Kildal, "A V-Band Inverted Microstrip Gap Waveguide End-Coupled Bandpass Filter," *IEEE Microwave and Wireless Components Letters*, vol. 26, no. 4, pp. 261–263, Apr. 2016, ISSN: 1558-1764. DOI: 10.1109/LMWC.2016.2538598.

[127] J.-S. Hong, "Lowpass and Bandpass Filters," in *Microstrip Filters for RF / Microwave Applications*, 2nd, Hoboken, New Jersey: John Wiley & Sons, Inc., 2011, pp. 112–161, ISBN: 978-0-470-40877-3.

[128] D.-J. Jung and K. Chang, "Microstrip Diplexer Design for X-Band RF/Microwave Front-end Applications," in *2011 IEEE International Symposium on Antennas and Propagation (APSURSI)*, ISSN: 1947-1491, Jul. 2011, pp. 5–7. DOI: 10.1109/APS.2011.5996367.

[129] A. K. Keskin, M. Dagcan Senturk, S. Demirel, A. Kizilay, and A. S. Turk, "Front-end Design for Ka Band mm-Wave Radar," in *2016 17th International Radar Symposium (IRS)*, ISSN: 2155-5753, May 2016, pp. 1–4. DOI: 10.1109/IRS.2016.7497267.

[130] M. Mbeutcha, T. K. Johansen, Y. Dong, B. Cimoli, and V. Krozer, "Replicability of a Millimeter-Wave Microstrip Bandpass Filter using Parallel Coupled Lines," in *2018 IEEE MTT-S Latin America Microwave Conference (LAMC 2018)*, Dec. 2018, pp. 1–3. DOI: 10.1109/LAMC.2018.8699012.

[131] Q.-h. Zhang, Y.-l. Dong, and J.-g. Cao, "Dual-mode Bandpass Filter Using Microstrip SIR at Ka Band," in *2009 Asia Pacific Microwave Conference*, ISSN: 2165-4743, Dec. 2009, pp. 1401–1404. DOI: 10.1109/APMC.2009.5384502.

[132] W. Zhao, Y. Zhang, and Y. Guo, "A Novel Ka-Band Bandpass Filter Using Microstrip Closed Loop Resonators," in *2009 Asia Pacific Microwave Conference*, ISSN: 2165-4743, Dec. 2009, pp. 1443–1445. DOI: 10.1109/APMC.2009.5384492.

[133] M. S. Sorkherizi and A. A. Kishk, "Lowloss Planar Bandpass Filters for Millimeter-Wave Application," in *2015 IEEE MTT-S International Microwave Symposium*, ISSN: 0149-645X, May 2015, pp. 1–4. DOI: 10.1109/MWSYM.2015.7167028.

[134] J. Liu, A. U. Zaman, and P.-S. Kildal, "Design of Transition from WR-15 to Inverted Microstrip Gap Waveguide," in *2016 Global Symposium on Millimeter Waves (GSMM) ESA Workshop on Millimetre-Wave Technology and Applications*, Jun. 2016, pp. 1–4. DOI: 10.1109/GSMM.2016.7500320.

[135] I. Ashiq and A. Khanna, "A Novel Ultra-Broadband DC-36-to-66-GHz Hybrid Diplexer Using Waveguide and SSL Technology," in *2014 44th European Microwave Conference*, Oct. 2014, pp. 1111–1114. DOI: 10.1109/EuMC.2014.6986634.

[136] S. Setoodeh, R. R. Mansour, and D. Gupta, "Multi-Layer Low Temperature Superconducting K-Band Filter and Diplexer Design," in *2013 IEEE MTT-S International Microwave Symposium Digest (MTT)*, Jun. 2013, pp. 1–4. DOI: 10.1109/MWSYM.2013.6697798.

[137] A. Brown and G. Rebeiz, "A High-Performance Integrated K-Band Diplexer," *IEEE Transactions on Microwave Theory and Techniques*, vol. 47, no. 8, pp. 1477–1481, Aug. 1999, ISSN: 1557-9670. DOI: 10.1109/22.780398.

[138] R. Bairavasubramanian, S. Pinel, J. Laskar, and J. Papapolymerou, "Compact 60-GHz Bandpass Filters and Duplexers on Liquid Crystal Polymer Technology," *IEEE Microwave and Wireless Components Letters*, vol. 16, no. 5, pp. 237–239, May 2006, ISSN: 1558-1764. DOI: 10.1109/LMWC.2006.873591.

[139] S. Hong and K. Chang, "Stub-Tuned Microstrip Bandpass Filters for Millimeter-Wave Diplexer Design," *IEEE Microwave and Wireless Components Letters*, vol. 15, no. 9, pp. 582–584, Sep. 2005, ISSN: 1558-1764. DOI: 10.1109/LMWC.2005.855376.

[140] D. Wang, K.-S. Chin, W. Che, C.-C. Chang, and Y. Wu, "60 GHz Duplexer Design Using Dual-Mode SIW Filters with Single-Sided Transmission Zeros," en, *Electronics Letters*, vol. 50, no. 21, pp. 1529–1531, 2014, ISSN: 1350-911X. DOI: 10.1049/el.2014.1288.

[141] P. Zurek, T. Cappello, and Z. Popovic, "Broadband Diplexed Power Amplifier," *IEEE Microwave and Wireless Components Letters*, vol. 30, no. 11, pp. 1073–1076, Nov. 2020, ISSN: 1558-1764. DOI: 10.1109/LMWC.2020.3026050.

[142] A. Rezaei and L. Noori, "Miniaturized Microstrip Diplexer with High Performance Using a Novel Structure for Wireless L-Band Applications," *Wireless Networks*, vol. 26, Apr. 2020. DOI: 10.1007/s11276-018-1870-5.

[143] I. Álvarez Olmos, "Implementación de la Técnica Monopulso para un Sistema de Array Digital en Recepción de Ocho Canales en Banda X," spa, Bachelor Thesis,

E.T.S.I. Telecomunicación (UPM), Madrid, Spain, 2018. [Online]. Available: https://oa.upm.es/49480/.

[144] S. M. Sherman and D. K. Barton, *Monopulse Principles and Techniques*, en. Artech House, 2011, ISBN: 978-1-60807-175-3.

[145] O. Quevedo-Teruel, G. Valerio, Z. Sipus, and E. Rajo-Iglesias, "Periodic Structures With Higher Symmetries: Their Applications in Electromagnetic Devices," *IEEE Microwave Magazine*, vol. 21, no. 11, pp. 36–49, Nov. 2020, ISSN: 1557-9581. DOI: 10.1109/MMM.2020.3014987.

[146] Z. Sipus, K. Cavar, and M. Bosiljevac, "Waveguide Technology Based on Glide-Symmetric Holey Structures: Design Considerations," in *2020 International Workshop on Antenna Technology (iWAT)*, Feb. 2020, pp. 1–4. DOI: 10.1109/iWAT48004.2020.1570609938.

[147] G. Valerio, F. Ghasemifard, Z. Sipus, and O. Quevedo-Teruel, "Glide-Symmetric All-Metal Holey Metasurfaces for Low-Dispersive Artificial Materials: Modeling and Properties," *IEEE Transactions on Microwave Theory and Techniques*, vol. 66, no. 7, pp. 3210–3223, Jul. 2018, ISSN: 1557-9670. DOI: 10.1109/TMTT.2018.2829885.

[148] M. Ebrahimpouri, E. Rajo-Iglesias, Z. Sipus, and O. Quevedo-Teruel, "Cost-Effective Gap Waveguide Technology Based on Glide-Symmetric Holey EBG Structures," *IEEE Transactions on Microwave Theory and Techniques*, vol. 66, no. 2, pp. 927–934, Feb. 2018, ISSN: 1557-9670. DOI: 10.1109/TMTT.2017.2764091.

[149] O. Quevedo-Teruel, "Overview on Glide-Symmetric Periodic Structures," in *2021 International Symposium on Antennas and Propagation (ISAP)*, Oct. 2021, pp. 1–2. DOI: 10.23919/ISAP47258.2021.9614551.

[150] O. Quevedo-Teruel, Q. Chen, F. Mesa, N. J. G. Fonseca, and G. Valerio, "On the Benefits of Glide Symmetries for Microwave Devices," *IEEE Journal of Microwaves*, vol. 1, no. 1, pp. 457–469, 2021, ISSN: 2692-8388. DOI: 10.1109/JMW.2020.3033847.

[151] Q. Chen, F. Mesa, X. Yin, and O. Quevedo-Teruel, "Accurate Characterization and Design Guidelines of Glide-Symmetric Holey EBG," *IEEE Transactions on*

Microwave Theory and Techniques, vol. 68, no. 12, pp. 4984–4994, Dec. 2020, ISSN: 1557-9670. DOI: 10.1109/TMTT.2020.3023751.

[152] Q. Liao, E. Rajo-Iglesias, and O. Quevedo-Teruel, "Groove Gap Waveguide Slot Array Based on Glide-Symmetric Holes," in *2020 14th European Conference on Antennas and Propagation (EuCAP)*, Mar. 2020, pp. 1–4. DOI: 10.23919/EuCAP48036.2020.9135299.

[153] M. Ebrahimpouri, E. Rajo-Iglesias, Z. Sipus, and O. Quevedo-Teruel, "Cost-Effective Gap Waveguide Technology Based on Glide-Symmetric Holey EBG Structures," *IEEE Transactions on Microwave Theory and Techniques*, vol. 66, no. 2, pp. 927–934, Feb. 2018, ISSN: 1557-9670. DOI: 10.1109/TMTT.2017.2764091.

[154] M. Ebrahimpouri, E. Rajo-Iglesias, and O. Quevedo-Teruel, "Wideband Glide Symmetric Holey Structures for Gap-Waveguide Technology," in *2017 11th European Conference on Antennas and Propagation (EUCAP)*, Paris, France: IEEE, Mar. 2017, pp. 1658–1660. DOI: 10.23919/EuCAP.2017.7928356.

[155] C. Sanchez-Cabello, Z. Sipus, and E. Rajo-Iglesias, "Consideration in Designing Holey Glided-Symmetrical Structures in Gap Waveguide," in *2022 Mediterranean Microwave Symposium*, Pizzo Calabro, Italy, May 2022.

[156] H. Sun, C. Yu, and X.-W. Zhu, "A Ka-Band Planar Compatible Traveling-Wave Spatial Power Combining Amplifier Based on Riblet Coupler," in *2017 IEEE Asia Pacific Microwave Conference (APMC)*, Nov. 2017, pp. 41–44. DOI: 10.1109/APMC.2017.8251372.

[157] J. A. Ruiz-Cruz, J. R. Montejo-Garai, J. M. Rebollar, A. I. Daganzo, and I. Hidalgo-Carpintero, "Design of Riblet-type Couplers for Ka Band Applications," in *2007 IEEE Antennas and Propagation Society International Symposium*, Jun. 2007, pp. 4276–4279. DOI: 10.1109/APS.2007.4396486.

[158] R. Toreinia and R. Safian, "Design and Tuning of Wideband Two-Layer Substrate Integrated Waveguide Drectional Couplers," in *6th International Symposium on Telecommunications (IST)*, Nov. 2012, pp. 70–74. DOI: 10.1109/ISTEL.2012.6482957.

[159] B. Hussain, "Short-Slot Hybrid Coupler in Gap Waveguides at 38 GHz," Ph.D. dissertation, Chalmers University of Technology, Göteborg, Sweden, Jun. 2011.

[160] L. F. Herrán, A. Algaba Brazalez, and E. Rajo-Iglesias, "Ka-Band Planar Slotted Waveguide Array Based On Groove Gap Waveguide Technology with a Glide-Symmetric Holey Metasurface," *Scientific Reports*, vol. 11, no. 1, p. 8697, Apr. 2021, ISSN: 2045-2322. DOI: 10.1038/s41598-021-88054-5.

[161] M. Ng Mou Kehn, C.-K. Hsieh, and E. Rajo-Iglesias, "Array of Horns Fed by a Transverse Slotted Groove Gap Waveguide at 28 GHz," *Sensors*, vol. 20, no. 18, p. 5311, Jan. 2020, ISSN: 1424-8220. DOI: 10.3390/s20185311.

[162] E. Rajo-Iglesias, M. Ebrahimpouri, and O. Quevedo-Teruel, "Wideband Phase Shifter in Groove Gap Waveguide Technology Implemented With Glide-Symmetric Holey EBG," *IEEE Microwave and Wireless Components Letters*, vol. 28, no. 6, pp. 476–478, Jun. 2018, ISSN: 1558-1764. DOI: 10.1109/LMWC.2018.2832013.

[163] C. A. Balanis, *Advanced Engineering Electromagnetics, 2nd Edition*. May 2012, ISBN: 978-0-470-58948-9.

[164] R. E. Collin, *Antennas and Radiowave Propagation*, en. McGraw-Hill, 1985, ISBN: 978-0-07-011808-9.

[165] A. Leggieri, F. Di Paolo, and D. Passi, "Thermal and Solid-Mechanics FEM Simulation of a Microwave Spatial Power Combiner Amplifier," in *Comsol Conference*, Rotterdam, NL, Nov. 2013.

[166] J. Mink, "Quasi-Optical Power Combining of Solid-State Millimeter-Wave Sources," *IEEE Transactions on Microwave Theory and Techniques*, vol. 34, no. 2, pp. 273–279, Feb. 1986, ISSN: 1557-9670. DOI: 10.1109/TMTT.1986.1133322.

[167] R. A. York and Z. B. Popovic, *Active and Quasi-Optical Arrays for Solid-State Power Combining*. May 2008.

[168] H. T. Than, G. W. Sun, G. S. Cuellar, *et al.*, "A 600-W C-Band Amplifier Using Spatially Combined GaAs FETs," in *2011 IEEE Compound Semiconductor Integrated Circuit Symposium (CSICS)*, ISSN: 2374-8443, Oct. 2011, pp. 1–4. DOI: 10.1109/CSICS.2011.6062434.

[169] B. Deckman, D. Deakin, E. Sovero, and D. Rutledge, "A 5-Watt, 37-GHz Monolithic Grid Amplifier," in *2000 IEEE MTT-S International Microwave Symposium Digest (Cat. No.00CH37017)*, ISSN: 0149-645X, vol. 2, Jun. 2000, 805–808 vol.2. DOI: 10.1109/MWSYM.2000.863303.

[170] S. Ortiz, J. Hubert, L. Mirth, E. Schlecht, and A. Mortazawi, "A 25 Watt and 50 Watt Ka-Band Quasi-optical Amplifier," in *2000 IEEE MTT-S International Microwave Symposium Digest (Cat. No.00CH37017)*, ISSN: 0149-645X, vol. 2, Jun. 2000, 797–800 vol.2. DOI: 10.1109/MWSYM.2000.863301.

[171] N.-S. Cheng, P. Jia, D. Rensch, and R. York, "A 120-W X-Band Spatially Combined Solid-State Amplifier," *IEEE Transactions on Microwave Theory and Techniques*, vol. 47, no. 12, pp. 2557–2561, Dec. 1999, ISSN: 1557-9670. DOI: 10.1109/22.809006.

[172] J. Sowers, D. Pritchard, A. White, *et al.*, "A 36 W, V-Band, Solid State Source," in *1999 IEEE MTT-S International Microwave Symposium Digest (Cat. No.99CH36282)*, vol. 1, Jun. 1999, 235–238 vol.1. DOI: 10.1109/MWSYM.1999.779465.

[173] A. Alexanian and R. York, "Broadband Spatially Combined Amplifier Array Using Tapered Slot Transitions in Waveguide," *IEEE Microwave and Guided Wave Letters*, vol. 7, no. 2, pp. 42–44, Feb. 1997, ISSN: 1558-2329. DOI: 10.1109/75.553053.

[174] J. Schoenberg and Z. Popovic, "Planar Lens Amplifier," in *1994 IEEE MTT-S International Microwave Symposium Digest (Cat. No.94CH3389-4)*, ISSN: 0149-645X, May 1994, 429–432 vol.1. DOI: 10.1109/MWSYM.1994.335424.

[175] A. Algaba Brazález, J. Flygare, J. Yang, V. Vassilev, M. Baquero-Escudero, and P.-S. Kildal, "Design of F-Band Transition From Microstrip to Ridge Gap Waveguide Including Monte Carlo Assembly Tolerance Analysis," *IEEE Transactions on Microwave Theory and Techniques*, vol. 64, no. 4, pp. 1245–1254, Apr. 2016, ISSN: 1557-9670. DOI: 10.1109/TMTT.2016.2535334.

[176] A. Aljarosha, R. Maaskant, A. U. Zaman, and P.-S. Kildal, "MM-Wave Contactless Connection for MMIC Integration in Gap Waveguides," in *2016 IEEE International Symposium on Antennas and Propagation (APSURSI)*, ISSN: 1947-1491, Jun. 2016, pp. 253–254. DOI: 10.1109/APS.2016.7695835.

[177] A. A. Brazález, E. Rajo-Iglesias, and P.-S. Kildal, "Design of a Transition from WR-15 to Microstrip Packaged by Gap Waveguide Technology," in *2014 International Symposium on Antennas and Propagation Conference Proceedings*, Dec. 2014, pp. 235–236. DOI: 10.1109/ISANP.2014.7026617.

[178] N. Memeletzoglou and E. Rajo-Iglesias, "Array of Stacked Leaky-Wave Antennas in Groove Gap Waveguide Technology," en, *Scientific Reports*, vol. 11, no. 1, p. 2260, Jan. 2021, ISSN: 2045-2322. DOI: 10.1038/s41598-021-81640-7.

[179] B. Ahmadi and A. Banai, "Substrateless Amplifier Module Realized by Ridge Gap Waveguide Technology for Millimeter-Wave Applications," *IEEE Transactions on Microwave Theory and Techniques*, vol. 64, no. 11, pp. 3623–3630, Nov. 2016, ISSN: 1557-9670. DOI: 10.1109/TMTT.2016.2607177.

[180] *MAAM-011101*. [Online]. Available: https://www.macom.com/products/product-detail/MAAM-011101 (visited on 06/10/2022).

[181] C. Sánchez-Cabello, L. F. Herrán, A. U. Zaman, and E. Rajo-Iglesias, "Ka Band Microstrip Fed Slot Array Antenna with PMC Packaging," *IET Microwaves, Antennas & Propagation*, vol. 14, no. 14, pp. 1837–1845, Nov. 2020, ISSN: 1751-8733. DOI: 10.1049/iet-map.2020.0565.

[182] Y. Miura, J. Hirokawa, M. Ando, Y. Shibuya, and G. Yoshida, "Double-Layer Full-Corporate-Feed Hollow-Waveguide Slot Array Antenna in the 60-GHz Band," *IEEE Transactions on Antennas and Propagation*, vol. 59, no. 8, pp. 2844–2851, Aug. 2011, ISSN: 1558-2221. DOI: 10.1109/TAP.2011.2158784.

[183] A. Farahbakhsh, D. Zarifi, and A. U. Zaman, "A mmWave Wideband Slot Array Antenna Based on Ridge Gap Waveguide With 30% Bandwidth," *IEEE Transactions on Antennas and Propagation*, vol. 66, no. 2, pp. 1008–1013, Feb. 2018, ISSN: 1558-2221. DOI: 10.1109/TAP.2017.2782263.

[184] J. Liu, A. Vosoogh, A. U. Zaman, and J. Yang, "A Slot Array Antenna With Single-Layered Corporate-Feed Based on Ridge Gap Waveguide in the 60 GHz Band," *IEEE Transactions on Antennas and Propagation*, vol. 67, no. 3, pp. 1650–1658, Mar. 2019, ISSN: 1558-2221. DOI: 10.1109/TAP.2018.2888730.

[185] D. Zarifi, A. Farahbakhsh, and A. U. Zaman, "A Gap Waveguide-Fed Wideband Patch Antenna Array for 60-GHz Applications," *IEEE Transactions on Antennas and Propagation*, vol. 65, no. 9, pp. 4875–4879, Sep. 2017, ISSN: 1558-2221. DOI: 10.1109/TAP.2017.2722866.

[186] D.-F. Guan, Z.-P. Qian, Y.-S. Zhang, and Y. Cai, "Novel SIW Cavity-Backed Antenna Array Without Using Individual Feeding Network," *IEEE Antennas and Wireless Propagation Letters*, vol. 13, pp. 423–426, 2014, ISSN: 1548-5757. DOI: 10.1109/LAWP.2014.2308291.

[187] D.-F. Guan, C. Ding, Z.-P. Qian, Y.-S. Zhang, W.-Q. Cao, and E. Dutkiewicz, "An SIW-Based Large-Scale Corporate-Feed Array Antenna," *IEEE Transactions on Antennas and Propagation*, vol. 63, no. 7, pp. 2969–2976, Jul. 2015, ISSN: 1558-2221. DOI: 10.1109/TAP.2015.2430369.

[188] E. Rajo-Iglesias, A. U. Zaman, and P. Kildal, "Parallel Plate Cavity Mode Suppression in Microstrip Circuit Packages Using a Lid of Nails," *IEEE Microwave and Wireless Components Letters*, vol. 20, no. 1, pp. 31–33, Jan. 2010, ISSN: 1558-1764. DOI: 10.1109/LMWC.2009.2035960.

[189] A. U. Zaman, M. Alexanderson, T. Vukusic, and P.-S. Kildal, "Gap Waveguide PMC Packaging for Improved Isolation of Circuit Components in High-Frequency Microwave Modules," *IEEE Transactions on Components, Packaging and Manufacturing Technology*, vol. 4, no. 1, pp. 16–25, Jan. 2014, ISSN: 2156-3985. DOI: 10.1109/TCPMT.2013.2271651.

[190] M. Li and K.-M. Luk, "A Low-Profile Unidirectional Printed Antenna for Millimeter-Wave Applications," *IEEE Transactions on Antennas and Propagation*, vol. 62, no. 3, pp. 1232–1237, Mar. 2014, ISSN: 1558-2221. DOI: 10.1109/TAP.2013.2295832.

[191] M. H. Awida, S. H. Suleiman, and A. E. Fathy, "Substrate-Integrated Cavity-Backed Patch Arrays: A Low-Cost Approach for Bandwidth Enhancement," *IEEE Transactions on Antennas and Propagation*, vol. 59, no. 4, pp. 1155–1163, Apr. 2011, ISSN: 1558-2221. DOI: 10.1109/TAP.2011.2109681.

[192] X.-P. Chen, K. Wu, L. Han, and F. He, "Low-Cost High Gain Planar Antenna Array for 60-GHz Band Applications," *IEEE Transactions on Antennas and Propagation*, vol. 58, no. 6, pp. 2126–2129, Jun. 2010, ISSN: 1558-2221. DOI: 10.1109/TAP.2010.2046861.

[193] K. Kibaroglu, M. Sayginer, T. Phelps, and G. M. Rebeiz, "A 64-Element 28-GHz Phased-Array Transceiver With 52-dBm EIRP and 8–12-Gb/s 5G Link at 300 Meters Without Any Calibration," *IEEE Transactions on Microwave Theory and Techniques*, vol. 66, no. 12, pp. 5796–5811, Dec. 2018, ISSN: 1557-9670. DOI: 10.1109/TMTT.2018.2854174.